



HAL
open science

Optimization of the Advanced LIGO gravitational-wave detectors duty cycle by reduction of parametric instabilities and environmental impacts

Sébastien Biscans

► **To cite this version:**

Sébastien Biscans. Optimization of the Advanced LIGO gravitational-wave detectors duty cycle by reduction of parametric instabilities and environmental impacts. Mechanics of materials [physics.class-ph]. Le Mans Université, 2018. English. NNT : 2018LEMA1019 . tel-01893462

HAL Id: tel-01893462

<https://theses.hal.science/tel-01893462>

Submitted on 11 Oct 2018

HAL is a multi-disciplinary open access archive for the deposit and dissemination of scientific research documents, whether they are published or not. The documents may come from teaching and research institutions in France or abroad, or from public or private research centers.

L'archive ouverte pluridisciplinaire **HAL**, est destinée au dépôt et à la diffusion de documents scientifiques de niveau recherche, publiés ou non, émanant des établissements d'enseignement et de recherche français ou étrangers, des laboratoires publics ou privés.

THÈSE DE DOCTORAT DE

LE MANS UNIVERSITÉ
COMUE UNIVERSITÉ BRETAGNE LOIRE

ÉCOLE DOCTORALE N°602
Sciences pour l'Ingénieur
Spécialité : *Mécanique des Solides, des Matériaux, des structures et des surfaces*

Par

Sébastien BISCANS

Optimization of the Advanced LIGO gravitational-wave detectors duty cycle by reduction of parametric instabilities and environmental impacts

Optimisation du cycle de service de l'observatoire d'ondes gravitationnelles LIGO par réduction des instabilités paramétriques et des impacts environnementaux

Thèse présentée et soutenue au Mans, le 21 septembre 2018

Unité de recherche: Laboratoire d'Acoustique de l'Université du Maine – UMR CNRS 6613

Thèse N°: 2018LEMA1019

Rapporteurs avant soutenance :

Christophe COLLETTE, Professeur étranger, Université libre de Bruxelles, Bruxelles

Emmanuel FOLTÊTE, Professeur des Universités, FEMTO-ST, Besançon

Composition du Jury :

Président :

Matteo BARSUGLIA, Directeur de Recherche CNRS, Université Paris Diderot – Astroparticule et Cosmologie, Paris

Examineurs :

Simon CHESNE, Maître de conférences, INSA Lyon, Villeurbanne

Cécile Guianvarc'h, Maître de conférences, CNAM, Paris

Dir. de thèse :

Charles PEZERAT, Professeur des Universités, Université du Maine, Le Mans

Co-dir. de thèse :

Pascal PICART, Professeur des Universités, Université du Maine, Le Mans

Co-encadrant de thèse :

Matthew EVANS, Professeur étranger, Massachusetts Institute of Technology, Cambridge

Invité :

David SHOEMAKER, porte-parole pour la Collaboration Scientifique LIGO, Massachusetts Institute of Technology, Cambridge

Optimization of the Advanced LIGO gravitational-wave detectors duty cycle by reduction of parametric instabilities and environmental impacts

Keywords: gravitational-wave, seismic isolation, earthquake, controls, parametric instability, materials, mechanics, optics.

Abstract

The LIGO project (Laser Interferometer Gravitational-Wave Observatory) is a large-scale physics experiment the goal of which is to detect and study gravitational waves of astrophysical origin. It is composed of two instruments identical in design, one located in Hanford, WA and the other in Livingston, LA in the United States. The two instruments are specialized versions of a Michelson interferometer with 4km-long arms. They observed a gravitational-wave signal for the first time in September 2015 from the merger of two stellar-mass black holes. This is the first direct detection of a gravitational wave and the first direct observation of a binary black hole merger. Five more detections from binary black hole mergers and neutron stars merger have been reported to date, marking the beginning of a new era in astrophysics. As a result of these detections, many activities within the LIGO collaboration are in progress to improve the duty cycle and sensitivity of the detectors. This thesis has been conducted at the Massachusetts Institute of Technology (MA, USA), as part of the LIGO Research & Development activities. It addresses two major issues limiting the duty cycle of the LIGO detectors: environmental impacts, especially earthquakes, and the issue of unstable opto-mechanical couplings in the cavities, referred to as parametric instabilities.

Earthquakes

LIGO requires an unprecedented level of isolation from the ground. When in operation, the interferometers are expected to measure motion of less than 10^{-19} meters. Strong teleseismic events like earthquakes disrupt the operation of the detectors, and result in a loss of data until the detectors can be returned to their operating states. A variety of seismic control strategies have been studied to reduce the downtime due to earthquakes. Early results have shown a downtime reduction of $\sim 40\%$ at one of the LIGO sites, thus suggesting that this strategy can significantly reduce the impact of earthquakes on the LIGO detectors. Other strategies have also shown promising results but will have to be tested in the future. We present a plan to implement these new earthquake configurations in the LIGO automation system.

Parametric instabilities

A parametric instability results from an opto-mechanical coupling between the mechanical modes of a mirror and the optical modes of the cavity. In the case of the LIGO interferometers, the large amount of stored optical power and high mechani-

cal quality factors of the optics lead to instabilities. These instabilities prevent the interferometers from functioning at high power, therefore limiting their duty cycles and sensitivities. To reduce these instabilities, an electro-mechanical device, called 'Acoustic Mode Damper' (AMD), has been designed and tested to damp the mechanical modes associated with parametric instabilities. Measurements have shown a significant reduction in the quality factor of several mechanical modes in accordance with our model. This suggests that AMDs should solve the issue of parametric instabilities for LIGO.

In conclusion, we will show that the issues tackled in this thesis improved the overall duty cycle of LIGO by 4.6%, which corresponds to an increase of the gravitational-wave detection rate by 14%.

Optimisation du cycle de service de l'observatoire d'ondes gravitationnelles LIGO par réduction des instabilités paramétriques et des impacts environnementaux.

Mots clés: onde gravitationnelle, isolation sismique, tremblement de terre, contrôle, instabilité paramétrique, matériau, mécanique, optique.

Résumé

Le projet LIGO (pour Laser Interferometer Gravitational-Wave Observatory) a pour but la détection et l'étude d'ondes gravitationnelles via un réseau de détecteurs. LIGO possède deux détecteurs d'architecture et de fonctionnement identiques, l'un situé dans l'État de Washington et l'autre dans l'État de Louisiane aux États-Unis. Chaque détecteur est une version considérablement améliorée d'un interféromètre de Michelson avec des bras optiques de 4 km de long. Ces interféromètres ont observés le signal émis par un trou noir binaire sous la forme d'une onde gravitationnelle pour la première fois en septembre 2015. Depuis, cinq autres détections ont été réalisées par les observatoires de LIGO. Ces détections marquent le début d'une nouvelle ère pour l'astrophysique, en liaison étroite avec la physique des trous noirs et des étoiles à neutrons.

Malgré ces détections, un grand nombre d'activités de la collaboration scientifique de LIGO sont en développement pour perfectionner les interféromètres. Cette thèse s'est déroulée au Massachusetts Institute of Technology (MA, USA), et s'inscrit dans le cadre du programme de recherche et développement du laboratoire LIGO. Elle a pour objectif d'améliorer le temps de service des détecteurs, en répondant en particulier à deux problématiques majeures: le problème des impacts environnementaux, et notamment celui des tremblements de terre, ainsi que le problème des instabilités paramétriques.

Tremblements de terre

LIGO requiert des besoins sans précédent en termes d'isolation sismique. Chaque interféromètre doit être capable de mesurer un mouvement de l'ordre de 10^{-19} mètres. L'importante amplification de l'activité sismique générée par certains tremblements de terre peut ainsi empêcher l'interféromètre de fonctionner correctement. Plusieurs stratégies de contrôle actif ont été étudiées pour réduire les périodes d'instabilités durant de tels événements. Les résultats préliminaires montrent une réduction du temps d'arrêt généré par les tremblements de terre d'environ 40% à un des observatoires. D'autres stratégies ont été développées et seront testées dans le futur. Un plan pour utiliser ces stratégies via le système d'automatisation de LIGO est présenté.

Instabilités paramétriques

Une instabilité paramétrique provient d'un couplage opto-mécanique entre le mode mécanique d'un miroir et un ou plusieurs mode(s) de cavité. Dans le cas des interféromètres de LIGO qui opèrent à haute puissance, ce couplage peut devenir rapidement instable. Ces instabilités empêchent les interféromètres de fonctionner correctement, limitant leur cycle de service et sensibilité. Pour pallier à ce problème, un amortisseur électromécanique, appelé 'Acoustic Mode Damper' (AMD) a été conçu et développé. Il permet de considérablement réduire le facteur de qualité des modes mécaniques problématiques, et par-delà même les instabilités. D'après le modèle et les premières mesures, les AMDs devraient complètement résoudre le problème des instabilités paramétriques pour LIGO.

En conclusion, il sera démontré en quoi les problématiques résolues pendant ce travail de thèse ont permis d'améliorer le cycle de service des détecteurs de LIGO de 4.6%, ce qui correspond à une augmentation du nombre d'ondes gravitationnelles détectées par an de 14%.

Acknowledgements

Over the years, before and during my thesis, LIGO has always been a fascinating, engaging challenge. It has been a singular privilege to interact and work with the numerous scientists of the LIGO Scientific Collaboration. This is a very long list of people, and it is not possible to name them all. However, I would be remiss not to draw attention to a certain number of people.

First, I would like to express my gratitude and appreciation to Dr Christophe Collette and Dr Emmanuel Foltête for reviewing this work as *rapporteurs*. My thanks also go to Dr Matteo Barsuglia, Dr Simon Chesne, Dr Cécile Guianvarc'h and Dr David Shoemaker for being part of this committee.

My supervisors in France, Charles Pezerat and Pascal Picart, deserve special thanks as well. Despite me being on the other side of the world, Charles and Pascal always seemed to know what I was doing better than I did. Without their knowledge, insight and guidance I'd never have made it this far.

Same goes to my supervisor at MIT, Matthew Evans, who is one of the most knowledgeable person I know. His guidance and vision on a project like LIGO has shaped what makes me a scientist today. Thank you Matt especially for your patience and the time you took for me.

Next, I have to give a special shout-out to the brilliant Slawek Gras, with whom I worked many (too many) hours in the lab on the AMD project. Thank you Slawek for the extra-hours you took for me, for your guidance, your advice, and the many coffees and beers. A-team forever.

Special thanks also to Richard Mittleman for putting up with me over all those years. Don't worry Rich, I still have a lot of stupid questions for you.

Thanks to Peter Fritschel for supporting me and giving me a fascinating project to work on. Thanks to Myron for all the help downstairs, could not have done it without you. Thanks to Betsy and Travis for the help and laughs in chamber and on the bocce court. Thanks to the Livingston team for making sure I always have a good time on site. Thanks to Rainer Weiss for this crazy project.

Lastly, to the loved ones in my life. To my mum, dad and sister, without you I wouldn't be where I am now. Thank you for your patience, love and for always believing in me.

To Astrid: we survived. See? It wasn't that hard! We can start living our life now...



Contents

1	Introduction	33
1.1	Gravitational radiation	33
1.2	Sources	34
1.2.1	Binary inspirals	35
1.2.2	Supernovae bursts	35
1.2.3	Continuous waves	36
1.2.4	Stochastic background	36
1.3	Interferometric gravitational-wave detectors	36
1.3.1	Michelson	36
1.3.2	Fabry-Perot arm cavities	37
1.3.3	Power and signal recycling	37
1.4	Detectors around the world	38
2	LIGO	41
2.1	Introduction	41
2.2	Detections	42
2.2.1	GW150914	42

2.2.2	GW151226	43
2.2.3	GW170104	43
2.2.4	GW170608	44
2.2.5	GW170814	45
2.2.6	GW170817	45
2.3	The LIGO interferometer	47
2.4	Noise	48
2.4.1	Seismic noise	48
2.4.2	Gravity gradient noise	49
2.4.3	Suspension and coating thermal noise	50
2.4.4	Residual gas noise	52
2.4.5	Quantum noise	52
2.5	Current limitations for Advanced LIGO	54
2.5.1	Sensitivity	54
2.5.2	Duty cycle	55
2.6	Objective of this thesis	56
3	Environmental impacts on large-scale interferometers: study of earthquakes	57
3.1	The problematic	57
3.2	Introduction to earthquakes	58
3.3	Seismon	59
3.3.1	Description	60
3.3.2	Arrival time prediction	60

3.3.3	Velocity prediction	61
3.3.4	Threat prediction	62
3.3.5	Output	66
3.4	Ground behavior at the sites	68
3.4.1	Local motion	68
3.4.2	Common motion	69
3.5	Control strategies	70
3.5.1	Seismic platform architecture	70
3.5.2	Seismic control scheme	72
3.5.3	Tilt-Horizontal coupling	76
3.5.4	O1 nominal configuration and performance	78
3.5.5	First strategy: Tilt reduction.	80
3.5.6	Second strategy: Gain peaking reduction	84
3.5.7	Third strategy: Common mode rejection along the arms	87
3.6	Implementation at the sites	93
3.7	Conclusion	93
4	Parametric Instabilities	96
4.1	Background	96
4.1.1	Introduction to PI	96
4.1.2	Calculation of the parametric gain	97
4.1.3	Overlap parameter $B_{m,n}$ calculation	102
4.1.4	Optical gain G_n estimation	104

4.2	PI model & prediction	111
4.2.1	Mechanical mode calculation (nominal values)	111
4.2.2	Model	113
4.3	Current status of LIGO	115
4.4	Damping solution: Acoustic Mode Damper	117
4.4.1	Description	117
4.4.2	Shunted piezoelectric	118
4.4.3	AMD material selection	124
4.5	Experiment	127
4.5.1	Approach	128
4.5.2	Limitations and preliminary results	129
4.5.3	Final design	132
4.6	Epoxy bulk loss factor	134
4.7	Epoxy thin layer loss	135
4.8	Piezoelectric results	138
4.9	AMD model	140
4.9.1	AMDs designs	141
4.9.2	Location	142
4.9.3	Performance against PI	144
4.9.4	AMD thermal noise	147
4.10	Installation	150
4.10.1	AMD assembly	150
4.10.2	Installation jig	155

4.11 Results	159
4.11.1 AMDs performance	159
4.11.2 AMDs thermal noise	161
4.12 Conclusion	162
A Logistic cost function simplification	166
B Radiation pressure calculation	168
C Relationship between HOM field and sideband field	170
D Calculation of the resistive shunt mechanical impedance	171
E PZT materials tested	172
F Thermoelastic effect	173
G Tuning of the mechanical oscillator	175
G.1 Tuning of the oscillator	175
G.2 Tuning of the suspension	176
G.2.1 Application	179
H FEA analysis	180
I Natural resonances of the AMDs	181

List of Figures

1.1	Evolution with time of a + and \times polarized GWs, propagating into the page.	34
1.2	Isometric view of a GW at a given instant. Propagation along the tube (Numerical simulation. Credits: <i>einstein-online.info</i>).	35
1.3	IFO response to the + polarized gravitational wave from figure 1.1. The test masses of the IFO behave as free masses and therefore are sensitive to strain. When the IFO is deformed, we observe light intensity modulations at the output photodetector (in green).	37
1.4	Overview of a Michelson IFO coupled with Fabry-Perot cavities in the arms. It is composed by an input laser, a beam-splitter (BS), two input mirrors (ITM), two output mirrors (ETM) and an output photodetector. The suffixes X and Y denote the two different arms in the x and y direction respectively.	38
1.5	Overview of a Fabry-Perot Michelson IFO, coupled with a power recycling cavity at the input, and a signal recycling cavity at the output.	39
1.6	Overview of the international network of ground-based GW detectors.	39
2.1	Location and orientation of the LIGO detectors at Hanford, WA (H1) and Livingston, LA (L1).	42
2.2	GW150914 event	43
2.3	GW151226 event	43
2.4	GW170104 event	44
2.5	GW170608 event	44

2.6	GW170814 event	45
2.7	GW170817 event	46
2.8	Layout of the Advanced LIGO detector.	47
2.9	Estimation of the seismic noise in the LIGO detection bandwidth. . .	49
2.10	Estimation of the Newtonian noise in the LIGO detection bandwidth. The change of slope around 10Hz is due to the different sources of noise. Below 10Hz, the noise is mostly generated by seismic waves (seismic gravity gradient noise), while above 10Hz, it is created by atmospheric disturbances (atmospheric gravity gradient noise).	50
2.11	Estimation of the thermal noise. The noise associated with the fibers is plotted in blue. The several high-frequency peaks correspond to the different violin modes and harmonics of the fibers. The noise associated with the mirrors is shown in red (it is grandly due to the coating). . .	51
2.12	Estimation of the excess gas noise.	52
2.13	Estimation of the quantum noise (in purple). All the strain noise are added in quadrature to calculate the total noise of Advanced LIGO at full power.	54
2.14	Strain sensitivity comparison between Advanced LIGO at Hanford (H1) and Livingston (L1) during O1 and the designed sensitivity for Advanced LIGO (same curve that the one presented in figure 2.13). . .	55
2.15	Advanced LIGO duty cycle distribution during the O1 period, from September 2015 to January 2016.	56
3.1	Summary of the different seismic waves generated by an earthquake. They are listed from the fastest to the slowest.	59
3.2	A flowchart of the Seismon pipeline. USGS information is used to estimate time arrivals, peak ground velocity and threat level for the IFO.	60
3.3	PREM velocity model	61
3.4	Seismon velocity prediction	62
3.5	Standard logistic function $h(x)$. Note that $h(x) \in \{0, 1\}$ for all x . . .	64

3.6	Performance of the logistic regression classifier at Hanford and Livingston. True positive rate is the ratio of the sum of predicted positive condition actually being true to the sum of all actually positive conditions. Positive condition here refers to a lockloss prediction by the classifier which in general can be true or false. False positive rate is the ratio of the sum of predicted positive condition being false to the sum of all actually negative conditions. Classifier prediction about the detector being in lock forms the negative condition. The area under the curves assesses the efficiency of this classifier.	65
3.7	Seismon graphical interfaces	67
3.8	Simplified optical layout of the LIGO detector, showing the approximate positions of the ground seismometers at the sites. For clarity, <i>Laser pre-treatment</i> and <i>Laser post-treatment</i> regroup all of non-core optics and the multiple vacuum chambers in which they are housed.	68
3.9	Ground spectra at the sites	69
3.10	Comparison between the common and differential motions in the corner station and along the Y-arm at both sites. Data were selected at random times (blue curves), and during earthquakes of Richter magnitude 5 or greater (red curves). In the corner station at Livingston, we see a ratio of 90% between 100mHz and 1Hz instead of 100%. We believe this is due to a calibration issue between the seismometers.	71
3.11	Overview of the BSC chamber	72
3.12	Control block diagram of a seismic isolation stage for one degree of freedom. The colored blocks are related to figure 3.13.	73
3.13	Example of the LIGO seismic control scheme performance on the BSC-ISI stage 1 platform. The dashed curves show the different filters used, as opposed to the solid curves showing the transfer functions from the ground motion with different loops engaged.	75
3.14	Model considered to estimate the tilt coupling in horizontal seismometers.	76
3.15	A more realistic control block diagram for one degree of freedom, including the tilt seen by the seismometers. The only difference between the translational degree of freedom Y and the rotational degree of freedom RX is that rotation has the feedback loop engaged only (no sensor correction nor feedforward), since there is no rotation sensors on the ground.	78

3.16	Simulink model for the BSC-ISI stage 1 platform.	79
3.17	Seismic isolation provided by BSC-ISI stage 1 in the Y-direction at both sites. The black curve represents a typical ground motion, and the blue curve the measured motion of the stage. The dotted curve indicates the LIGO goal to obtain from 200mHz to higher frequencies for stage 1. The thinner curves indicate the estimated noise contributions, and the red curve shows the simulated overall motion.	80
3.18	Comparison between the common and differential motion in the corner station and along the Y-arm at both sites. Data were selected at random times (blue curves), and during earthquakes of Richter magnitude 5 or greater (red curves).	81
3.19	Comparison of the filters used during O1 (dashed lines) and the new designed filters for earthquakes (solid lines). The left part of the figure shows the complementary low-pass and high-pass filters. The right part shows the sensor correction filters.	82
3.20	Seismic isolation provided by BSC-ISI stage 1 in the Y-direction at both sites. The black curve represents a typical ground motion, and the blue curve the measured motion of the stage during O1 and the red curve the predicted stage motion with the new filters. The thinner curves indicate the estimated noise contributions with these new filters.	83
3.21	Comparison of the interferometer behavior between O1 and O2 at Hanford. The figure shows the IFO status versus the peak ground velocity in the [30mHz-100mHz] band, with the blue bars for when the IFO stayed lock and the yellow bars for when the IFO lost lock. The y-axis represents the percentage of events per bin, with the number above each bar being the total number of events per bin.	84
3.22	Comparison of stage 1 ITM behavior in the [30mHz-100mHz] band for different ground motions: stretches selected during earthquakes when the interferometer survived(blue curve), stretches selected during earthquakes when the interferometer stops functioning (red curve). The top part of the figure represents the cumulative distribution function for the ground and the stage respectively, as a function of the peak velocity for each stretch. The plots indicate the direct correlation between velocity and the interferometer status at both sites. We observe a net increase of the stage velocity compared to the ground, due to self-inflicted gain peaking in this frequency band. The bottom part of the plots represents $P(LL v)$, the smoothed probability of losing lock as a function of peak velocity. It is computed by fitting the measured probability with a hyperbolic tangent function.	85

3.23	Comparison of the filters used during O1 (dashed lines) and the new designed filters for earthquakes (solid lines). The left part of the figure shows the complementary low-pass and high-pass filters. The right part shows the sensor correction filters.	86
3.24	Seismic isolation provided by BSC-ISI stage 1 in the Y-direction at both sites. The black curve represents a typical ground motion, and the blue curve the measured motion of the stage during O1 and the red curve the predicted stage motion with the new filters. The thinner curves indicate the estimated noise contributions with these new filters.	86
3.25	New $P(v_{\text{new}})$ distribution based on O1 data with $P(v_{\text{new}}) = \frac{P(v)}{1.5}$. As a reminder from figure 3.22, we plotted the probability of losing lock as a function of stage velocity $P(\text{LL} v)$ in black.	87
3.26	Overview of the implementation necessary to control only on local differential motion at low frequency during earthquakes.	88
3.27	Control scheme of the new configuration. To obtain the local differential motion of ITMY, the local ground Y'_G from ETMY is subtracted from the local ground Y_G . The difference $(Y_G - Y'_G)$ is then multiply by 0.5 and added to the sensor correction path. N'_{in} and S'_{tilt} represent the noise and tilt associated with the ETMY ground seismometer. . .	89
3.28	Simulink models developed for the presented strategy. In the first model, the differential motion is added as an additional input. In the second model, both ITMY and ETMY platforms are simulated. In this model, tilt, noise and feedforward are not considered.	90
3.29	Time-series of the seismometers close to the Hanford ITMY chamber (blue curve) and the ETMY chamber (orange curve) during a Richter magnitude 6.5 in Alaska. We clearly see the first arrival of the P-waves around 300s. A vertical offset was put on the two curves for visibility. The differential signal is in yellow. This data is used in the Simulink models presented in this section.	91

3.30 *Left figure:* Comparison of performance between the nominal configuration and the new configuration described in this section. The orange and red curves are simulated using the frequency domain Simulink model shown in figure 3.28. We observe a disparity between the measured and simulated performance for the nominal configuration above 500mHz (blue and orange curves). This is due to the simple plant model used in the simulation, as explained before. The new configuration degrades the performance above 500mHz and improves it around 50mHz. *Right figure:* Time-series (generated with the time domain Simulink model) of the Y drive signal (as a velocity) of the nominal and new configuration. We observe a reduction of the peak velocity by $\sim 25\%$ 92

3.31 State graph of the BSC-ISI Guardian system. The ovals represent the different states, and the arrows the authorized transitions from one state to another. Eight different states are needed to fully isolated a BSC chamber to a nominal configuration. Represented in orange is the new states necessary to have the earthquake configuration part of the automation system. The solid arrows show the path to go from nominal to Earthquake configuration, and the dash arrows the path from Earthquake to nominal. 94

4.1 PI feedback mechanism 97

4.2 Illustration of the interaction between the fundamental mode of the cavity ω_0 , a mechanical mode ω_m and a higher optical mode ω_1 . The vibrating mirror scatters the fundamental mode into side-band modes $\omega_0 \pm \omega_m$. If the frequency between a side-band and a higher optical mode are similar (i.e. if $\Delta \approx 0$), and the optical and mechanical modes have a suitable spatial overlap ($B_{m,n} > 0$), a strong interaction between the modes can occur. 100

4.3 *Top:* amplitude displacement $\vec{u}_m \cdot \hat{z}$ of a test mass mechanical mode near 15.5kHz. *Bottom:* Amplitude f_n of three optical modes. We observe a very strong geometrical overlap between the mechanical mode and the HOM01, with $B^2 > 0.9$ 104

4.4 Simple mirror with reflective surface to construct the S-matrix. 105

4.5 Simple Fabry-Perot cavity of length L . For our calculation, only the electromagnetic fields in the cavity are of interest. We are not including the reflective field from the first mirror or the transmitted field from the second mirror. 107

4.6	Simplified node's notation for a simple Fabry-Perot cavity.	108
4.7	LIGO dual-recycled Fabry-Perot-Michelson IFO.	109
4.8	Overview of the modal analysis with the test mass+ears+coating layer.	113
4.9	List of the test mass mechanical modes and their associated quality factors.	114
4.10	Advanced LIGO 'worst case' parametric gains at full power (95% confidence). Only the mechanical modes with parametric gains superior than 0.1 are represented.	114
4.11	LIGO quadruple suspension	116
4.12	PI during O1	117
4.13	AMD concept. Each AMD is composed by a base, a shunted piezoelectric plate acting as a spring and a reaction mass. The plate is bonded to the base and the reaction mass with conductive epoxy. The AMD is glued to the flat part of the test mass with epoxy.	118
4.14	Equivalent circuit of the PZT plate shunted with a resistor.	121
4.15	Shunt modulus and loss factor of a PIC181 plate as a function of frequency. The resistors have been chosen to get the maximum dissipation between 10kHz and 80kHz. The resistor for the AMD1 targets the 15.5kHz frequency.	123
4.16	Overview of the jig used to measure the minimum thickness achievable for different bonds. The bond layer (in red) is exaggerated for visibility	125
4.17	Experiment concept. A sample, represented in red, is mounted between to aluminum masses (hatched areas), acting as rigid bodies. The system is excited with an impact hammer and the transient response recorded with an accelerometer. The quality factor Q of each mode is computed using the ring-down method (see section 4.5.3)	128

4.18	Overview of the final design. Three samples, represented in red, are mounted between a bottom aluminum mass (in grey) and a top aluminum mass (slightly transparent for more visibility). The experiment is optimally suspended to operate in a free configuration and therefore avoid dissipation through the joints. The clamps and wires are represented in black. The suspension's cage is clamped to an optic table (not represented here). The location of the samples is controlled by a masked positioned with a dowel pin (both removed after installation).	132
4.19	Representation of the two principal resonances studied. On the top left are the mode for which the samples work mostly in shear (referred as rotation). On the top right are the mode for which the samples work mostly in compression (referred as bend). From the FEA, the displacement vector sum for each mode is shown at the bottom of the figure.	133
4.20	Overview of the oscillator without the clamps and wires. Three identical samples are placed between the masses. Three types of samples have been tested: epoxy cylinders, epoxy+fused silica cubes and epoxy+PZT plates.	134
4.21	Evolution of the epoxy loss factor as a function of time. A measurement has been conducted every 24 hours during one month to monitor the samples properties. The loss factor reaches 95% of its final value after 8 days.	136
4.22	Overview of the jig used to calculate the appropriate amount of pressure to apply on the bond. The epoxy layer (in red) is exaggerated for visibility.	136
4.23	Evolution of the measured 302-3M+graphite loss as a function of the bond thickness. Measurements for layers of 5.7, 4.3, 2.2 and 1.2 μm have been done. The dash purple line shows the bulk loss of 10.1×10^{-3} as a reference from the previous section.	137
4.24	Top view of the mechanical oscillator to measure the loss of PZT material. Three different configurations have been considered in order to measure all the terms of η_{PZT} , with two different polarization's plate (shear and compression). The arrows indicate the polarization direction for each plate (the dots indicate a polarization toward the page). The color code for each configuration corresponds to the color in equation 4.82.	139

4.25	Principal resonances of the AMDs from modal analysis as a function of the calculated parametric gains from section 4.2.2. Only the resonances for which most of the energy is in the PZT plate in the polarization direction are shown. AMDs have been tuned to target the problematic modes and cover the entire frequency band from 10kHz to 80kHz. The list of resonances is shown in appendix I.	141
4.26	Dimensions of the different reaction masses (units in mm). The little cut on the side of each RM is the designated location for the resistor. Not to scale.	142
4.27	Orientation of the RM (<i>transparent red</i>) with respect to the PZT plate (<i>pink</i>). The polarization of the plate is represented by the white arrow. The RM's flat parts are turned 45° compared to the polarization direction. This is true for all the AMDs.	142
4.28	Overview of the AdvLIGO BSC5-L1 SolidWorks model. The full quadruple suspension with its cage and hardware is represented. On the right is a zoom on the test mass, where one of the flat is highlighted. . . .	143
4.29	View of one the test mass flat. Three different areas on the flat have been identified to locate the AMDs. Are 1 & 2 are close to the front face, while area 3 is next to the ring heater (represented in transparent cyan).	143
4.30	Suggestion for the location of the AMDs on the flats. <i>Right</i> and <i>left</i> locations are defined with respect to the front face.	144
4.31	Overview of the FEA model of the ETM mirror with four AMDs. AMD 2 and 3 are placed on the opposite suspension flat at the same location as AMD 1 and 4.	145
4.32	Quality factors between 10kHz and 80kHz, before and after installing 4 AMDs on the test mass (simulation).	145
4.33	Comparison between the maximum estimated parametric gains at full Advanced LIGO power without the AMDs (<i>blue dots</i>) and with the four AMDs on the test mass (<i>black plus</i>). Overall, 100% of the parametric gains are reduced, with no gain remaining above 1 (out of 47 without the AMDs).	146
4.34	Overview of the ANSYS harmonic analysis done to estimate the new thermal noise of the AMDs. The color map on the front face corresponds to the profile of the applied pressure. It mimics the carrier laser beam profile, centered on the test mass with a waist of 62mm.	148

4.35 Energy dissipation in AMD1 at 100Hz. Note that the most energy is concentrated in the AMD base but the largest amount of energy is dissipated in the epoxy layer between the test mass and the base. The shunt has insignificant energy dissipation and thus insignificant contribution to thermal noise degradation of the mirror. 149

4.36 The thermal noise associated with 16 AMDs (4 per test mass) corresponds to the thick cyan line. The total noise with the AMDs is plotted in orange (dash line). The blue dot line, corresponding to the right y-axis, shows the excess on the total noise in percent as a result of adding 16 AMDs. 149

4.37 Overview of the alignment jig used to glue the PZT to the base. The base is sitting on a flat optics, which is embedded in the alignment jig. The jig has two different diameter holes, one to fit the base, one to fit the PZT plate. 151

4.38 Pictures of the Base+PZT assembly without the wire soldered to the base (*left*) and with the wire soldered (*right*). The black rim around the PZT plate corresponds to a slight excess in epoxy. 152

4.39 Overview of the alignment jig used to glue the RM to the PZT. On a flat optics is sitting the base, embedded in the alignment jig. The jig has two different diameter holes, one to fit the base, one to fit the RM (a different jig is require for each AMD.). On top of the jig is a groove to align the RM with regards to the PZT plate. 153

4.40 Pictures of the fully assembled AMD1, AMD2, AMD3 and AMD4 (in that order). 153

4.41 Simple self-sensing bridge applied to PZT. If C matches the capacity of the PZT, the resulting signal voltage V_s is independent from the control voltage V_a , and only proportional to the voltage generated by the PZT plate under stress. 154

4.42 Overview of the AMD installation jig. The test mass is shown in transparent and the suspension's cage in glue. The hardware is not shown for clarity. The jig cross-bar (in green) can slide horizontally for adjustment. The angle bracket (in black) supporting the rest of the jig can slide vertically. 156

4.43 Overview of the AMD alignment jig. Before being installed, the AMD is oriented properly using the jig circled in blue and shown to the right. The RM (in pink) is oriented properly using the slanted marks of the jig. The AMD is then grabbed via a suction cup and the jig is transferred to the cross-bar installed on the quadruple suspension. . . 157

4.44 The side cut view of the overall installation jig is shown at the top. The zone circled in blue is show in more details at the bottom, with the different gluing steps. The soft spring is shown in blue and the stiff spring in yellow. 158

4.45 Pictures of the AMDs on the test mass during and after installation. Top right picture, we see some irregularities in the AMD2 bond due to a dust particle (circled in red). 159

4.46 Representation of the measured quality factors without (*blue bars*) and with (*red bars*) AMDs, and comparison with the model (*black bars*). The mode numbers correspond to the mode numbers listed in table 4.11.161

4.47 Noise spectra of the Livingston IFO pre and post-AMD. The blue and red solid lines show the total noise level of the IFO measured (classical + quantum noise). The dotted curves show the level of classical noise only, after the quantum has been subtracted via a cross-correlation technique. The solid green curve is the estimated coating thermal noise of Advanced LIGO. 162

F.1 Overview of one monolithic experiment used. The flexure size is 11 x 3 x 1.5 mm height. The experiment is symmetric around the flexure. The experiment profile is smaller around the flexure to facilitate machining. It was suspended by a wire (single point contact). 173

F.2 Three modes have been studied, marked at 'flag soft', 'flag stiff' and 'rotation'. The mode shape is shown on the left part of the figure. The deformation of the flexure and its thermal gradient are shown next. The complex displacement is extracted and the quality factor computed.174

G.1 Representation of the geometry and nomenclature used. The z-direction is the vertical direction. The samples are represented in red and the wires in black. Only the outline of the oscillator is shown for visibility. 175

G.2 Model of the coupling between one suspension mode, characterized by a stiffness k_{sus} and a damping factor c_{sus} , and an oscillator mode, characterized by a stiffness k_{osc} and a damping factor c_{osc} . The amount of energy transferred by the suspension mode to the oscillator mode is defined by the ratio α	177
--	-----

List of Tables

2.1	Summary of LIGO detections to date.	46
2.2	List of the Advanced LIGO optical parameters	48
3.1	Detectors' status over the O1 period. Commissioning time represents the vital maintenance tasks needed to keep the interferometers running. Environmental disturbances encompass earthquakes, high wind and storms.	57
3.2	Values of the different θ calculated for each input. This calculation has been done based on the gradient descent method, with 50,000 iterations and an increment of $\alpha = 0.04$	65
4.1	List of the parameters necessary to calculate the parametric gains. The power's transmittance T is listed for each mirror. Since the reflectivity and transmissivity used in \mathbb{S} are amplitude values, we have $t = \sqrt{T}$ and $r = \sqrt{1 - T}$. $L_{\{x\}}$ and $\phi_{\{x\}}$ correspond of the length and phase of the cavity associated with the node x from figure 4.7.	112
4.2	Coating properties of an Advanced LIGO ITM.	112
4.3	List of the PI observed in H1 during O1. Similar behavior has been seen at L1. We observe slightly different frequencies between the mirrors for a same mechanical mode due to thermal transients.	115
4.4	Summary of the shunted plate performance. The shunt loss angle is effective in the polarization direction of the PZT plate. Keeping the polarization direction perpendicular to the laser beam direction ensures very weak coupling to the strain sensitivity at lower frequencies.	123

4.5	List of the different bonds tested for the AMD. Overall, we achieved the appropriate thickness of a few micrometers only with epoxy 353ND and 302-3M.	125
4.6	Parameters chosen for the mechanical oscillator and the suspension. Some preliminary tests have been done to measure the quality factors of the suspension. All of them are ~ 1000 . The location d of the samples varies from one experiment to another.	133
4.7	Calculation of the epoxy loss factor, based on the measured quality factors and the energy distribution (in percentage) from finite element models.	135
4.8	Measured loss factors for PZT material.	140
4.9	Details of the thermal noise contribution for each material at 100Hz. The worst measured value has been taken for the loss factor of the PZT plates.	148
4.10	Comparison between the FEA and the measured values of the AMDs modes in free and clamped configurations. The values marked as 'NA' refer to frequencies above 100kHz, which were not measured.	155
4.11	List of the quality factors measured before and after AMDs installation. The last column corresponds at the corresponding quality factors calculated with the model presented in the previous section. The quality factors marked as 'NA' were too small to measure.	160
E.1	List of all the piezoelectric materials considered for the AMD. Based on the listed characteristics in this table (from constructors), PIC181 has been selected.	172
F.1	Comparison between the measurements and the FEA results.	174
G.1	Analytical estimation of the suspension and oscillator modes for $d=1.5\text{cm}$	179
G.2	Estimation of the percentage of energy transferred from the suspension to the measured oscillator's modes. Estimation done for the worst case with $\alpha = 1$	179
H.1	Strain distribution of the PZT plates for each AMD at 100Hz.	180

I.1	Frequencies of the different AMD resonance frequencies (in kHz). . .	181
-----	--	-----

Acronyms

AMD Acoustic Mode Damper.

BBH Binary Black Hole.

BNS Binary Neutron Star.

BS Beam Splitter.

BSC Basic Symmetric Chamber.

Caltech California Institute of Technology.

CM Common Mode.

DM Differential Mode.

ESD Electrostatic drive.

ETM End Test Mass.

FEA Finite Element Analysis.

FI Faraday Isolator.

GW Gravitational Wave.

GWINC Gravitational-Wave Interferometer Noise Calculator.

H1 LIGO Hanford, WA observatory.

HAM Horizontal Access Module.

HEPI Hydraulic External Pre-Isolator.

HOM Higher Optical Mode.

IFO interferometer.

IMC Input Mode Cleaner.

ISI Internal Seismic Isolation.

ITM Input Test Mass.

L1 LIGO Livingston, LA observatory.

LIGO Laser Interferometer Gravitational-Wave Observatory.

MC Monte-Carlo.

MIT Massachusetts Institute of Technology.

O1 First Advanced LIGO observation run.

O2 Second Advanced LIGO observation run.

OMC Output Mode Cleaner.

PDL Product Distribution Layer.

PI Parametric Instability.

PMC Pre Mode Cleaner.

PRM Power Recycling Mirror.

PZT Piezoelectric.

RH Ring Heater.

RM Reaction Mass.

RM Reaction Mass.

SQL Standard Quantum Limit.

SRM Signal Recycling Mirror.

TM Test Mass.

USGS United States Geological Survey.

V1 Virgo observatory.

Preface

In **chapter 1** we introduce the concept of gravitational waves and the sources considered for detections. The idea behind interferometric detectors is explained.

In **chapter 2** we focus on the LIGO detectors and their achievements (detections). We explain the current sensitivity, noise limitations, and what could be done to improve the LIGO interferometers' performance and duty cycle in the future. In particular, we address two major limitations: earthquakes and parametric instabilities. These two issues are studied in depth in this manuscript.

Chapter 3 focuses on the issue of earthquakes for LIGO. The tools and controls strategies developed to tackle this issue are presented.

Chapter 4 focuses on the issue of parametric instabilities (PI). Specifically, it presents the device developed to solve this problem, called Acoustic Mode Damper (AMD).

In **conclusion**, we explain how the work presented in this manuscript helped to improve the LIGO overall performance and duty cycle.

Chapter 1

Introduction

In this section we introduce the fundamental concept of gravitational waves (GWs) and interferometric detectors. The discussion on GW theory is kept to its minimum, as this manuscript focuses more on the experimental aspect of GW astronomy.

1.1 Gravitational radiation

GWs emerge from Einstein's general relativity [1, 2]. One of the basic differences between the general relativity and the standard laws of Newtonian theory concerns the speed of propagation in the gravitational field. As an apple falls, the mass distribution on Earth is changed and the gravitational field is altered. According to Newtonian laws, this change in the gravitational field is instantaneous, which would indicate a propagation at infinite speed. If this were true, the principle of causality would break down: no information can travel faster than the speed of light. In Einstein's theory, this disturbance of the gravitational field propagates with finite speed, the speed of light c , and is called GW [3].

In Einstein's theory, the Universe is defined as a four-dimensional manifold, referred to as the Minkowski space or Minkowski spacetime [4]. It is a combination of the three-dimensional Euclidean space (x, y, z) with time t as a fourth dimension. It is defined by the Minkowsky metric η in the (t, x, y, z) coordinates:

$$\eta = \begin{pmatrix} -c^2 & 0 & 0 & 0 \\ 0 & 1 & 0 & 0 \\ 0 & 0 & 1 & 0 \\ 0 & 0 & 0 & 1 \end{pmatrix}. \quad (1.1)$$

GWs are small disturbances in the space-time metric g caused by accelerating aspherical mass distributions. Far from the source (in the weak-field regime), the disturbance in space-time induced by GWs can be approximated as a small perturbation h with

$$g \approx \eta + h. \quad (1.2)$$

h can be expressed as a wave equation, propagating with a frequency ω in the z direction:

$$h(z, t) = A e^{j\omega(ct-z)} = \begin{pmatrix} 0 & 0 & 0 & 0 \\ 0 & -h_+ & h_\times & 0 \\ 0 & h_\times & h_+ & 0 \\ 0 & 0 & 0 & 0 \end{pmatrix} e^{j\omega(ct-z)} \quad (1.3)$$

with j the imaginary unit. The fact the amplitude A has only two independent components means that a GW is completely described by two dimensionless amplitudes, h_+ and h_\times . We also notice that GWs create disturbances in the two directions transverse to their direction of propagation. Transverse quadripolar properties of a GW are depicted in figures 1.1 and 1.2.

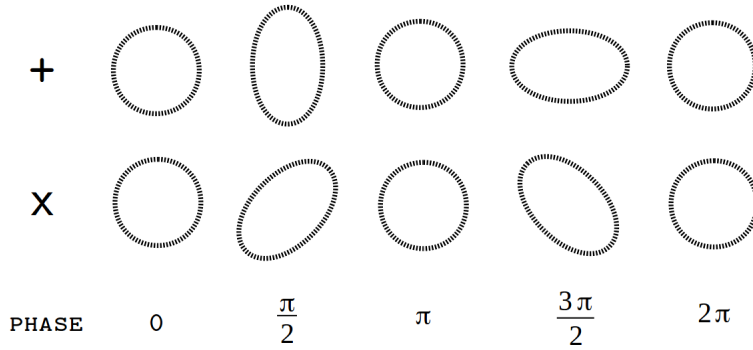


Figure 1.1: Evolution with time of a + and \times polarized GWs, propagating into the page.

1.2 Sources

The challenge of GW detection is the infinitesimal effect GWs have on Earth. The typical strain created by a GW when received on Earth is [5]:

$$h \approx \frac{GMv^2}{c^2r} \quad (1.4)$$

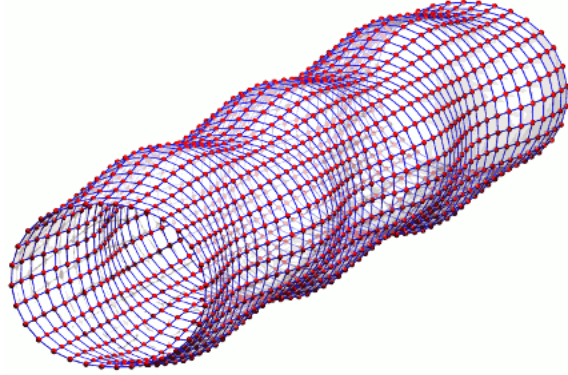


Figure 1.2: Isometric view of a GW at a given instant. Propagation along the tube (Numerical simulation. Credits: *einstein-online.info*).

where r is the distance to the object which has a mass M and a velocity v . G is Newton's gravitational constant. If we consider a source as close as $r \approx 15Mpc$ (which is the approximate distance of the closest cluster of galaxies from Earth [6]) with a mass close to the mass of our Sun ($M = 1M_{\odot}$), the expected strain is $h \ll 10^{-21}$. Therefore, only close high-mass, high-speed objects are valuable candidates for terrestrial detection. The likely sources of detectable GWs are summarized in the following sections.

1.2.1 Binary inspirals

At the time of writing, coalescent binaries are the only sources of GWs observed, with as much as six detections (more details about these detections are given in chapter 2.2). This is not surprising, as most of the terrestrial detectors were designed with them in mind [7, 8]. The high-speed collisions of these heavy, compact objects, such as neutron stars and black holes, are the perfect candidates for GW detections. As the two massive bodies orbit about each other, they continually lose energy to gravitational radiation. During this millions of years long process, the two objects are getting closer from each other, with increasing speed and frequency. In the final seconds before the impact, the energy radiated as GWs enters the detection band of the terrestrial detectors, as the signal rapidly increases in amplitude and frequency (known as a *chirp* signal).

1.2.2 Supernovae bursts

Core collapse supernovae are the spectacular explosions that mark the death of massive stars. If the initial conditions allow it, the supernovae collapse can be asymmetric and generate detectable GWs [9].

1.2.3 Continuous waves

Asymmetric spinning stars, such as neutron stars and pulsars, could produce detectable GWs [10, 11]. Such object would generate a single frequency GW, which is then Doppler shifted as the star moves away from the Earth. A catalog of known pulsars [12] has been studied and upper limits on GW radiated power have been calculated [13].

1.2.4 Stochastic background

Assuming that the noises of the different GW detectors are statistically independent, the underlying GW background could be measured by cross-correlated the detectors' outputs over a long period of time [14]. This background could be an ensemble of single sources (inspirals, supernovae, etc.), but could also be generated by the density fluctuations from the early Universe and the Cosmological Microwave Background [15]. This analysis takes years, as the measurement improves with the integration time.

1.3 Interferometric gravitational-wave detectors

The observation of GWs requires an instrument capable of converting tiny strain ($h < 10^{-21}$) into a measurable signal. Early efforts started in the 1960s with resonant bars, usually referred as Weber bars, from its pioneer J. Weber [16]. These bars operate by measuring the effects of a GW on their fundamental resonant modes. Given the lack of detections and the very narrow frequency bandwidth of these instruments, Weiss, Drever and Billing started working on ground-based interferometric detectors in the 1970s [17, 18]. In this section, we explain the core idea behind the detectors. The more advanced optical scheme of such instruments will be detailed in section 2.3.

1.3.1 Michelson

The core idea of the GW detector is Michelson interferometry. A beam-splitter is used to separate the input light into the two arms with identical length L_{arm} . The returning lights from the arms are in phase opposition and the detector outputs no light (dark fringe condition). As a gravitational wave passes through Earth, the interferometer (IFO) is subject to an oscillating distortion. Due to the quadripolar property of GWs (see section 1.1), one arm will be squeezed by $L_{arm} - \Delta L$ while the other will be stretch by $L_{arm} + \Delta L$, and vice-versa (see figure 1.3). In other word,

the first arm will measure a displacement of $\Delta L = -hL_{arm}$, while the other arm will undertake a displacement of $\Delta L = hL_{arm}$. This change of length will introduce phase shift in the injected light, which will be measured by the output photodetector. This observed modulation characterizes the GW.

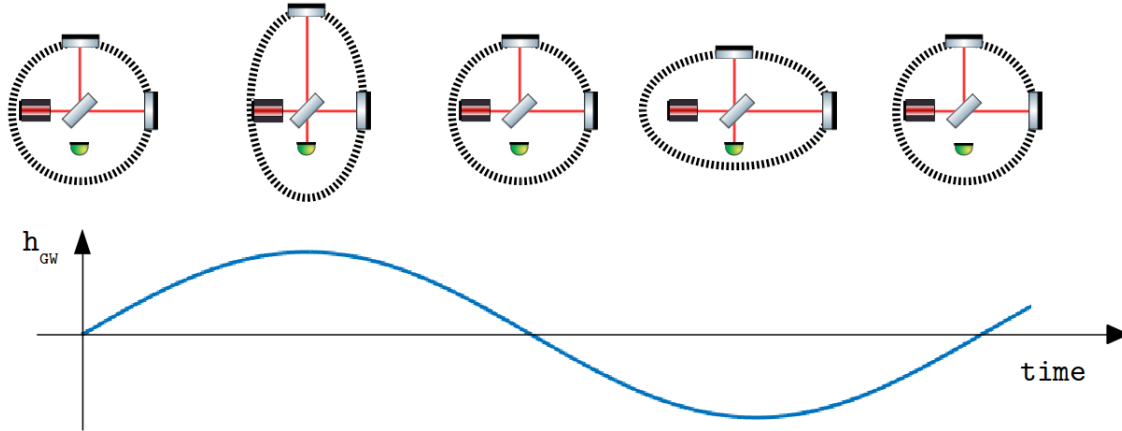


Figure 1.3: IFO response to the $+$ polarized gravitational wave from figure 1.1. The test masses of the IFO behave as free masses and therefore are sensitive to strain. When the IFO is deformed, we observe light intensity modulations at the output photodetector (in green).

1.3.2 Fabry-Perot arm cavities

For a given GW strain h , the displacement ΔL of the arms is directly proportional to the length L_{arm} : the longer the arms, the more sensitive the IFO would be. To observe strains $h \sim 10^{-21}$, the optimal arm length is around 75 km [19]. Building an IFO with 75km-long arms is technically challenging (large beam spots, Earth surface curvature, etc.). It is however possible to virtually increase L_{arm} while keeping the physical arms relatively short, using Fabry-Perot cavities. A Fabry-Perot cavity consists of a pair of partially reflective spherical mirrors arranged such that light bouncing back and forth between them may form a standing wave. It ultimately increases the phase shift effected by a gravitational wave without changing the physical length of the arm. By coupling a Michelson IFO with Fabry-Perot cavities in the arms, the effective length is increased by a factor $2\mathcal{F}/\pi$, with \mathcal{F} the arm finesse cavity. Figure 1.4 shows a Michelson IFO with Fabry-Perot arms.

1.3.3 Power and signal recycling

In order to reduce shot noise (which scales with the square root of incident power - see section 2.4.5), light recycling techniques [20, 21] are implemented at the input symmetric port and the output anti-symmetric port of the IFO to increase the power in the arms. The idea consists of adding a power recycling mirror (PRM) in the

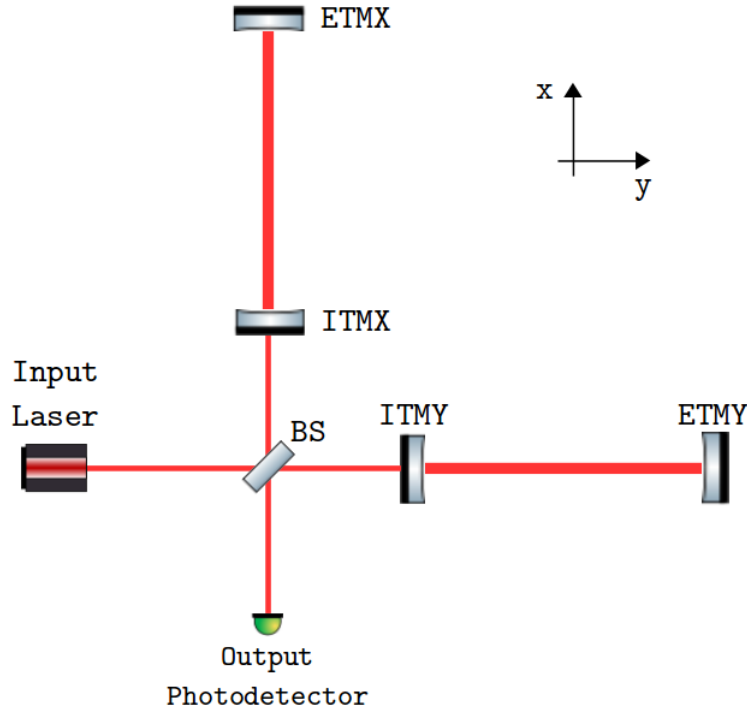


Figure 1.4: Overview of a Michelson IFO coupled with Fabry-Perot cavities in the arms. It is composed by an input laser, a beam-splitter (BS), two input mirrors (ITM), two output mirrors (ETM) and an output photodetector. The suffixes X and Y denote the two different arms in the x and y direction respectively.

input beam to coherently send back the reflected light in the IFO. It is also possible to re-inject the leaked light from the output of the IFO with a signal recycling mirror (SRM). The power and signal recycled Fabry-Perot Michelson is shown in figure 1.5. In this dual recycled configuration, the power in the arms is increased by a factor of ~ 8000 with respect to a simple Michelson.

1.4 Detectors around the world

To date, we count a global network of four operational IFOs, namely the German-British detector GEO 600 (with an arm length of 600m [22]), the two LIGO observatories in the United States (with 4km arms [23]) and the Virgo project of the European Gravitational Observatory (with 3km arms [24]). Future observatories are already under construction (KAGRA in Japan [25]) or planned (IndIGO in India [26]). It is worth mentioning LISA, an ESA mission with NASA participation, which objective is to deploy a several million kilometers IFO in space [27]. Figure 1.6 shows a world-map of the different sites for the different projects mentioned. In chapter 2, we will present in more depth the LIGO project specifically.

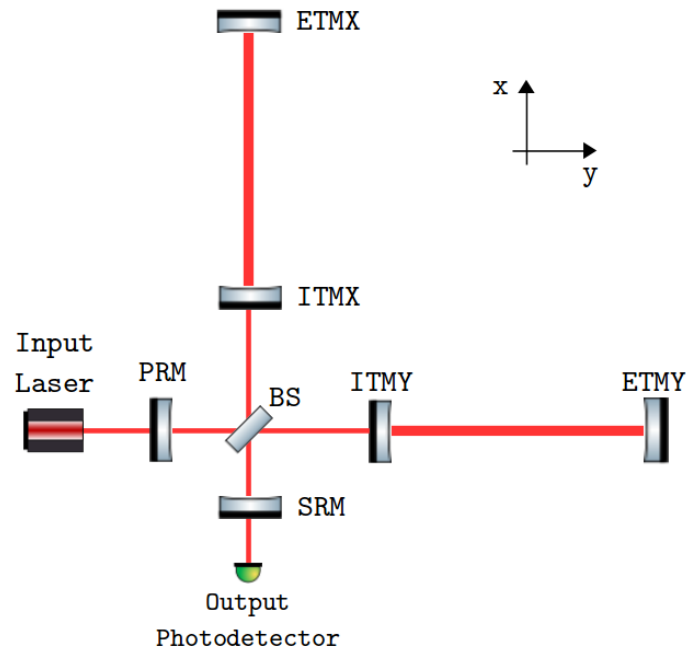


Figure 1.5: Overview of a Fabry-Perot Michelson IFO, coupled with a power recycling cavity at the input, and a signal recycling cavity at the output.

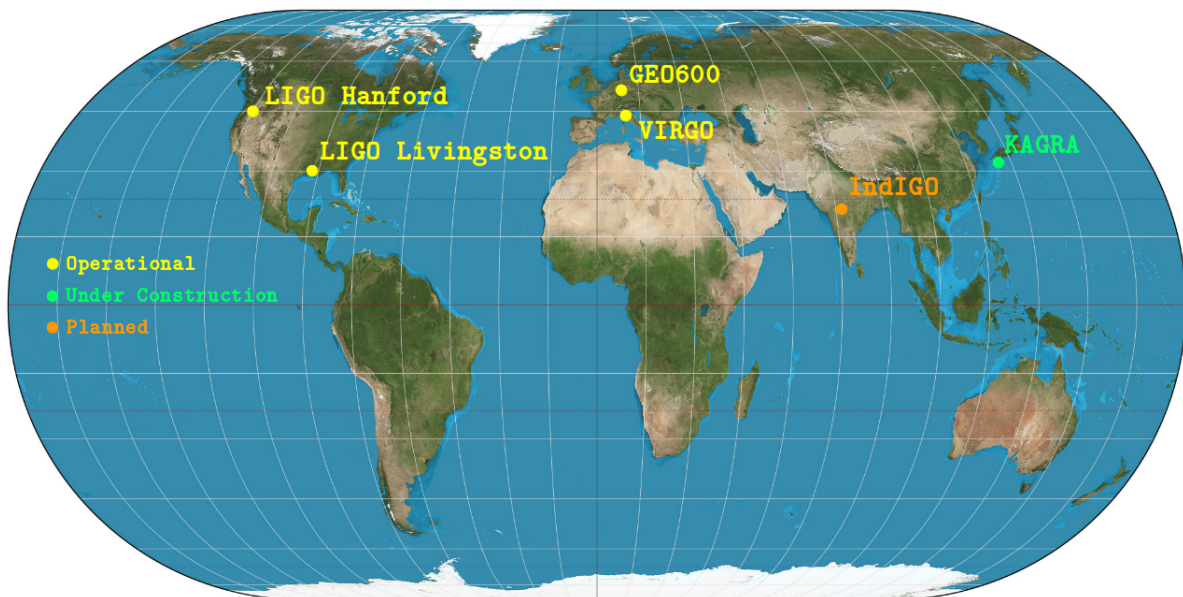


Figure 1.6: Overview of the international network of ground-based GW detectors.

Chapter 2

LIGO

2.1 Introduction

LIGO, which stands for Laser Interferometer Gravitational-Wave Observatory, is an American project funded by the US National Science Foundation and overseen jointly by the California Institute of Technology (Caltech) and the Massachusetts Institute of Technology (MIT). Started in 1992, this project is the world's largest observatory, with two identical 4km-arms long detectors, one in Hanford (Washington State) and one in Livingston (Louisiana State). Pictures of the detectors are shown in figure 2.1.

The project went through two distinct periods. The first version of LIGO's IFOs, referred as Initial LIGO [28, 29], took place from the late 1990s to 2008. It was intended as a 'pathfinder', used to test and spur the technologies required. The initial LIGO detectors reached their design sensitivity in 2006 [30] and have produced astrophysical interesting results [31, 32, 33], but no detection. In 2008 started the second and current period, referred as Advanced LIGO [34]. Advanced LIGO uses the initial LIGO buildings and vacuum systems but otherwise consist of completely new instruments, which give better sensitivity [35]. Currently, Advanced LIGO has the world most sensitive instruments with a strain sensitivity of $\sim 10^{-23}/\sqrt{\text{Hz}}$ at 100Hz [36]. Thanks to this sensitivity, Advanced LIGO claims six detections to this date.

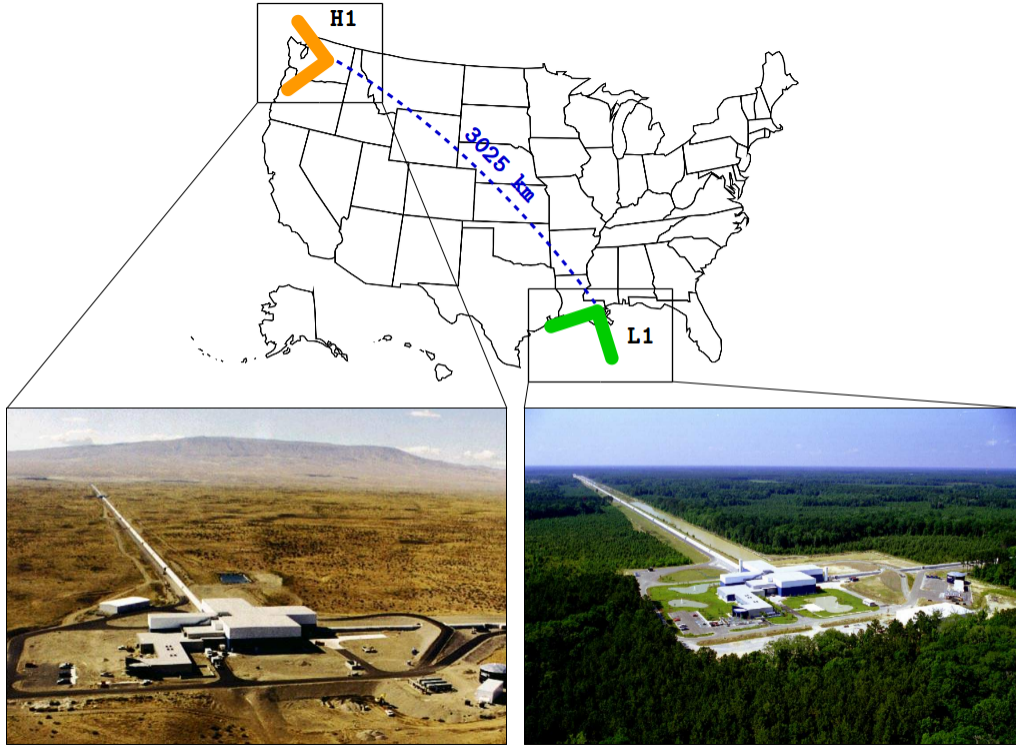


Figure 2.1: Location and orientation of the LIGO detectors at Hanford, WA (H1) and Livingston, LA (L1).

2.2 Detections

2.2.1 GW150914

Advanced LIGO achieved a milestone on September 14, 2015 at 09:50:45 UTC by observing a GW signal for the first time [37]. One hundred years after Einstein's theory of general relativity, the two detectors of LIGO simultaneously measured a transient GW signal of two black holes collapsing with each other, as shown in figure 2.2 (phenomenon usually referred as a binary black hole merger, or BBH merger). The detectors were sensitive enough to observe a signal for 0.2 seconds, from 35 to 250Hz with a peak strain of 1×10^{-21} . Based on relativity models, this signal tells us that a BBH system, distant by 410Mpc (i.e. 1.3 billion light-years) from Earth, and composed by two black holes with masses of $36M_{\odot}$ and $29M_{\odot}$ (i.e. 36 and 29 times the mass of our Sun), merged to form a single $62M_{\odot}$ mass black hole. During that process, the equivalent of $3M_{\odot}$ was released as radiated GW. It is to this date the heaviest BBH system ever observed.

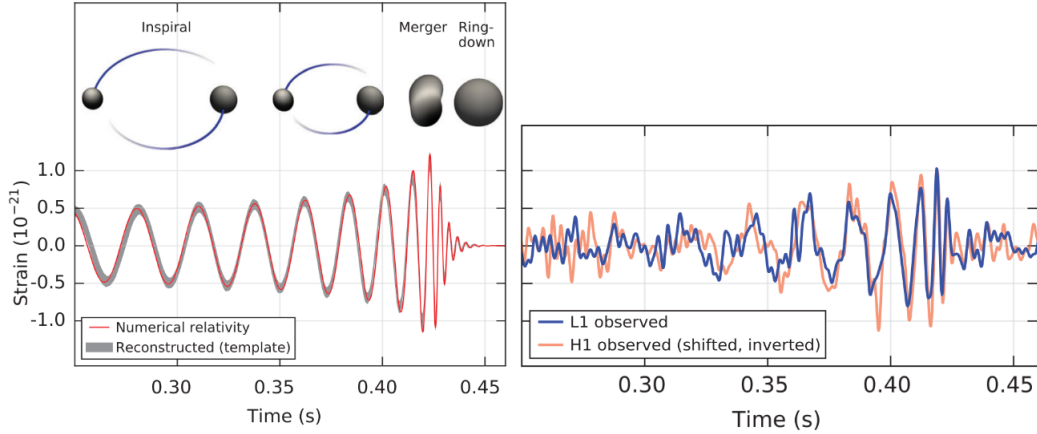


Figure 2.2: From reference [37]. *Left panel:* Estimated strain amplitude produced by the GW150914 event, as the black holes collapsed with each other (numerical relativity model). *Right panel:* measured signal by the L1 and H1.

2.2.2 GW151226

On December 26, 2015, both LIGO detectors observed the signal produced by the coalescence of a BBH system [38]. The system, distant by 440Mpc (i.e. 1.4 billion light-years), was composed by $14.2M_{\odot}$ and $7.5M_{\odot}$ masses black holes, and form a final single black hole of $20.8M_{\odot}$ (equivalent of $0.9M_{\odot}$ radiated as GW). The detected signal lasted for 1 second in the IFOs from 35 to 450Hz, and reach a peak gravitational strain of 3.4×10^{-22} . The signal measured by the LIGO IFOs is shown in figure 2.3.

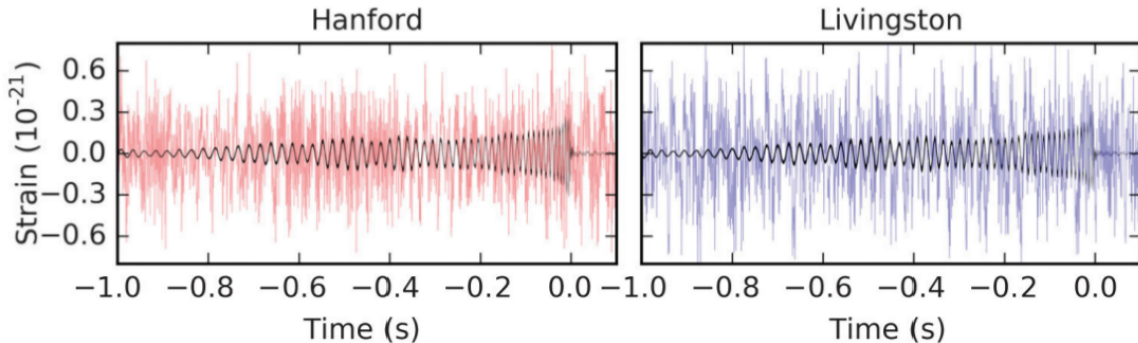


Figure 2.3: From reference [38]. Measured signal filtered between [30-600Hz] for H1 (left plot) and L1 (right plot) with the best-match template from numerical models (in black).

2.2.3 GW170104

On January 4, 2017, a $31.2M_{\odot}$ and a $19.4M_{\odot}$ black hole merged to form a $48.7M_{\odot}$ black hole [39]. During that process, almost $2M_{\odot}$ of GW was radiated. The LIGO detectors observed a 0.3s signal from 160 to 199Hz with a peak strain amplitude of $\sim 5 \times 10^{-22}$, as shown in figure 2.4.

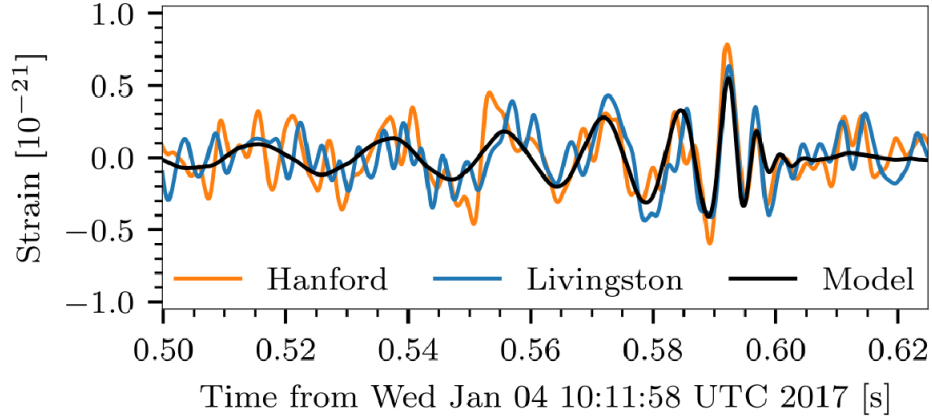


Figure 2.4: From reference [39]. Measured signal filtered between [30-600Hz] for H1 (left plot) and L1 (right plot) with the best-match template from numerical models (in black).

2.2.4 GW170608

On June 8, 2017, both LIGO detectors observed the merging of a BBH system, made of a $12M_{\odot}$ and a $7M_{\odot}$ black hole [40]. The merging formed a $18M_{\odot}$ black hole, releasing the equivalent of $1M_{\odot}$ of GW in the process. The detectors caught a 2s signal from 30 to 500Hz with a peak strain amplitude of $\sim 4 \times 10^{-22}$

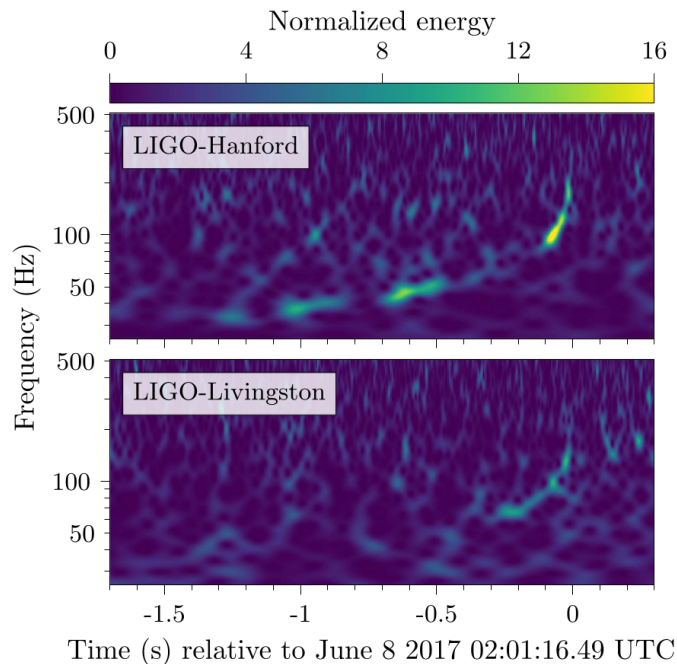


Figure 2.5: From reference [40]. Power maps of LIGO strain data at the time of GW170608. The characteristic upward-chirping morphology of a BBH driven by GW emission is visible in both detectors, with a higher signal amplitude in LHO.

2.2.5 GW170814

On August 14, 2017, a new milestone was reached with the first joint detection between LIGO and VIRGO [41]. The signal was emitted in the final moments of the coalescence of two black holes of $31M_{\odot}$ and $25M_{\odot}$, about 540Mpc away (1.8 billion light-years).

This detection marks the beginning of the international GW network, but also shows the advantages of having three detectors. Thanks to VIRGO, the sky localization of the event went from 1160deg^2 with only two detectors to 60deg^2 , as shown in figure 2.6.

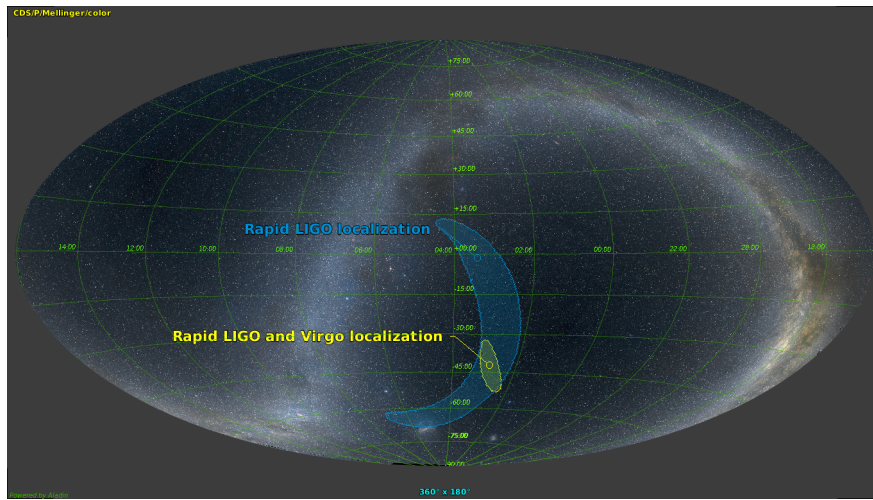


Figure 2.6: Having three detectors allowed a huge improvement in the localization of the signal’s origin. The origin is constraint to the area showed in yellow, just above the Magellanic clouds and generally toward the constellation Eridanus. Credits: *apod.nasa.gov*

2.2.6 GW170817

On August 17, 2017, not only LIGO observed the merger of two neutron stars (binary neutron stars merger, or BNS merger) for the first time, but also this event was seen by many (~ 70) electromagnetic telescopes [42]. Unlike all previous GW detections, which had no detectable electromagnetic signal, this event has an electromagnetic counterpart. 1.7 seconds after LIGO’s detection, a short gamma-ray burst was observed by FERMI and Interval telescopes [43, 44]. 11 hours later, many telescopes, from radio to X-ray wavelengths, observed an optical transient matching the characteristics and location of the GW, as shown in figure 2.7.

It was the longest (more than a minute) and loudest (peak strain at 7.5×10^{-20}) signal observed by LIGO, marking the beginning of multi-messenger astronomy. All

the detections are summarized in table 2.1

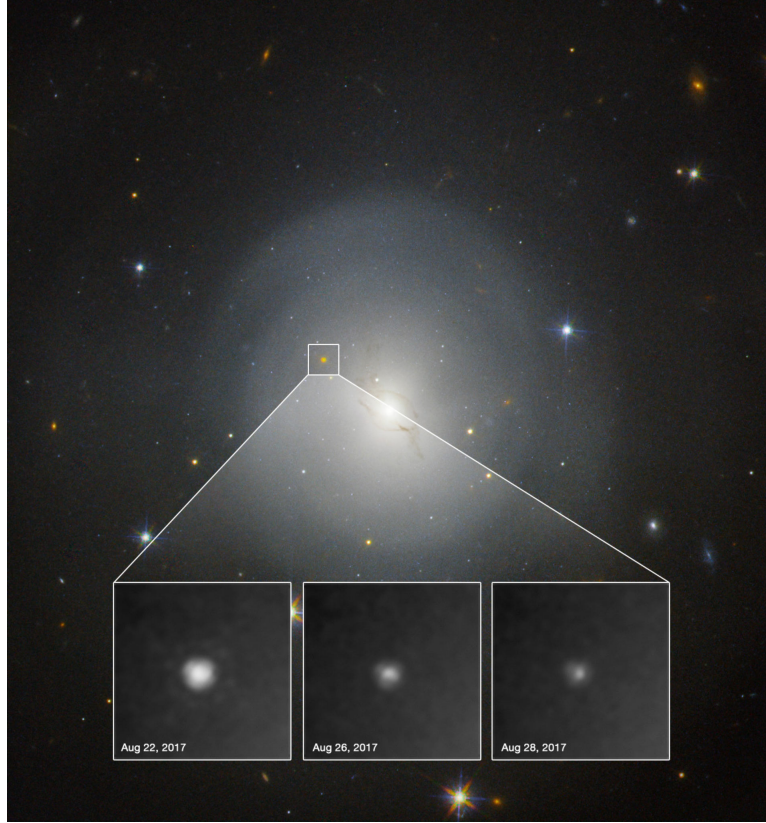


Figure 2.7: Hubble picture of the galaxy NGC 4993 with inset showing the gamma ray burst associated with GW170817 over 6 days. Credits: *NASA and ESA*).

Table 2.1: Summary of LIGO detections to date.

<i>Event</i>	<i>Seen by</i>	<i>Source</i>	<i>Masses</i>	<i>GW energy</i>	<i>Peak strain</i>	<i>Distance</i>
GW150914	H1,L1	BBH	$m_1 = 36M_\odot$ $m_2 = 29M_\odot$ $m_{\text{final}} = 62M_\odot$	$3M_\odot$	1×10^{-21}	410Mpc
GW151226	H1,L1	BBH	$m_1 = 14.2M_\odot$ $m_2 = 7.5M_\odot$ $m_{\text{final}} = 20.8M_\odot$	$0.9M_\odot$	3.4×10^{-22}	440Mpc
GW170104	H1,L1	BBH	$m_1 = 31.2M_\odot$ $m_2 = 19.4M_\odot$ $m_{\text{final}} = 48.7M_\odot$	$2M_\odot$	5×10^{-22}	880Mpc
GW170608	H1,L1	BBH	$m_1 = 12M_\odot$ $m_2 = 7M_\odot$ $m_{\text{final}} = 18M_\odot$	$1M_\odot$	4×10^{-22}	340Mpc
GW170814	H1,L1,V1	BBH	$m_1 = 31M_\odot$ $m_2 = 25M_\odot$ $m_{\text{final}} = 53M_\odot$	$3M_\odot$	5×10^{-22}	540Mpc
GW170818	H1,L1,V1 EM partners	BNS	$m_1 = 2.26M_\odot$ $m_2 = 1.36M_\odot$ $m_{\text{final}} = 3.29M_\odot$	$0.33M_\odot$	7.5×10^{-20}	40Mpc

2.3 The LIGO interferometer

The Advanced LIGO detectors are designed to detect GWs from distant astrophysical sources in the frequency range from 10Hz to 5kHz. Despite some minor technical differences, the detectors are identical. They are based on the dual recycled Fabry-Perot Michelson design described in section 1.3.3. The laser source is a Nd:YAG master-oscillator-power-amplifier emitting up to 180W at a single wavelength of 1064nm [45]. The laser power and frequency are actively stabilized with a transmissive ring cavity, called pre-mode cleaner (PMC). This cavity stabilizes the power fluctuations of the beam to $\sim 10^{-7}/\sqrt{\text{Hz}}$ at 100Hz [46]. This stabilized beam passes through an input mode cleaner (IMC) and a faraday isolator (FI) before reaching the PRM. The IMC is a 33m (round-trip) triangular Fabry-Perot cavity which cleans the spatial profile and the polarization of the laser beam [47]. At the output side, an output mode cleaner (OMC) is present after the SRM to reject unwanted spatial and frequency components of the light, before the signal is detected by the main photodetector. Finally, to avoid acoustical coupling and reduce phase fluctuations from light scattering off residual gas [48], the main optical components and beam paths are enclosed in an ultra-high vacuum system ($10^{-6} - 10^{-7}$ Pa).

An accurate scheme of the LIGO IFO is shown in figure 2.8, with its optical parameters summarized in table 2.2. At full power, the IFO is designed to operate with an input laser power of 125W, which corresponds to ~ 1 MW of circulating power in each arm.

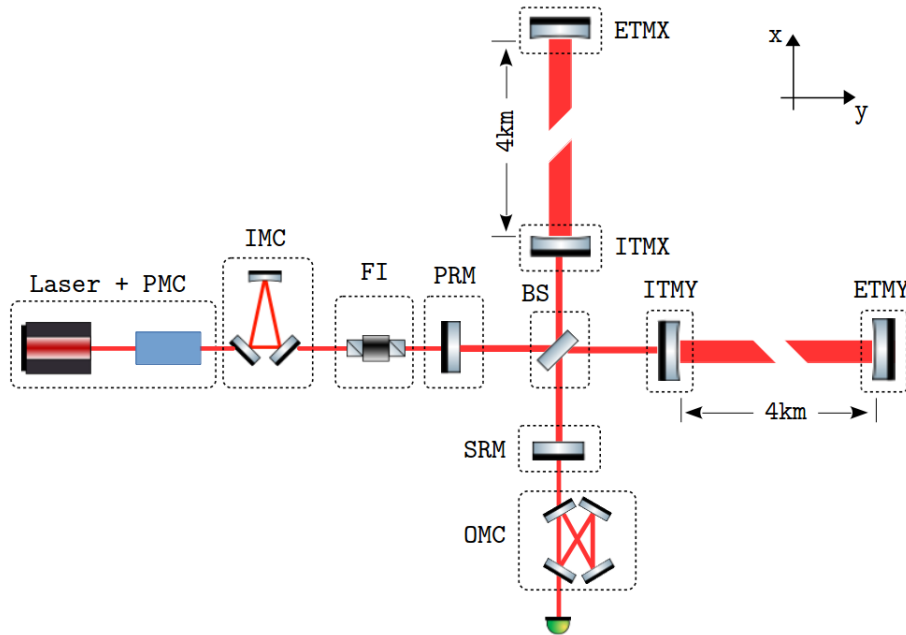


Figure 2.8: Layout of the Advanced LIGO detector.

Table 2.2: List of the Advanced LIGO optical parameters

Parameter (unit)	Value
Laser wavelength (nm)	1064
Input power at PRM (W)	up to 125
Arm cavity length (m)	3994.5
Arm cavity finesse	450
Power recycling cavity length (m)	57.6
Signal recycling cavity length (m)	56.0
IMC length - round trip (m)	32.9
OMC length - round trip (m)	1.13
IMC finesse	500
OMC finesse	390

2.4 Noise

To reach the LIGO designed sensitivity, there are stringent requirements on the noise. In this section, we present the major limiting noise sources for the different frequency bands, from 5Hz to 5kHz. Since the IFOs are designed to detect the strain amplitudes of GWs, it is convenient to talk about the equivalent strain amplitude for each given noise.

2.4.1 Seismic noise

At low frequency (i.e. $< 10\text{Hz}$), the predominant noise is due to seismic motion: the residual seismic vibrations impose displacement noise on the test masses of the detectors. At 1Hz and above, anthropogenic activities generate non-negligible surface vibrations. We typically measured a ground motion of $\sim 10^{-9}\text{m}/\sqrt{\text{Hz}}$ at 10Hz. The [0.1-1Hz] bandwidth is dominated by the Earth natural seismic background, referred to as microseism. It is caused by meteorological storms in the oceans and complex atmospheric disturbances [49]. Microseism is a constant disturbance composed by a primary and secondary (or double-frequency) microseism, covering two distinct frequencies: $\sim 75\text{mHz}$ and $\sim 150\text{mHz}$ respectively. The secondary microseism is the largest seismic disturbance, which varies from season to season (winter being the worst) and from site to site (L1 being the worst). A rough estimate would be a motion of $\sim 10^{-6}\text{m}/\sqrt{\text{Hz}}$ at 150mHz. The motion below 0.1Hz is less important compared to the other frequencies, except during earthquakes (see chapter 3). It is hard to measure the ground behavior in this band due to technological limitations (namely noise and tilt re-injection in the ground seismometers). However, we do believe that most of the motion is due to rotation induced by wind tilting the observatories' buildings [50]. Tilt will be discussed in more details in chapter 3.

To overcome the seismic motion, it is filtered using a combination of passive and active stages. The test masses are suspended by quadruple pendulums [51], which are mounted on multistage active platforms [52]. Overall, there are seven stages of isolation between the test masses and the ground, providing almost $1/f^{10}$ isolation in the detection bandwidth. The seismic noise is represented in figure 2.9.

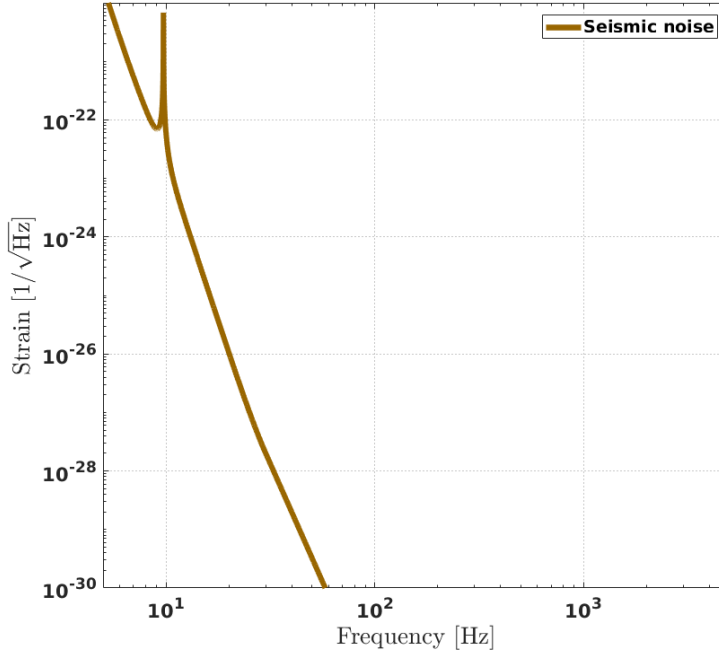


Figure 2.9: Estimation of the seismic noise in the LIGO detection bandwidth. The peak at 10Hz corresponds to the highest resonant mode of one of the isolation stages (*bounce mode*). Figure generated by the GWINC (Gravitational-Wave Interferometer Noise Calculator) package [53].

2.4.2 Gravity gradient noise

The local fluctuations of the gravitational field around the vacuum chambers couple with the test masses as a noise force [54]. These fluctuations, known as gradient noise or Newtonian noise, are due to passing seismic waves and surface phenomenon changing the local density of Earth. We can define the Newtonian noise transfer function $T(f)$ by:

$$T(f) = \frac{\tilde{x}(f)}{\tilde{W}(f)} \quad (2.1)$$

with $\tilde{x}(f) = |\Delta x(\omega)|$ the displacements of the test masses and $\tilde{W}(f) = |\Delta X(\omega)|$ the motions in Earth produce by seismic activity. From reference [55], an estimate of

$T(f)$ is:

$$T(f) = \frac{4\pi G\rho}{\sqrt{(\omega - \omega_0)^2 + \omega^2/\tau^2}}\beta(f) \quad (2.2)$$

where ρ is the density of the earth near the test mass, ω is the angular frequency of the seismic waves and ω_0 and τ are the resonant frequency and damping time of the test mass pendulums. The parameter $\beta(f)$ is a modeled, frequency dependent, dimensionless parameter related to environmental conditions (see [55] for more details on $\beta(f)$ calculation). An estimate of the Newtonian is shown on figure 2.10.

There is currently no strategy implemented to mitigate this noise, but an array of seismometers has been installed at H1 to do active noise subtraction in the near future [56].

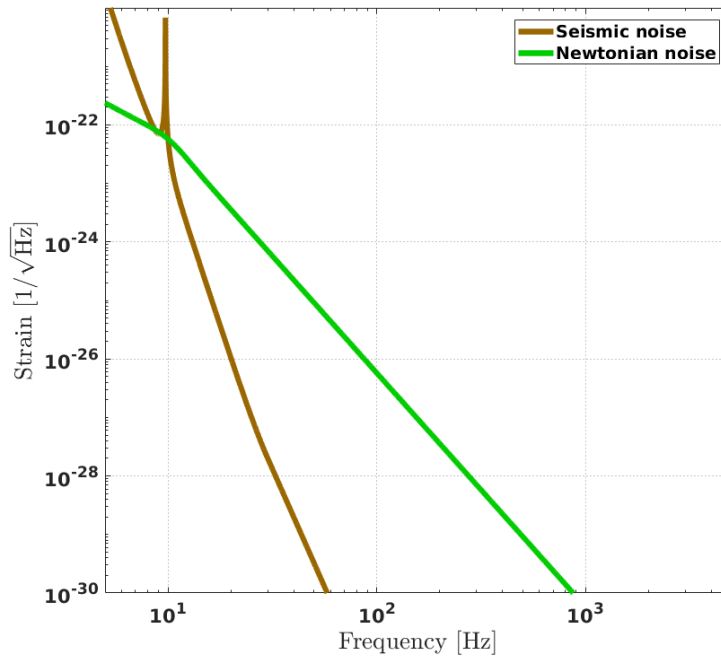


Figure 2.10: Estimation of the Newtonian noise in the LIGO detection bandwidth. The change of slope around 10Hz is due to the different sources of noise. Below 10Hz, the noise is mostly generated by seismic waves (seismic gravity gradient noise), while above 10Hz, it is created by atmospheric disturbances (atmospheric gravity gradient noise).

2.4.3 Suspension and coating thermal noise

In a mechanical system, the loss is characterized by the conversion of mechanical energy into thermal energy. Based on the fluctuation-dissipation theorem of Callen

and Welton [57], the reciprocal statement is true: thermal fluctuations are spontaneously converted into mechanical fluctuations, creating displacement noise. These thermal fluctuations could be generated by externally imposed temperature variations (e.g. the laser beam on the test mass surface [58]), or could be driven by internal fluctuations (Brownian motion [59]). In both cases, we call this noise thermal noise.

There are three main thermal noise sources in LIGO. The first one is the thin suspension fibers holding the test masses [60]. The small diameter of these fused silica fibers ($d = 400\mu\text{m}$) conceive non-negligible thermal fluctuations, especially via thermoelastic damping [61]. Thermal noise is also generated by the optical coatings of the test masses (the front face of the mirrors are covered with multilayers of silica and titania-doped tantala [62] to provide the required high reflectivity). Finally, noise is generated by the substrates of the test masses, but with less impact for Advanced LIGO [63].

The fibers, coatings and test masses have been designed to limit the thermal noise re-injection in the LIGO IFOs. The noise is shown in figure 2.11.

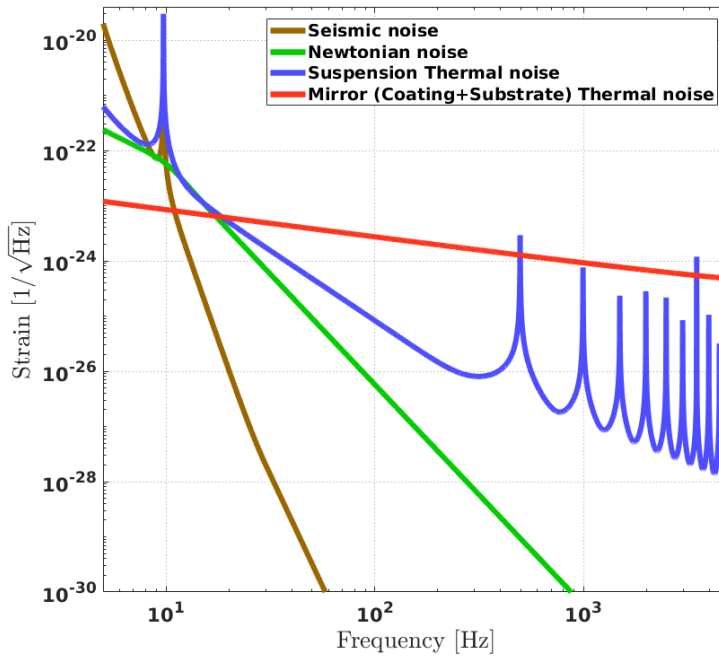


Figure 2.11: Estimation of the thermal noise. The noise associated with the fibers is plotted in blue. The several high-frequency peaks correspond to the different violin modes and harmonics of the fibers. The noise associated with the mirrors is shown in red (it is grandly due to the coating).

2.4.4 Residual gas noise

Despite the ultra-high vacuum system of Advanced LIGO, the statistical fluctuations in the density of the residual gas create non-negligible noise. Residual gas can disturb the laser field's phase as a gas molecule moves through the beam. The model developed by Zucker *et al.* [48] predicts the power spectral density of the arm length variation to be:

$$S_{L_{arm}}(f) = \frac{4\rho(2\pi\alpha)^2}{\nu_0} \int^{L_{arm}} \frac{\exp[-2\pi fw(z)/\nu_0]}{w(z)} dz \quad (2.3)$$

for a particular molecule with number density ρ , speed ν_0 and polarizability α . $w(z)$ is the beam's Gaussian radius. The residual gas noise is plotted in figure 2.12.

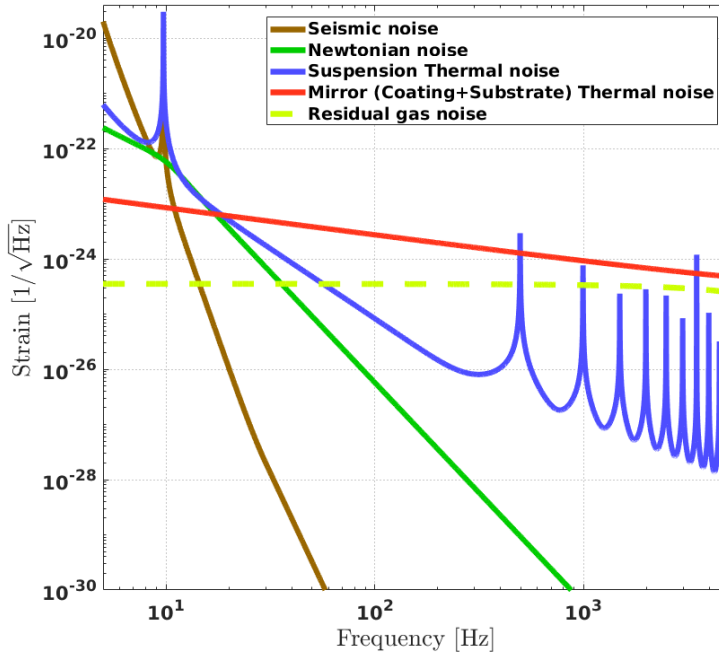


Figure 2.12: Estimation of the excess gas noise.

2.4.5 Quantum noise

In 1927, Heisenberg introduced a fundamental limit to the precision with which one can determine the position of a free mass. This is known as Heisenberg's uncertainty principle, and it's defined by:

$$\sigma_x \sigma_p \geq \frac{\bar{h}}{2} \quad (2.4)$$

with σ_x the standard deviation of position and σ_p the standard deviation of momentum. \bar{h} is the Dirac constant.

In interferometry, due to the discrete nature of light, the Heisenberg's principle applies and derives as the Standard Quantum Limit (SQL). This principle limits the accuracy with which the interferometer can measure the test masses' displacements over time [64]. In a measurement of duration τ , the minimum possible error in the position x of a mirror of mass m is given by:

$$(\Delta x)_{SQL} = \sqrt{\frac{2\bar{h}\tau}{m}}. \quad (2.5)$$

If we consider the two arms of the IFO, this implies a relative difference δx between the displacements of the two end test masses. This difference will produce a change in phase $\delta\phi$ and hence a change in the number of photons per unit time in the arms and at the output [65]. This fluctuation of the number of photons, and therefore of the laser intensity, characterizes the quantum noise.

The quantum noise usually shows up in two forms: shot noise and radiation pressure noise. The shot noise accounts for the fluctuations in the number of photons measured at the output photodetector (photon-counting error). The radiation pressure noise is generated by pressure fluctuations at the mirror surfaces, which are produced by the laser beam intensity fluctuations. Radiation pressure noise is predominant at low frequencies ($< 100\text{Hz}$) while shot noise is more important at high frequencies. As the input laser power increases, the photon-counting error decreases, while the radiation-pressure error increases. Therefore, the optimal light power and best sensitivity can be reached by trading shot noise versus radiation pressure. The quantum noise spectral density is given by [66]:

$$S_h = \left(\frac{1}{\kappa} + \kappa\right) \frac{h_{SQL}^2}{2} \quad \text{with} \quad \kappa = \frac{4P\omega_0}{c^2 m \omega^2} \quad \text{and} \quad h_{SQL} = \sqrt{\frac{4\bar{h}}{m\omega^2 L_{arm}^2}}. \quad (2.6)$$

The quantum noise and total noise from all the noise sources presented in this section are shown in figure 2.13. The designed strain sensitivity of Advanced LIGO is $4 \times 10^{-24}/\sqrt{\text{Hz}}$ at 100Hz.

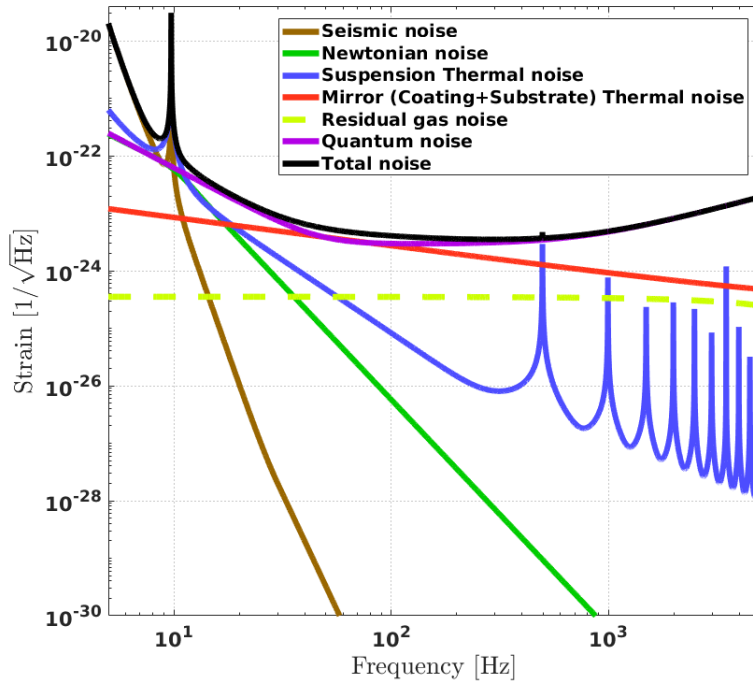


Figure 2.13: Estimation of the quantum noise (in purple). All the strain noise are added in quadrature to calculate the total noise of Advanced LIGO at full power.

2.5 Current limitations for Advanced LIGO

The first Advanced LIGO observational run (O1) started in September 2015 and concluded in January 2016. During this period, the detectors were kept in an operating mode and the commissioning activities reduced to minimum. With this run, Advanced LIGO became the most sensitive instrument to begin the GW hunt. However, the sensitivity of the IFOs during O1 was far from the designed sensitivity presented in section 2.4. A variety of technical noises prevented the IFOs to run full time at full power. In this section, we will briefly explain what limited the duty cycle and performance of Advanced LIGO, and how the work presented in this manuscript addresses some of these limitations.

2.5.1 Sensitivity

The black curve in figure 2.13 shows the expected sensitivity of the Advanced LIGO IFOs at full power ($P_{\text{input}} = 125\text{W}$). Advanced LIGO is currently far from this goal with a nominal laser input power of 25W during O1. A wide range of technical sources prevented the IFOs to operate at higher power, all explained in [67]. Scattered light, unwanted cross-couplings from auxiliary servo loops or beam jitter are a few examples

of the technical issues encountered. Most of these issues created extra-noise below 100Hz, making it hard to use higher power without losing the lock of the different cavities. At this power level, the photon shot noise is the biggest limitation above 100Hz, with a contribution higher by a factor of ~ 4 . Figure 2.14 compares the strain sensitivity obtained during O1 with the designed sensitivity.

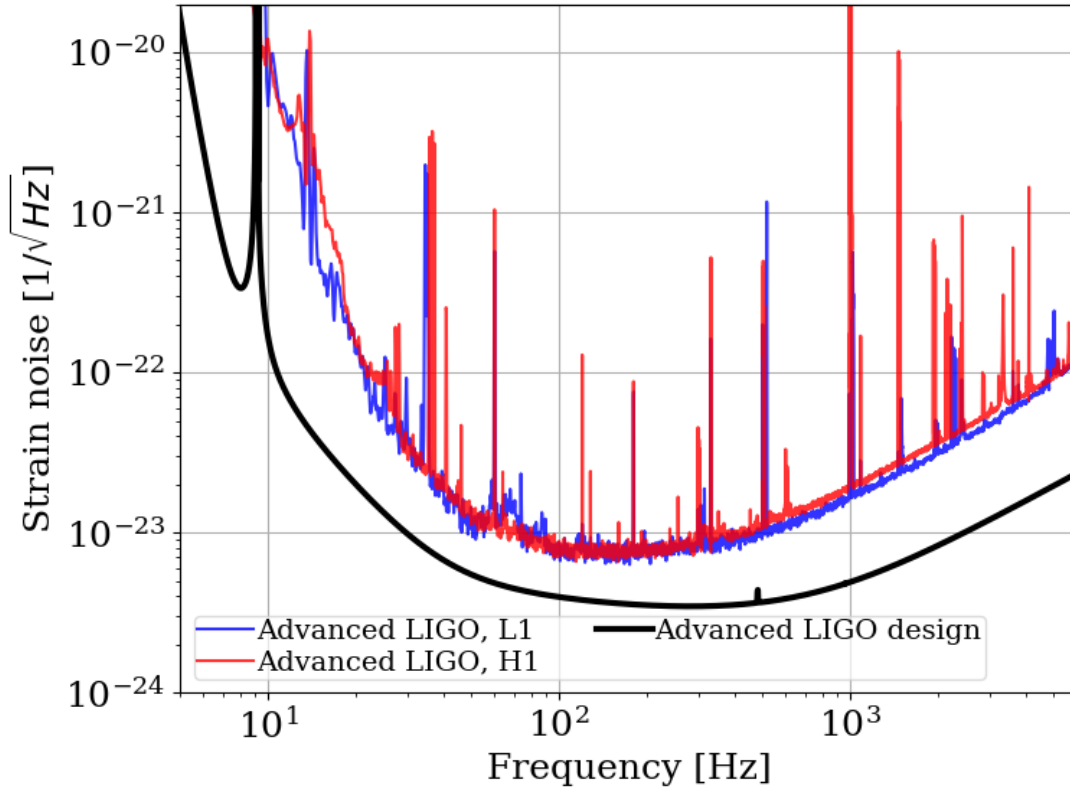


Figure 2.14: Strain sensitivity comparison between Advanced LIGO at Hanford (H1) and Livingston (L1) during O1 and the designed sensitivity for Advanced LIGO (same curve that the one presented in figure 2.13).

2.5.2 Duty cycle

Keeping the detectors in operation is a complex task, and a variety of disturbances can disrupt this process. Seismic difficulties such as earthquakes, anthropogenic activities or high-speed wind represent the biggest cause of lock-losses. During the 5-months period of O1, the duty factor for H1 was around 62.6% and 55.4% for L1. However, existing searches for GW rely on the simultaneous operation of the detectors [68, 69]. By having at least two detectors, local noise transients (ground motion, power line fluctuations, etc.) are automatically rejected as GW candidates, and detections can be made with great confidence. We recorded the equivalent of ~ 49 days of coincidence

time between H1 and L1, which corresponds to only 42.8% of the O1 total duration (see figure 2.15).

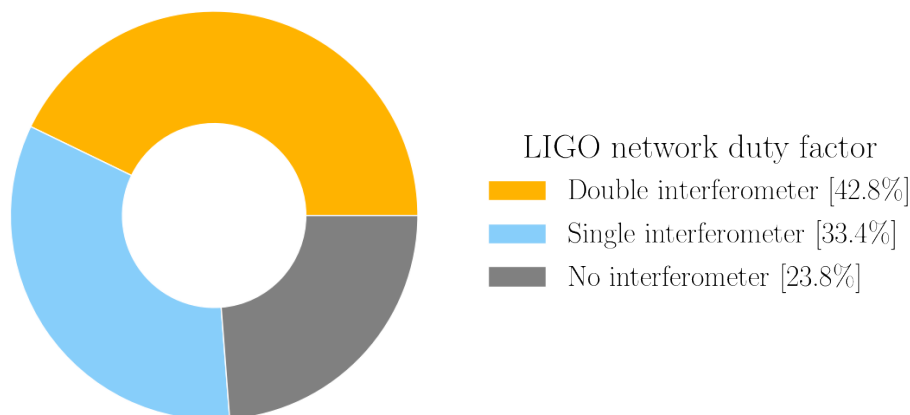


Figure 2.15: Advanced LIGO duty cycle distribution during the O1 period, from September 2015 to January 2016.

2.6 Objective of this thesis

Despite a healthy number of detections by Advanced LIGO, the IFOs are still limited in sensitivity and duty cycle. After O1, a commissioning period of ~ 10 months has been designated to improve the performance before the second run O2. For that period and after O2, a list of requirements and action items has been defined [70]. The work presented in this thesis focuses on two urgent issues regarding the current performance of Advanced LIGO.

- Chapter 3 will discuss the issue of environmental disturbances on the duty cycle, and more especially the issue of earthquakes. We will present the control strategies developed and demonstrate how they will reduce the IFOs downtime due to earthquakes by at least 40%.
- Chapter 4 will discuss the issue of parametric instabilities, which arise at high power and prevent the detectors from functioning properly (limiting their sensitivity and duty cycle). We will show that the electro-mechanical device developed during this thesis should solve the issue of parametric instabilities for Advanced LIGO.

This work has been conducted at the Massachusetts Institute of Technology (MA, USA), as part of the LIGO Research & Development activities.

Chapter 3

Environmental impacts on large-scale interferometers: study of earthquakes

3.1 The problematic

During O1, environmental hazards such as earthquakes were one of the primary sources of disturbances (see table 3.1). According to the U.S. Geological Survey (USGS), H1 experienced 265 earthquakes and L1 243 earthquakes of Richter magnitude 5 and greater while observing [71]. Some of these events overwhelmed the LIGO seismic isolation system and prevented the detectors from operating (i.e. the IFO loses its lock). Loss of the IFO lock occurred 62 times at Hanford and 83 times at Livingston during these earthquakes. Once the IFO has lost lock, it can take hours to return to normal operation. As the number of detected astrophysical signals is proportional to the detector observing time, minimizing the detector downtime is of utmost importance.

Table 3.1: Detectors' status over the O1 period. Commissioning time represents the vital maintenance tasks needed to keep the interferometers running. Environmental disturbances encompass earthquakes, high wind and storms.

	H1	L1
Observation	66 %	59 %
Commissioning	9 %	7 %
Environmental disturbances	17 %	24 %
Other	8 %	10 %

The objective of this study is to develop an earthquake mitigation scheme to limit the extra disturbance induced by earthquakes. The goal of this configuration is to maintain lock, even if doing so decreases the IFO sensitivity to gravitational-wave sources. For this reason, it cannot be permanently activated and needs to be part of the LIGO automation system called Guardian [72]. To make this switch viable, it is critical to know in advance earthquake arrival times at the sites, and an earthquake early warning system needs to be developed.

We will start by introducing the general mechanics of earthquakes and will present Seismon, the earthquake early warning system that we developed for LIGO. Then, we will talk about the effects of earthquakes at each site and the different control strategies considered to mitigate them. At the time of writing, some strategies have been already implemented and some have still to be tested. In both cases, we will present the improvement in duty cycle thanks to these strategies, either measured or estimated. Finally, we will discuss how the control configurations have been (or will be) implemented into the LIGO infrastructure.

3.2 Introduction to earthquakes

An earthquake is the shaking of the surface of the Earth, resulting from the sudden release of energy in the Earth's lithosphere. Earthquakes are mostly due to a slip between two tectonic plates, but can also be caused by volcanic activity. The seismic waves generated by an earthquake can be split into two major categories, surface and body waves. Surface waves travel across the surface of the Earth, while body waves travel through the interior. Body waves propagate in three dimensions, radiating away from the hypocenter. There is two types of body waves: primary waves (or P-waves) and secondary waves (or S-waves). P-waves are the fastest seismic waves, with a typical velocity in the range of 5 to 8 km/s. They are compression waves that can move through solid and liquid. S-waves are a little slower, with a typical velocity of 2 to 7 km/s. They are transverse waves that travel only through solid.

Surface waves instead propagate in two dimensions, which means they decay more slowly with distance than the body waves. Surface waves tend to have larger displacement amplitude than body waves, which increases the damage they cause. There is also two types of surface waves: Love waves and Rayleigh waves. Love waves are named after A.E.H. Love, a British mathematician who worked out the mathematical model for this kind of wave in 1911. It's the fastest surface wave (ranged between 2 to 6 km/s) and moves the ground from side-to-side. Confined to the surface of the crust, Love waves produce entirely horizontal motion. The other kind of surface wave is the Rayleigh wave, named for John William Strutt, Lord Rayleigh, who mathematically predicted the existence of this kind of wave in 1885. A Rayleigh wave, with a typical velocity between 2 to 5 km/s, rolls along the ground just like a wave rolls

across a lake or an ocean. Because it rolls, it moves the ground up and down, and side-to-side in the same direction that the wave is moving. Most of the shaking felt from an earthquake is due to the Rayleigh wave, which can be much larger than the other waves. For this reason, we usually refer to Rayleigh waves when we talk about surface waves. All the seismic waves described here are summarized in figure 3.1.

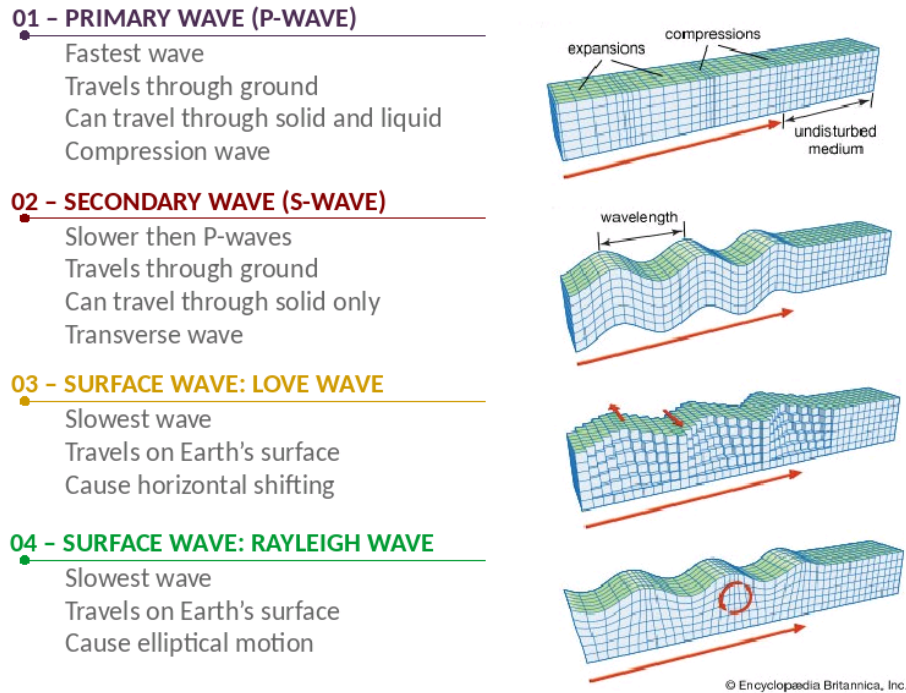


Figure 3.1: Summary of the different seismic waves generated by an earthquake. They are listed from the fastest to the slowest.

3.3 Seismon

Seismon [73] is an early warning system developed in Python, available online at <https://github.com/ligovirgo/seismon>. It has three purposes. Its primary function is to estimate the arrival time of the P, S and surface waves at each site. It uses early earthquake parameters provided by USGS and Earth models to do these estimations. Its second role is to estimate the maximum peak ground velocity generated by the surface waves at the sites (surface waves being the most problematic for LIGO, as they generate the biggest ground motion). Based on this information and on USGS parameters, a machine learning algorithm estimates the likelihood of the IFO to lose lock due to a given earthquake.

These three purposes will be explained in more details in the following sub-sections. First, the general structure of the Seismon code is described.

3.3.1 Description

USGS provides worldwide monitoring of the Earth, with over 150 seismic stations distributed globally. Thanks to this network, USGS automatically detects earthquakes when P-wave arrivals are measured at several seismic stations. Preliminary estimates of the earthquake's parameters, such as time, location, depth and magnitude, are thus generated. A collaboration between USGS and LIGO (via the IRIS consortium) allows these parameters to be distributed via a XML file through the USGS's product distribution layer (PDL) to Seismon. Seismon estimates the travel time, peak velocity and threat level of a particular event, and generates a XML file as an output. This output file is then handle by the LIGO infrastructure (see section 3.3.5). A flowchart summarizing the Seismon pipeline is shown in figure 3.2.

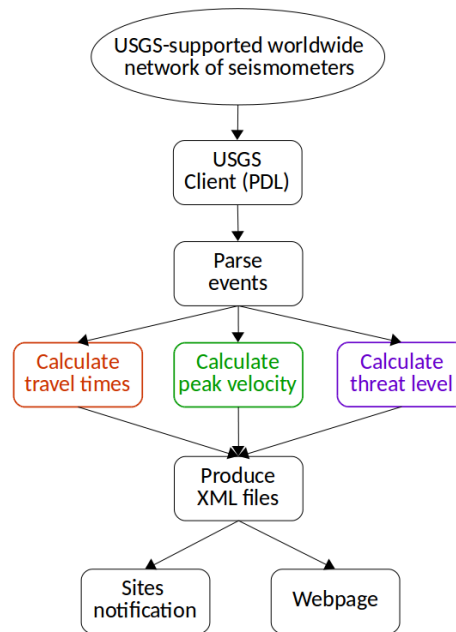


Figure 3.2: A flowchart of the Seismon pipeline. USGS information is used to estimate time arrivals, peak ground velocity and threat level for the IFO.

3.3.2 Arrival time prediction

Arrival times can easily be calculated by knowing the distance of the epicenter from the sites and the velocity of each type of wave. However, the velocity profile of the waves can be complex, as it depends on how waves interact with the rocks that make up the Earth. It of course depends on the different material properties (elastic moduli and density), but also on the depth, as the change of pressure and temperature affect the material properties. Travel time tables and Earth models have been developed in the last 90 years thanks to observation [74, 75, 76]. Great progress was made quickly

because for the most part Earth's interior is relatively simple, divided into a sphere (the inner core) surrounded by roughly uniform shells of iron and rock (the mantle). Figure 3.3 is a plot of the P and S-wave velocities and the density as a function of depth into Earth, based on the Preliminary Reference Earth Model (PREM) by Adam M. Dziewonski and Don L. Anderson [76]. Using this speed model, location and depth information from USGS, Seismon can predict P-waves and S-waves arrival with a few seconds accuracy.

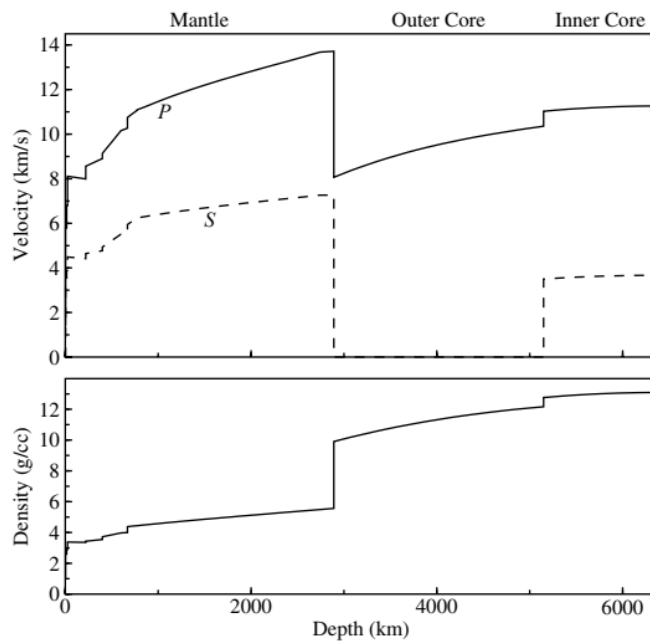


Figure 3.3: Velocity and density variations within Earth based on seismic observations. The main regions of Earth and important boundaries are labeled. The top of the Earth is located at 0 km depth, the center of the planet is at 6371 km. Credits: *chegg.com*

The estimation of surface wave velocity is trickier, as the Earth's crust is highly heterogeneous. A Rayleigh wave having a typical velocity between 2 to 5 km/s, Seismon approximates surface waves as having an averaged constant 3.5 km/s velocity, which can give an error in the arrival time of a few minutes. This is however sufficient for our purpose, as the earthquake mitigation scheme will most likely be activated before the body wave arrival. A mistake on the surface wave arrival time is therefore acceptable.

3.3.3 Velocity prediction

Because we have found no instances of P-wave arrivals causing the detector to lose lock, and very rare cases of the S-wave arrivals doing so, we considered it sufficient to calculate only the peak ground velocity of surface waves. The estimation was developed as a fit to historical earthquakes at the sites (prior O1), based on USGS

parameters. Early parameters provided by USGS are magnitude, depth and location. Unfortunately, other parameters like moment tensor solutions and finite fault models are calculated from more data, and usually arrive tens of minutes to hours after the initial notice, too late to be used by Seismon. We thus estimate the peak velocity of surface waves R_f at the sites using the equation:

$$R_f = M \frac{a}{f_c^b} \frac{e^{-2\pi h f_c / c}}{r^d} \quad (3.1)$$

where $f_c = 10^{2.3-M/2}$, M is the magnitude of the earthquake, h its depth, r the distance to the detectors and c the speed of the surface waves (assumed to be 3.5 km/s). The difference between the prediction R_f and the set of historical data is then minimized using the parameters a , b , c and d , calculated with a Monte-Carlo algorithm. More details about the velocity prediction in [73].

Overall, about 90% of events are within a factor of 5 of the predicted value, as shown in figure 3.4. This velocity prediction is not very accurate yet, and further efforts using more advanced techniques like machine learning and neural network algorithms are currently on-going [77].

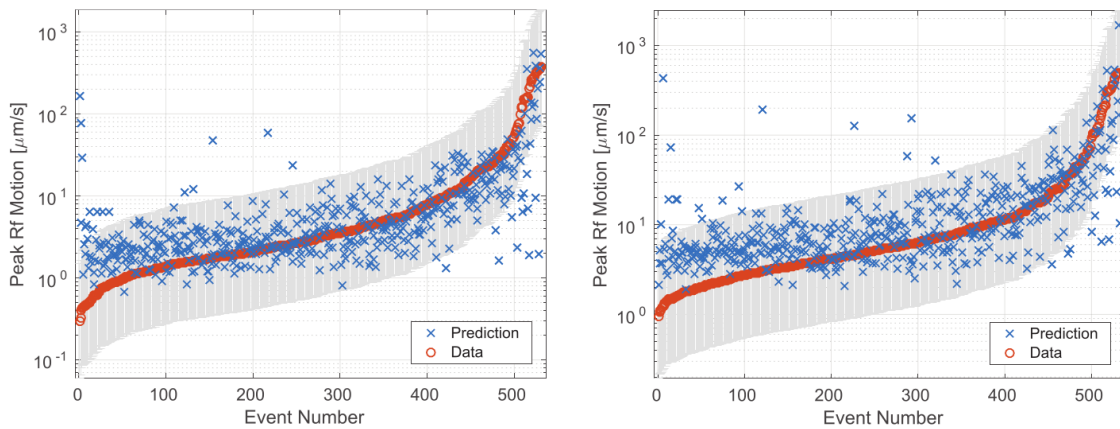


Figure 3.4: Fit of peak velocities using data prior to O1. Hanford is shown on the left and Livingston on the right. The events have been ordered by their measured peak ground velocity (in red) and the blue crosses correspond to the prediction from the equation. About 90% of events (H1 and L1) are within a factor of 5 of the predicted value. From [73].

3.3.4 Threat prediction

An earthquake monitor is useful only if we can assess which earthquakes will cause the IFO to lose lock and which will not. Based on USGS early parameters and O1

data, we used machine learning algorithms to develop a lockloss prediction model. The goal of this predictor is to assess the likelihood of the interferometer to lose lock.

Machine learning algorithms have been successfully used in the past for gravitational-wave data analysis [78, 79]. Three classifiers have been tested and compared for Seismon: logistic regression [80], naive Bayes [81] and support vector machine [82]. In this section, we will only present the most efficient algorithm that is currently used in Seismon, based on logistic regression.

We trained a set of data to predict the IFO status y . During an earthquake, the IFO either stays locked ($y = 0$) or loses lock ($y = 1$). It can be modeled by a statistical binary classification problem, using the earthquake's early parameters x_n as inputs. During O1, H1 experienced 265 earthquakes and L1 243. 200 of these events were used for each site ($\sim 80\%$ of the total) to train the logistic regression model. The rest has been used later on as a testing set to check the viability of the model. We thus defined a training set of length m , with $m = 200$:

$$\{(x^{(1)}, y^{(1)}), (x^{(2)}, y^{(2)}), \dots, (x^{(m)}, y^{(m)})\} \quad (3.2)$$

where

$$x \in \begin{bmatrix} x_0 \\ x_1 \\ \vdots \\ x_n \end{bmatrix}, \quad x_0 = 1 \quad \text{and} \quad y \in \{0, 1\}. \quad (3.3)$$

In order to map x into an output value between 0 and 1, we defined the sigmoid function $h_{\Theta}(x)$ as our logistic function:

$$h_{\Theta}(x) = \frac{1}{1 + e^{-\Theta^T x}}. \quad (3.4)$$

A graph of this logistic function is shown in figure 3.5. The parameter Θ in equation 3.4 represents the 'weight' to apply on the input x , and is defined by:

$$\Theta = \begin{bmatrix} \theta_0 \\ \theta_1 \\ \vdots \\ \theta_n \end{bmatrix}. \quad (3.5)$$

For example, if $\theta_1 \sim 0$, it means that the parameter x_1 has almost no influence on the output y_1 . The parameters θ_n are calculated with a cost function. Because the sigmoid function is very non-linear, we cannot use the square cost function that we would normally use in linear regression, but the following convex function:

$$J(\Theta) = -\frac{1}{m} \left[\sum_{i=1}^m y^{(i)} \log(h_{\Theta}(x^{(i)})) + (1 - y^{(i)}) \log(1 - h_{\Theta}(x^{(i)})) \right]. \quad (3.6)$$

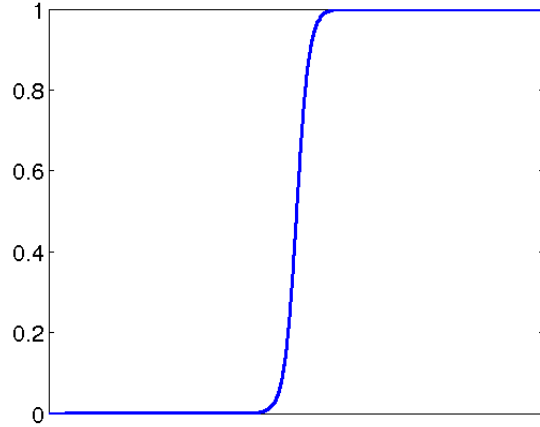


Figure 3.5: Standard logistic function $h(x)$. Note that $h(x) \in \{0, 1\}$ for all x .

This cost function is minimized using the gradient descent method. Gradient descent is an iterative optimization algorithm to find a function's minimum. It is done simultaneously for each parameter θ with the loop:

$$\theta_n := \theta_n - \alpha \frac{\partial}{\partial \theta_n} J(\theta) \quad (3.7)$$

where α is an increment parameter defined by the user. The smaller α is, the longer the calculation will take, but if α is too big, the loop will diverge. Equation 3.7 can be simplified by (see detailed calculation in annex A):

$$\theta_n := \theta_n - \alpha \sum_{i=1}^m (h_{\Theta}(x^{(i)}) - y^{(i)}) x_n^{(i)}. \quad (3.8)$$

Four early inputs are available: local peak ground velocity, magnitude, distance from the site (i.e. location) and depth. Equation 3.8 is thus used to calculate the parameter θ_n for each input x_n , and the results are shown in table 3.2. Note that among the available inputs, velocity has the most correlation with the IFO status at both sites

Table 3.2: Values of the different θ calculated for each input. This calculation has been done based on the gradient descent method, with 50,000 iterations and an increment of $\alpha = 0.04$.

Site	θ_0 (for $x_0 = 1$)	θ_1 (velocity)	θ_2 (magnitude)	θ_3 (distance)	θ_4 (depth)
Hanford	3.8028	18.7395	0.3278	0.4340	0.3605
Livingston	5.7161	13.9594	0.8673	0.2702	0.2012

(biggest θ). It will be thus important to improve the accuracy of the Seimon velocity prediction in the future if we want to increase the accuracy of this model.

Now that the model has been trained, we check its efficiency with the remaining $\sim 20\%$ input data left from O1. Based on this data and the parameters in table 3.2, the logistic function (equation 3.4) is calculated for each event and compared with the real output. The efficiency of the predictor is proved from the receiver operator characteristic curve (ROC) shown in figure 3.6: the bigger the area under the ROC curves, the more efficient is the model (an area of 1 will be a perfect model). With an area of ~ 0.75 for both Hanford and Livingston, the model developed is pretty reliable.

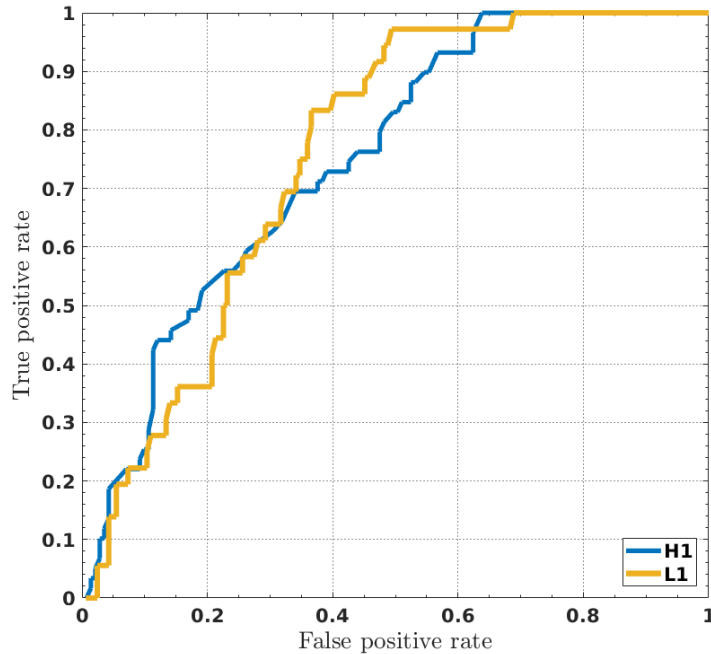


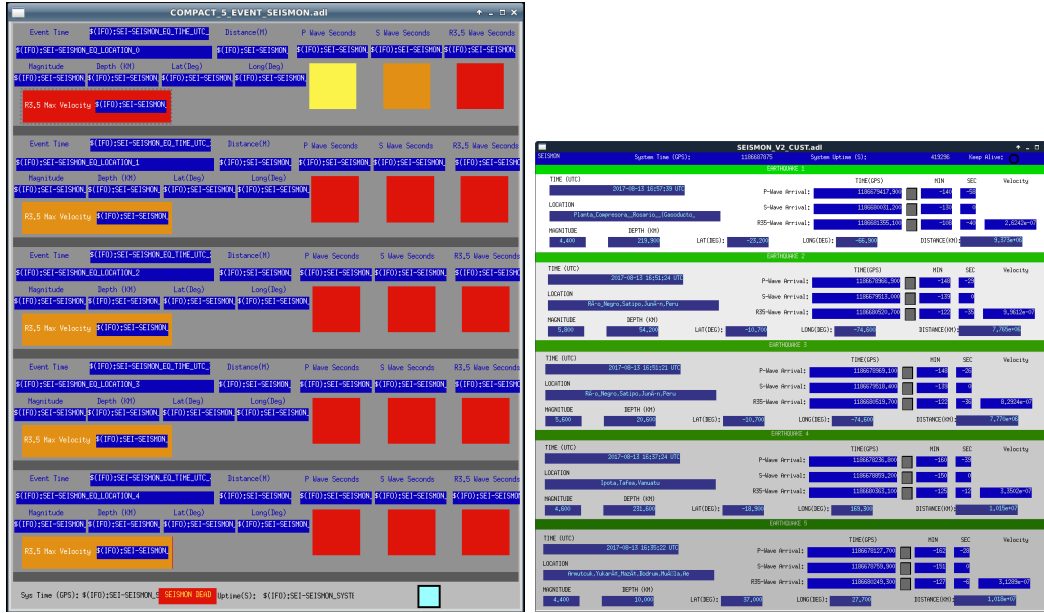
Figure 3.6: Performance of the logistic regression classifier at Hanford and Livingston. True positive rate is the ratio of the sum of predicted positive condition actually being true to the sum of all actually positive conditions. Positive condition here refers to a lockloss prediction by the classifier which in general can be true or false. False positive rate is the ratio of the sum of predicted positive condition being false to the sum of all actually negative conditions. Classifier prediction about the detector being in lock forms the negative condition. The area under the curves assesses the efficiency of this classifier.

3.3.5 Output

In summary, Seismon is a low-latency earthquake warning system, which predict likely earthquake arrival times, ground velocity amplitudes and threat levels for the IFO. In most cases, there is more than 10 min available between notification and wave arrivals. This is more than sufficient time for gravitational-wave detectors to respond by changing control configurations. The ultimate goal would be to automatically switch configurations based on Seismon information. However, as this project is still in development, this part is not implemented yet. Nevertheless, Seismon information is already available in the control room at both sites via graphical user interfaces. It is also accessible through the web with LSC (Ligo Scientific Collaboration) credentials for people within the collaboration. All the different interfaces are shown in figure 3.7.

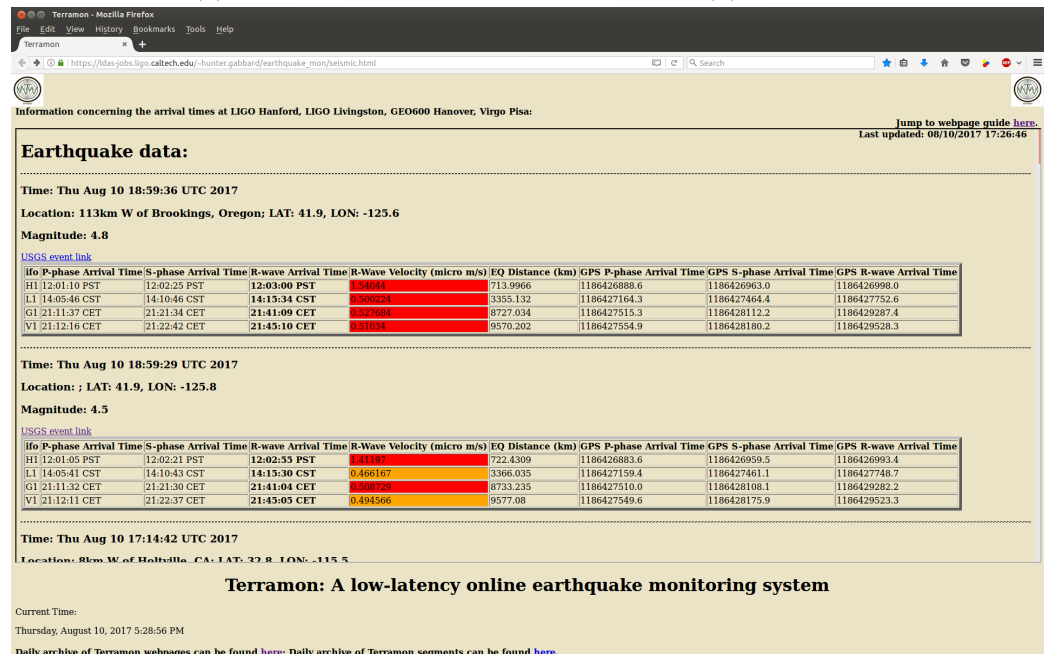
Even if Seismon is not part of the LIGO automation system yet, its early warning information is already available to the LIGO commissioners and operators. Based on this information, they can decide to act on the IFO configuration or not.

We will now study what can be done in terms of controls to improve the IFO robustness during earthquakes. We will describe the ground behavior at both sites during earthquakes before presenting controls strategies.



(a) Hanford

(b) Livingston



(c) Webpage

Figure 3.7: Screenshots of the different interfaces used for Seismon. *a)* and *b)* are the graphical interfaces used in the control rooms at Hanford and Livingston respectively. *c)* is the webpage accessible with LIGO credentials at https://ldas-jobs.ligo.caltech.edu/~hunter.gabbard/earthquake_mon/seismic.html. Each screen displays the USGS early information: time of the event, location and magnitude. It also provides the P, S and R waves arrival times from Seismon, both in local time and GPS time. Note that information for the GEO site in Germany (G1) and VIRGO site in Italy (V1) are available on the webpage. Finally, the Seismon predicted peak velocity is displayed in $\mu\text{m/s}$, attached with a color code. Color indicates likelihood of appreciable seismic disturbance at that observatory: Green is good data quality, Yellow is potentially-reduced data quality, Orange is definitive reduced data quality, and Red is likely lock loss. Data quality indicators are based on seismic noise floor studies done for Livingston [83]. Ultimately, this color code will be based on Seismon predictor model (in development).

3.4 Ground behavior at the sites

3.4.1 Local motion

Each site is equipped with several Trillium T240 ground seismometers, located at different strategic points along the interferometer arms. Data stretches from the seismometer close to the ITMY vacuum chamber (see figure 3.8) have been extracted over the total time span of the O1 period at both sites. Some stretches were selected at random times, while other were selected during earthquakes of Richter magnitude 5 and higher. The seismic spectra generated with this data are shown in figure 3.9.

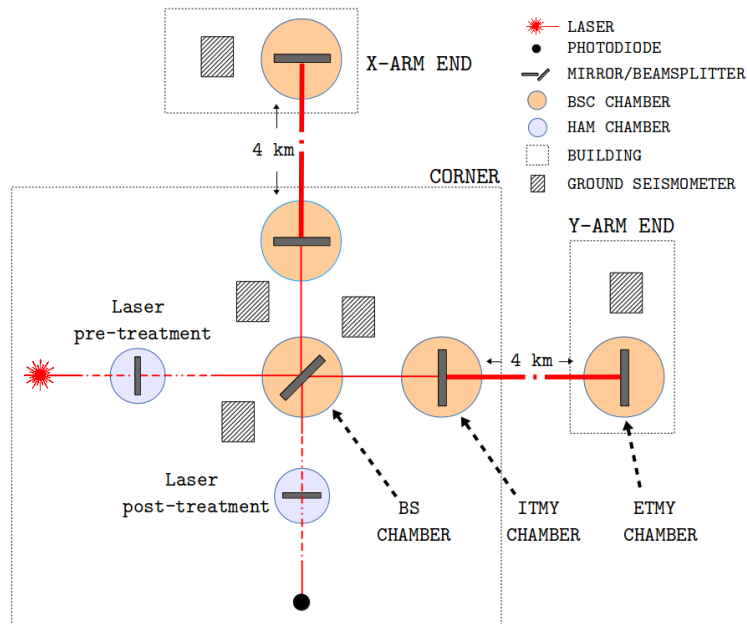


Figure 3.8: Simplified optical layout of the LIGO detector, showing the approximate positions of the ground seismometers at the sites. For clarity, *Laser pre-treatment* and *Laser post-treatment* regroup all of non-core optics and the multiple vacuum chambers in which they are housed.

Overall, we observe higher seismic activities at Livingston compared to Hanford, earthquake or not. The Livingston site, located only 130 km away from the Gulf of Mexico, experiences many storms through the year and suffers from significant ground motion variations. Moreover, the interferometer buildings rest on earth banking, consisting of local silt and sand, while the Hanford buildings rest on sediments and hard rock. For these reasons Livingston experiences high microseism around $\sim 200\text{mHz}$ and large tilt motion below 100mHz , due to wind gusts tilting the buildings. At both sites we notice that any earthquake, independent of their epicenter location or depth, generated a non-negligible increase of the ground motion from 30 mHz to 100mHz . For this reason our study will focus on the $[30\text{mHz}-100\text{mHz}]$ band, usually referred to as the earthquake band.

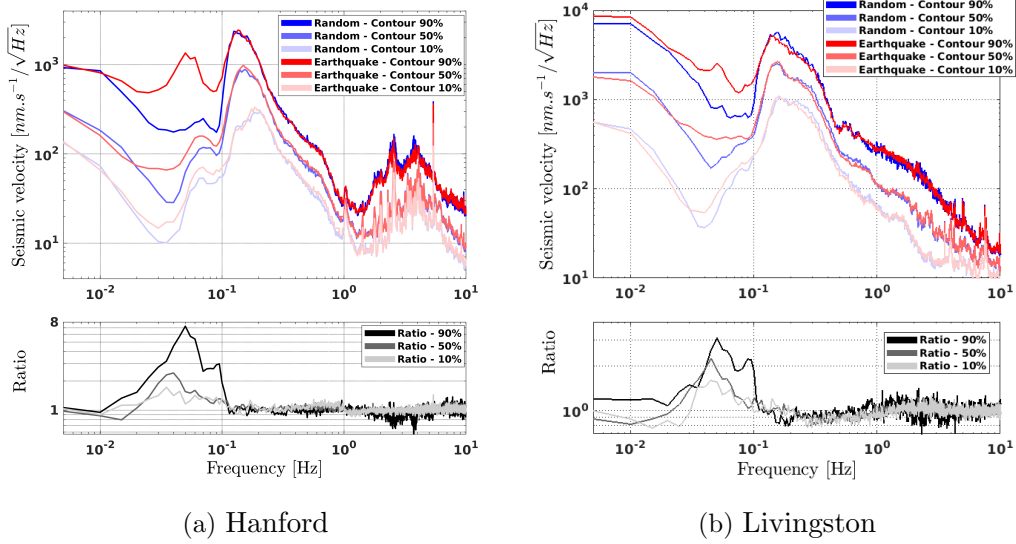


Figure 3.9: 1000-second long data stretches were selected over the total time span of the O1 period. Specifically, the blue curves correspond to stretches selected at random times, while the red curves correspond to stretches selected during earthquakes of Richter magnitude 5 and above. For each frequency bin, the data were histogrammed and a set of probabilities was found. The different shades of color indicate different probability values (10%, 50%, 90%), the darkest tone being a 90% probability. The bottom part of this figure represents the ratio between the red and the blue curves for each set. We observe an amplification of the ground motion up to a factor of 7 at Hanford and 3 at Livingston in the [30mHz-100mHz] band. Only the horizontal direction along the Y-arm of the interferometer is represented here, but we obtain similar results in the X-horizontal direction and the vertical direction. From [71].

3.4.2 Common motion

The stability of the IFO depends heavily on the relative motion between the different chambers, as we will discuss later in section 3.5.5. We compared the difference of ground motion along the Y-arm between the input and output optics ITMY and ETMY (4km apart), but also in the corner station between the input optics ITMY and the beam-splitter BS (only a few meters apart). Stretches were selected at random times as well as during earthquakes of Richter magnitude 5 and above. Based on this data, we can calculate the averaged common mode motion of the arm and in the corner station:

$$CM_{arm} = \frac{ETMY + ITMY}{2} \quad \text{and} \quad CM_{corner} = \frac{ITMY + BS}{2} \quad (3.9)$$

as well as the local differential mode motion at the input optics:

$$DM_{arm} = ITMY - CM_{arm} = \frac{ITMY - ETMY}{2}, \quad (3.10)$$

$$DM_{corner} = ITMY - CM_{corner} = \frac{ITMY - BS}{2}. \quad (3.11)$$

The seismic spectra generated with this data are shown in figure 3.10. In the corner station, the ground motion is common between 100mHz and a few Hertz (earthquake or not), as the slab/building is moving in one block. Above ~ 1 Hz, we see an increase in differential motion, suggesting specific close sources of vibration and local deformation of the ground, as observed before [84]. Below 100mHz, coherence between the seismometers starts to drop, as the signals are dominated by sensor noise and coupled tilt (more details on tilt in section 3.5.3). This is less true during earthquakes, since we have a bigger horizontal signal generated by the earthquakes in the [30mHz-100mHz] band. Along the 4km arm, the motion between the corner and end station is mostly differential above ~ 300 mHz, but we still observe common motion at lower frequencies, especially during earthquakes (with the same limitation in terms of tilt and sensor noise). Overall, the motion is dominated by the common mode in the earthquake frequency band, along the arm and in the corner station. This is especially true during earthquakes, with $\sim 80\%$ common motion in this band along the arm.

3.5 Control strategies

Advanced LIGO has an impressive array of sensors and a flexible control system, and different control strategies are being considered to reduce the impact of earthquakes on the IFO. We will present three strategies studied during this thesis, referred to as 'tilt reduction', 'gain peaking reduction' and 'common mode rejection along the arms'. These strategies rely on changes in the control configuration of the LIGO seismic platforms. Before going further, it is thus necessary to describe the seismic isolation systems and the performance they achieved during O1.

3.5.1 Seismic platform architecture

All of the LIGO optics are mounted on seismic isolation platforms, which seek to decouple the optics from the ground. A Hydraulic External Pre-Isolator (HEPI) is used as a pre-isolation and positioning stage outside the vacuum chamber. It supports an active Internal Seismic Isolation (ISI) system inside the chamber, on which are mounted the optics. There are two types of ISI systems: a single-stage platform and a two-stage platform. The single-stage platforms are used for the auxiliary optics in the small vacuum chambers called Horizontal Access Modules (HAMs). The two-stage platforms are used for the core optics of the interferometer in the large vacuum tanks called Basic Symmetric Chambers (BSCs). In total, a detector has 11 vacuum

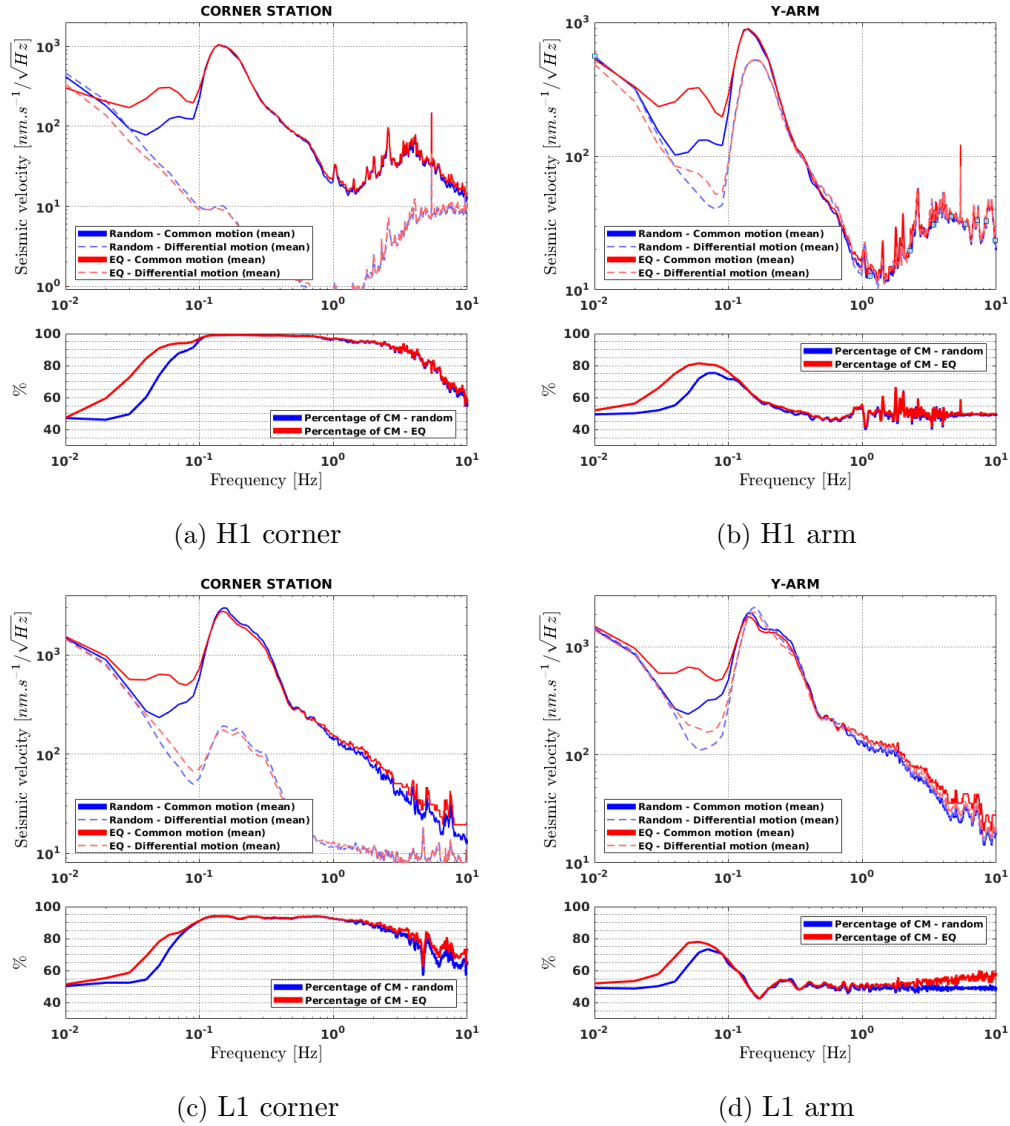


Figure 3.10: Comparison between the common and differential motions in the corner station and along the Y-arm at both sites. Data were selected at random times (blue curves), and during earthquakes of Richter magnitude 5 or greater (red curves). In the corner station at Livingston, we see a ratio of 90% between 100mHz and 1Hz instead of 100%. We believe this is due to a calibration issue between the seismometers.

tanks (six HAM chambers, five BSC chambers) each with a seismic isolation platform. Despite some mechanical differences between the vibration isolation systems, the general concept is identical for all of them. A combination of active and passive isolation is provided to bring the BSC-ISI platform motion down to $1 \cdot 10^{-12} \text{ m}/\sqrt{\text{Hz}}$ at 10Hz and the HAM-ISI platform motion down to $2 \cdot 10^{-11} \text{ m}/\sqrt{\text{Hz}}$ at 10Hz.

The mechanics and functioning of these platforms have been extensively studied in previous works ([52, 85, 86, 87]). In this study, we are particularly interested in the active isolation configuration and performance of the BSC-ISI stage 1 platform.

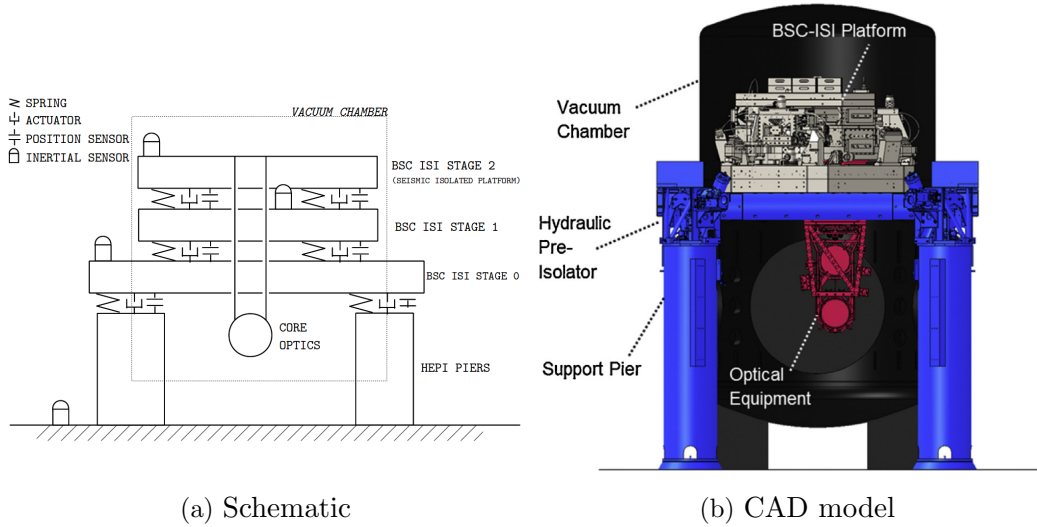


Figure 3.11: Presentation of a LIGO BSC chamber. Each stage is equipped with multiple actuators, position and inertial sensors (only a few are represented here for clarity). The core optics are supported by a quadruple pendulum which provides additional seismic isolation in all degrees of freedom. From [71] and [85].

The BSC-ISI stage 1 platform is the only stage that has low noise Trillium T240 seismometers, which are used to mitigate low frequency disturbances. Figure 3.11 illustrates the layout of the BSC chamber.

3.5.2 Seismic control scheme

Each stage is equipped with a set of actuators, displacement sensors and inertial sensors. They are used to actively control the stage in the three translational and three rotational degrees of freedom. The platforms have been designed to limit the cross-coupling between the different degrees of freedom, therefore, each degree of freedom can be actively controlled independently with Single-Input Single-Output compensators.

The LIGO seismic control scheme is a combination of feedback, feedforward and sensor correction. The block diagram in figure 3.12 shows the simplified control topology for one degree of freedom. Note that this particular diagram doesn't take the issue of tilt in account: it will be discussed later on.

Feedback control

A control force F is used to reduce the inertial motion of the stage (Y_{Stage}), which is induced by the ground (Y_G). This control force is created using a combination of

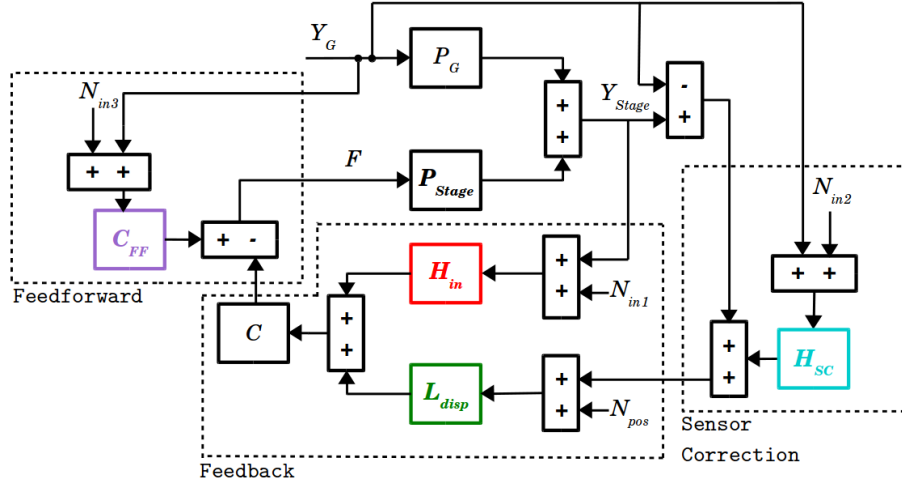


Figure 3.12: Control block diagram of a seismic isolation stage for one degree of freedom. The colored blocks are related to figure 3.13.

feedback and feedforward controllers. The feedback controller is fed by two sensors: a displacement sensor measuring the relative motion between the stage and the input motion ($Y_{Stage} - Y_G$), and an inertial sensor (seismometer) measuring the inertial motion of the stage (Y_{Stage}). Below 25mHz, the seismometer noise becomes comparable to the ground motion, making inertial isolation impossible. Therefore, a displacement sensor is used at low frequencies and both sensors are blended together to feed the controller. The relative motion signal is low-passed by a filter L_{disp} , and the inertial motion signal is high-passed by a filter H_{in} . L_{disp} and H_{in} are designed to be complementary, meaning $L_{disp} + H_{in} = 1$. The frequency at which the low-pass and high-pass filters cross is called the blend frequency. The controller provides isolation up to 30Hz, with high loop gain below 1Hz. The squared modulus of the expected inertial motion of the stage, when only the feedback control is engaged, is given by equation 3.12 (it is expressed as the squared modulus since the different sources are incoherent). N_{pos} and N_{in} represent the noise associated with the displacement sensors and inertial sensors respectively. P_G and P_{Stage} represent the transfer functions from the ground motion and applied force respectively.

$$\begin{aligned}
 |Y_{Stage}|^2 = & \left| \frac{P_G + L_{disp}CP_{Stage}}{1 + CP_{Stage}} Y_G \right|^2 \\
 & + \left| \frac{H_{in}CP_{Stage}}{1 + CP_{Stage}} N_{in1} \right|^2 \\
 & + \left| \frac{L_{disp}CP_{Stage}}{1 + CP_{Stage}} N_{pos} \right|^2
 \end{aligned} \tag{3.12}$$

Sensor Correction

Sensor correction is a feedforward technique using a seismometer from the ground. The seismometer signal Y_G is filtered by H_{SC} and added to the position sensor signal ($Y_{Stage} - Y_G$) to create a virtual inertial sensor [88]. Our sensor correction is designed to maximize performance around 100mHz. By adding the sensor correction to the feedback loop, the stage inertial motion becomes:

$$\begin{aligned}
|Y_{Stage}|^2 = & \left| \frac{P_G + L_{disp}CP_{Stage}(1 - H_{SC})}{1 + CP_{Stage}} Y_G \right|^2 \\
& + \left| \frac{H_{in}CP_{Stage}}{1 + CP_{Stage}} N_{in1} \right|^2 \\
& + \left| \frac{L_{disp}H_{sc}CP_{Stage}}{1 + CP_{Stage}} N_{in2} \right|^2 \\
& + \left| \frac{L_{disp}CP_{Stage}}{1 + CP_{Stage}} N_{pos} \right|^2.
\end{aligned} \tag{3.13}$$

Feedforward control

A standard feedforward controller C_{FF} is added from the ground in parallel with the feedback and sensor correction loops. This operates where the coherence with the ground is high (above 1Hz). Ultimately, the sensor correction and feedforward controllers are both feedforward techniques added to the feedback loop. However, these two controllers are implemented at different levels in the control scheme for technical reasons, as they target different frequency bandwidths and use different sensors. Overall, the stage absolute motion becomes:

$$\begin{aligned}
|Y_{Stage}|^2 = & \left| \frac{P_G + L_{disp}CP_{Stage}(1 - H_{SC}) + C_{FF}P_{Stage}}{1 + CP_{Stage}} Y_G \right|^2 \\
& + \left| \frac{H_{in}CP_{Stage}}{1 + CP_{Stage}} N_{in1} \right|^2 \\
& + \left| \frac{L_{disp}H_{sc}CP_{Stage}}{1 + CP_{Stage}} N_{in2} \right|^2 \\
& + \left| \frac{C_{FF}P_{Stage}}{1 + CP_{Stage}} N_{in3} \right|^2 \\
& + \left| \frac{L_{disp}CP_{Stage}}{1 + CP_{Stage}} N_{pos} \right|^2.
\end{aligned} \tag{3.14}$$

Equations 3.12, 3.13 and 3.14 are plotted in figure 3.13. In this example, we used a BSC-ISI stage 1 model with the filters used during O1 to simulate the performance of each loop and the combined overall performance. The figure shows the transfer function between the stage and ground motion $\frac{Y_{\text{Stage}}}{Y_{\text{G}}}$ with the feedback loop only (solid orange curve), with the feedback loop and sensor correction on (solid brown curve) and with feedback, sensor correction and feedforward on (solid black curve). The motion associated with sensor noise is not represented on this figure for clarity. The open loop (not represented) has a 30Hz unity gain frequency. The sensor correction filter (dashed cyan curve) is designed to provide extra isolation between 50mHz and 200mHz, whereas the feedforward filter (dashed purple curve) provides isolation at 1Hz and above. At low frequencies where the loop gain is effectively infinite, the performance is limited by the low-pass filter (dashed green curve), and limited by the finite loop gain at higher frequencies. Typically, the low-pass filter is tuned to provide as much isolation as possible in the control bandwidth at the cost of some gain peaking around the blend frequency (in this case $\sim 45\text{mHz}$). Below the blend frequency, the motion is dominated by the position sensor signal and the platform moves with the ground (transfer function of 1). Finally, some sharp notches are also present in the low-pass filter to target known payload resonances.

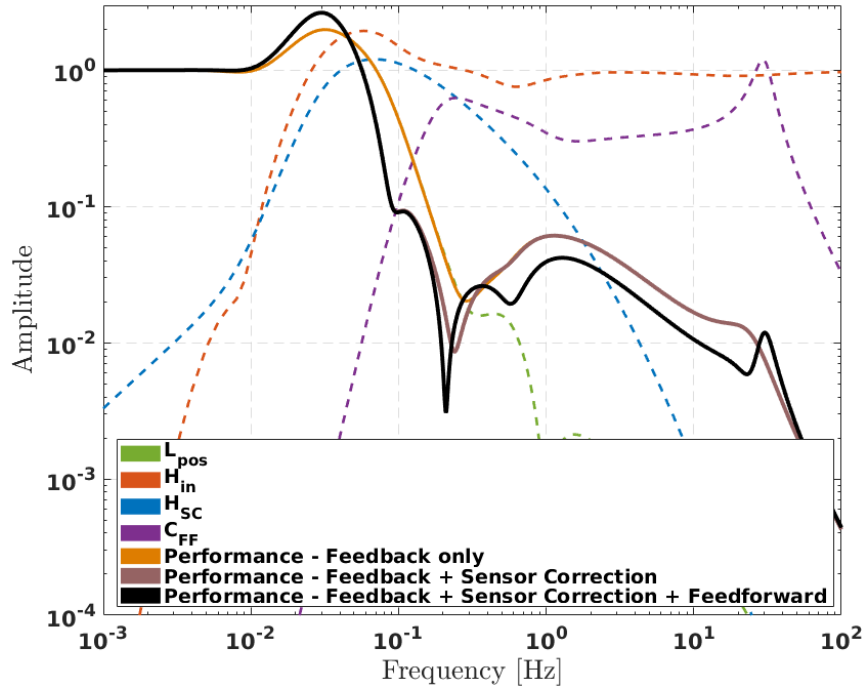


Figure 3.13: Example of the LIGO seismic control scheme performance on the BSC-ISI stage 1 platform. The dashed curves show the different filters used, as opposed to the solid curves showing the transfer functions from the ground motion with different loops engaged.

3.5.3 Tilt-Horizontal coupling

When working with seismometers at low frequencies, tilt is a recurrent topic [89, 90]. Because they are based on mass-spring systems, horizontal seismometers are sensitive to both translation and rotation in the presence of gravity. Let's consider a mass-spring system of mass m , stiffness k and damping c , housed in a cage on the floor. The mass location is x_m with respect to the cage location x_0 . The floor is allowed to tilt with respect to local gravity g by an angle θ (because the motions are small, we ignore centrifugal forces). This system, shown in figure 3.14, can be described by

$$m\ddot{x}_m(t) + c(\dot{x}_m(t) - \dot{x}_0(t)) + k(x_m(t) - x_0(t)) = -mg\sin(\theta(t)). \quad (3.15)$$

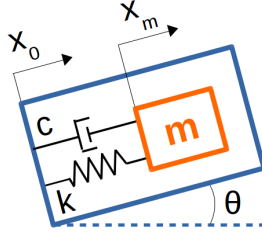


Figure 3.14: Model considered to estimate the tilt coupling in horizontal seismometers.

Taking the Laplace transform of these equations, and assuming small angles ($\sin(\theta) \sim \theta$), we can write the signal measured by the seismometer $X_m(s) - X_0(s)$ as

$$X_m(s) - X_0(s) = -\frac{ms^2}{ms^2 + cs + k}X_0(s) - \frac{mg}{ms^2 + cs + k}\Theta(s). \quad (3.16)$$

Equation 3.16 clearly shows that the differential motion measured is sensitive to both floor motion and floor tilt. The ratio of the sensitivity to rotation to the sensitivity of horizontal motion is

$$\frac{(X_m(s) - X_0(s))_{rotating}/\Theta(s)}{(X_m(s) - X_0(s))_{translating}/X_0(s)} = \frac{g}{s^2}. \quad (3.17)$$

Hence, in the frequency domain, for a specific frequency ω :

$$\frac{\text{rotation response}}{\text{translation response}} = -\frac{g}{\omega^2}. \quad (3.18)$$

Due to the $\frac{1}{\omega^2}$ frequency dependence, tilt pollutes the signal of the horizontal seismometers only at low frequencies, typically below 100mHz. It is taken into account

in our model by adding the extra signals S_{tilt1} and S_{tilt2} . S_{tilt2} represents the tilt measured by the seismometer on the ground and S_{tilt1} the tilt measured by the seismometer on the stage. Note that tilt can be sensed by the position sensors due to misalignment of the sensors with respect to the platform. However, corrections have been implemented to suppress this coupling [91], and the tilt seen by the position sensors is negligible.

Figure 3.15 shows the updated control diagram with the tilt signals. The stage absolute motion becomes:

$$\begin{aligned}
 |Y_{Stage}|^2 = & \left| \frac{P_G + L_{disp}CP_{Stage}(1 - H_{SC}) + C_{FF}P_{Stage}}{1 + CP_{Stage}} Y_G \right|^2 \\
 & + \left| \frac{H_{in}CP_{Stage}}{1 + CP_{Stage}} N_{in1} \right|^2 + \left| \frac{H_{in}CP_{Stage}}{1 + CP_{Stage}} S_{tilt1} \right|^2 \\
 & + \left| \frac{L_{disp}H_{sc}CP_{Stage}}{1 + CP_{Stage}} N_{in2} \right|^2 + \left| \frac{L_{disp}H_{sc}CP_{Stage}}{1 + CP_{Stage}} S_{tilt2} \right|^2 \\
 & + \left| \frac{C_{FF}P_{Stage}}{1 + CP_{Stage}} N_{in3} \right|^2 \\
 & + \left| \frac{L_{disp}CP_{Stage}}{1 + CP_{Stage}} N_{pos} \right|^2.
 \end{aligned} \tag{3.19}$$

Based on the complete control diagram, we have developed a Simulink model (shown in figure 3.16) to budget the different noise sources and estimate the performance of the strategies that we will present. In this model, inputs $T240_Noise$, LAC_Noise and CPS_Noise are the noises associated with the different sensors, extracted from the GWINC (Gravitational-Wave Interferometer Noise Calculator) package [53]. The input Y_Ground is 1000-stretch data from the O1 period, representative of a typical ground motion. We however had to make some assumptions regarding the input RX_Ground , since LIGO doesn't have sufficiently sensitive rotation sensors to measure the rotation of the ground yet¹. There are, in theory, many ways to extract rotation by combining the measurements of several vertical and horizontal sensors [92, 93, 94], but these techniques are sensor noise limited in the case of LIGO [95]. We thus have developed a simple estimation of the tilt by matching the model with the measured data from O1. If we consider that tilt dominates the horizontal signal at low frequencies, based on equation 3.18 we define

$$RX_Ground = \alpha \frac{\omega^2}{g} \cdot Y_Ground \tag{3.20}$$

with α a calibration gain. This gain is tuned to match the modeled absolute motion

¹Rotation sensors are currently being installed at the sites. We will come back to this point in the general conclusion.

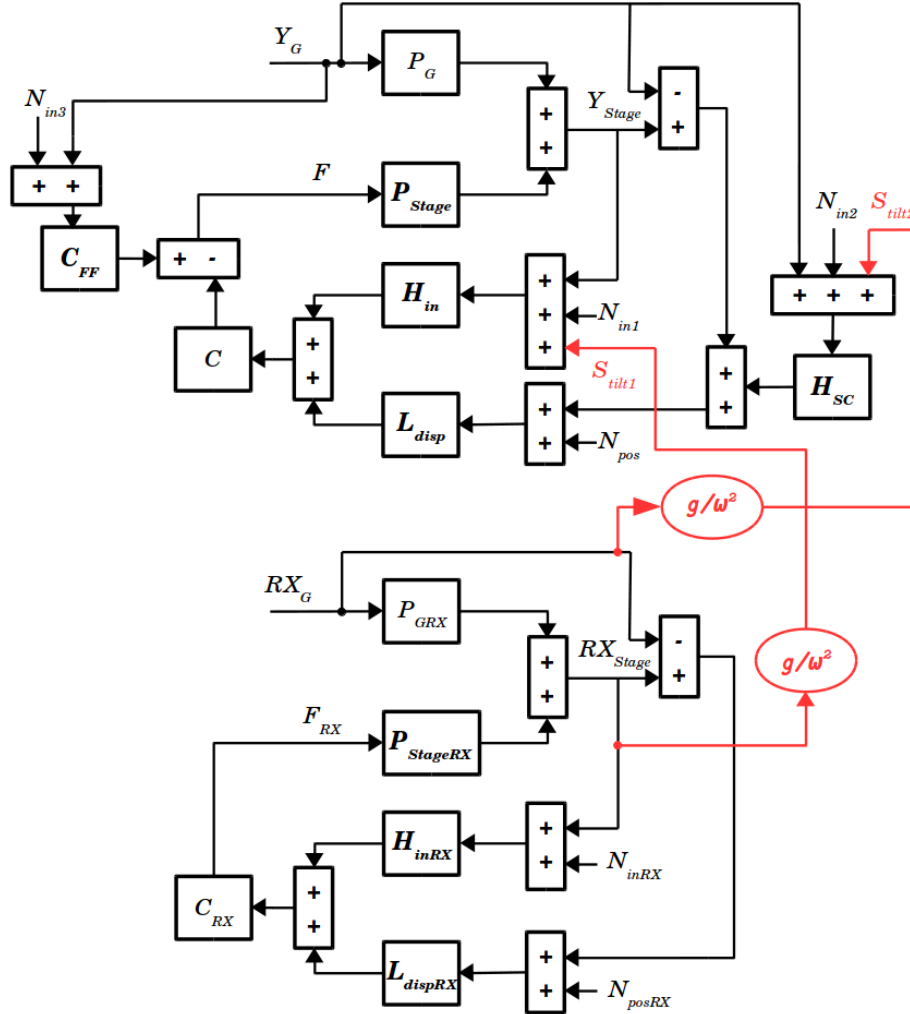


Figure 3.15: A more realistic control block diagram for one degree of freedom, including the tilt seen by the seismometers. The only difference between the translational degree of freedom Y and the rotational degree of freedom RX is that rotation has the feedback loop engaged only (no sensor correction nor feedforward), since there is no rotation sensors on the ground.

of the platform Y_Motion with the actual measured signal on the platform at low frequencies (i.e. below 50mHz). By using this technique, the tilt modelization is not accurate at higher frequencies, but it is sufficient for our purpose. The fidelity of the model will be shown in the next section.

3.5.4 O1 nominal configuration and performance

The filters used during O1 were designed to meet LIGO requirements and maximize the seismic isolation above 100mHz, at the expense of some gain peaking at lower frequencies. It was similar on all the BSC-ISI stage 1 platforms at both sites. Figure 3.17 shows the measured performance of this configuration during a typical ground

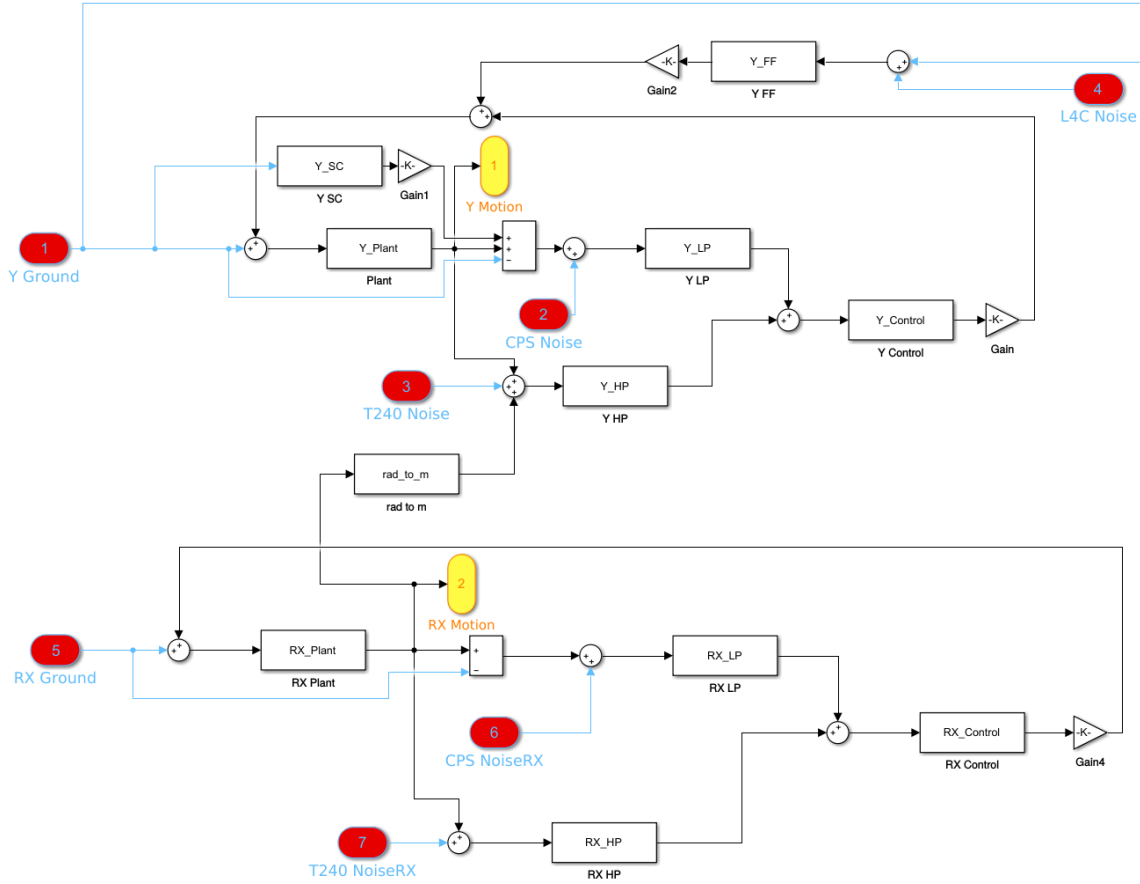


Figure 3.16: Simulink model developed based on the control diagram presented in figure 3.15. The output Y_Motion and RX_Motion represent the close loop the stage in the Y and RX directions respectively.

motion period (blue curve). The stage provides a factor ~ 40 of isolation at 200mHz at the expense of a gain peaking of ~ 4 at 50mHz. Below 50mHz, the signal is polluted by tilt at Hanford, especially by tilt from the seismometers on the stage (purple curve). At Livingston, while tilt is also the main noise source, typical horizontal ground motion is dominant at low frequencies. The red curve shows the motion predicted by the model, and we observe a very good agreement with the measured velocity below 600mHz. Above this frequency, we start seeing some disparities between the model and the measurement, especially at Livingston where we are not noise limited. This is due to the fact that the model uses a simplified transfer function model of the stage, and doesn't take into account the payload resonances at ~ 450 mHz and ~ 1 Hz. This is not a concern since we are focusing our effort on low frequencies in this study. The model being properly tuned, it will be used to estimate the performance of the strategies presented.

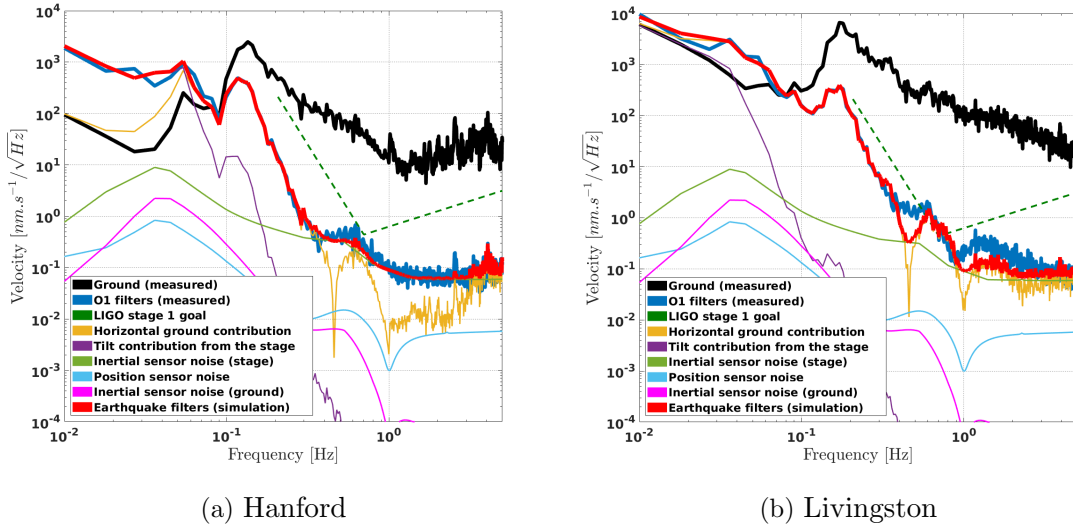


Figure 3.17: Seismic isolation provided by BSC-ISI stage 1 in the Y-direction at both sites. The black curve represents a typical ground motion, and the blue curve the measured motion of the stage. The dotted curve indicates the LIGO goal to obtain from 200mHz to higher frequencies for stage 1. The thinner curves indicate the estimated noise contributions, and the red curve shows the simulated overall motion.

3.5.5 First strategy: Tilt reduction.

In section 3.4.2, we presented the difference of ground motion between chambers during O1. In the earthquake band, we observed mostly common motion in the corner station and along the Y-arm. Figure 3.18 shows similar analysis regarding stage 1 motion between chambers, during random times as well as during earthquakes (data is extracted from the in-loop seismometers on the stages). Overall, we see a huge reduction of the common displacement at all times, especially in the corner station. It is not clear why the relative motion is larger on the platforms compared to the ground, and we presume it results from excess tilt on the stages. The goal of the control strategy presented in this section is therefore to reduce the tilt re-injection S_{tilt1} on the platforms, since the feedback loop converts this to unwanted, differential displacement. Reducing the differential displacement will relax the control authority of the cavity-length control loop, which will reduce angle displacement. Indeed, even if we observe small cross-coupling between the different degrees of freedom on a seismic isolation platform, this is not true for the LIGO suspensions. LIGO suspensions in general (quadruple and auxiliary suspensions) present strong length to angle coupling according to LIGO standards. This coupling is primarily due to mismatch between the various blades (i.e. springs) supporting a suspension [96]. In the earthquake band, it is in the order of 2% for the ITM/ETM suspension according to models, but measurements have shown that it can be worse, varying greatly from one suspension to another [97]. The consequence of this large cross-coupling in the suspensions is that the longitudinal control signals generate unwanted angular motion. Given the

4km long cavities of LIGO, the stability of the IFO is very dependent on the angular fluctuations, as demonstrated in previous works [98, 99].

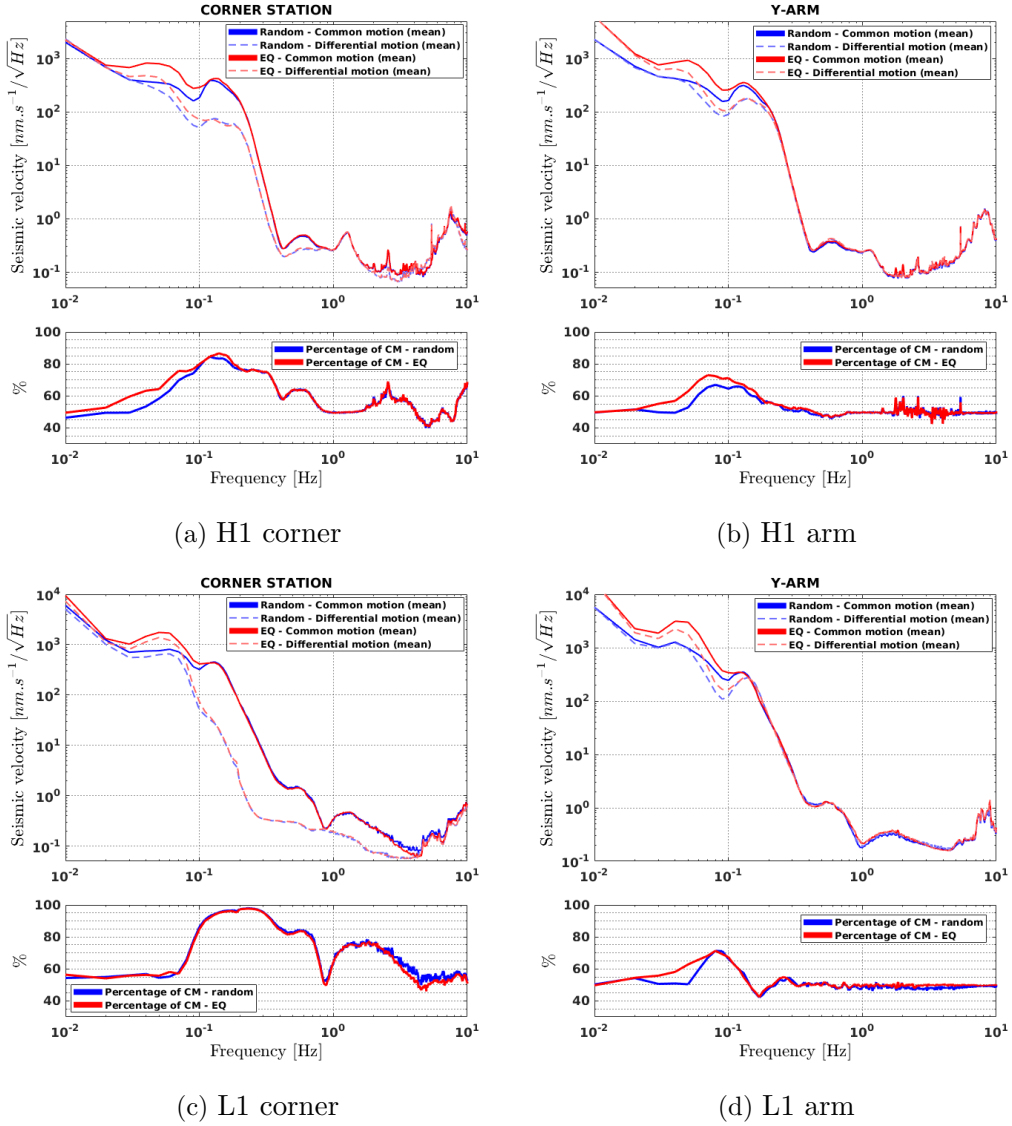


Figure 3.18: Comparison between the common and differential motion in the corner station and along the Y-arm at both sites. Data were selected at random times (blue curves), and during earthquakes of Richter magnitude 5 or greater (red curves).

To summarize, by reducing the tilt on the platforms, we should reduce the differential motion and relax the cavity longitudinal control force, which reduces the angular fluctuations of the IFO and improve its stability. This should improve the robustness of the IFO at all times, earthquake or not.

A simple way to reduce tilt re-injection in the horizontal direction is to have a higher blend frequency. At low frequencies, the loop gain is effectively infinite and the coupled tilt is defined by $H_{in}S_{tilt1}$, as demonstrated in equation 3.21. Having more

roll-off on the H_{in} filter at low frequencies would limit the impact of tilt. However, an increase in blend frequency will significantly reduce the performance of the isolation at the microseism and above, which might not be viable for the detectors. Therefore, the sensor correction has to be more aggressive to compensate this loss in performance, as the stage motion is directly dependent on the low-pass filter L_{disp} and the sensor correction filter H_{SC} . The low-pass filter, high-pass filter and sensor correction are thus tuned to find a good compromise between performance and tilt reduction. The feedback and feedforward controllers stay untouched.

$$\begin{aligned} \lim_{CP_{Stage} \rightarrow \infty} |Y_{Stage}|^2 &= |(L_{disp}(H_{SC} - 1)Y_G)|^2 \\ &+ |H_{in}N_{in1}|^2 + |H_{in}S_{tilt1}|^2 \\ &+ |L_{disp}H_{SC}N_{in2}|^2 + |L_{disp}H_{SC}S_{tilt2}|^2 \\ &+ |L_{disp}N_{pos}|^2 \end{aligned} \quad (3.21)$$

Figure 3.19 shows a comparison between the newly designed low, high and sensor correction filters with the O1 filters. To reduce the tilt below 50mHz, the blend frequency between the low-pass and the high-pass filters has been increased from 45mHz to 250mHz. To keep a good isolation performance at higher frequency, the sensor correction filter is made more aggressive, with some gain peaking around 50mHz. We also favorize a steep roll-off at low frequency in the sensor correction to avoid noise/tilt re-injection from the ground.

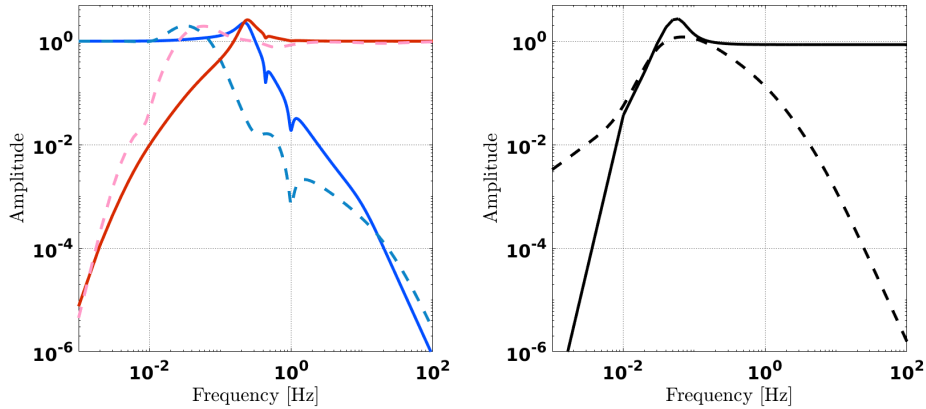


Figure 3.19: Comparison of the filters used during O1 (dashed lines) and the new designed filters for earthquakes (solid lines). The left part of the figure shows the complementary low-pass and high-pass filters. The right part shows the sensor correction filters.

The simulated stage 1 motion with the new earthquake configuration is shown in figure 3.20 (red curve). We used the model presented in section 3.5.3 to do this simulation. At Hanford, we observe a reduction of the stage motion by a factor of ~ 5 at very low frequencies, with similar performance compared to the O1 filters in the [50mHz-150mHz] band. Improvement is less visible at Livingston since the stage motion is mostly horizontal at low frequencies, but is still present by a factor

of ~ 1.5 . However, we see a lack of isolation between 200mHz and 700mHz at both sites, which could limit gravitational-wave detection even if the interferometer stays locked. The increase of motion can get upconverted through the control chain to the mirror's motion and affect LIGO sensitivity in the detection band. The green dashed curve in figure 3.20 shows the estimated maximum stage 1 motion allowed to not degrade LIGO designed sensitivity, and the new filters do not meet this requirement at Livingston. For this reason, this configuration cannot be activate at all time at this particular site and needs to be part of an automation system (see section 3.6).

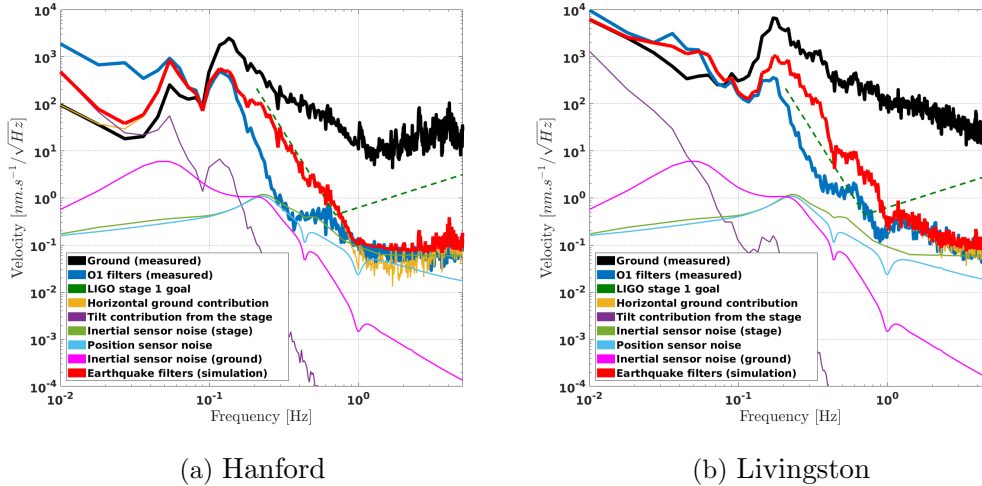


Figure 3.20: Seismic isolation provided by BSC-ISI stage 1 in the Y-direction at both sites. The black curve represents a typical ground motion, and the blue curve the measured motion of the stage during O1 and the red curve the predicted stage motion with the new filters. The thinner curves indicate the estimated noise contributions with these new filters.

LIGO second observation run

The second observing run (O2) of LIGO took place from November 30, 2016 to August 25, 2017. At Hanford, the decision was made to use the described earthquake control configuration as the nominal configuration during the run. The degradation in isolation above 200mHz was not considered as a limitation to operate, since the stage 1 requirement is still met according to simulation. The Livingston site however experiences many storms through the year and suffers from relatively high ground motion. For this reason, isolation above 200mHz is not sufficient to meet the stage 1 requirement with the new configuration and the O1 control configuration was kept at this site at all times. In the future, it will be important to test this configuration as part of the LIGO automation system, by switching filters when a problematic earthquake arrives at the site. Only the Hanford data is considered in this section.

H1 experienced 416 earthquakes of Richter magnitude 5 or greater while observing during O2. Figure 3.21 compares O1 and O2 data when the interferometer stayed

locked. As expected, we observe a net improvement of the robustness against high-velocity ground motion (above 250nm/s), while being more sensitive below 250nm/s by only $\sim 1\%$. Overall, the interferometer lost lock 81 times, which represents a downtime reduction of $\sim 40\%$ compared to O1.

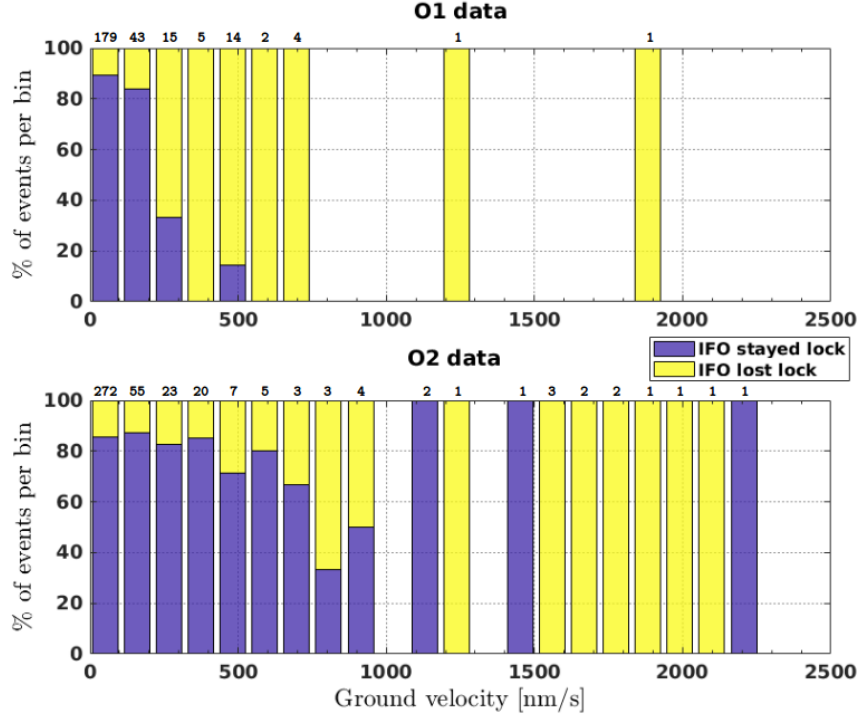


Figure 3.21: Comparison of the interferometer behavior between O1 and O2 at Hanford. The figure shows the IFO status versus the peak ground velocity in the [30mHz-100mHz] band, with the blue bars for when the IFO stayed lock and the yellow bars for when the IFO lost lock. The y-axis represents the percentage of events per bin, with the number above each bar being the total number of events per bin.

3.5.6 Second strategy: Gain peaking reduction

While the previous filters reduce the tilt seen by the stage at very low frequencies, we still observe gain peaking in the [50mHz-100mHz] frequency band. Gain peaking becomes problematic during an earthquake, as it induces a clear amplification of the ground motion by the stage over the bandwidth of interest. There is a direct correlation between the operating status of the IFO and the ground velocity, as shown in figure 3.22: the IFO becomes unstable at higher velocities. By amplifying the ground motion over the bandwidth of interest (figure 3.22a vs figure 3.22b), we therefore increase the chance of losing lock during an earthquake.

The goal of this earthquake control configuration is to go one step further, and limit the gain peaking in the earthquake band as well as tilt re-injection. Figure 3.23

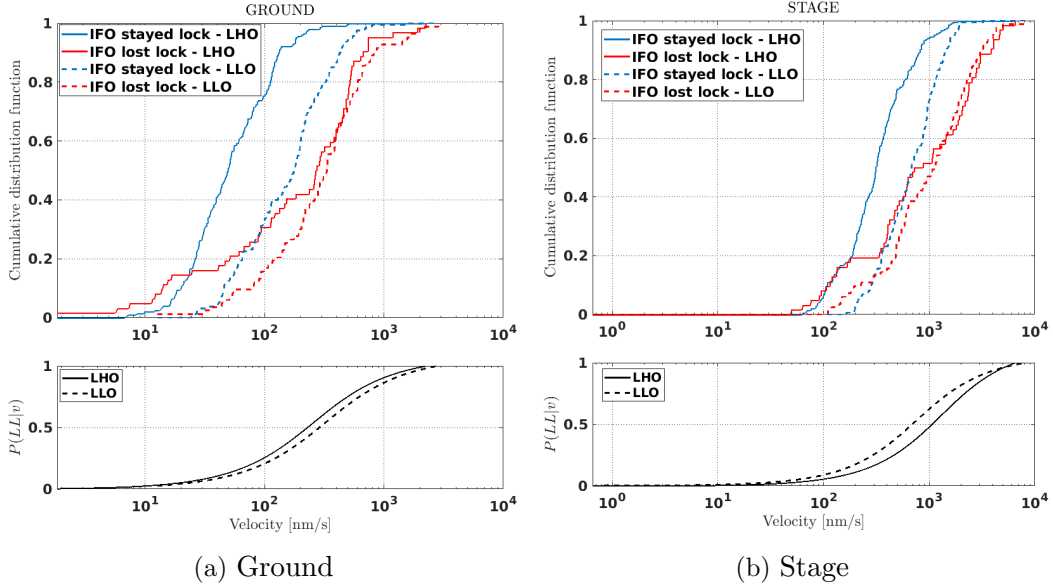


Figure 3.22: Comparison of stage 1 ITM behavior in the [30mHz-100mHz] band for different ground motions: stretches selected during earthquakes when the interferometer survived (blue curve), stretches selected during earthquakes when the interferometer stops functioning (red curve). The top part of the figure represents the cumulative distribution function for the ground and the stage respectively, as a function of the peak velocity for each stretch. The plots indicate the direct correlation between velocity and the interferometer status at both sites. We observe a net increase of the stage velocity compared to the ground, due to self-inflicted gain peaking in this frequency band. The bottom part of the plots represents $P(LL|v)$, the smoothed probability of losing lock as a function of peak velocity. It is computed by fitting the measured probability with a hyperbolic tangent function.

shows a comparison between the O1 filters and the newly designed low, high and sensor correction filters. To move the gain peaking out of the earthquake band, the blend frequency between the low-pass and the high-pass filters has been increased from 45mHz to 250mHz, using the filters presented in the previous section. The sensor correction has been modified to be less aggressive and suppress gain peaking in the earthquake band. Figure 3.24 shows the simulated stage 1 motion with the new earthquake configuration (red curve). In this case, the maximum gain peaking is reduced by a factor of ~ 3 , while still reducing the tilt. However, there is no longer any isolation at 200mHz, which could be problematic for the detectors. Seismic motion in the [100mHz-300mHz] frequency band is dominated by secondary microseism, whose amplitude is associated with storms in the ocean. The proposed earthquake control configuration might not provide enough isolation to keep the detector locked if other disturbances like storms increase the ground motion around 200mHz. Between [200mHz-1Hz], the new filters do not meet the LIGO stage 1 requirements at both sites. For these reasons, this configuration needs to be part of the LIGO automation system (see section 3.6).

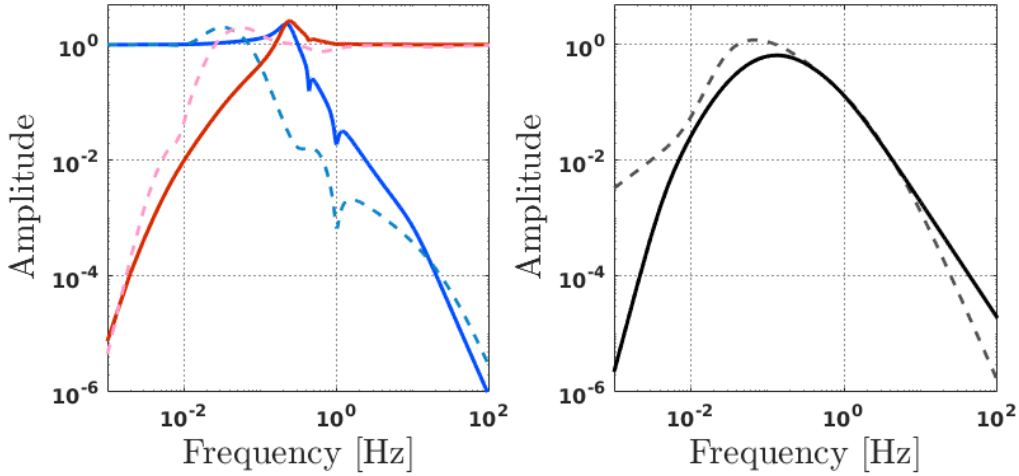


Figure 3.23: Comparison of the filters used during O1 (dashed lines) and the new designed filters for earthquakes (solid lines). The left part of the figure shows the complementary low-pass and high-pass filters. The right part shows the sensor correction filters.

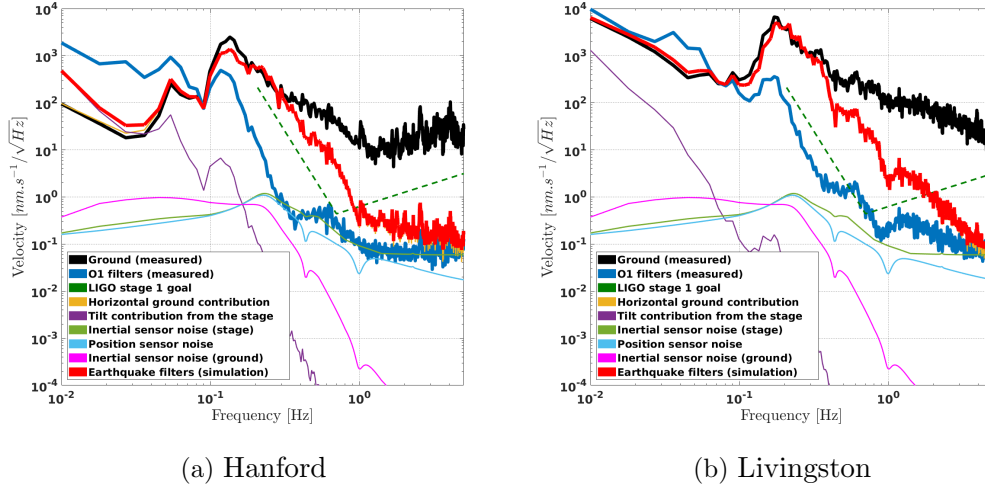


Figure 3.24: Seismic isolation provided by BSC-ISI stage 1 in the Y-direction at both sites. The black curve represents a typical ground motion, and the blue curve the measured motion of the stage during O1 and the red curve the predicted stage motion with the new filters. The thinner curves indicate the estimated noise contributions with these new filters.

Comparison and expected improvement in the duty cycle

This control strategy was not part of the LIGO second observation run and still has to be implemented. However, in this section, we estimate the improvement in duty cycle due to reducing the sensitivity to earthquakes. Earthquake data collected during O1 is used to simulate the effect of the new earthquake filters on stage 1 velocity. We compare the averaged gain peaking induced by earthquakes in the [30mHz-100mHz] band between O1 filters and the earthquake filters. During O1, the isolation controls

amplified the ground motion of earthquakes by a factor of 1.8 on average. With the new proposed filters, this amplification would be reduced to 1.2. Therefore, the stage velocity distribution in the [30mHz-100mHz] bandwidth will change from $P(v)$ to $P(v_{new})$, with $P(v_{new}) = \frac{1.2}{1.8}P(v) = \frac{P(v)}{1.5}$. Based on this new distribution (plotted in figure 3.25), and on the known probability of losing lock as a function of velocity $P(LL|v)$ from O1 (see figure 3.22), we can calculate the estimated number of lock-losses $P(LL)$ using Bayes' theorem, as written in equation 3.22. During O1, H1 lost lock 62 times and L1 83 times because of earthquakes. With the new earthquake filters and stage velocity, we estimate only 45 lock-losses at Hanford and 72 at Livingston, meaning a $\sim 27\%$ and $\sim 13\%$ reduction respectively (Hanford performance is better as Livingston ground velocities are overall higher). Although this estimate has an uncertainty of $\pm 6\%$, it leads us to expect a significant improvement from this new configuration.

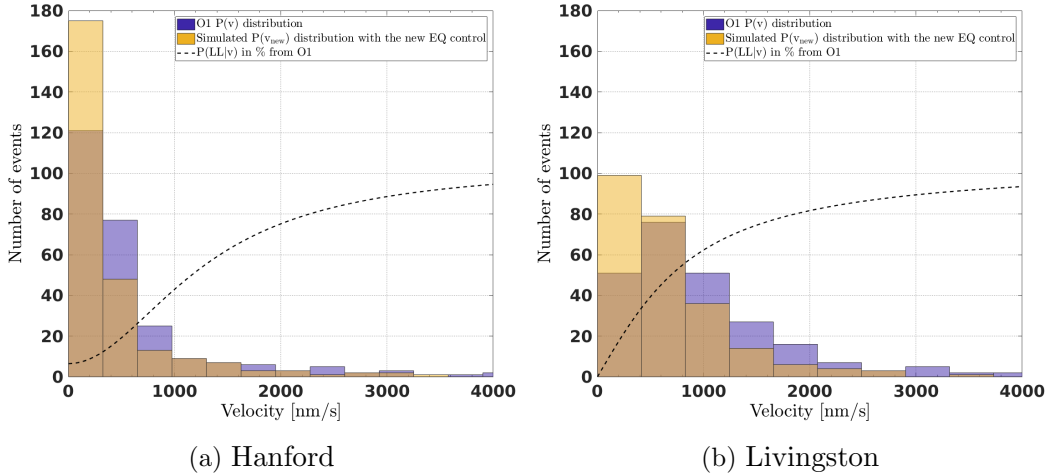


Figure 3.25: New $P(v_{new})$ distribution based on O1 data with $P(v_{new}) = \frac{P(v)}{1.5}$. As a reminder from figure 3.22, we plotted the probability of losing lock as a function of stage velocity $P(LL|v)$ in black.

$$P(LL) = \sum_{\substack{\text{velocity} \\ \text{bin}}} P(LL|v)P(v_{new}) \quad (3.22)$$

3.5.7 Third strategy: Common mode rejection along the arms

We have seen that the amplification of the ground motion in the earthquake frequency band can overwhelm the seismic system. This is especially true during big earthquakes, when the input motion is so large that the stage actuators saturate. We consider 'big earthquakes' events that generate a peak ground velocity greater than 250nm/s, which corresponds to a $\sim 50\%$ chance of losing lock at both sites according to figure 3.22. To reduce control authority, this last strategy allows the

IFO to ride on the common-mode, and only isolate on the residual local differential mode. Isolating differential motion will relax the required actuation force during an earthquake (since only $\sim 20\%$ of the motion is differential - see figure 3.10), which should prevent saturation and reduce length-to-angle fluctuations.

The general concept is presented in figure 3.26. It requires that data be sent in real time between chambers along the arms, which is currently being implemented. The averaged common mode signal is subtracted from the local signal to generate the differential mode signal for control. The local differential signal would be used instead of the local signal only when needed, thanks to the Seismon warnings and the Guardian switching structure.

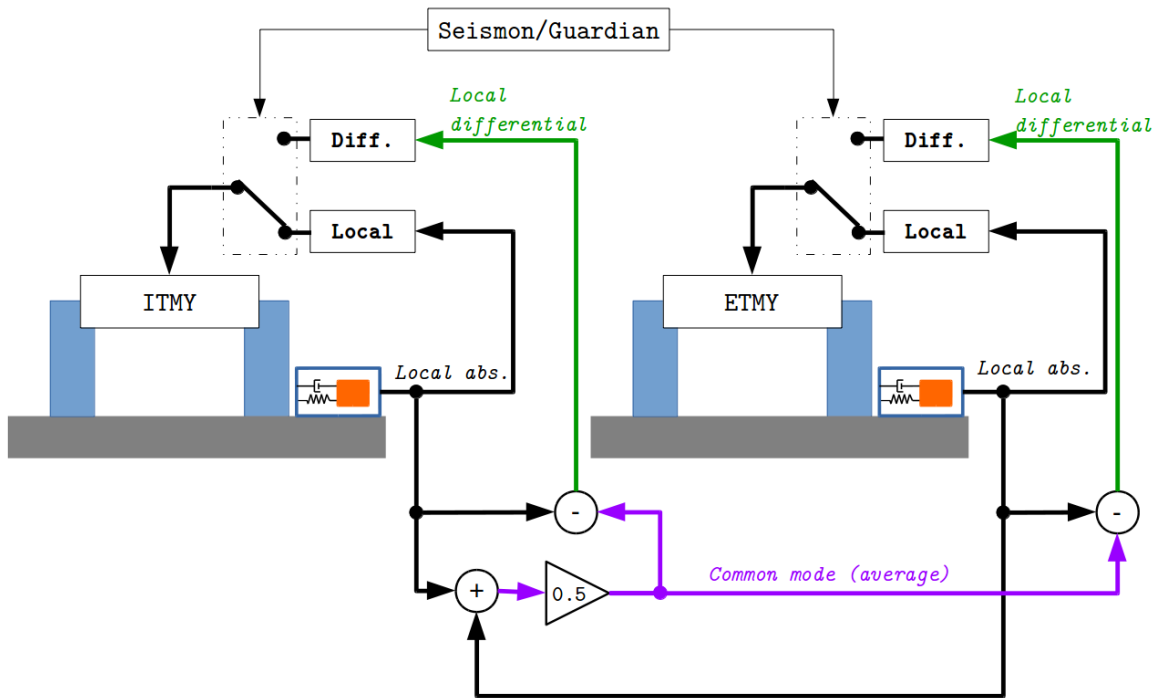


Figure 3.26: Overview of the implementation necessary to control only on local differential motion at low frequency during earthquakes.

The block diagram in figure 3.27 shows the control topology for this new configuration, where the differential motion is used for low frequency control via the sensor correction path. The absolute stage motion becomes:

$$\begin{aligned}
 |Y_{Stage}|^2 = & \left| \frac{P_G + L_{disp}CP_{Stage} + C_{FF}P_{Stage}}{1 + CP_{Stage}} Y_G \right|^2 + \left| \frac{1}{2} \cdot \frac{L_{disp}H_{SC}CP_{stage}}{1 + CP_{stage}} (Y_G - Y'_G) \right|^2 \\
 & + \left| \frac{1}{2} \cdot \frac{L_{disp}H_{SC}CP_{Stage}}{1 + CP_{Stage}} N'_{in} \right|^2 + \left| \frac{1}{2} \cdot \frac{L_{disp}H_{SC}CP_{Stage}}{1 + CP_{Stage}} S'_{tilt} \right|^2 \\
 & + \left| \frac{H_{in}CP_{Stage}}{1 + CP_{Stage}} N_{in1} \right|^2 + \left| \frac{H_{in}CP_{Stage}}{1 + CP_{Stage}} S_{tilt1} \right|^2 \\
 & + \left| \frac{1}{2} \cdot \frac{L_{disp}H_{sc}CP_{Stage}}{1 + CP_{Stage}} N_{in2} \right|^2 + \left| \frac{1}{2} \cdot \frac{L_{disp}H_{sc}CP_{Stage}}{1 + CP_{Stage}} S_{tilt2} \right|^2 \\
 & + \left| \frac{C_{FF}P_{Stage}}{1 + CP_{Stage}} N_{in3} \right|^2 \\
 & + \left| \frac{L_{disp}CP_{Stage}}{1 + CP_{Stage}} N_{pos} \right|^2.
 \end{aligned} \tag{3.23}$$

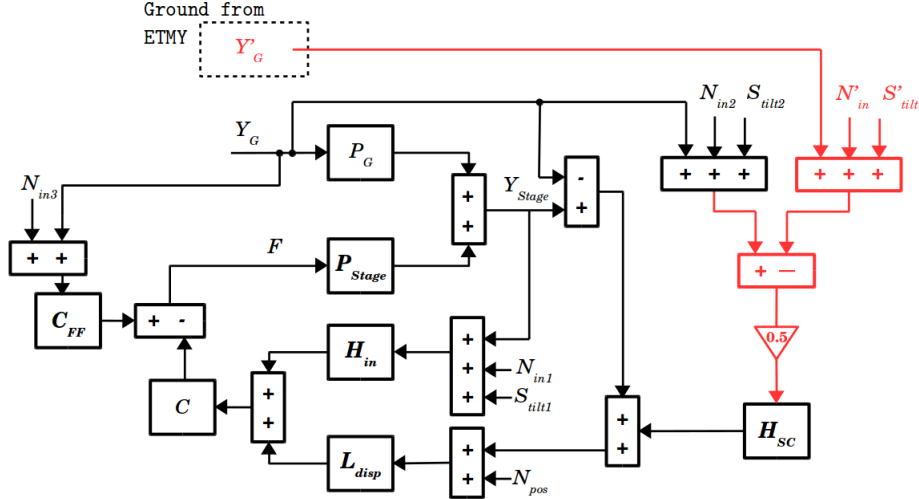
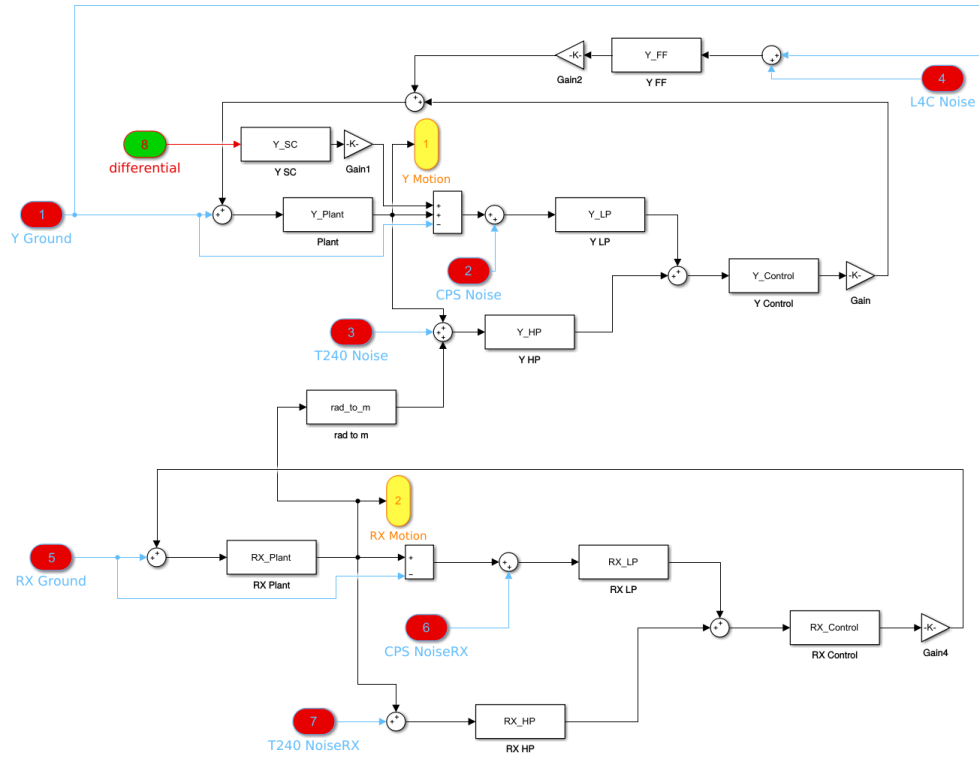


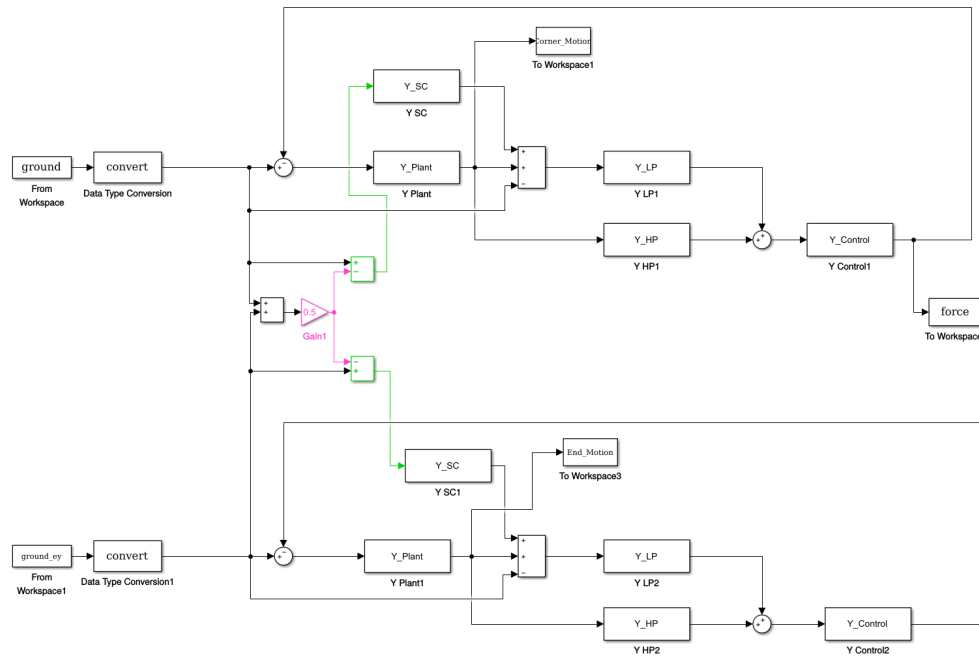
Figure 3.27: Control scheme of the new configuration. To obtain the local differential motion of ITMY, the local ground Y'_G from ETMY is subtracted from the local ground Y_G . The difference $(Y_G - Y'_G)$ is then multiply by 0.5 and added to the sensor correction path. N'_{in} and S'_{tilt} represent the noise and tilt associated with the ETMY ground seismometer.

Based on this control scheme, two Simulink models have been developed, one in the frequency domain and one in the time domain, both shown in figure 3.28. The objective of the first model is to estimate the performance of the new configuration, while the second evaluates the change in the amplitude of the actuation drive. We keep the O1 filters and a low blend frequency ($\sim 45\text{mHz}$) to have enough isolation at the microseism.

We chose to study a Richter magnitude 6.5 earthquake in Alaska from November 09, 2015. We selected this event as it generated a huge peak ground velocity of more than $\sim 10\mu\text{m} \cdot \text{s}^{-1}$ at Hanford (see figure 3.29) where greater than 90% of the motion is common. The data is extracted from seismometers close to the ITMY and ETMY



(a) Frequency domain model



(b) Time domain model

Figure 3.28: Simulink models developed for the presented strategy. In the first model, the differential motion is added as an additional input. In the second model, both ITMY and ETMY platforms are simulated. In this model, tilt, noise and feedforward are not considered.

chambers. The differential signal is calculated and added to the frequency domain model as an independent input source, *differential* (in green in figure 3.28). The model is therefore identical to the model presented in section 3.5.4, except for that extra input.

In the time domain model, we use the time-series of the ITMY and ETMY seismometers (inputs *ground* and *ground.ey*) to simulate the stage motion in the horizontal Y direction of both chambers (ITMY and ETMY). We only consider the feedback and sensor correction paths in this model, omitting noise and tilt for simplicity. We believe this is acceptable in this case, as large earthquakes generate mostly extra horizontal motion [100], making tilt and noise not a limitation in the actuation drive. Feedforward is also neglected as it only affects higher frequencies (above ~ 1 Hz).

Figure 3.30 shows the simulated stage 1 motion with this new configuration. We observe a degradation of performance above 200mHz with a reduction of velocity by $\sim 25\%$ around 50mHz: the configuration still provides efficient isolation at the microseism and above to keep the IFO locked, while reducing the motion amplification in the earthquake band. This trade-off will not work during normal conditions, as the signal is dominated by tilt and noise at low frequency. However, this is not true during big earthquakes, and this slight reduction in velocity in the earthquake frequency band might prevent the actuators from saturating and reduce the coupling to angle.

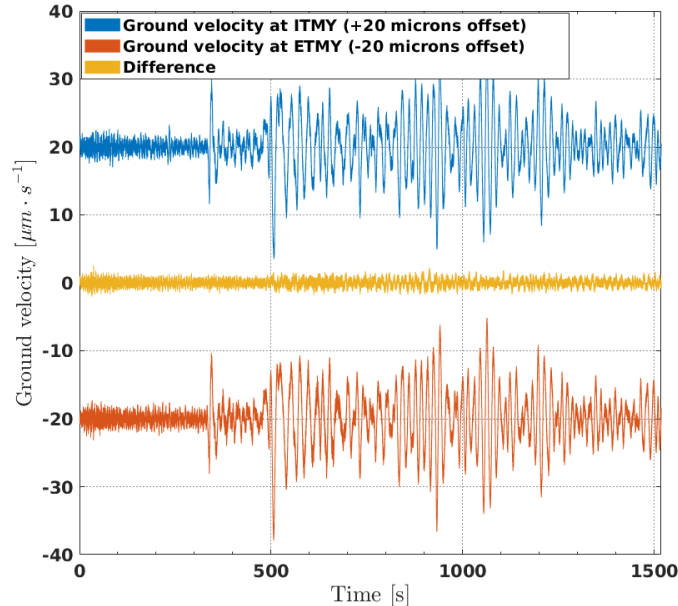


Figure 3.29: Time-series of the seismometers close to the Hanford ITMY chamber (blue curve) and the ETMY chamber (orange curve) during a Richter magnitude 6.5 in Alaska. We clearly see the first arrival of the P-waves around 300s. A vertical offset was put on the two curves for visibility. The differential signal is in yellow. This data is used in the Simulink models presented in this section.

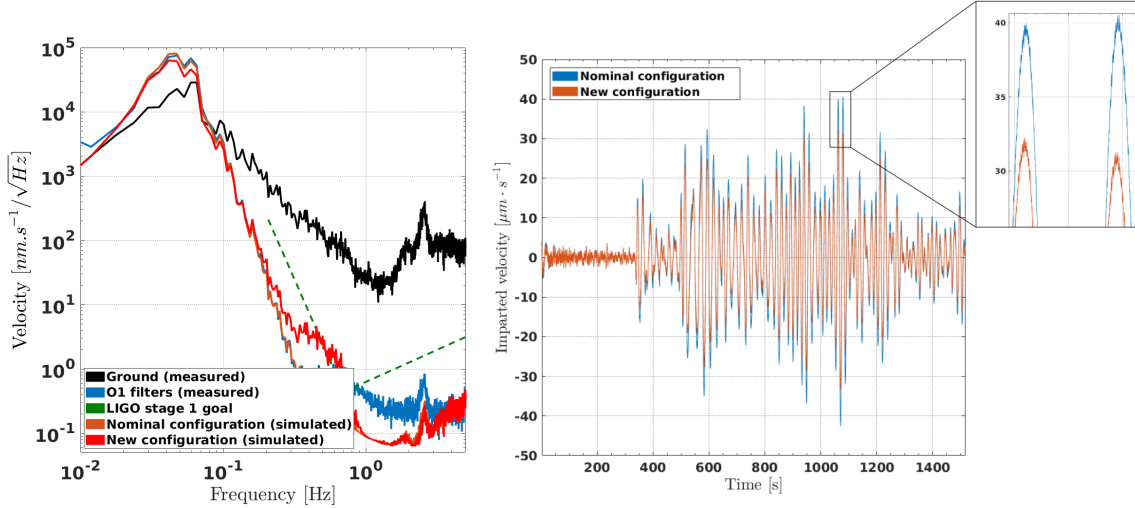


Figure 3.30: *Left figure:* Comparison of performance between the nominal configuration and the new configuration described in this section. The orange and red curves are simulated using the frequency domain Simulink model shown in figure 3.28. We observe a disparity between the measured and simulated performance for the nominal configuration above 500mHz (blue and orange curves). This is due to the simple plant model used in the simulation, as explained before. The new configuration degrades the performance above 500mHz and improves it around 50mHz. *Right figure:* Time-series (generated with the time domain Simulink model) of the Y drive signal (as a velocity) of the nominal and new configuration. We observe a reduction of the peak velocity by $\sim 25\%$

Expected improvement in the duty cycle

It is harder to estimate the overall advantage of this configuration, as it is efficient only when tilt and noise are not a limitation in the earthquake frequency band (i.e. during large earthquakes). During O1, 48 and 96 earthquakes generated a peak ground velocity greater than $250\text{nm} \cdot \text{s}^{-1}$ at Hanford and Livingston respectively. If we assume that the new configuration will be used only during events like these, we can estimate the new velocity distribution P_{new} , like we did for the second strategy (section 3.5.6). During large earthquakes, the isolation controls amplified the ground motion by a factor of 1.9 on average. With the new proposed configuration, this amplification would be reduced to 1.5, meaning $P(v_{new}) = \frac{1.5}{1.9}P(v) = \frac{P(v)}{1.3}$. During O1, H1 lost lock 18 times and L1 40 times out of the 48 and 96 earthquakes considered. With the new configuration and stage velocity, we estimate a reduction of 3 lock-losses at Hanford and 4 at Livingston. If we bring these numbers back to the overall numbers of lock-losses during O1, we expect a reduction from 62 to 59 lock-losses at Hanford and from 83 to 79 at Livingston, meaning a $\sim 5\%$ reduction at both sites.

3.6 Implementation at the sites

For all the strategies at Livingston, and the last two at Hanford, it is required to switch to the new configuration only when a problematic earthquake arrives at the site. The early alert system Seismon gives enough time to switch the seismic configuration as needed. Using this information and the current state of the IFO, a decision can be made on whether to trigger a change in the control configuration with the LIGO automation system.

Each interferometer is supervised by a state machine called Guardian [72]. It consists of state machine automation nodes capable of handling control changes automatically. It is composed of multiple nodes, organized in a hierarchical fashion for each system and subsystem. In the case of the BSC-ISI, multiple intermediate states are required to bring the platform from the initial state (state READY) to a full isolation of a chamber (FULLY_ISOLATED). The intermediate states activate the different control loops of the different platforms (HEPI, BSC-ISI stage 1 and BSC-ISI stage 2) in a sequential order. Figure 3.31 shows the state graph of the BSC-ISI Guardian system, with the modifications implemented to allow the switch between nominal and Earthquake configuration (from FULLY_ISOLATED to EQ_ISOLATED). It enables the switch between low-pass, high-pass and sensor correction filters. This change of state typically requires a few minutes, as it is possible to switch these filters in either direction without having to turn off the isolation loops. This is due to a filter switching system which is already part of the LIGO infrastructure [101].

3.7 Conclusion

In this chapter, we have provided an introduction to the mechanics of earthquakes and the problem they induce on the LIGO gravitational-wave detectors. The early-warning system Seismon and its functionalities have been presented. Seismon estimates the arrival of earthquakes at both sites tens of minutes before the actual arrival within a few minutes accuracy. It also predicts the peak velocity that an event would generate at the site's ground and its likelihood to unlock the IFO. Despite the current uncertainty on the velocity prediction, this tool gives the opportunity to change the seismic control strategy beforehand to minimize the impact of the earthquake on the detectors.

The seismic isolation platforms have been introduced and three earthquake mitigation strategies presented. Out of the three strategies, one strategy has been implemented and used as the nominal BSC-ISI control configuration at Hanford during the second observation run. We observed a $\sim 40\%$ improvement of the interferometers' robustness to earthquakes, which resulted in an increase of the LIGO duty cycle. Indeed,

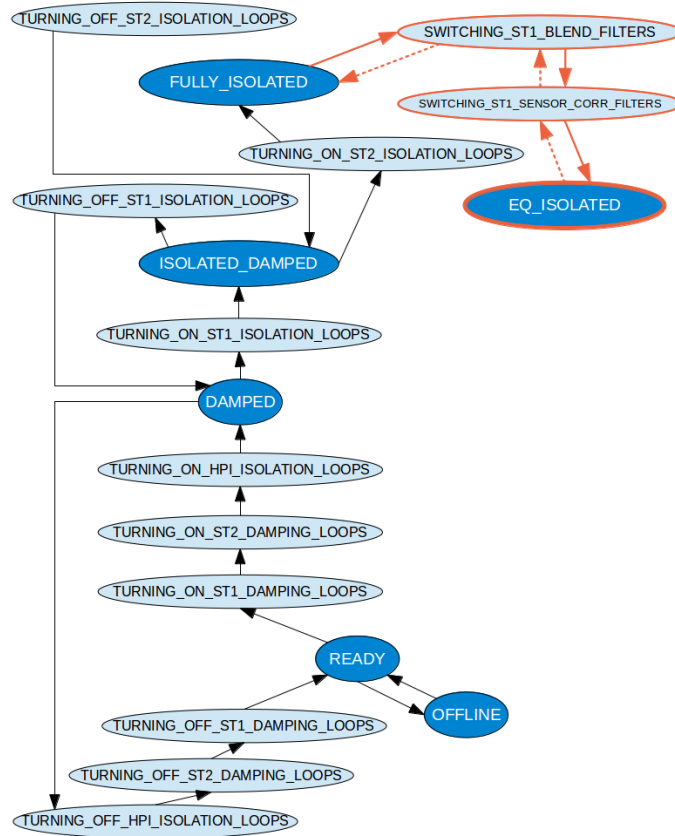


Figure 3.31: State graph of the BSC-ISI Guardian system. The ovals represent the different states, and the arrows the authorized transitions from one state to another. Eight different states are needed to fully isolate a BSC chamber to a nominal configuration. Represented in orange is the new states necessary to have the earthquake configuration part of the automation system. The solid arrows show the path to go from nominal to Earthquake configuration, and the dash arrows the path from Earthquake to nominal.

each time the IFO goes out of operation there is an associated downtime. Due to the complexity of the instrument and the duration of an earthquake, it can take several hours to return to operating conditions. During O1, it took an average of 1.8 hours to go back to science mode after an earthquake: H1 was down more than 111 hours because of earthquakes. Thanks to the increase of robustness observed during O2, the downtime has been reduced from 111 to 67 hours, which represents a direct increase of the overall LIGO duty cycle by 1.6 %.

We have shown that this configuration is not viable as a default configuration at Livingston and needs to be part of a smart automation system. The other two strategies presented also need to be part of an automation system to reduce the earthquake downtime by $\sim 30\%$ and $\sim 5\%$ respectively. The LIGO automation infrastructure is capable of switching to these new filters based on Seismon early-warning predictions. This switching was not part of the LIGO second observation

run and still has to be implemented. Further effort will be spent on integrating the presented strategies for the future observation runs, as well as improving the velocity peak prediction of Seismon.

Chapter 4

Parametric Instabilities

4.1 Background

Parametric instabilities (PI) result from a non-linear coupling between the higher-optical-modes (HOMs) of an arm cavity and the mechanical modes of the cavity mirrors. The principle was introduced in 2001 by Braginsky *et al.* [102], but had not been observed from previous generations of GW interferometers. With Advanced LIGO, as the circulating power in the Fabry-Perot cavities has already increased from $\sim 25\text{kW}$ (Initial LIGO) to $\sim 100\text{kW}$ (O1), PI are becoming a real challenge (see section 4.3).

4.1.1 Introduction to PI

PI are the result of energy transferred from optical energy stored into the IFO's arms to the mechanical energy stored in internal mechanical modes of the test masses. The process that lead to PI can be approached as a feedback mechanism, as defined in [103] and shown in figure 4.1. Thermal (or otherwise) transients excite the different mechanical modes of the test masses, which will scatter light. If the mirror surface motion of a mode spatially overlaps with the electric field distribution of a HOM, there is a possibility for the fundamental cavity mode to be scattered into this HOM. Radiation pressure then couples the scattered light into mechanical motion, thus closing the feedback loop. Based on the overall loop phase, the mechanical mode may be suppressed (*anti-Stokes process*) or further excited (*Stokes process*), leading in this former case to optical sensors saturation and cavity lock-loss.

For each mechanical mode, the open-loop gain of this opto-mechanical feedback loop can be calculated. This gain, called the parametric gain, will be described in more

details in the next section.

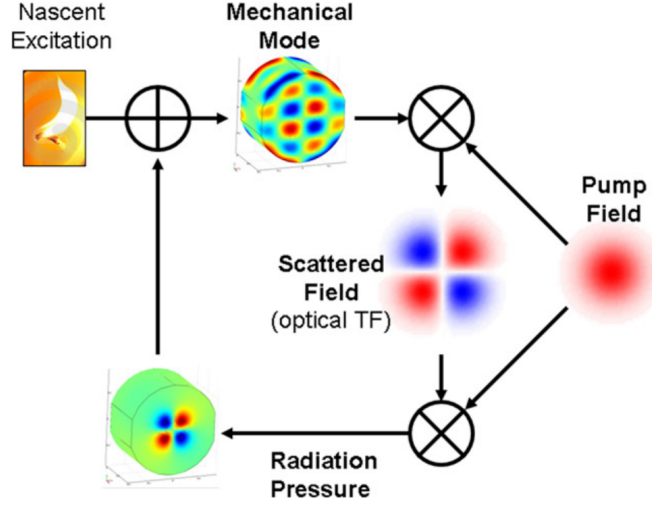


Figure 4.1: From reference [103]. Illustration of the coupling mechanism between a mechanical mode and a HOM, leading to PI.

4.1.2 Calculation of the parametric gain

In this section we calculate the parametric gain R_m for the mechanical mode m of resonance frequency ω_m . The mode m is excited and the fundamental cavity mode of frequency ω_0 is scattered via Brillouin scattering [104]. In this process, the incident photons of the carrier laser beam may lose energy (*Stokes process*) or gain energy (*anti-Stokes process*). This results in the frequency shift of the reflected beam compared to the incident beam, slightly lower (*Stokes*) or higher (*anti-Stokes*) in frequency by $\omega_0 \pm \omega_m$.

A more classical way to look at this phenomena is to consider the incident laser as a plane wave of amplitude E_0 defined by:

$$E_{inc}(t) = E_0 \cdot e^{j\omega_0 t} \quad \text{with} \quad \omega_0 = \frac{2\pi c}{\lambda_0} \quad (4.1)$$

where c is the speed of light and λ_0 the wavelength. The small oscillations $a_m \cos(\omega_m t)$ of the mirror modulate the phase of the incident beam by:

$$E_{refl}(t) = E_0 \cdot e^{j(\omega_0 t + 2k \cdot a_m \cos(\omega_m t))} = E_0 \cdot e^{j\omega_0 t} \times e^{j2ka_m \cos(\omega_m t)}. \quad (4.2)$$

Notice the term $2ka_m$ in equation 4.2 with $k = \frac{2\pi}{\lambda_0}$ the wave number. The factor of 2

comes from the fact that as the beam bounces off the mirror's surface, the distance a_m is traveled twice (see figure 4.2).

Assuming $ka_m \ll 1$ and using the first order Taylor series, we can approximate equation 4.2 to:

$$\begin{aligned} E_{refl}(t) &\simeq E_0 e^{j\omega_0 t} \times (1 + j2ka_m \cos(\omega_m t)) \\ &= E_0 e^{j\omega_0 t} + j \frac{2\pi}{\lambda_0} E_0 a_m (e^{j\omega_m t} + e^{-j\omega_m t}) e^{j\omega_0 t}. \end{aligned} \quad (4.3)$$

Equation 4.3 shows that two scattering sidebands of amplitude $j \frac{2\pi}{\lambda_0} E_0 a_m$ and frequency $\omega_0 \pm \omega_m$ are created around the fundamental frequency.

In this example, we considered a single-frequency incident beam on a perfect mirror with no spatial information. In reality, the laser beam is composed by the fundamental mode but also higher optical modes generated by the mirror imperfections. These higher modes need to be taken in account, as well as the spatial profile of the beam and of the mirror displacement along the cavity axis. We thus define:

$$\Psi_{scat} = f_0 \cdot E_{refl}(t) + \sum_{n=1}^{\infty} f_n \cdot E_{refl,n}(t) = \sum_{n=0}^{\infty} f_n \cdot E_{refl,n}(t) \quad (4.4)$$

which described the complete optical pattern of the scattering process, with $f_0 \cdot E_{refl}$ the fundamental mode and f_n the normalized spatial distribution of the mode n along the cavity axis. The mirror amplitude motion can be written in a more general form as:

$$a_m = A_m (\vec{u}_m \cdot \hat{z}) \quad (4.5)$$

where \hat{z} is the unit vector along the cavity axis, A_m is the modal amplitude of test mass mechanical mode m and $\vec{u}_m = (u, v, w)$ is its displacement field.

Based on these new definitions, the scattered field is:

$$\Psi_{scat} = \sum_{n=0}^{\infty} f_n \cdot E_n \cdot e^{j(\omega_0 t + 2kA_m \cos(\omega_m t))} \quad (4.6)$$

with E_n the amplitude of the optical mode n . Similarly to equation 4.3, we then calculate:

$$\Psi_{scat} = \sum_{n=0}^{\infty} j \frac{2\pi}{\lambda_0} E_n A_m f_n (e^{j\omega_m t} + e^{-j\omega_m t}) e^{j\omega_0 t}. \quad (4.7)$$

The amplitude E_n depends on how much energy is scattered from the fundamental optical mode to the HOM n , and is defined by

$$E_n = E_0 \cdot B_{m,n}. \quad (4.8)$$

$B_{m,n}$ is the geometric overlap between the mechanical mode m and higher mode n , with:

$$B_{m,n} = \iint_S f_0 f_n (\vec{u}_m \cdot \hat{z}) dS \quad \text{and} \quad 0 \leq B_{m,n} \leq 1 \quad (4.9)$$

where S is the test mass surface normal to the direction of beam propagation. The modal displacement and basis functions have normalizations

$$\iint_{\infty} |f_n|^2 dS = 1 \quad \text{and} \quad \iiint_V \rho |\vec{u}_m|^2 dV = 1 \quad (4.10)$$

where ρ is the mass density of the test mass and V is its volume. Calculation of the parameters f_0 , f_n and \vec{u}_m will be discussed in the next section.

We rewrite the equation 4.7:

$$\Psi_{scat} = \sum_{n=0}^{\infty} E_{scat,n} f_n (e^{j\omega_m t} + e^{-j\omega_m t}) e^{j\omega_0 t} \quad (4.11)$$

with

$$E_{scat,n} = j \frac{2\pi}{\lambda_0} A_m E_0 B_{m,n}. \quad (4.12)$$

It is important to evaluate the cavity's response to the scattered field Ψ_{scat} . The amplitude of the returning field from the excited optic's surface after a round trip is defined by:

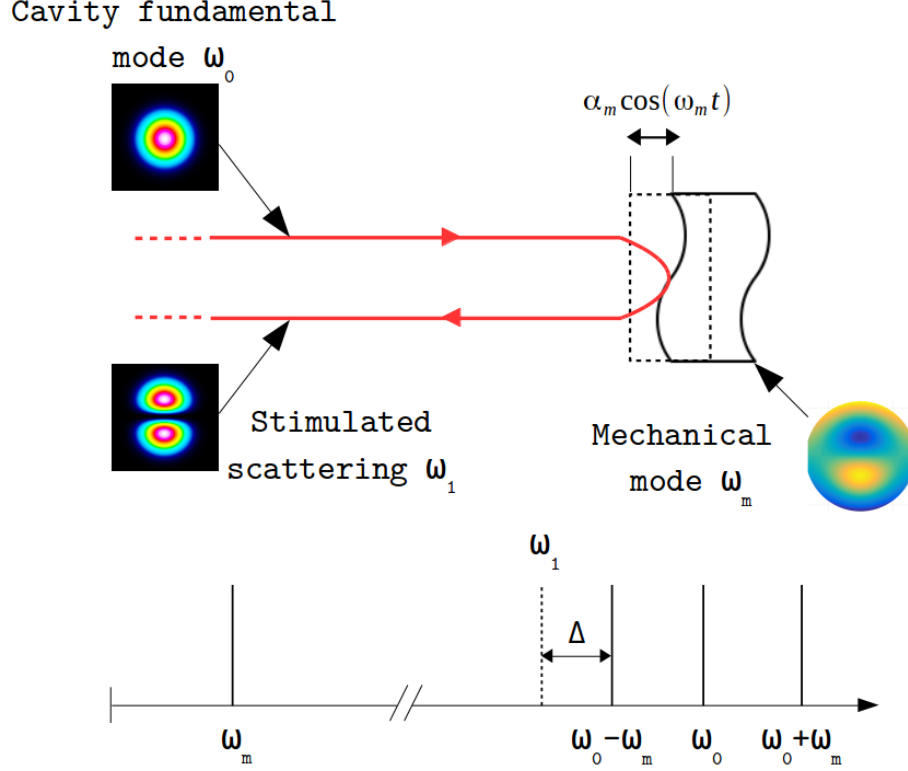


Figure 4.2: Illustration of the interaction between the fundamental mode of the cavity ω_0 , a mechanical mode ω_m and a higher optical mode ω_1 . The vibrating mirror scatters the fundamental mode into side-band modes $\omega_0 \pm \omega_m$. If the frequency between a side-band and a higher optical mode are similar (i.e. if $\Delta \approx 0$), and the optical and mechanical modes have a suitable spatial overlap ($B_{m,n} > 0$), a strong interaction between the modes can occur.

$$\Psi_{ret} = \sum_{n=0}^{\infty} E_{scat,n} f_n (G_n^+ e^{j\omega_m t} + G_n^- e^{-j\omega_m t}) e^{j\omega_0 t} \quad (4.13)$$

where G_n^\pm is the optical gain of the cavity. G_n is a complex value representing the amplitude and phase of the optical system's response at the mechanical mode frequency. It is usually different for the upper (G_n^+) and lower (G_n^-) sidebands, since LIGO's cavities are non-degenerated. Computation of the G_n^\pm coefficient would be discussed in more details later on.

Finally, the circulating field Ψ_{ret} in the cavity exerts a force on the mechanical modes of the mirror via radiation pressure. For a linear cavity, a light with normal incidence (i.e. angle of incidence $\theta = 0$) on a perfectly reflecting mirror can be considered for this calculation. We define the radiation pressure as:

$$P_{rad} = \frac{2}{c} \cdot |\Psi_0 + \Psi_{ret}|^2. \quad (4.14)$$

For a given mechanical mode m , the radiation pressure generated at frequency ω_m is

$$P_{rad,m} = \frac{4}{c} \left(E_0 f_0 \sum_{n=0}^{\infty} f_n (E_{scat,n} G_n^-)^* + E_0^* f_0 \sum_{n=0}^{\infty} f_n (E_{scat,n} G_n^+) \right). \quad (4.15)$$

A detailed calculation of equation 4.15 is made in appendix B. We integrate this pressure over the mirror surface to obtain the equivalent force:

$$F_{rad,m} = \frac{4}{c} \left(E_0 \sum_{n=0}^{\infty} (E_{scat,n} G_n^-)^* B_{m,n} + E_0^* \sum_{n=0}^{\infty} (E_{scat,n} G_n^+) B_{m,n} \right). \quad (4.16)$$

By substituting $E_{scat,n}$ from equation 4.12, we obtain:

$$\begin{aligned} F_{rad,m} &= \frac{4P}{c} j \frac{2\pi}{\lambda_0} A_m \sum_{n=0}^{\infty} (G_n^+ - G_n^{-*}) B_{m,n}^2 \\ &= j \frac{8\pi P A_m}{\lambda_0 c} \sum_{n=0}^{\infty} G_n B_{m,n}^2 \end{aligned} \quad (4.17)$$

with $P = |E_0|^2$ the circulating power in the cavity and $G_n = G_n^+ - G_n^{-*}$.

The change in modal displacement ΔA_m generated at the resonance frequency ω_m by the force $F_{rad,m}$ on the oscillating mirror is governed by the following differential equation:

$$\frac{d^2 \Delta A_m}{dt^2} + \frac{\omega_m}{Q_m} \frac{d \Delta A_m}{dt} + \omega_m^2 \Delta A_m = \frac{F_{rad,m}}{M}. \quad (4.18)$$

Hence

$$\Delta A_m = \frac{-j Q_m}{M \omega_m^2} F_{rad,m} = \frac{Q_m}{M \omega_m^2} \cdot \frac{8\pi P A_m}{\lambda_0 c} \sum_{n=0}^{\infty} G_n B_{m,n}^2 \quad (4.19)$$

where M is the mass of the mirror and Q_m the quality factor of the mode m . The parametric gain is defined as the real part of the open loop gain of the PI feedback loop:

$$R_m = \Re \left[\frac{\Delta A_m}{A_m} \right] = \frac{8\pi P Q_m}{M \omega_m^2 \lambda_0 c} \sum_{n=0}^{\infty} \Re[G_n] B_{m,n}^2 \quad (4.20)$$

If $R_m > 1$, the displacement generated by radiation pressure is bigger than the oscillations of the mirror and the cavity becomes unstable. The amplitude of the mechanical mode m rises exponentially with specific time [105]:

$$\tau_m = \frac{2Q_m}{\omega_m(R_m - 1)}. \quad (4.21)$$

Note that we assumed that only a single mechanical mode of a single test mass is involved in PI, and there is no cross-correlation between the mechanical modes. Given the high-Q of the mirror's mode ($\geq 10^7$), the fact that several modes will have significance at a single frequency is unlikely.

A PI model is developed by calculating the parametric gains for each mechanical mode in section 4.2. Before that, the overlap parameter $B_{m,n}$ and optical gain G_n need to be define in more details.

4.1.3 Overlap parameter $B_{m,n}$ calculation

To compute the parametric gain, it is necessary to calculate the overlapping parameter $B_{m,n}$ between the mechanical mode m and a given cavity mode n . Mathematically, it is defined by three modes - the carrier, the HOM and the mechanical mode:

$$B_{m,n} = \iint_S f_0 f_n (\vec{u}_m \cdot \hat{z}) dS. \quad (4.22)$$

$\vec{u}_m \cdot \hat{z}$ represents the displacement of the mechanical mode normal to the test mass front surface. This displacement is extracted for each mode m from a modal analysis of the test mass using the software ANSYS. On the other hand, the carrier and HOM mode shapes normal to the front surface are solved using an approximate solution of the wave equation in cylindrical coordinates (Laguerre-Gaussian basis) [106, 107]. The electric field amplitude is given by:

$$\begin{aligned}
u_{l,p}(r, \psi, z) &= \frac{C_{lp}}{w(z)} \left(\frac{r\sqrt{2}}{w(z)} \right)^{|l|} \exp\left(-\frac{r^2}{w^2(z)}\right) L_p^{|l|} \left(\frac{2r^2}{w^2(z)} \right) \\
&\times \exp\left(-jk \frac{r^2}{2ROC(z)}\right) \exp(-jl\psi) \exp(-jkz) \exp(j\phi_G(z))
\end{aligned} \tag{4.23}$$

where C_{lp} is the normalization constant given by

$$C_{lp} = \sqrt{\frac{2p!}{\pi(p+|l|)!}} \tag{4.24}$$

and $L_p^{|l|}$ is the generalized Laguerre polynomial. $w(z)$ is the spot size of the beam along the cavity axis z , k the wave number and ϕ_G the Gouy phase shift. The Gouy phase shift is defined by the following equation [108]:

$$\phi_G = \cos^{-1} \sqrt{g_1 g_2} \tag{4.25}$$

with

$$g_1 = 1 - \frac{L}{ROC_A} \quad \text{and} \quad g_2 = 1 - \frac{L}{ROC_B}. \tag{4.26}$$

ROC_A and ROC_B being the curvature radii of the cavity mirrors A and B respectively. The indices l and p in equation 4.23 determine the shape of the profile in the radial r and azimuthal ψ direction respectively, while the quantities w and ROC evolve in the z direction. For each HOM, the index p is the number of radial modes (number of additional concentric rings around the central zone) and l is the number of intertwined helices (relates to the phase). For $l = r = 0$, we obtain a Gaussian beam (i.e. the cavity's carrier). By convention, we define the amplitude of the electric field distribution as $f_n = u_{l,p}$ with $n = |l| + 2p$ and $f_0 = u_{0,0}$.

Knowing f_0 , f_n and $\vec{u}_m \cdot \hat{z}$, the overlap parameters can be calculated. In an optical system like LIGO, the beam size on the optics is made as big as possible without introducing significant power loss for the carrier. As we go higher in the mode order n , more power will be concentrated at the mirror's edge, resulting in larger loss [109]. Because of this phenomena (usually referred to as clipping or diffraction loss), we only consider HOMs up to the 10th order ($n = 10$) for the overlap parameter calculation, as modes above this order are too low in power to matter [110]. As for the mirror, the mode shapes become too intricate at high frequencies and don't couple with any

HOM above $\sim 80\text{kHz}$. Overall, $\sim 120,000$ B parameters must be computed ($\sim 2,000$ mechanical modes for ~ 60 HOMs). As an example, figure 4.3 shows one test mass mechanical mode and its associated HOMs. The mechanical mode presented in this figure is associated with an instability already observed in LIGO (see section 4.3).

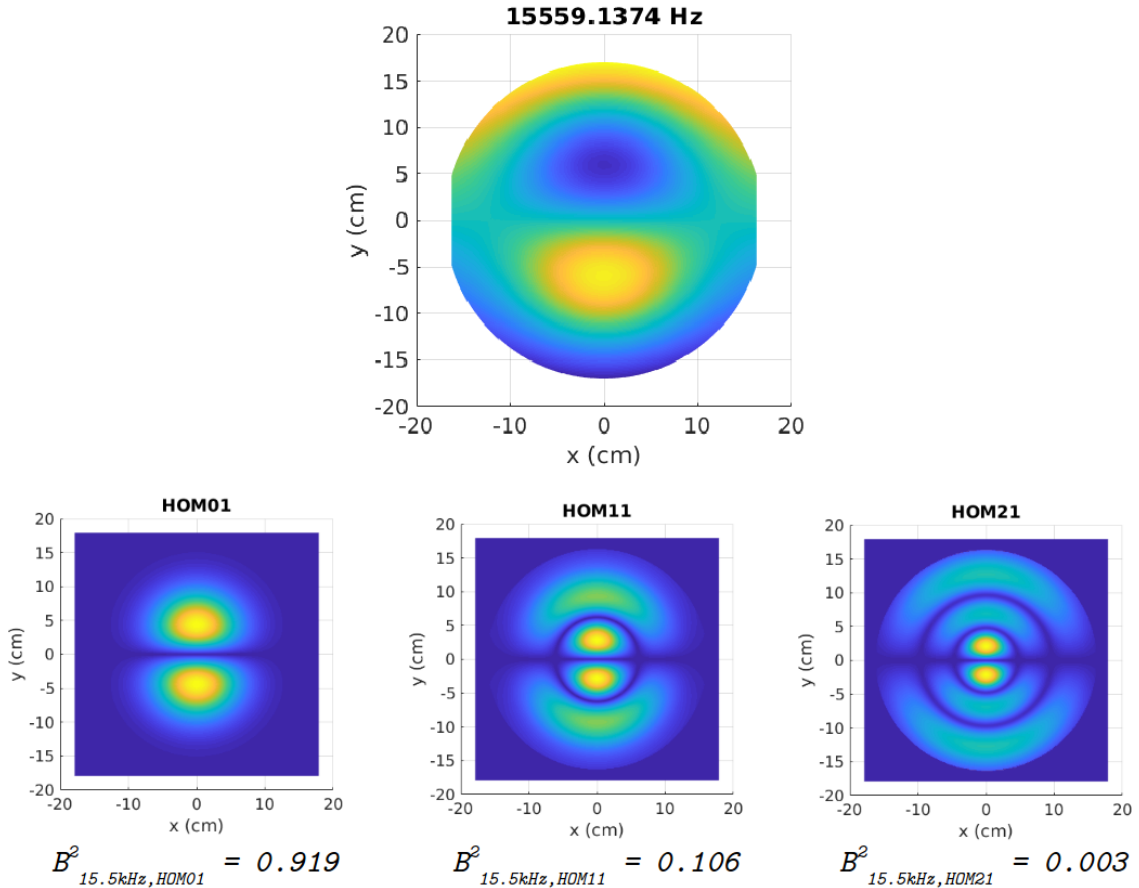


Figure 4.3: *Top*: amplitude displacement $\vec{u}_m \cdot \hat{z}$ of a test mass mechanical mode near 15.5kHz. *Bottom*: Amplitude f_n of three optical modes. We observe a very strong geometrical overlap between the mechanical mode and the HOM01, with $B^2 > 0.9$.

4.1.4 Optical gain G_n estimation

Geometrical overlap is not sufficient to ensure that the parametric gain will exceed unity. The right frequency combination between the carrier, a HOM and a mechanical mode is necessary to create instability. This combination is characterized by the cavity optical gain G .

The properties of each HOM could be characterize as it traverses the optical system. We define a scattering matrix \mathbb{S} , which contains the transfer coefficient of a given HOM field E from one point to another:

$$\mathbb{S} = \begin{pmatrix} E_1 \rightsquigarrow E_1 & \dots & E_n \rightsquigarrow E_1 \\ \vdots & \ddots & \vdots \\ E_1 \rightsquigarrow E_n & \dots & E_n \rightsquigarrow E_n \end{pmatrix}. \quad (4.27)$$

Let's take the example of a single LIGO test mass, as shown in figure 4.4. The coating layers are deposited on the front surface of the optics (i.e. $z = 0$) to make the surface reflective. The normalized wave amplitude of the incident waves \tilde{a} and the reflected waves \tilde{b} depend on the complex reflection and transmission coefficients \tilde{r} and \tilde{t} .

$$\begin{pmatrix} \tilde{b}_2 \\ \tilde{b}_4 \end{pmatrix} = \begin{pmatrix} \tilde{t} & \tilde{r} \\ \tilde{r} & \tilde{t} \end{pmatrix} \times \begin{pmatrix} \tilde{a}_1 \\ \tilde{a}_3 \end{pmatrix} \quad (4.28)$$

with (from reference [106]¹):

$$\tilde{r} = r_0 \cdot \frac{1 - e^{-j2\theta}}{1 - (r_0 e^{-j\theta})^2} \quad (4.29)$$

and

$$\tilde{t} = e^{j\theta} \cdot \frac{1 - r_0^2}{1 - (r_0 e^{-j\theta})^2}. \quad (4.30)$$

In these expressions, θ and r_0 represent the optical thickness and reflection coefficient of the surface, with $\theta = n_r \omega d / c$ and $r_0 = (1 - n_r)(1 + n_r)$. d and n_r are the physical thickness and refractive index of the surface.

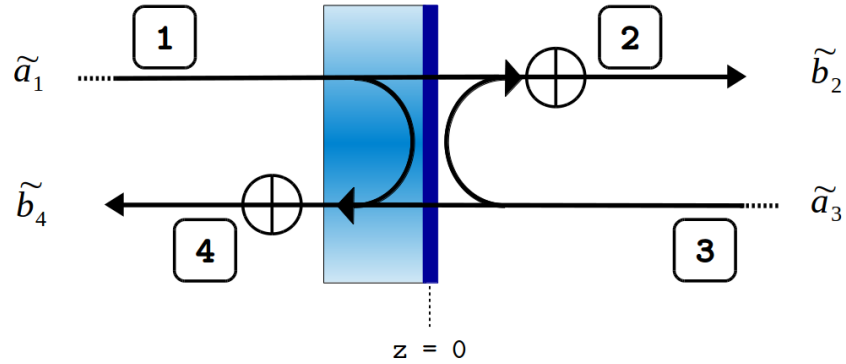


Figure 4.4: Simple mirror with reflective surface to construct the S-matrix.

¹Equation (6) page 401 in [106] is missing a factor 2. Corrected here.

The coating structure is chosen to tune θ . In LIGO, it is adjusted to be an odd integer multiple of $\pi/2$. By doing so, equation 4.28 takes the simple form:

$$\begin{pmatrix} \tilde{b}_2 \\ \tilde{b}_4 \end{pmatrix} = \begin{pmatrix} jt & r \\ r & jt \end{pmatrix} \times \begin{pmatrix} \tilde{a}_1 \\ \tilde{a}_3 \end{pmatrix} \quad (4.31)$$

where r and t are real with $r^2 + t^2 = 1$.

An other way to characterize the interaction between the mirror and the waves is to look at the electric fields in four different nodes (marked in the figure 4.4). We can re-write equation 4.31 in the equivalent following format:

$$\vec{E}^{t+\Delta t} = \mathbb{S} \cdot \vec{E}^t \quad (4.32)$$

$$\begin{pmatrix} E_1^{t+\Delta t} \\ E_2^{t+\Delta t} \\ E_3^{t+\Delta t} \\ E_4^{t+\Delta t} \end{pmatrix} = \begin{pmatrix} 1 & 0 & 0 & 0 \\ jt & 0 & 0 & r \\ r & 0 & 0 & jt \\ 0 & 0 & 0 & 1 \end{pmatrix} \times \begin{pmatrix} E_1^t \\ E_2^t \\ E_3^t \\ E_4^t \end{pmatrix} \quad (4.33)$$

where $\vec{E}^{t+\Delta t}$ and \vec{E}^t are the field amplitudes at the different nodes separated by some small increment of time Δt . In this equation, only the electric fields associated with the HOM are taken in account. As the mirror moves, we need to take in account the fields associated with the sidebands \vec{E}^{SB} . Also, we impose a steady state regime, meaning $\vec{E}^{t+\Delta t} = \vec{E}^t = \vec{E}$:

$$\begin{pmatrix} E_1 \\ E_2 \\ E_3 \\ E_4 \end{pmatrix} = \begin{pmatrix} 1 & 0 & 0 & 0 \\ jt & 0 & 0 & r \\ r & 0 & 0 & jt \\ 0 & 0 & 0 & 1 \end{pmatrix} \times \begin{pmatrix} E_1 \\ E_2 \\ E_3 \\ E_4 \end{pmatrix} + \begin{pmatrix} E_1^{SB} \\ E_2^{SB} \\ E_3^{SB} \\ E_4^{SB} \end{pmatrix} \quad (4.34)$$

$$\begin{pmatrix} E_1 \\ E_2 \\ E_3 \\ E_4 \end{pmatrix} = (\mathbb{I} - \mathbb{S})^{-1} \times \begin{pmatrix} E_1^{SB} \\ E_2^{SB} \\ E_3^{SB} \\ E_4^{SB} \end{pmatrix} \quad (4.35)$$

\mathbb{I} being the identity matrix. The calculation to go from equation 4.34 to 4.35 is developed in appendix C.

We will now extend this example to a full Fabry-Perot cavity of length L , shown in figure 4.5. For each HOM n , we define the field in five nodes (numbered in the figure), which requires a 5×5 scattering matrix²:

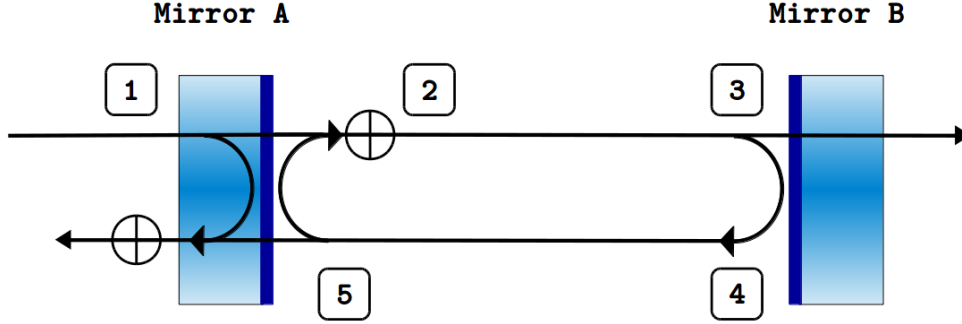


Figure 4.5: Simple Fabry-Perot cavity of length L . For our calculation, only the electromagnetic fields in the cavity are of interest. We are not including the reflective field from the first mirror or the transmitted field from the second mirror.

$$\mathbb{S}_n^\pm = \begin{pmatrix} 0 & 0 & 0 & 0 & 0 \\ jt_A & 0 & 0 & 0 & r_A \\ 0 & p_n^\pm & 0 & 0 & 0 \\ 0 & 0 & r_B & 0 & 0 \\ 0 & 0 & 0 & p_n^\pm & 0 \end{pmatrix} \quad (4.36)$$

where p_n^\pm is the propagation wave:

$$p_n^\pm = e^{j(\phi_n \pm \omega_m t)} = e^{j(\phi_n \pm \omega_m L/c)}. \quad (4.37)$$

The phase ϕ_n depends on the fundamental mode phase ϕ_0 (we have defined $\phi_0 = 0$ in previous expressions) and the additional Gouy phase shift ϕ_G accumulated by the HOM with respect to the fundamental mode:

$$\phi_n = \phi_0 - n\phi_G \quad (4.38)$$

where n is the mode order of the n th mode, and ϕ_G the Gouy phase shift as defined before.

We can simplify the scattering matrix in equation 4.36 by only defining two nodes, as shown in figure 4.6. Having less nodes reduces the scattering matrix size, which will be useful for the full IFO. Equation 4.36 becomes:

²The symbol \pm refers to the lower and higher sidebands generated for one HOM.

$$\mathbb{S}_n^\pm = \begin{pmatrix} 0 & -r_B \cdot p_n^\pm \\ -r_A \cdot p_n^\pm & 0 \end{pmatrix}. \quad (4.39)$$

Equation 4.39 can be split into a diagonal propagation matrix populated by p_n^\pm , and a mirror matrix populated by reflectivity and transmissivity coefficients, as follows

$$\mathbb{S}_n^\pm = \mathbb{M}\mathbb{P}_n^\pm \quad (4.40)$$

with

$$\mathbb{P}_n^\pm = \begin{pmatrix} p_n^\pm & 0 \\ 0 & p_n^\pm \end{pmatrix} \quad \text{and} \quad \mathbb{M} = \begin{pmatrix} 0 & -r_B \\ -r_A & 0 \end{pmatrix} \quad (4.41)$$

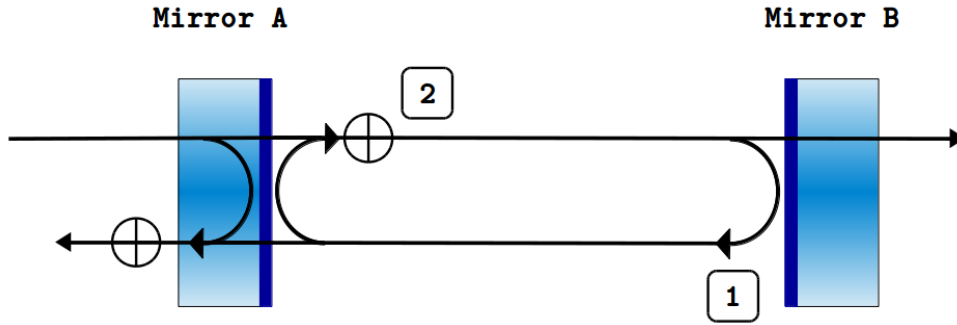


Figure 4.6: Simplified node's notation for a simple Fabry-Perot cavity.

Based on this new expression, we extend the scattering matrix of a single Fabry-Perot cavity to the full LIGO interferometer. The full IFO and nodes are represented in figure 4.7. The propagation and mirror matrices are:

$$\mathbb{P}_n^\pm = \begin{pmatrix} p_{n,1}^\pm & \cdot & \cdot & \cdot & \cdot \\ \cdot & p_{n,2}^\pm & \cdot & \cdot & \cdot \\ \cdot & \cdot & \ddots & \cdot & \cdot \\ \cdot & \cdot & \cdot & p_{n,11}^\pm & \cdot \\ \cdot & \cdot & \cdot & \cdot & p_{n,12}^\pm \end{pmatrix} \quad (4.42)$$

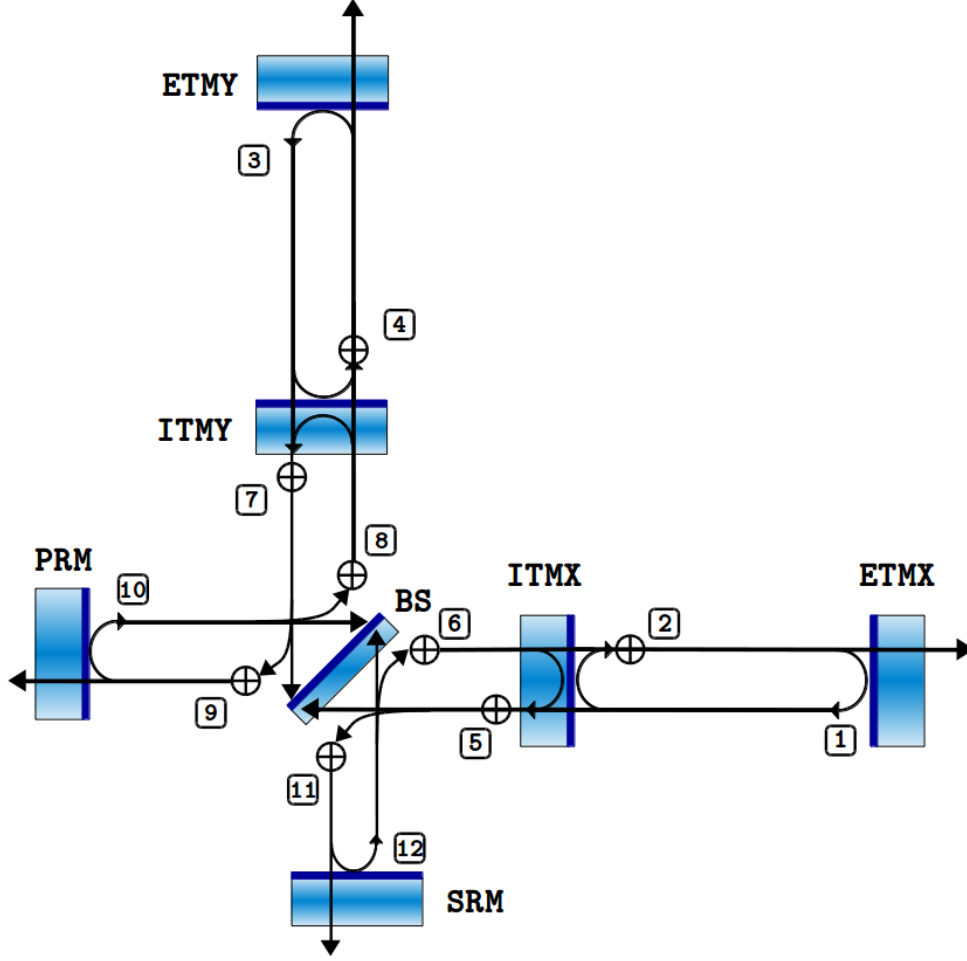


Figure 4.7: LIGO dual-recycled Fabry-Perot-Michelson IFO.

$$\mathbb{M} = \begin{pmatrix}
 \cdot & -r_{ETMX} & \cdot \\
 -r_{ITMX} & \cdot & \cdot & \cdot & t_{ITMX} & \cdot & \cdot & \cdot & \cdot & \cdot & \cdot \\
 \cdot & \cdot & \cdot & -r_{ETMY} & \cdot \\
 \cdot & \cdot & -r_{ITMY} & \cdot & \cdot & \cdot & t_{ITMY} & \cdot & \cdot & \cdot & \cdot \\
 t_{ITMX} & \cdot & \cdot & \cdot & r_{ITMX} & \cdot & \cdot & \cdot & \cdot & \cdot & \cdot \\
 \cdot & t_{BS} & r_{BS} & \cdot & \cdot \\
 \cdot & \cdot & t_{ITMY} & \cdot & \cdot & \cdot & \cdot & r_{ITMY} & \cdot & \cdot & \cdot \\
 \cdot & -r_{BS} & t_{BS} & \cdot \\
 \cdot & \cdot & \cdot & \cdot & t_{BS} & -r_{BS} & \cdot & \cdot & \cdot & \cdot & \cdot \\
 \cdot & -r_{PRM} & \cdot & \cdot & \cdot \\
 \cdot & \cdot & \cdot & \cdot & r_{BS} & t_{BS} & \cdot & \cdot & \cdot & \cdot & \cdot \\
 \cdot & -r_{SRM} & \cdot
 \end{pmatrix} \quad (4.43)$$

Note that we added an index i to the propagation parameters so it became:

$$p_{n,i}^{\pm} = e^{j(\phi_n \pm \omega_m L_i/c)} \quad (4.44)$$

where L_i is the length of the cavity associated with the node x .

One last thing that needs to be added to fully characterize the LIGO IFO are the losses, as they can strongly impact the parametric gain. As explained in the previous section, clipping losses are very important for modes with $n > 10$, but still need to be taken in account for lower order modes. Based on the HOM electric field distribution f_n , we can calculate the amplitude loss associated with the aperture for each propagation in the IFO. Therefore, we define a diagonal matrix \mathbb{C}_n

$$\mathbb{C}_n = \begin{pmatrix} c_{n,1}^{\pm} & \cdot & \cdot & \cdot & \cdot \\ \cdot & c_{n,2}^{\pm} & \cdot & \cdot & \cdot \\ \vdots & \vdots & \ddots & \vdots & \vdots \\ \cdot & \cdot & \cdot & c_{n,11}^{\pm} & \cdot \\ \cdot & \cdot & \cdot & \cdot & c_{n,12}^{\pm} \end{pmatrix} \quad (4.45)$$

where

$$c_{n,i} = \sqrt{\iint_S f_n^2 dS} \quad (4.46)$$

with S the test mass surface normal to the direction of beam propagation. The scattering matrix becomes

$$\mathbb{S}_n^{\pm} = \mathbb{M} \mathbb{C}_n \mathbb{P}_n^{\pm} \quad (4.47)$$

This scattering matrix fully characterizes the IFO and contains the optical gain G_n^{\pm} from one point to the next. By definition, the optical gain is the transfer function between the HOM field and the sideband field at a node i :

$$G_n^{\pm} = \frac{E_i}{E_i^{SB}} = \vec{e}_i^T (\mathbb{I} - \mathbb{S}_n^{\pm})^{-1} \vec{e}_i \quad (4.48)$$

where the basis vector \vec{e}_i is the i th column of the identity matrix, and \vec{e}_i^T is its transpose. We select the node i to study the reflective field of interest. For example, if we want to evaluate G_n^{\pm} for a mode of mirror ETMX, we would use:

$$\vec{e}_1 = \begin{pmatrix} 1 \\ 0 \\ 0 \\ \vdots \end{pmatrix} \quad (4.49)$$

We have now fully defined the expressions to estimate the optical gains and overlap parameters. We can properly calculate the parametric gain R_m for each mechanical mode m . In the next section, we estimate these parametric gains for the full Advanced LIGO IFO.

4.2 PI model & prediction

The IFO parameters and their nominal values to estimate the parametric gains are listed in table 4.1. The calculation is done for a circulating laser power close to the Advanced LIGO full power ($P = 750\text{kW}$) for an ETM mirror (assuming very similar results for ITM). Based on a finite element analysis (FEA), we calculate the nominal frequencies and quality factors of the different mechanical modes m , as explained in section 4.2.1. However, mode frequencies obtained from finite element models may not accurately match those witnessed experimentally due to small differences in material properties or prevailing temperature. Optical gain may thus be different due to deviations of mirror radii of curvature from their nominal values, causing small but consequential changes in Gouy phase.

This variation on the mechanical mode frequencies and radii of curvature has to be taken in account. A probability distribution is done via Monte-Carlo method to estimate the 'worst-case' parametric gains, as explained in section 4.2.2.

4.2.1 Mechanical mode calculation (nominal values)

The fused silica used for the Advanced LIGO test masses is Heraeus Suprasil Type III, which has a quality factor $\geq 10^7$ [111]. But as explained in section 2.4.3, the loss is altered by the damping of the high-reflecting coating layers. Each ETM mirror is coated with alternative layers of silica (18 layers) and tantala (18 layers). The mechanical properties of the Advanced LIGO coating have been extensively studied [112, 113], and are summarized in table 4.2.

A modal analysis of the test mass+coating+ears has been performed with the software ANSYS, as shown in figure 4.8. The 'ears' are fused silica parts doing the liaison between the test mass and the fibers holding the test mass. They are mounted on the

Table 4.1: List of the parameters necessary to calculate the parametric gains. The power's transmittance T is listed for each mirror. Since the reflectivity and transmissivity used in \mathbb{S} are amplitude values, we have $t = \sqrt{T}$ and $r = \sqrt{1-T}$. $L_{\{x\}}$ and $\phi_{\{x\}}$ correspond of the length and phase of the cavity associated with the node x from figure 4.7.

	Parameter	Nominal Value
Optical properties	Circulating arm power (P)	$750 \cdot 10^3$ W
	Laser wavelength (λ_0)	1064 nm
	Input mirror power transmittance ($ITMX, ITMY$)	0.014
	End mirror power transmittance ($ETMX, ETMY$)	10^{-5}
	Power recycling mirror power transmittance (PRM)	0.03
	Signal recycling mirror power transmittance (SRM)	0.33
	Beam splitter power transmittance (BS)	0.5
Lengths	Arm cavity length ($L_{\{1,2,3,4\}}$)	3994.5 m
	Power recycling cavity length ($L_{\{9,10\}}$)	52.3 m
	Signal recycling cavity length ($L_{\{11,12\}}$)	50.6 m
	Beam splitter - X-arm cavity length ($L_{\{5,6\}}$)	4.85 m
	Beam splitter - Y-arm cavity length ($L_{\{7,8\}}$)	4.9 m
Phases	Carrier phase ($\phi_{0,\{1-8,11,12\}}$)	0°
	Carrier phase ($\phi_{0,\{9,10\}}$)	90°
	Arm cavity Gouy phase ($\phi_{G,\{1,2,3,4\}}$)	156°
	Power recycling cavity Gouy phase ($\phi_{G,\{9,10\}}$)	25°
	Signal recycling cavity Gouy phase ($\phi_{G,\{11,12\}}$)	20°
Mechanical properties	Beam splitter - arm cavities Gouy phase ($\phi_{G,\{5,6,7,8\}}$)	0°
	Mass of the test mass (M)	40 kg
	Mechanical mode quality factor (Q_m)	see section 4.2.1

Parameters	Silica	Tantala
Mechanical loss (η_{coat})	$5 \cdot 10^{-5}$	$3.7 \cdot 10^{-4}$
Young's Modulus	72GPa	140GPa
Poisson's ratio	0.15	0.34
Density	2650 kg/m ³	1640 kg/m ³
Total thickness	5.90 μ m	3.68 μ m

Table 4.2: Coating properties of an Advanced LIGO ITM.

flats of the optics with silicate bond [114]. We assume that the loss associated with silicate bond is negligible [115]. The fibers are not taken in account in this analysis, as almost no energy is transferred from the fibers to the ears.

The total mechanical quality factor for each mode m is defined by [116]:

$$Q_{tot,m} = \eta_{tot,m}^{-1} = \frac{2\pi E_{tot,m}}{W_m} \quad (4.50)$$

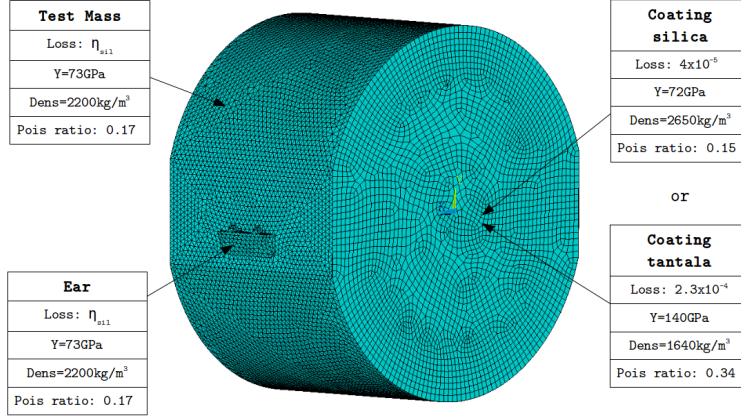


Figure 4.8: Overview of the modal analysis with the test mass+ears+coating layer.

where W denotes the total amount of energy dissipated per cycle and E_{tot} the maximum strain energy stored in the system during a cycle. We used our model to estimate the strain energy E_i of each component i for each mode. The energy dissipated is defined as the sum of the individual loss factors η_i weighted by E_i :

$$Q_{tot,m} = \frac{E_{tot,m}}{\sum_i E_{i,m} \eta_i} = \frac{E_{tot,m}}{E_{TM,m} \eta_{sil,m} + E_{ear,m} \eta_{sil,m} + E_{coat,m} \eta_{coat}} \quad (4.51)$$

with $\eta_{sil,m}$ the frequency-dependent loss factor of suprasil from reference [117]. Given the nano-size of the coating layers, a single analysis with multi-layers coating was not possible. We had to consider a single layer of coating thickness. We thus realized two analysis: one analysis with the properties of silica and $5.90 \mu\text{m}$ of coating, the other with the properties of tantala and $3.68 \mu\text{m}$ of coating. The estimated quality factors and frequencies are shown in figure 4.9.

4.2.2 Model

The Monte-Carlo method, or method of statistical trials, is based on simulation by random variables. In our case, we randomize the mechanical mode frequencies and the mirror radius of curvature around their nominal values in order to statistically simulate the change in the IFO properties due to thermal transients. To allow realistic variations, we generate uniformly distributed random numbers around the nominal value within a range of $\pm 2\%$. By repeating this process many times ($N = 250,000$ iterations), we obtain sensitive parametric gains. For each mechanical mode, a parametric gain is thus calculated with 95% confidence (i.e. the smallest value greater than 95% of the results).

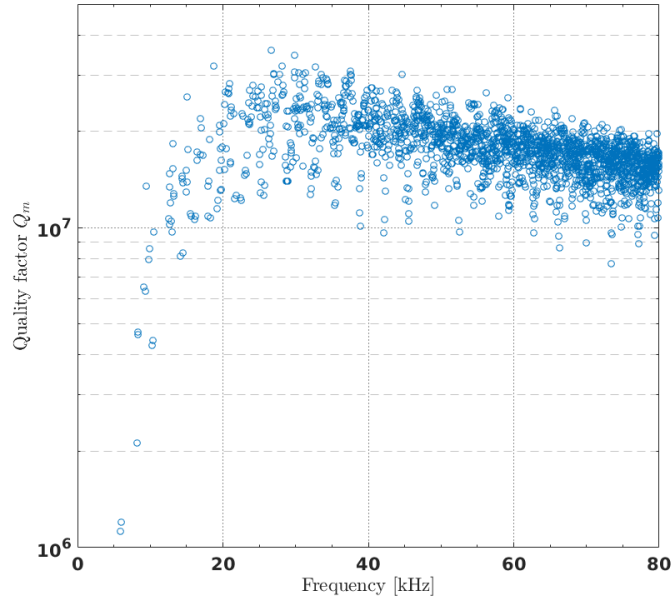


Figure 4.9: List of the test mass mechanical modes and their associated quality factors.

Results are shown in figure 4.10. The calculation has been done for node 1 in figure 4.7 (ETM mirror). We find 275 modes with $R > 0.1$ and 47 modes with $R > 1$. The maximum gain is less than 20. These results confirm that PI will be a real challenge for LIGO as we go up to full power.

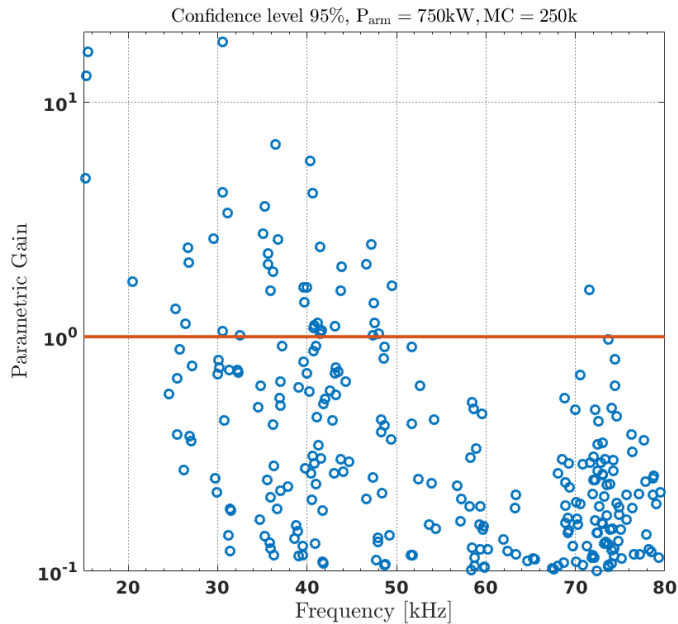
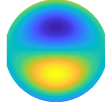
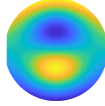
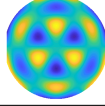
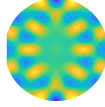
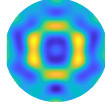


Figure 4.10: Advanced LIGO 'worst case' parametric gains at full power (95% confidence). Only the mechanical modes with parametric gains superior than 0.1 are represented.

4.3 Current status of LIGO

PI have already been observed in both LIGO detectors, with only $P \sim 100\text{kW}$ of circulating power in the arms [105, 118]. These instabilities exponentially grew until the saturation of the electronic readout chain, causing the detectors to lose optical lock. We experienced 9 PI in the LIGO arms during O1, all listed in table 4.3. To mitigate these instabilities and keep the IFO in operation, active control techniques via electrostatic drive and thermal tuning have been implemented [119].

Table 4.3: List of the PI observed in H1 during O1. Similar behavior has been seen at L1. We observe slightly different frequencies between the mirrors for a same mechanical mode due to thermal transients.

Frequency [Hz]	Mirror	Mechanical mode shape	Main associated HOM
15009	ETMY		HOM01 
15518 15522 15541 15542	ITMY ITMX ETMX ETMY		HOM11 
32761.5 32768.5	ETMY ETMX		HOM03 
47480	ETMY		HOM10 
47498	ETMY		HOM10 

Thermal tuning is achieved using radiative ring heaters (see figure 4.11). Around the barrel of each test mass, a non-contact nichrome resistance wire heats the outer edge of the mirror, changing its radius of curvature. This change of curvature is used to shift in frequency the problematic HOM and increase the mode space between this HOM and a mechanical mode. This effectively reduced the G factor and therefore the parametric gain. This method has been used during O1 to decouple the mechanical mode around 15.5kHz and its main associated HOM, as shown in figure 4.12. The ring heater is located close to the rear surface of the test mass to limit excessive noise increase at the front surface.

The other observed PI have been mitigated using electrostatic drive (ESD). The ESD provides longitudinal actuation on the test mass via electric fields between the test mass and the reaction mass (for more details on the reaction mass, see figure 4.11).

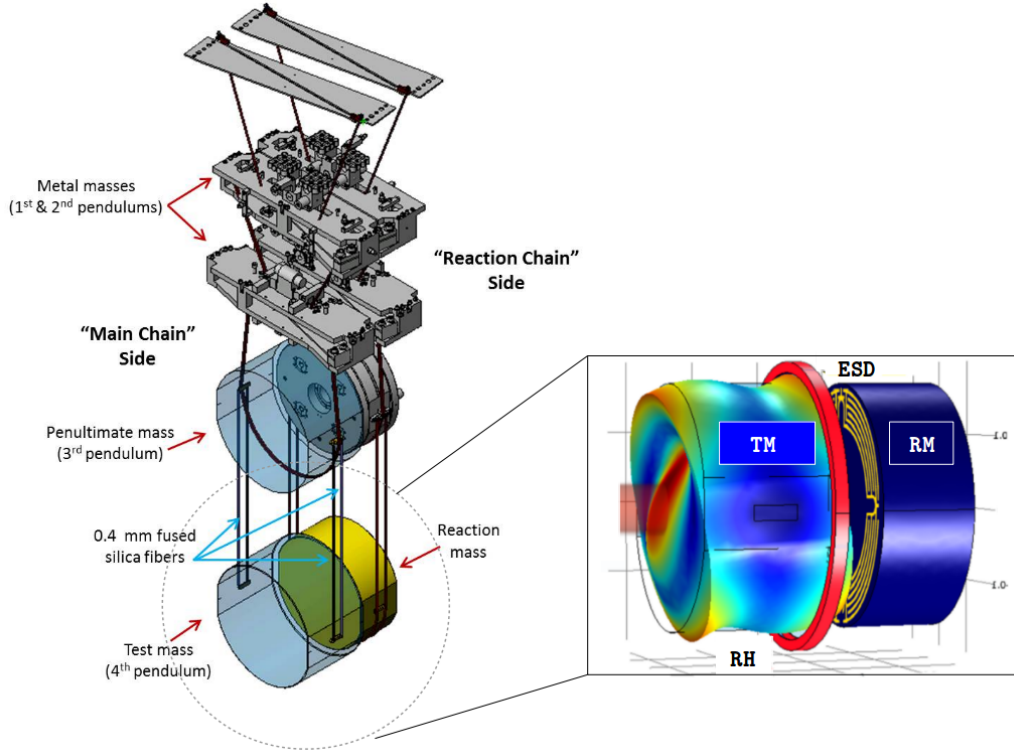


Figure 4.11: Overview of the LIGO suspension system. On the left is represented the core of the suspension only (the cage surrounding the suspension is not represented for visibility). Each of LIGO's 40 kg test masses is suspended within a 360 kg quadruple pendulum system. Two 'chains' of suspended masses hang back to back in each suspension system: the main chain (with the test mass) and the reaction chain. The reaction chain actively acts on the main chain for alignment purposes. On the right is a schematic of the test mass (TM) and the reaction mass (RM) inspired by figure 1 in reference [119]. The ring heater (RH) is represented in red and the ESD comb in gold. An exaggerated deformation of the mirror due to the mechanical mode $\sim 15.5\text{kHz}$ is shown. The distance between the reaction mass and the test mass is exaggerated by a factor of 10 for visibility.

The fields are generated by a comb of gold conductors that are deposited on the reaction mass. This force is used in a feedback fashion to control the time constant associated with problematic mechanical modes. The ring heater and the ESD are both shown in figure 4.11.

The current techniques used to control PI present major limitations. The ESD loop involves precise tracking of all the modes, which could be difficult due to large thermal transients in the arms. It thus requires important commissioning effort everytime the IFO is locked, limiting its duty cycle. Moreover, the large number of expected unstable modes at full power will make this method even harder, if not impossible, to use in the future.

For these reasons, efforts have been made over the years to find alternative solutions to suppress PI. In 2008, Gras *et al.* suggested to suppress PI by use of a damping ring optimally located on the circumference of the test masses [120]. Schediwy *et al.*

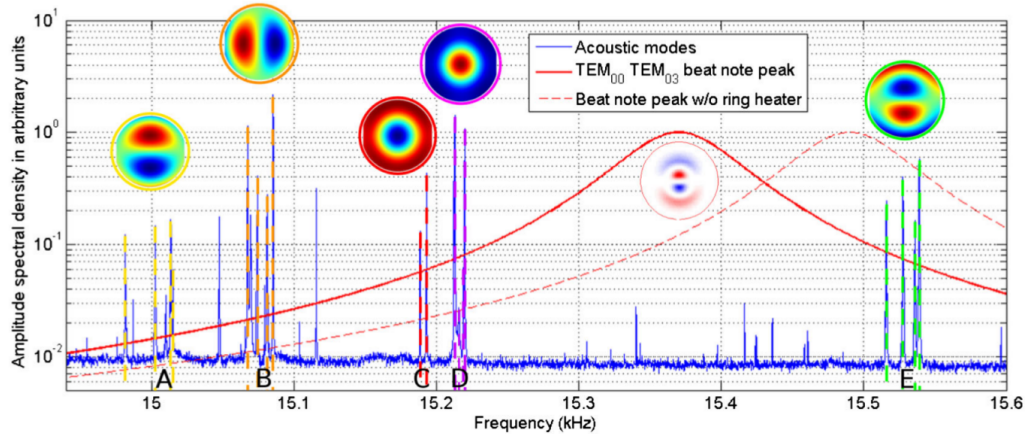


Figure 4.12: From reference [119]. The measured mechanical modes are shown in blue. These modes appear in groups of four, one for each test mass in the interferometer. The group of modes labeled *E* around 15.5kHz couple with one of the HOM. The dash and plain red curves represent the simulated shape of this HOM, with and without ring heater respectively. The HOM is shifted in frequency to a 'sweet spot' to reduce the coupling.

in 2008 and Green *et al.* in 2016 proposed PI mitigation schemes via optical tuning [121, 122]. However, these proposed methods greatly degrade the sensitivity of LIGO (in the case of the damping ring) or increase the complexity of the LIGO optical configuration without resolving the issue of PI entirely (in the case of optical tuning).

The device presented in this manuscript offers a simple alternative solution to get rid of all the PI (even at full power) with minimum noise increase. We will now report on the development and performance of this passive device, referred to as Acoustic Mode Damper (AMD). We will start by describing the general concept of the AMD in section 4.4.1, presented for the first time by Gras *et al.* in 2015 [123]. We will then explain why we developed this particular design and chose these specific materials. Finally, we will show the AMD performance against PI and its associated thermal noise.

4.4 Damping solution: Acoustic Mode Damper

4.4.1 Description

The AMD concept is shown in figure 4.13. It is a passive damper directly mounted to the test mass via epoxy bond. This device is able to suppress PI by reducing the quality factors Q_m of the problematic mechanical modes. Each AMD is made of a fused silica base, a piezoelectric (PZT) plate (acting as a lossy spring) and an aluminum reaction mass (RM), as shown in figure 4.13. The PZT electrodes are shunted with a resistor: the mechanical energy converted in electrical energy by the

PZT plate is dissipated through the resistor (see section 4.4.2). To assure flowing current between the PZT plate and the resistor, the top surface of the fused silica base is gold coated. Also, the PZT plate is bonded to the base and the reaction mass using conductive epoxy (see section 4.7).

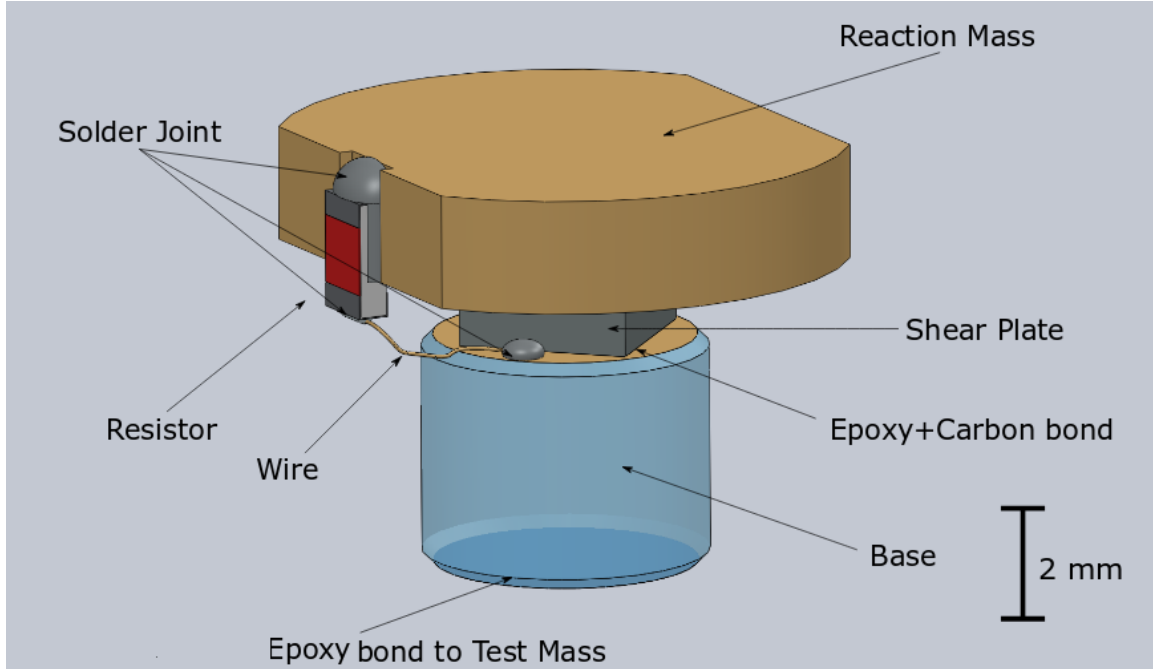


Figure 4.13: AMD concept. Each AMD is composed by a base, a shunted piezoelectric plate acting as a spring and a reaction mass. The plate is bonded to the base and the reaction mass with conductive epoxy. The AMD is glued to the flat part of the test mass with epoxy.

To assure good contact between the base of the AMD and the test mass, the AMD will be mounted on the flat parts of the test masses. We plan on having four different AMDs per test mass in order obtain good performance for a broad selection of mechanical modes (see performance in section 4.9.3). The AMD different designs will be shown in section 4.9.1 and the exact locations of the AMDs on the flats will be discussed in section 4.9.2.

4.4.2 Shunted piezoelectric

PZT materials possess interesting properties for damping applications. In this section, we will explain why a shunted PZT is better than a more "classic" material as a spring for the AMD device.

The basic properties of piezoelectric materials are expressed mathematically as a relationship between two electric and two mechanical variables:

$$\begin{bmatrix} \vec{D} \\ \vec{\epsilon} \end{bmatrix} = \begin{bmatrix} e^T & d \\ d^{-1} & s^E \end{bmatrix} \cdot \begin{bmatrix} \vec{E} \\ \vec{\sigma} \end{bmatrix} \quad (4.52)$$

where D and E are the vectors of electrical displacements (charge/area) and electrical field in the material (volts/meter), and ϵ and σ are the vectors of strain (length/length) and stress (force/area). s^E , e^T and d are a set of matrices characterizing the properties of the PZT. s^E is the compliance matrix (6x6) at constant electric field, e^T the permittivity matrix (3x3) at constant stress and d the strain coupling matrix (6x3) [124]. d^{-1} is the transpose of d . Using standardized notation, we can write:

$$\vec{D} = \begin{bmatrix} D_1 \\ D_2 \\ D_3 \end{bmatrix}, \quad \vec{E} = \begin{bmatrix} E_1 \\ E_2 \\ E_3 \end{bmatrix}, \quad \vec{\epsilon} = \begin{bmatrix} \epsilon_1 \\ \epsilon_2 \\ \epsilon_3 \\ \epsilon_4 \\ \epsilon_5 \\ \epsilon_6 \end{bmatrix}, \quad \vec{\sigma} = \begin{bmatrix} \sigma_1 \\ \sigma_2 \\ \sigma_3 \\ \sigma_4 \\ \sigma_5 \\ \sigma_6 \end{bmatrix} \quad (4.53)$$

where "3" is the direction associated with the polarized direction of the plate. To study the shunted PZT properties, we assume the simplest scenario with non-zero stress and polarization in the "3" direction. Hence, equation 4.52 becomes:

$$\begin{bmatrix} D_3 \\ \epsilon_3 \end{bmatrix} = \begin{bmatrix} e_{33}^T & d_{33} \\ d_{33} & s_{33}^E \end{bmatrix} \cdot \begin{bmatrix} E_3 \\ \sigma_3 \end{bmatrix}. \quad (4.54)$$

For a PZT plate with a surface area A and a thickness L , the voltage V across the electrodes and the resulting displacement current I can be defined as:

$$V = \int_0^L E_3 \cdot dx \quad , \quad I = \int_A D_3 \cdot da. \quad (4.55)$$

In the Laplace domain, these quantities can be written as $V = L \cdot E_3(s)$ and $I = sA \cdot D_3(s)$. Therefore, equation 4.54 becomes:

$$\begin{bmatrix} I \\ \epsilon \end{bmatrix} = \begin{bmatrix} s \frac{Ae_{33}^T}{L} & sAd_{33} \\ \frac{d_{33}}{L} & s_{33}^E \end{bmatrix} \cdot \begin{bmatrix} V \\ \sigma \end{bmatrix}. \quad (4.56)$$

Note that $\frac{Ae_{33}^T}{L}$ is the capacitance of the PZT, and we write $C^T = \frac{Ae_{33}^T}{L}$. We also define the impedance of the PZT without shunt (open circuit) as $Z_{OC} = \frac{1}{sC^T}$. Equation 4.56 becomes:

$$\begin{bmatrix} I \\ \epsilon \end{bmatrix} = \begin{bmatrix} sC^T & sAd_{33} \\ \frac{d_{33}}{L} & s_{33}^E \end{bmatrix} \cdot \begin{bmatrix} V \\ \sigma \end{bmatrix} = \begin{bmatrix} \frac{1}{Z_{OC}} & sAd_{33} \\ \frac{d_{33}}{L} & s_{33}^E \end{bmatrix} \cdot \begin{bmatrix} V \\ \sigma \end{bmatrix}. \quad (4.57)$$

Equation 4.57 shows that the equivalent circuit of the PZT plate is a current source in parallel with a capacitor, as highlighted in figure 4.14.

In the shunted configuration as in the case of the AMD, we add a resistor R_{SH} in parallel, connected to the electrodes of the PZT plate. The impedance becomes

$$\frac{1}{Z_{TOT}} = \frac{1}{Z_{OC}} + \frac{1}{R_{SH}} \quad (4.58)$$

and equation 4.57 for the shunted PZT

$$\begin{bmatrix} I \\ \epsilon \end{bmatrix} = \begin{bmatrix} \frac{1}{Z_{TOT}} & sAd_{33} \\ \frac{d_{33}}{L} & s_{33}^E \end{bmatrix} \cdot \begin{bmatrix} V \\ \sigma \end{bmatrix}. \quad (4.59)$$

The top part of this matrix can be solved for the voltage across the electrodes:

$$V = Z_{TOT}(I - sAd_{33}\sigma). \quad (4.60)$$

In our application, the PZT plate is fully passive and not actively driven ($I = 0$), and hence:

$$V = -sZ_{TOT}Ad_{33}\sigma. \quad (4.61)$$

By using the part of equation 4.59 related to the mechanical properties of the PZT, we obtain a linear expression of the strain for the shunted PZT system:

$$\epsilon = \frac{d_{33}}{L}V + s_{33}^E\sigma = (s^E - s\frac{Ad_{33}^2Z_{TOT}}{L})\sigma = s_{33}^{SH}\sigma \quad (4.62)$$

with s_{33}^{SH} the compliance of the shunted system. The shunt affects the mechanical properties of the PZT plate such that

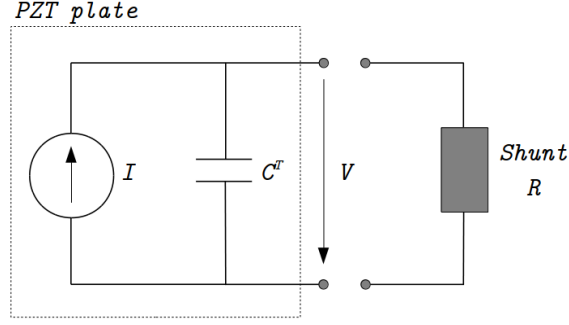


Figure 4.14: Equivalent circuit of the PZT plate shunted with a resistor.

$$s_{33}^{SH} = s^E - s \frac{C d_{33}^2 Z_{TOT}}{e^T} = s^E - \frac{d_{33}^2 \bar{Z}_{TOT}}{e^T} \quad (4.63)$$

knowing that $C^T = \frac{Ae_{33}^T}{L}$ and defining the non-dimensional electrical impedance:

$$\bar{Z}_{TOT} = \frac{Z_{TOT}}{Z_{OC}} = \frac{R_{SH} C^T s}{R_{SH} C^T s + 1}. \quad (4.64)$$

Note that for the open circuit configuration, $\bar{Z}_{TOT} = 1$.

The capacitance C^T is defined by e^T , meaning for constant stress conditions within the PZT plate. In our case, this doesn't hold and the change of stress affects the capacitance. This change in capacitance is found to be [125]:

$$C^S = C^T (1 - k_{33}^2) \quad (4.65)$$

with k the electromechanical coupling coefficient of the PZT plate, defined by:

$$k_{33}^2 = \frac{d_{33}^2}{s_{33}^E e_{33}^T}. \quad (4.66)$$

Hence, we can also re-write the compliance s_{33}^{SH} as

$$s_{33}^{SH} = s^E (1 - k_{33}^2 \bar{Z}_{TOT}). \quad (4.67)$$

Equation 4.67 indicates that mechanical properties of the PZT plate can be controlled as the electrical boundary conditions are changed. We thus define the mechanical

impedance Z_M depending on the electrical impedance Z_{TOT} . We write \bar{Z}_M , the dimensionless expression of the mechanical impedance by dividing by the open circuit impedance ($\bar{Z}_{TOT} = 1$):

$$\bar{Z}_M = \frac{1 - k_{33}^2}{1 - k_{33}^2 \bar{Z}_{TOT}}. \quad (4.68)$$

After calculation (see appendix D for details), the expression becomes:

$$\bar{Z}_M = 1 - \frac{k_{33}^2}{jR_{SH}C^S\omega + 1} \quad (4.69)$$

which corresponds to the expression introduced for the first time by Hagood and Flotow [126].

This complex, frequency dependent impedance can be represented as a complex modulus, as is typically done in material damping [127, 128]:

$$\bar{Z}_M = Y(1 + j\eta) \quad (4.70)$$

with Y and η the frequency dependent Young's modulus and loss factor of the shunted direction:

$$Y = \Re[\bar{Z}_M] \quad \text{and} \quad \eta = \frac{\Im[\bar{Z}_M]}{\Re[\bar{Z}_M]}. \quad (4.71)$$

By using equation 4.69, these expressions become:

$$Y = 1 - \frac{k_{33}^2}{(R_{SH}C^S\omega)^2 + 1} \quad (4.72)$$

$$\eta = \frac{k_{33}^2 R_{SH} C^S \omega}{(R_{SH} C^S \omega)^2 + 1 - k_{33}^2} \quad (4.73)$$

Equations 4.72 and 4.73 show the usefulness of the shunted system for the AMD. By choosing the appropriate PZT plate and resistor, the stiffness and loss can easily be tuned. The resistor's value is chosen to maximize the damping efficiency of the AMD

in the bandwidth of interest (between 10kHz and 80kHz), while limiting the thermal noise re-injection at lower frequencies. Moreover, the shunt is active only in the polarization direction of the plate. By having the plate polarized in shear (direction "15" instead of "33" in our example) perpendicular to the laser beam direction, the thermal noise is greatly minimized (see section 4.9.4).

In conclusion, a shunt PZT system offers easily tunable properties while limiting excess noise in the LIGO detection bandwidth. Different PZT materials have been studied and tested, all summarized in appendix E. At the end, material PIC181 has been selected for all the AMDs. In order to cover a larger frequency bandwidth, the resistors are slightly different between AMD1, AMD2, AMD3 and AMD4. The results are summarized in table 4.4 and figure 4.15.

Note that other external electric networks have been considered for the shunt (capacitor, inductor+resistor, etc.). Overall, a simple resistor provides the easiest broadband damping solution.

Table 4.4: Summary of the shunted plate performance. The shunt loss angle is effective in the polarization direction of the PZT plate. Keeping the polarization direction perpendicular to the laser beam direction ensures very weak coupling to the strain sensitivity at lower frequencies.

	Resistor	Maximum loss	Loss at 100Hz
AMD1	200k Ω	0.2545 at 15.7 kHz	3.23×10^{-3}
AMD2	50k Ω	0.2545 at 63.0 kHz	0.81×10^{-3}
AMD3	50k Ω	0.2545 at 63.0 kHz	0.81×10^{-3}
AMD4	25k Ω	0.2545 at 126 kHz	0.40×10^{-3}

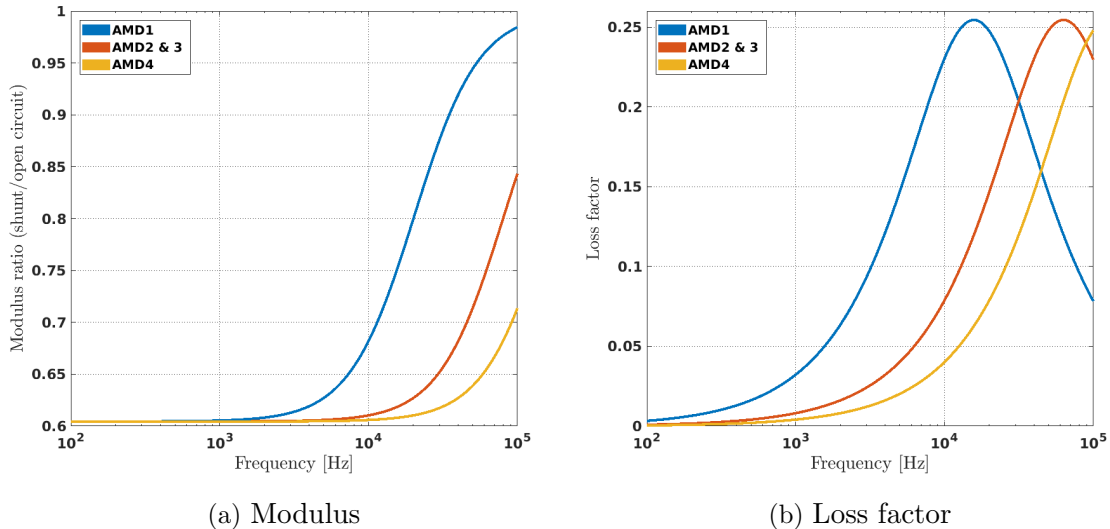


Figure 4.15: Shunt modulus and loss factor of a PIC181 plate as a function of frequency. The resistors have been chosen to get the maximum dissipation between 10kHz and 80kHz. The resistor for the AMD1 targets the 15.5kHz frequency.

4.4.3 AMD material selection

Most of the damping to reduce Q_m comes from the shunted PZT. Therefore, the loss associated with the other AMD components will have little impact on the overall performance between 10kHz and 80kHz. However, the materials loss plays a crucial role in the sensitivity degradation of the interferometer in the detection bandwidth [10-1000] Hz. It is important to select low-loss materials, such that the thermal noise increase due to the AMDs is kept to a minimum. We aim for a maximum $\sim 1\%$ degradation of the detector's strain sensitivity.

The base

The properties of fused silica are well defined in literature [111, 129]. We choose this material as it is a low-loss, stiff material. A surface flatness of few nanometers can be done, which is necessary to obtain a thin homogeneous bond with the flats of the test mass. We assume a frequency-independent loss factor of $\eta_{base} = 1 \cdot 10^{-6}$. Note that this value is pessimistic compared to the numbers found in [111]. We adopt this strategy to estimate the 'worst-case scenario' in our thermal noise calculation (section 4.9.4).

The reaction mass

In early designs, tungsten-copper alloy was first considered as a reaction mass material. Its high-density properties made it a strong candidate to achieve compact design. However, analysis shown that heavy mass means important straining of the AMD at low frequencies, resulting in a non-negligible noise increase. Ultimately, aluminum was chosen for the reaction mass as it is lighter, low-loss and easy to machine. Easy machining gives us freedom in the design, which is important to properly tune the AMD resonance frequencies (see section 4.9.3). Moreover, a surface flatness $< 1\mu\text{m}$ can be achieved with lapping technique, which is important to obtain thin bonds. We assume frequency-independent loss factor of $\eta_{al} = 1 \cdot 10^{-4}$ from [130] (still as a 'worst-case scenario' number).

Conductive bond

The bond between the PZT plate and the rest of the AMD needs to be conductive (for the shunt), and as thin as possible to limit noise. Different types of bonding agents have been tested. To determine which material was the most appropriate for the AMD, a first series of thickness and conductivity tests has been performed. From

literature, it is hard to find precise measurements of the loss associated with bonding agents like epoxy. However, from a previous LIGO study [131], we know that the loss of epoxy TRA-DUCT 2902 [132] is $\sim 4 \times 10^{-2}$. Taking this number as a reference, analysis shown that the thickness of the bond layer must not be greater than a few micrometers to limit impact on the LIGO sensitivity..

The jig shown in figure 4.16 has been built to measure the minimum thickness achievable with each bond agent. A small quantity of bond agent (shown in red) is dropped between two flat optics (in white). The thickness of each optics is precisely measured before hand, using a sub-micrometer from Mitutoyo (precision of $0.1\mu\text{m}$). A point of known force is exerted on the assembly with a bearing ball. The bearing ball is embedded in a sliding cylinder (represented in yellow), which is guided by an aluminum plate. A precision weight (shown in black) is used to control the force applied. The different cuts on top of the cylinder correspond of the different sizes of the precision weights that could be used to apply force. For these tests, a large force of 100N is used to reduce the thickness to a minimum. After curing, the bond thickness is deducted by subtracting the total thickness with the thickness of each individual component. Results are shown in table 4.5.

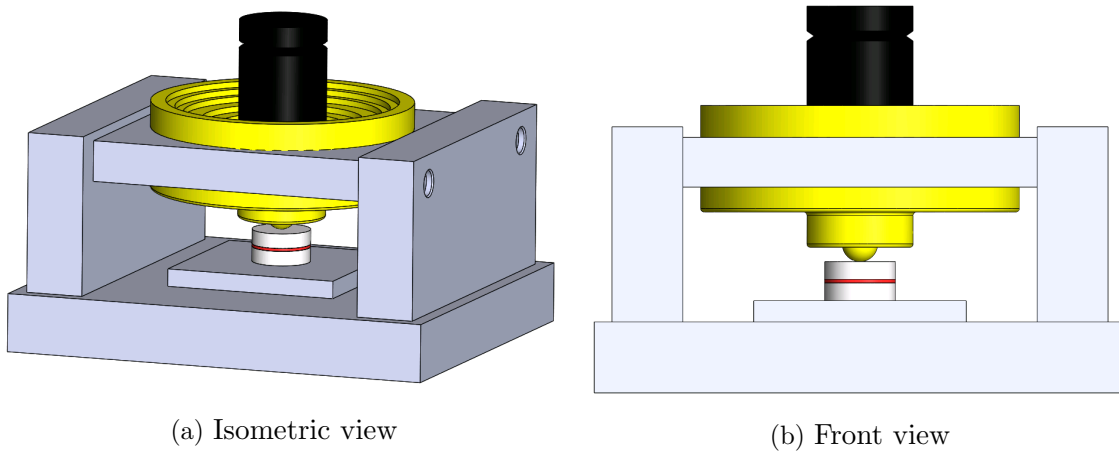


Figure 4.16: Overview of the jig used to measure the minimum thickness achievable for different bonds. The bond layer (in red) is exaggerated for visibility

Table 4.5: List of the different bonds tested for the AMD. Overall, we achieved the appropriate thickness of a few micrometers only with epoxy 353ND and 302-3M.

Name	Type	Curing Temp.	Vacuum compatible	Conductive	Thickness obtained
3-M Scotch-Weld EZ-2216	Epoxy	Room Temp	Yes	No	$48\mu\text{m}$
Armstrong A-12	Epoxy	Room Temp	Yes	No	$37\mu\text{m}$
Epo-Tek 302-3M	Epoxy	Room Temp	Yes	No	$0.5\mu\text{m}$
Epo-Tek 353ND	Epoxy	150°C	Yes	No	$0.7\mu\text{m}$
Tra-Duct 2902	Epoxy	Room Temp	Yes	Yes	$12\mu\text{m}$

For most of the agents tried, it was hard to achieve a thickness smaller than $10\ \mu\text{m}$, except for epoxy 302-3M [133] and 353ND [134] from Epo-Tek. 302-3M and 353ND have lower viscosity compared to the other agents, and thin layers were easily achievable. The issue with 353ND is its elevated curing temperature of 150°C . While it was not an issue for this test, the different materials (with different thermal expansion rate) of the AMD might weakened the thin bond during the curing procedure.

At the end, we selected the non-conductive epoxy 302-3M mixed with graphite powder from US Research Nanomaterials [135]. 302-3M is a low out-gassing, vacuum compatible, LIGO-approved [136] epoxy with a room-temperature curing of 24 hours. We mix it with $400\text{nm} - 1.2\ \mu\text{m}$ particles of graphite to make it conductive. The powder is also a nice way to control the thickness of the bond: while applying a large pressure, the thickness goes down to the size of the particles ($1.2\ \mu\text{m}$). The mix ratio between epoxy and powder is 1:0.05 (5%) by weight, as higher ratios change the viscosity and make the bond harder to handle. The conductivity of the mix is checked with the same jig from figure 4.16. Instead of optics, lapped pieces of aluminum are used, and the conductivity of the assembly is measure. For a $1.2\ \mu\text{m}$ layer, we measured a resistance of $\sim 1\ \Omega$, assuming negligible resistivity from the aluminum. This result is good enough to ensure flowing current between the PZT plate and the electrodes.

To measure the loss associated with this thin bond, an experiment has been made and is presented in section 4.5.

PZT plate

As explained in section 4.4.2, PIC181 material is used as a spring. Custom-made plates of dimensions $3\ \text{mm} \times 3\ \text{mm} \times 1.5\ \text{mm}$ height from PI-Ceramics [137] were made. Even if the loss associated with the shunt has been well defined, it is important to know the mechanical loss of the plate itself in the non-shunted directions. Several measurements of the mechanical loss of piezoelectric material have been published over the past decades [138, 139, 140]. However, these studies present numbers only at high frequencies (above kHz), and usually only in the active direction. There are thus not usable in this case, and the new experiment presented in section 4.5 is used to do this measurement.

Resistor

We considered two types of resistor: a thin film resistor (CMF type) and a thick film resistor (CHR type). The thick film resistors are fully vacuum compatible, while thin film resistors are caped with protective layer made of mixture of titanium dioxide and

unknown epoxy material, which vacuum compatibility is in question. Unfortunately, thick film resistors characterize large flicker noise [141] as in comparison to thin film resistors. Therefore, our preference went to thin film resistors due to their low flicker noise. In order to minimize outgassing of the thin film resistor, we used the small CHR0805 resistor which contains 0.0588 mg of organic substance (epoxy), what corresponds to 1.4% of the resistor total mass. A residual gas analyze of the resistors has been done, showing no noticeable vacuum degradation.

In conclusion, before being able to fully characterize the noise of the AMDs, we need to measure the loss associated with the conductive epoxy and the PZT plate. A method and experiment has been designed for that purpose.

4.5 Experiment

It exists different methods to measure the loss factor of a material. The most popular approach is the standard method [142], also referred to as the Oberst beam method. It involves using the response of a cantilevered laminated beam, composed by a base beam and one or two layers of the material to be tested. Beam theory is then used to calculate the loss factor η . A common alternative approach, referred to as an impedance method [143, 144], is to directly measure the stiffness of the sample when it is deformed dynamically via a force gauge or an actuator.

These techniques are both widely used, but present limitations in our application. First, they measure the sample in extensional deformation only, which is not adequate to characterize the anisotropic properties of the PZT plate. Second, the clamped boundary condition can introduce unwanted dissipation [145, 146]. Finally, the sample geometry is very limited. To measure the loss of a $1.2\mu\text{m}$ layer, a microbeam must be use (assuming we want to keep a 1:1 ratio between the sample and the base beam). Microbeams are complex, and unwanted damping effects such as thermoelastic damping and air damping can be introduced [147, 148].

For these reasons, we decided to get away from cantilevers method and develop our own experiment [149]. The goal of this experiment is to test samples, even micro-sized samples, in both shear and compression without introducing extra-damping. First, we will present the concept of this experiment and the different prototypes it went through. We will finally show the final version and the results obtained for the epoxy and PZT plate.

4.5.1 Approach

The developed experiment is based on a mechanical oscillator with natural frequencies in the range of [50Hz-1000Hz]. The general concept is illustrated in figure 4.17, where two aluminum masses are connected to one (or several) sample(s). The masses act as rigid bodies, meaning most of the strain energy is stored in the sample(s). The measure of damping is made from the transient response of the system at resonance. The oscillator modes are excited by hitting one of the mass with an impact hammer and the time series is recorded with an accelerometer. The quality factor Q of each mode is then computed from the time series using the ring-down method. This method is based on the fitting of the time constant τ of the exponential decreasing signal envelope. By exploiting several mechanical resonances, we cover a broad range of frequencies while straining the sample(s) in shear and compression. A general expression of the loss factor η [116] can be written as

$$\eta = Q^{-1} = \frac{2}{\omega_0 \tau} = \frac{W}{2\pi E_s} \quad (4.74)$$

where W denotes the total amount of energy dissipated per cycle, E_s the maximum strain energy stored in the oscillator during a cycle, and τ the measured time constant of the mode at frequency ω_0 . In order to extract the loss factor of the sample(s), we take into account all the other components of the oscillator which can also dissipate energy. The strain energy E_i of each component i for a given mode is estimated with a finite element model. Since the amplitude of the excited modes is small, we assume linear behavior of the model.

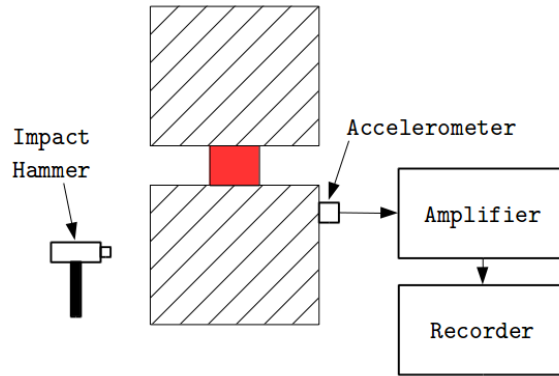


Figure 4.17: Experiment concept. A sample, represented in red, is mounted between two aluminum masses (hatched areas), acting as rigid bodies. The system is excited with an impact hammer and the transient response recorded with an accelerometer. The quality factor Q of each mode is computed using the ring-down method (see section 4.5.3)

The energy dissipated in the oscillator can be defined as the sum of the individual loss factors η_i weighted by E_i :

$$\eta = Q^{-1} = \frac{1}{E_s} \sum_i E_i \eta_i. \quad (4.75)$$

Based on this definition, three series of early experiments have been conducted:

1. The first series of experiments used monolithic devices: an aluminum structure is machined to leave a small aluminum flexure between the masses (no bonding). The flexure section has the size of the piezoelectric material used in the next series of experiments. This very low-loss oscillator permits to estimate the optimal quality factor that can be obtained in this ideal case (no glue, no lossy flexure), with $\eta = Q^{-1} = \frac{E_{Al}\eta_{Al}}{E_{Al}} = \eta_{Al}$. It also permits to identify unwanted damping.
2. The aluminum flexure is now glued with epoxy between the two rigid masses, making the device non-monolithic. This step permits to characterize the structural loss induced by the epoxy layers, with:

$$\eta_{epoxy} = \frac{E_s/Q - E_{Al}\eta_{Al}}{E_{epoxy}}. \quad (4.76)$$

3. In the last series of experiments, the aluminum flexure is replaced by piezoelectric plates to characterize the structural loss induced by the piezoelectric material, with:

$$\eta_{PZT} = \frac{E_s/Q - E_{Al}\eta_{Al} - E_{epoxy}\eta_{epoxy}}{E_{PZT}}. \quad (4.77)$$

By following these guidelines, we 1. validate the experiment, 2. measure the loss factor of epoxy and 3. the loss of the PZT material.

4.5.2 Limitations and preliminary results

Different early designs have been tried and numerous iterations made. The goal of these preliminary experiments was not to directly measure the loss of materials, but to identify the obstacles and define precise specifications. In this section, we will summarize the difficulties encountered, and present the final design in the next section.

Damping in the joints

In a high quality factor measurement like in our case, the dissipation mechanisms to be characterized can easily be masked by unwanted dissipation effects. Several different

boundary conditions have been modeled and tested. In particular, the clamped-free configuration in which the bottom is clamped on a rigid and massive structure, and the free-free configuration in which the device is suspended by the top mass. Experimental results shown that the free-free configuration, in which the device is optimally suspended, is the most appropriate for our purpose.

Thermoelastic damping

The quality factors measured with monolithic experiments were about ten times smaller than the expected value of $\sim 10,000$ (which corresponds to the quality factor of aluminum [130]). Different boundary conditions have been tested, without improvement. It turns out that the limitation came from thermoelastic damping, or Zener damping [150]. In 1937, Zener has interpreted internal damping in reeds as an effect of thermal diffusion: temperature couples to the strain because materials have nonzero coefficients of thermal expansion. As a reed is flexed, one side heats and the other cools. Heat flows to attempt to restore equilibrium, causing the restoring force from the flexure to relax from its initial value to a smaller equilibrium value. The loss associated with this damping effect is defined by:

$$\eta_{te} = \Delta \frac{f/f_0}{1 + (f/f_0)^2} \quad (4.78)$$

with Δ a factor depending on the physical properties of the material ($\Delta = 0.0046$ for aluminum), f is the frequency of interest and, for a flexure:

$$f_0 = \frac{\pi}{2} \cdot \frac{D}{s^2} \quad (4.79)$$

D being the coefficient of diffusion ($0.84 \times 10^{-4} \text{m}^2/\text{s}$ for aluminum) and s being the thickness of the flexure.

In our experiment, the flexure is mounted between two aluminum masses acting as heat sinks. Therefore, the thermal gradients become complex, and the equation 4.79 for a simple flexure doesn't hold. A structural-thermal model has been done in ANSYS to estimate this damping and compare it to the measurements. We observe a good agreement between the simulation and the experiment, as shown in appendix F, confirming the limitation induced by thermoelastic damping on monolithic experiments.

To compensate this damping, the material used as a flexure is chosen carefully for the final design. We selected fused silica, as the parameters Δ and D for fused silica

are $3.24 \cdot 10^{-6}$ and $6.91 \times 10^{-7} \text{m}^2/\text{s}$ respectively, making the thermoelastic damping $\sim 70,000$ times smaller for a millimeter-sized flexure.

Epoxy distribution, surface quality and flatness

Controlling the average thickness and distribution of epoxy was particularly challenging in early prototypes. To ensure thin homogeneous bonds, asperities need to be avoided and all the surfaces polished.

PZT material fragility

Many iterations were also necessary to overcome difficulty related to the device fragility. These difficulties are due to the heavy masses used to lower the modes below 1000 Hz, which induce high stress in piezoelectric material during transportation, installation and testing process. To avoid overwhelming stress in each sample and assure mechanical stability, we favor three samples instead of one, positioned in a 'triangle' configuration.

Miscellaneous

- Some measurements have been done in both helium (atmospheric pressure) and in low-vacuum. The results obtained were similar than in air at atmospheric pressure, confirming that viscous damping is negligible.
- Contact sensors (accelerometers) and non-contact sensors (capacitive position sensors) were used. Similar results were obtained, confirming that accelerometers don't introduce extra-stiffness or damping to the system.

In conclusion, we defined the following requirements with this series of tests :

- Experiment needs to be suspended (free-free configuration).
- To avoid thermoelastic damping, the flexures used to measure the loss of a thin epoxy layer have to be made of fused silica material.
- To control the thickness and quality of the epoxy layers, surfaces flatness are to be $< 1\mu\text{m}$.
- To mitigate the PZT fragility, three samples are needed instead of one.

- Prototypes confirmed that the whole experiment can be conducted in air with an impact hammer and an accelerometer.

Based on these guidelines, the final design has been constructed and is presented in the next section.

4.5.3 Final design

A sketch of the mechanical oscillator final design is shown in figure 4.18. The material under test consists of three identical samples, each sample being mounted between two aluminum reaction masses. The experiment is suspended by three steel wires that are mechanically fastened to the bottom mass with clamps. Simple suspension clamps are used [151]: they are made of two steel plates bolted to the bottom mass that squeeze the suspension wires. Each plate has a transverse groove where the wire is inserted. In this way, we localize the pressure exerted on the wire to two tangent lines.

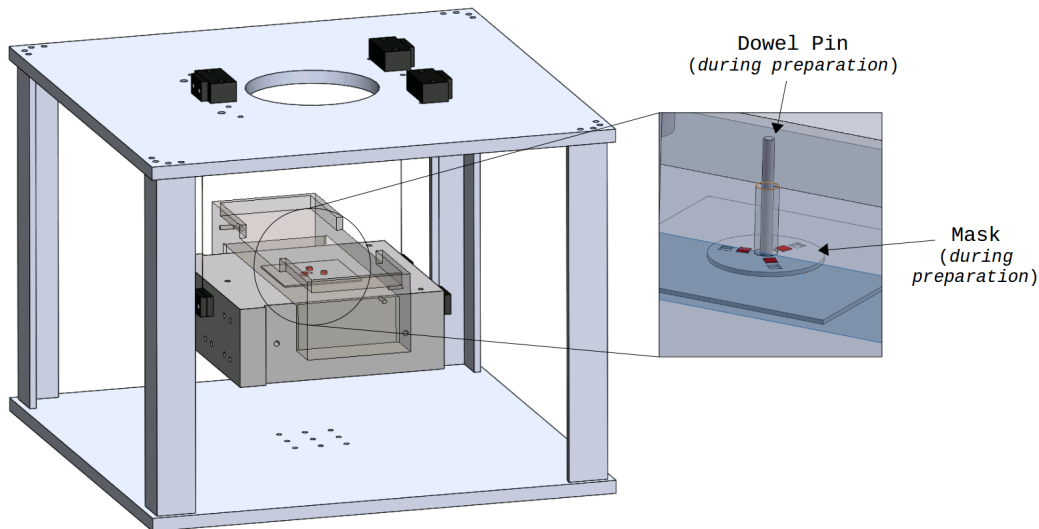


Figure 4.18: Overview of the final design. Three samples, represented in red, are mounted between a bottom aluminum mass (in grey) and a top aluminum mass (slightly transparent for more visibility). The experiment is optimally suspended to operate in a free configuration and therefore avoid dissipation through the joints. The clamps and wires are represented in black. The suspension's cage is clamped to an optic table (not represented here). The location of the samples is controlled by a masked positioned with a dowel pin (both removed after installation).

The size and shape of the masses, as well as the position of the samples are calculated to tune the mechanical oscillator to the desired modal frequencies. The resonant frequencies of the suspension are kept well below the oscillator modal frequencies to avoid suspension to oscillator mode couplings. The full analytical model developed to calculate this tuning is shown in appendix G and [149]. Overall, the oscillator has

been designed to have its first resonant mode around 80Hz, and the highest resonant mode of the suspension below 45Hz. The bottom mass dimensions are 20.3 x 20.3 x 7.6 cm and the U-shaped top mass dimensions are 30.5 x 10.2 x 7.6 cm. The top mass has this peculiar shape to provide a bigger moment of inertia in one horizontal direction than the other. All the parameters are summarized in table 4.6.

Table 4.6: Parameters chosen for the mechanical oscillator and the suspension. Some preliminary tests have been done to measure the quality factors of the suspension. All of them are ~ 1000 . The location d of the samples varies from one experiment to another.

Parameters	Value
Top mass weight m_1 (kg)	2.64
Bottom mass weight m_2 (kg)	8.07
Wire length L (cm)	45
Wire radius (cm)	0.021
Distance d between samples and oscillator's center (cm)	$1 \leq d \leq 8$
Distance h between wires and oscillator's center (cm)	11
Q_{sus} (all modes)	1000

We exploit the first two principal resonances of the oscillator, as the samples strain in shear (mode 1) and compression (mode 2). The modes are shown in figure 4.19.

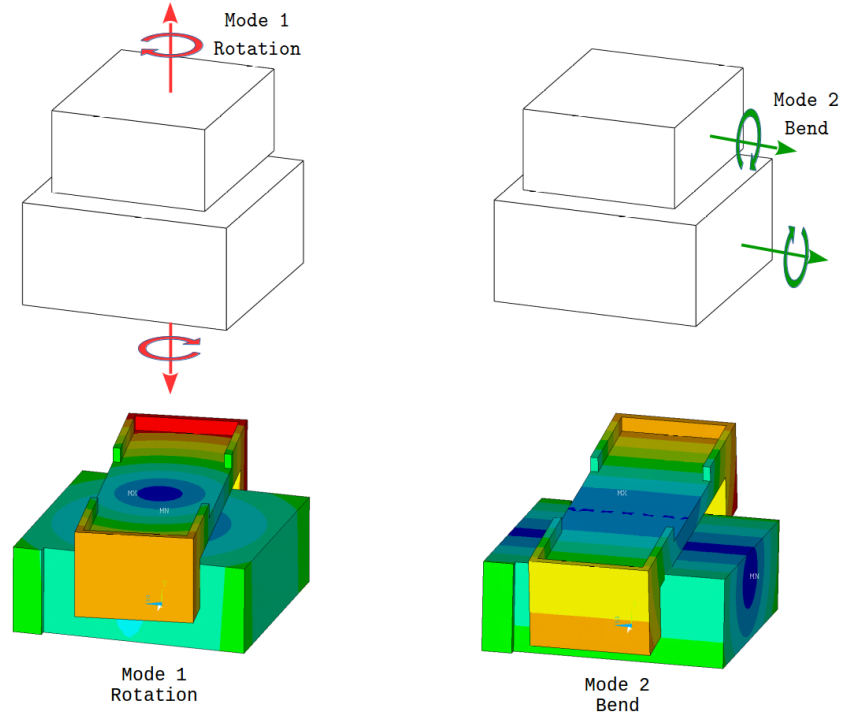


Figure 4.19: Representation of the two principal resonances studied. On the top left are the mode for which the samples work mostly in shear (referred as rotation). On the top right are the mode for which the samples work mostly in compression (referred as bend). From the FEA, the displacement vector sum for each mode is shown at the bottom of the figure.

Three different samples are used with this oscillator, shown in figure 4.20:

1. The bulk loss factor of epoxy is measured as a reference, using millimeter-sized, cylinder-shaped samples (*bottom left image of figure 4.20*).
2. A second series of tests is done with micrometer's layers epoxy, from 1 to 6 micrometers. In this case, thin layers are made between the masses and fused silica cubes (*bottom middle image of figure 4.20*). The size of the cubes are the same than the PZT plates used in the next series of measurements.
3. The loss factor of the PZT plates is measured. The plates are glued to the aluminum masses with $1.2\mu\text{m}$ layers of epoxy, for which the loss factor was measured in step 2 (*bottom right image of figure 4.20*).

The results associated with the different samples listed are presented in the next section.

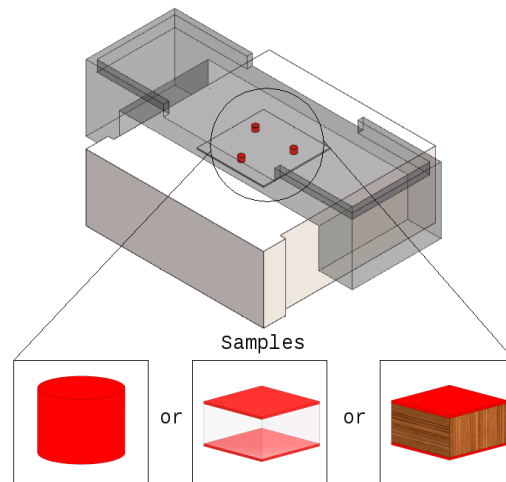


Figure 4.20: Overview of the oscillator without the clamps and wires. Three identical samples are placed between the masses. Three types of samples have been tested: epoxy cylinders, epoxy+fused silica cubes and epoxy+PZT plates.

4.6 Epoxy bulk loss factor

A first batch of samples is made to measure the bulk loss factor of epoxy. All the samples are prepared in the same cylinder-shaped Teflon molds. First, epoxy is stirred by hand with a glass rod in a small beaker, then put in a centrifuge machine to remove trapped air. It is then poured into the molds and cured for 24 hours. After this lapse of time, the samples are glued (using the same epoxy) between the two aluminum masses of the mechanical oscillator. Two different types of mixes are used to make

these samples: some samples are made of pure epoxy (sample #1), while other are mixed with graphite (ratio of 1:0.05 by weight) (sample #2). The samples produced are 6mm in diameter and 8mm in height.

A measurement is conducted for each type of sample, and the quality factors of the oscillator's first two resonances measured. Based on these results and on strain energies from FEA, the loss factor of the epoxy is calculated. For this case however, there is no distinction between the glue and the samples, thus equation 4.77 can be simplified to

$$\eta_{sample} = \frac{E_s/Q - E_{Al}\eta_{Al}}{E_{sample}}. \quad (4.80)$$

The results are summarized in table 4.7.

Table 4.7: Calculation of the epoxy loss factor, based on the measured quality factors and the energy distribution (in percentage) from finite element models.

Samples	Measured freq. [Hz]	Q	E_{sample}	E_{Al}	η_{sample}
#1 (mode 1)	144.0	96.7	98.1%	1.9%	$10.5 \cdot 10^{-3}$
#1 (mode 2)	235.1	101.7	95.7%	4.3%	$10.3 \cdot 10^{-3}$
#2 (mode 1)	113.7	107.3	96.8%	3.2%	$9.62 \cdot 10^{-3}$
#2 (mode 2)	221.1	120.1	86.2%	13.8%	$9.63 \cdot 10^{-3}$

We observe a frequency independent, isotropic loss factor of $10.1 \times 10^{-3} \pm 0.5 \times 10^{-3}$. There is no evidence of loss variations between shear (mode 1) and compression (mode 2). We also notice a slightly lower loss angle ($\sim 7\%$) when the epoxy is mixed with graphite, which might indicate a small change in mechanical properties. It is also worth noticing that it took approximately 8 days for the cured epoxy to reach a steady loss value (see figure 4.21).

4.7 Epoxy thin layer loss

For this second series of tests, we used 3mm x 3mm x 1.5mm height fused silica cubes, where thin epoxy layers mixed with graphite were applied as a bond.³ The cubes are glued by depositing a single drop of epoxy on their surfaces. This process has been done reliably by using a 3cc syringe with a 32 gauge dispense tip. The small tip gives enough precision to deposit epoxy while limiting excess. Ten days of curing are allowed before measurements. During this period, a known pressure

³Only epoxy mixed with graphite has been used for these tests, as it is ultimately what is needed for the AMD.

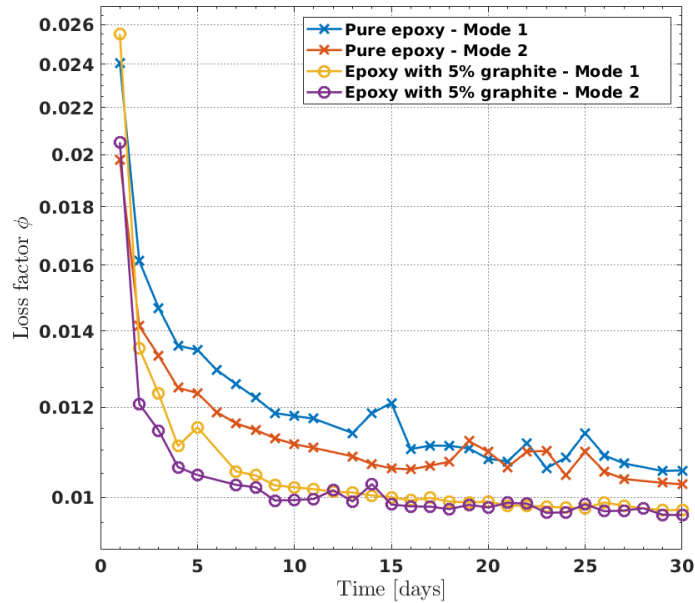


Figure 4.21: Evolution of the epoxy loss factor as a function of time. A measurement has been conducted every 24 hours during one month to monitor the samples properties. The loss factor reaches 95% of its final value after 8 days.

is applied on the oscillator to obtain the wanted thickness of the bonds. Different bond thicknesses have been tried, between 1 and 6 μm . The appropriate pressure was estimated beforehand with the jig used in section 4.4.3. A small quantity of epoxy is dropped between one thick optics and three fused silica cubes, as shown in figure 4.22. The cubes have the same size and arrangement than the samples used for the mechanical oscillator.

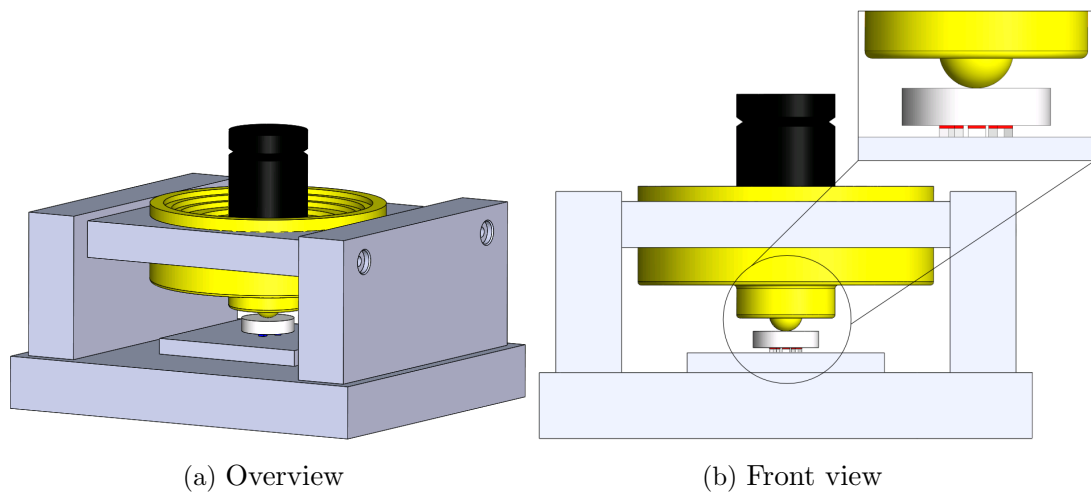


Figure 4.22: Overview of the jig used to calculate the appropriate amount of pressure to apply on the bond. The epoxy layer (in red) is exaggerated for visibility.

The loss factor associated with the epoxy is extracted for each resonant mode using the following equation:

$$\eta_{layer} = \frac{E_{total}/Q_{meas} - E_{Al}\eta_{al} - E_{sil}\eta_{sil}}{E_{layer}} \quad (4.81)$$

where $E_{sil}\eta_{sil}$ is the energy dissipated by the fused silica cubes.

The results of these experiments are summarized in figure 4.23. We observe a direct correlation between the mechanical properties of the epoxy and the thickness of the bond used. The damping measured is inversely proportional to thickness, with a loss factor of $11.7 \times 10^{-3} \pm 1.3 \times 10^{-3}$ for $5.7 \mu\text{m}$ layers to $38.8 \times 10^{-3} \pm 0.5 \times 10^{-3}$ for $1.2 \mu\text{m}$ layers. This behavior is consistent between measurements but stays unexplained. It might be related to frictional energy dissipation arising at the interface (surface loss), but other reasons can not be excluded.

Based on these results, we need to optimize the thickness ϵ to limit energy dissipation ($\frac{\partial(E \cdot \phi)}{\partial \epsilon} \rightarrow 0$). For this reason we choose a bond thickness of $\epsilon = 1.2 \mu\text{m}$ with a loss of 38.8×10^{-3} for the AMD.

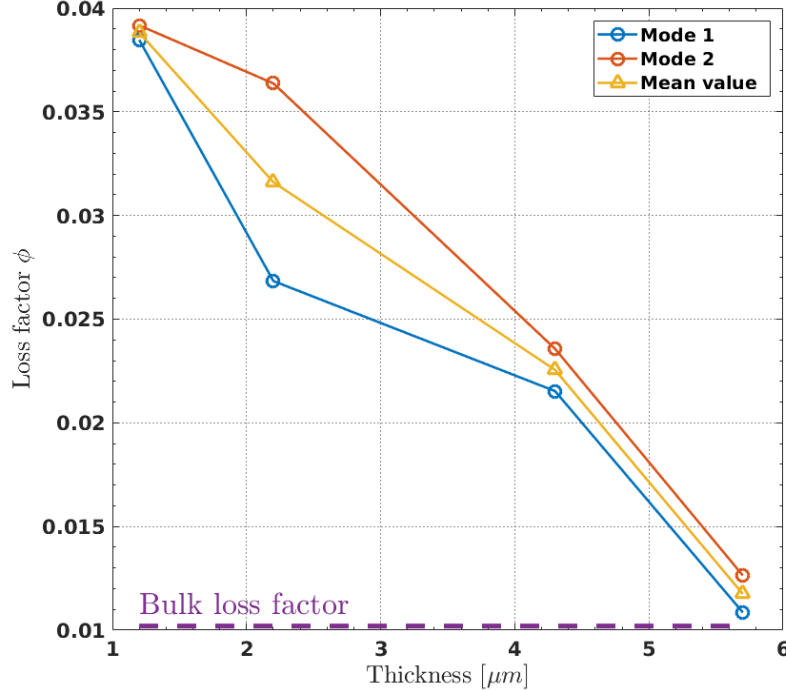


Figure 4.23: Evolution of the measured 302-3M+graphite loss as a function of the bond thickness. Measurements for layers of 5.7, 4.3, 2.2 and $1.2 \mu\text{m}$ have been done. The dash purple line shows the bulk loss of 10.1×10^{-3} as a reference from the previous section.

4.8 Piezoelectric results

PIC181 is a 'hard' PZT, meaning a modified lead zirconate-lead titanate material with a supposedly high mechanical quality factor. The plate is anisotropic due to a poling process (i.e. single direction polarized), and possesses specific crystalline structure called high-symmetry (notated C_∞) [152, 153]. The loss for PZT with C_∞ symmetry is defined by the following matrix [154]:

$$\eta_{PZT} = \begin{bmatrix} \eta_{11} & \eta_{12} & \eta_{13} & 0 & 0 & 0 \\ \eta_{12} & \eta_{11} & \eta_{13} & 0 & 0 & 0 \\ \eta_{13} & \eta_{13} & \eta_{33} & 0 & 0 & 0 \\ 0 & 0 & 0 & \eta_{55} & 0 & 0 \\ 0 & 0 & 0 & 0 & \eta_{55} & 0 \\ 0 & 0 & 0 & 0 & 0 & \eta_{66} \end{bmatrix} \quad (4.82)$$

where the polarization direction corresponds to the "33" direction. Note that in the directions perpendicular to the poling direction, the material is transversely isotropic.

A preliminary FEA has been done to evaluate the AMD behavior around 100Hz (see appendix H). We observed that more than 90% of the PZT plate deformation is in shear, in the laser beam direction (direction "55" for the PZT plate). The ultimate goal is thus to measure the loss η_{55} , the other terms being negligible. However, even if η_{55} is the most important parameter, the mechanical oscillator allows us to easily measure all the diagonal terms of the loss factor matrix. The results will be presented in this section.

3 mm x 3 mm x 1.5 mm PZT plates are used for this series of tests (same size that the fused silica cubes used before). The plates are glued with 1.2 μ m layers of epoxy+graphite, assuming $\eta_{\text{layer}} = 38.8 \times 10^{-3}$ from section 4.7. Each plate is studied under a microscope to ensure surface quality (scratch-free) before gluing. The gluing procedure is identical to the procedure presented in section 4.7. In order to measure all the different loss terms, two types of plate (polarization in shear and compression), as well as three configurations were necessary, summarized in figure 4.24:

1. First configuration (*in red*): three shear plates with polarization towards the center of the oscillator are used. At the rotation mode (mode 1), the samples are strained in the "55" direction (reminder: the polarization direction is always "33"). At the bend mode (mode 2), the samples are strained in the "11" direction.
2. Second configuration (*in green*): three shear plates with polarization about the center of the oscillator are used. At the rotation mode (mode 1), the samples

are strained in the "66" direction.

3. Third configuration (*in blue*): three compression plates are used. At the rotation mode (mode 1), the samples are strained in the "55" direction. At the bend mode (mode 2), the samples are strained in the "33" direction.

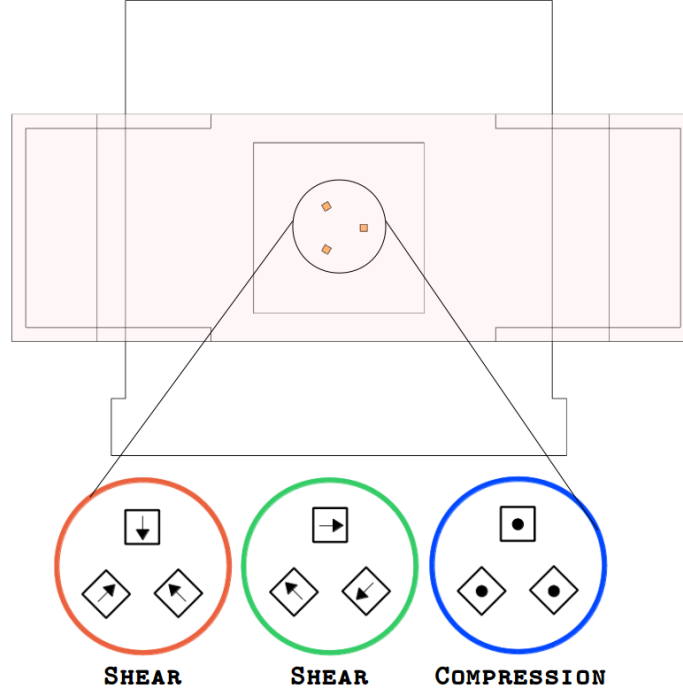


Figure 4.24: Top view of the mechanical oscillator to measure the loss of PZT material. Three different configurations have been considered in order to measure all the terms of η_{PZT} , with two different polarization's plate (shear and compression). The arrows indicate the polarization direction for each plate (the dots indicate a polarization toward the page). The color code for each configuration corresponds to the color in equation 4.82.

During the gluing, the mask and dowel pin shown in figure 4.18 are used to precisely position the samples and avoid cross-coupling between directions. Of course, positioning can not be perfect and residual coupling can not be avoided. However, by assuming that all the diagonal terms have the same order of magnitude (which is fairly realistic for piezo-ceramics materials), the effect is minimized.

For each configuration, a series of measurements have been performed. Each loss term is calculated with the following equation:

$$\eta_{dir} = \frac{E_{total}/Q - E_{Al}\eta_{Al} - E_{layer}\eta_{layer}}{E_{dir}} \quad (4.83)$$

where E_{dir} is the strain energy extracted from the FEA in the direction dir :

$$E_{dir} = \sum_{j=0}^{N_e} \frac{1}{2} V^j \sigma_{dir}^j \epsilon_{dir}^j \quad (4.84)$$

with j the element number and N_e the total number of elements. σ_{dir}^j and ϵ_{dir}^j are the stress and strain of the element j in the direction dir . V^j is the volume of the element.

The results are shown in table 4.8. The different losses have roughly the same order of magnitude, but we observe a substantial standard deviation for each loss measured. To overcome this discrepancy, we decided to use the worst loss factor for all the directions to estimate the performance and the thermal noise of the AMDs in the next sections. This will still give us the 'worst case scenario' and ensure validity of the models. We thus pick $\eta_{PZT} = 1.76 \cdot 10^{-3}$ to calculate the damping performance (see section 4.9.3) and $\eta_{PZT} = 2.79 \cdot 10^{-3}$ to calculate the thermal noise (see section 4.9.4).

Table 4.8: Measured loss factors for PZT material.

η_{PZT}	Value
η_{11}	$2.07 \times 10^{-3} \pm 1.0 \times 10^{-3}$
η_{33}	$2.09 \times 10^{-3} \pm 1.0 \times 10^{-3}$
η_{55}	$1.76 \times 10^{-3} \pm 1.1 \times 10^{-3}$
η_{66}	$2.79 \times 10^{-3} \pm 0.8 \times 10^{-3}$

4.9 AMD model

In the previous section, we have determined the characteristics associated with each material for the AMD. Based on these results, a final design has been developed. The challenge of the design was to achieve broadband Q-factor reduction in [10-80] kHz band, while limiting noise in the [10-5000] Hz band. Several models and iterations have been tried. It is worth mentioning that an early AMD model was made with three PZT plates instead of one. By having the three plates polarized in different directions, the damping of this device was efficiently covering many mechanical modes. Unfortunately, it was bringing the total noise of LIGO up by $\sim 25\%$. To keep the thermal noise low and achieve good damping performance, four different AMDs per test mass (and a single plate per AMD) are required, with the plates polarized in the non-beam direction, as previously presented in section 4.4.1.

4.9.1 AMDs designs

The designs of AMD1, AMD2, AMD3 and AMD4 are very similar, the only differences being the resistors used (see section 4.4.2) and the reaction masses (RMs). The base is a fused silica cylinder, 5 mm dia. x 4 mm height (0.16 gm), with the top face gold coated for electrical conductivity (several hundred nanometers thick film). The PZT plate is a 3 mm x 3 mm x 1.5 mm height polarized in shear with a mass of 0.11gm. The RMs are 6061-T6 aluminum masses, slightly different in sizes to target different frequency bands, as shown in figure 4.25 (the full list of resonance frequencies from modal analysis is shown in appendix I). Each RM is asymmetric to avoid degenerate modes, as shown in figure 4.26. The orientation of the RMs compared to the polarization of the PZT plate is shown in figure 4.27. The masses are lapped to ensure an homogeneous bond and gold coated for ease of electrical connection (soldering).

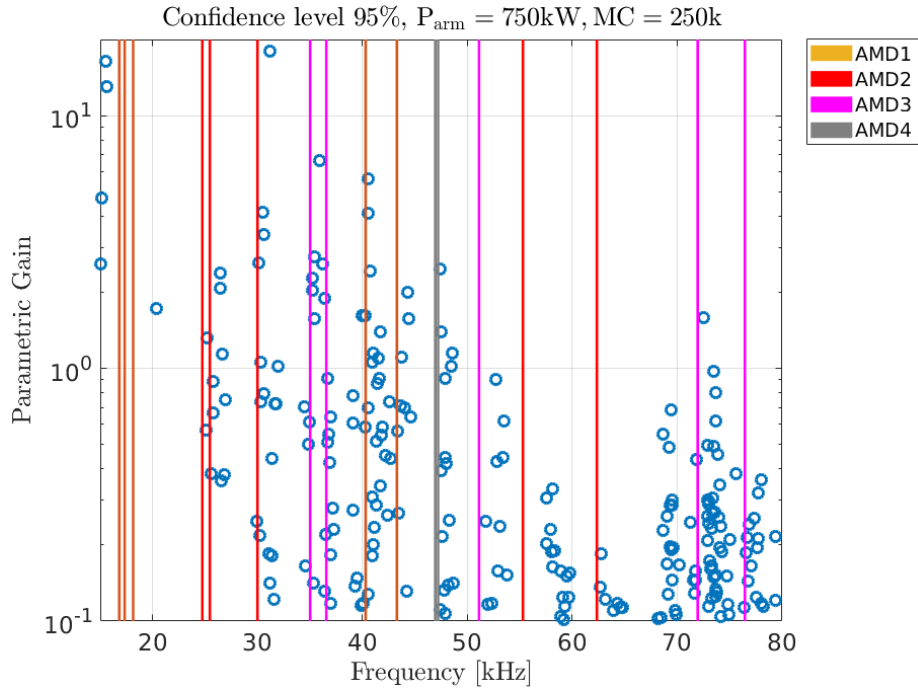


Figure 4.25: Principal resonances of the AMDs from modal analysis as a function of the calculated parametric gains from section 4.2.2. Only the resonances for which most of the energy is in the PZT plate in the polarization direction are shown. AMDs have been tuned to target the problematic modes and cover the entire frequency band from 10kHz to 80kHz. The list of resonances is shown in appendix I.

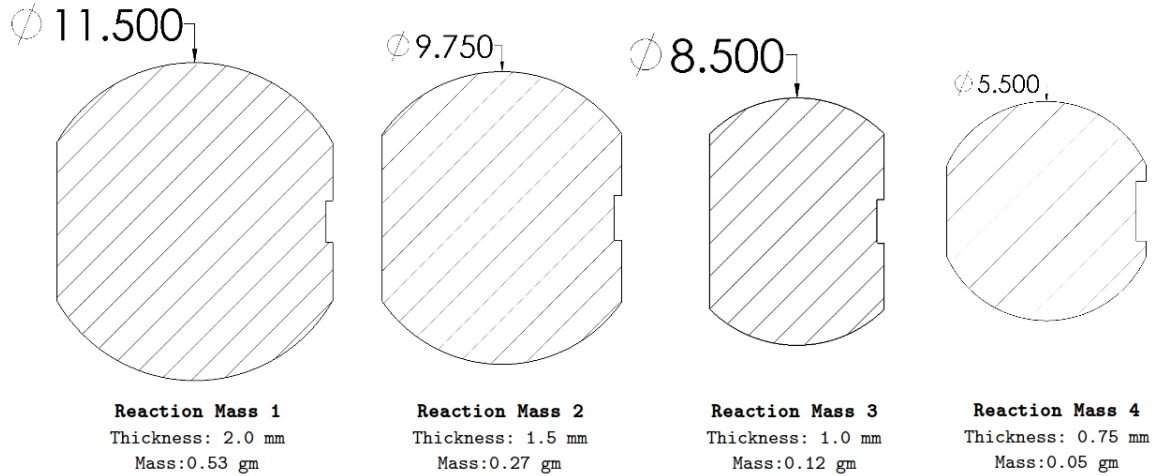


Figure 4.26: Dimensions of the different reaction masses (units in mm). The little cut on the side of each RM is the designated location for the resistor. Not to scale.

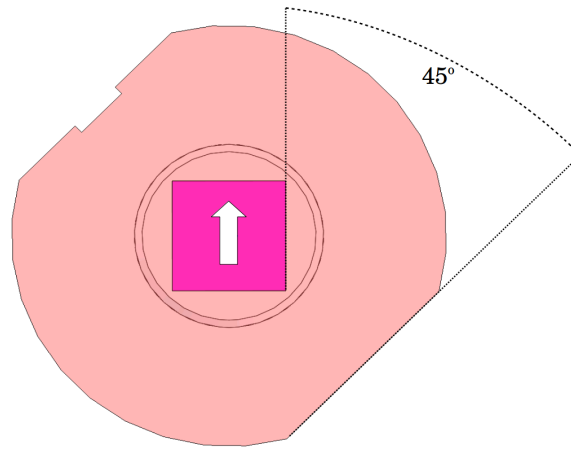


Figure 4.27: Orientation of the RM (*transparent red*) with respect to the PZT plate (*pink*). The polarization of the plate is represented by the white arrow. The RM's flat parts are turned 45° compared to the polarization direction. This is true for all the AMDs.

4.9.2 Location

The total mass of AMD1, 2, 3 and 4 is 0.80gm, 0.54gm, 0.39gm and 0.32gm respectively. To keep the test mass balanced, AMD1 and AMD4 will be mounted on one of the test mass flat and AMD2 and AMD3 on the other. By doing so, we are introducing a negligible asymmetry in the mass distribution of ~ 0.2 gm. However, each flat has limited available space and access. Figure 4.28 shows the quadruple LIGO suspension with its cage and hardware. Only three areas have been identified at potentially accessible to install AMDs on the flat, marked in figure 4.29. Area 3 is close to the ring heater, which might introduce some unwanted thermal coupling with the AMD. Between area 1 & 2, area 1 seems the more accessible and is selected to install the AMDs. Chosen locations for the four AMDs are shown in figure 4.30. With this

configuration, the center of mass of the test mass will shift by less than a micron in the three translational directions. The installation procedure and jig is presented in section 4.10.

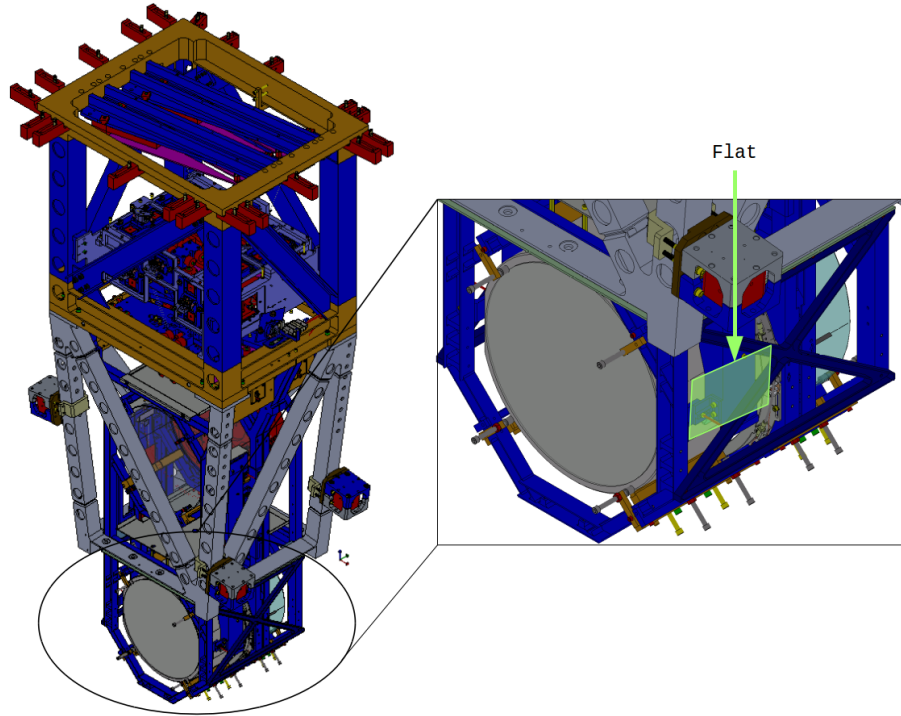


Figure 4.28: Overview of the AdvLIGO BSC5-L1 SolidWorks model. The full quadruple suspension with its cage and hardware is represented. On the right is a zoom on the test mass, where one of the flat is highlighted.

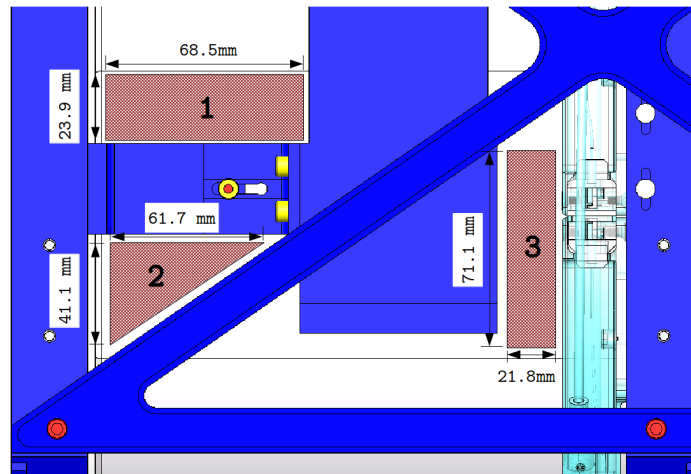


Figure 4.29: View of one of the test mass flats. Three different areas on the flat have been identified to locate the AMDs. Areas 1 & 2 are close to the front face, while area 3 is next to the ring heater (represented in transparent cyan).

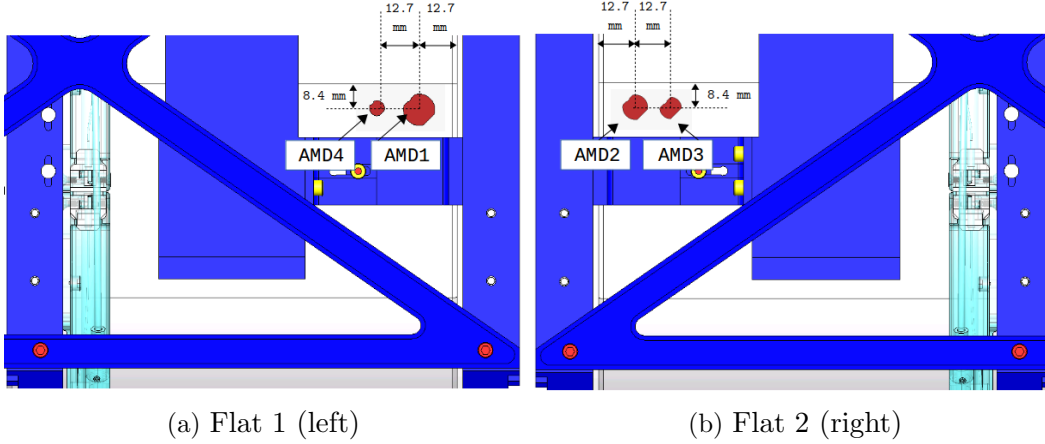


Figure 4.30: Suggestion for the location of the AMDs on the flats. *Right* and *left* locations are defined with respect to the front face.

4.9.3 Performance against PI

A modal analysis has been done to evaluate the damping efficiency of the AMDs. The model computed is shown in figure 4.31. By looking at the strain energy distribution, we can estimate the effective quality factor Q_{eff} for each mechanical mode:

$$Q_{eff} = \frac{E_{total}}{E_{TM} \cdot \eta_{TM} + E_{AMD} \cdot \eta_{AMD}} \quad (4.85)$$

where

$$E_{AMD} \cdot \eta_{AMD} = E_{shunt} \cdot \eta_{shunt} + E_{PZT} \cdot \eta_{PZT} + E_{RM} \cdot \eta_{RM} + E_{base} \cdot \eta_{base} + E_{layer} \cdot \eta_{layer}. \quad (4.86)$$

Note that even if the loss factors η_{PZT} and η_{layer} have been measured around 100Hz, we used the same values to estimate the performance between [10-80] kHz. Since most of the damping is due to the shunt in this frequency bandwidth, the error made on the overall performance is minimized. For η_{TM} , we used the loss factors calculated from the prior modal analysis presented in section 4.2.1.

The computed new Q_{eff} are shown in figure 4.32. Based on these new values, we can re-calculate the maximum parametric gains for the potential unstable modes at full power (figure 4.33).

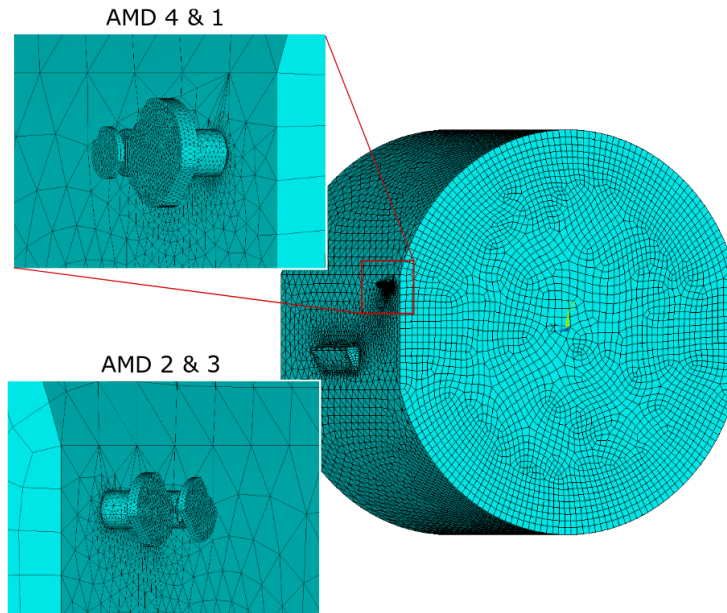


Figure 4.31: Overview of the FEA model of the ETM mirror with four AMDs. AMD 2 and 3 are placed on the opposite suspension flat at the same location as AMD 1 and 4.

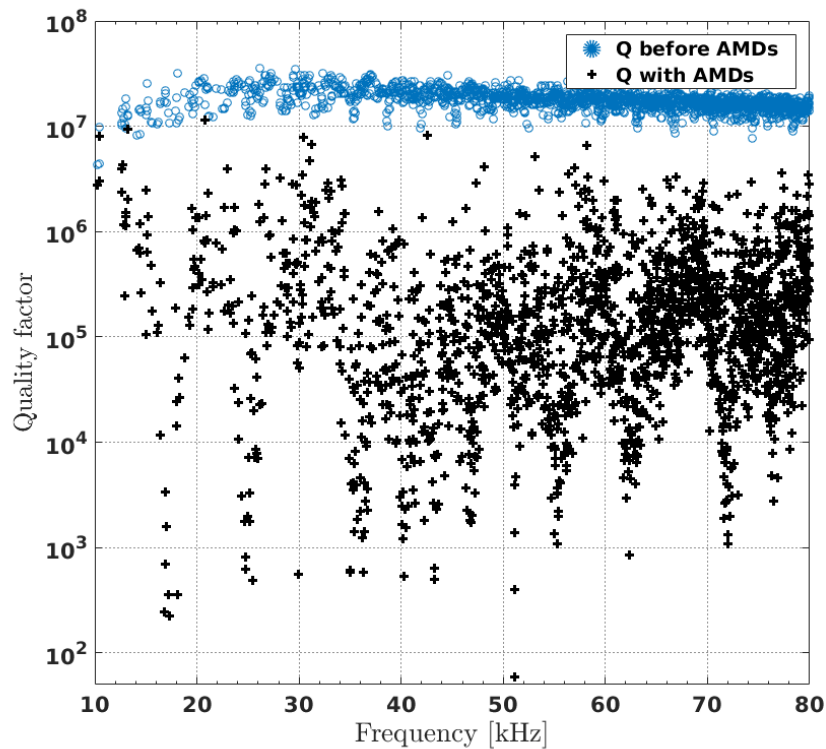


Figure 4.32: Quality factors between 10kHz and 80kHz, before and after installing 4 AMDs on the test mass (simulation).

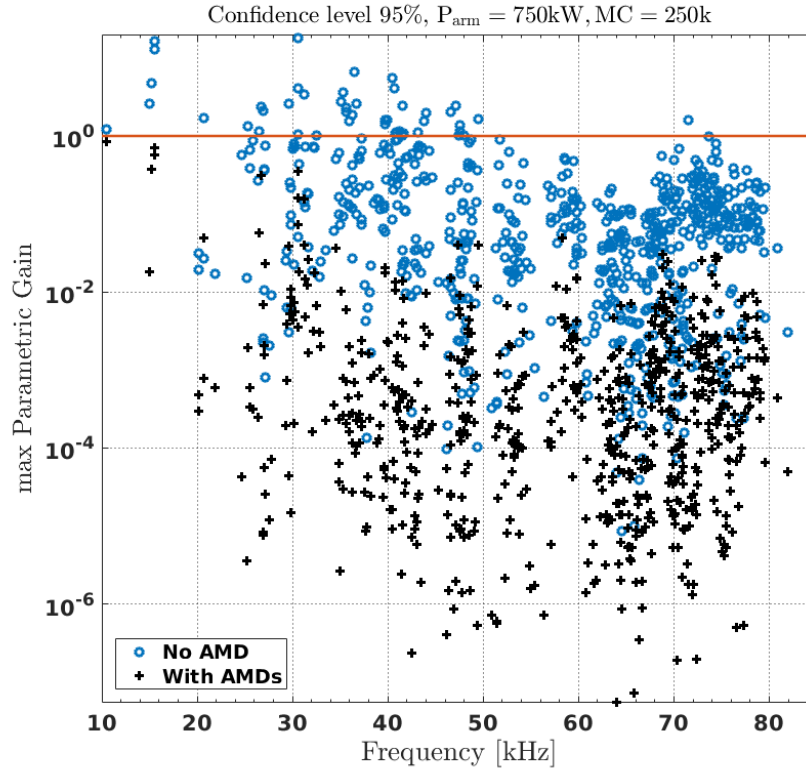


Figure 4.33: Comparison between the maximum estimated parametric gains at full Advanced LIGO power without the AMDs (*blue dots*) and with the four AMDs on the test mass (*black plus*). Overall, 100% of the parametric gains are reduced, with no gain remaining above 1 (out of 47 without the AMDs).

Overall, the results suggest that:

- 100% of the mechanical modes of the test mass are damped.
- the AMDs are very efficient in the most problematic bandwidth [20kHz - 50kHz].
- More than 94% of the mechanical modes' nominal Q-factors are suppressed by a factor larger than 10.
- According to this simulation, no remaining mechanical mode will be associated with a parametric gain exceeding 1. For example, the biggest PI during O1 (around $\sim 15\text{kHz}$ and $\sim 15.5\text{kHz}$) will become stable, with an estimated maximum parametric gain of 0.02 and 0.71 respectively.

4.9.4 AMD thermal noise

As introduced in chapter 2, Brownian thermal noise is generated by thermally induced fluctuations in a material. If we take the example of a LIGO test mass, these fluctuations introduce phase shift in the reflected laser beam of the IFO because of the test mass surface motion. According to the generalized fluctuation-dissipation theorem [57], the spectral density of the fluctuations for each test mass at a frequency f and a temperature T is given by the formula

$$S(f) = \frac{k_B T}{\pi^2 f^2} |\Re[Y(f)]| \quad (4.87)$$

where k_b is the Boltzman's constant and $Y(f)$ is the complex admittance of the test mass, associated with its displacement along the arm cavity.

Based on this general definition, Levin [58] demonstrates that $|\Re[Y(f)]|$ is proportional to the mechanical dissipation in the test mass W_{diss} , which is defined by

$$|\Re[Y(f)]| = 2 \cdot \frac{W_{diss}}{F_0^2} = 4\pi f \cdot \frac{E_{TM} \cdot \eta_{TM}(f)}{F_0^2} \quad (4.88)$$

with F_0 the amplitude of the oscillating force applied to the surface (i.e. the pressure integrated over the surface), E_{TM} the maximum strain energy stored in the test mass at the frequency f and $\eta_{TM}(f)$ its frequency dependent loss factor. Therefore, the thermal noise of a LIGO test mass can expressed as

$$S_{TM}(f) = \frac{4k_B T}{\pi f} \cdot \frac{E_{TM} \eta_{TM}(f)}{F_0^2}. \quad (4.89)$$

To estimate the total thermal noise of the test mass with AMDs, we can derive equation 4.89:

$$S(f) = S_{TM}(f) + S_{AMD1}(f) + S_{AMD2}(f) + S_{AMD3}(f) + S_{AMD4}(f) \quad (4.90)$$

with

$$S_{AMD}(f) = \frac{4k_B T}{\pi f} \cdot E_{AMD} \eta_{AMD}. \quad (4.91)$$

The definition of $E_{AMD}\eta_{AMD}$ is given in equation 4.86.

To do this calculation, we make an harmonic analysis at 100Hz, in which a pressure is applied on the test mass surface, as shown in figure 4.34. This pressure has the same spatial distribution as the LIGO laser beam intensity profile. The pressure is normalized so that $F_0 = 1$.

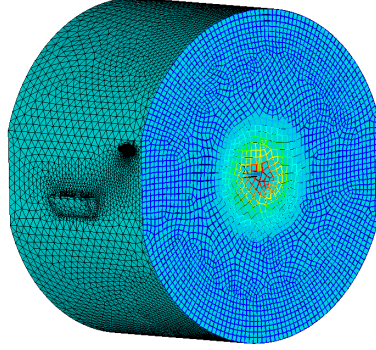


Figure 4.34: Overview of the ANSYS harmonic analysis done to estimate the new thermal noise of the AMDs. The color map on the front face corresponds to the profile of the applied pressure. It mimics the carrier laser beam profile, centered on the test mass with a waist of 62mm.

The details of the AMD thermal noise for each material is shown in table 4.9 and figure 4.35. The total thermal noise of four AMDs is $11.62 \times 10^{-22} \text{m}/\sqrt{\text{Hz}}$ at 100Hz. Knowing that we have four test masses per IFO (i.e. 16 AMDs total), this corresponds to a total noise of $23.24 \times 10^{-22} \text{m}/\sqrt{\text{Hz}}$ at 100Hz. This value is extrapolated over the whole LIGO detection range and added to the Advanced LIGO noise budget presented in section 2.4, figure 2.13. We observed a maximum increase of the total LIGO noise by 1.18% at 61Hz, as shown in figure 4.36.

Table 4.9: Details of the thermal noise contribution for each material at 100Hz. The worst measured value has been taken for the loss factor of the PZT plates.

	Thermal noise at 100Hz [$\times 10^{-22} \text{m}/\sqrt{\text{Hz}}$]				Loss factor used
	AMD1	AMD2	AMD3	AMD4	
Base	0.19	0.12	0.07	0.06	1.00×10^{-6}
RM	0.50	0.23	0.10	0.03	1.00×10^{-4}
Epoxy between:					
TM & Base	6.52	4.19	3.00	2.46	38.8×10^{-3}
Base & PZT	4.16	2.24	1.21	0.73	
PZT & RM	2.49	1.23	0.54	0.2	
PZT mechanical	4.48	2.31	1.16	0.62	2.79×10^{-3}
PZT shunt	0.031	0.009	0.011	0.003	see table 4.4
Total AMD	9.30	5.43	3.48	2.65	
Total noise for 1 TM \rightarrow 11.62					

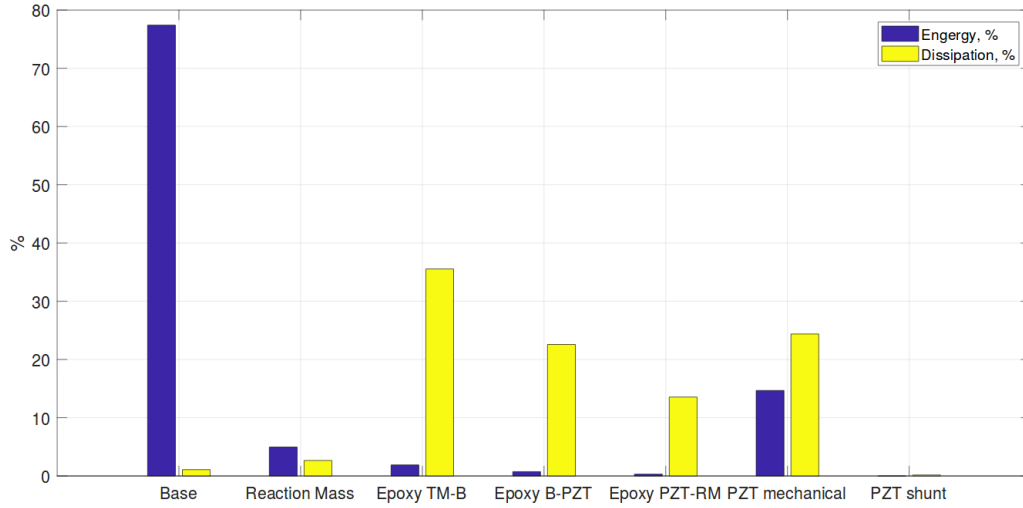


Figure 4.35: Energy dissipation in AMD1 at 100Hz. Note that the most energy is concentrated in the AMD base but the largest amount of energy is dissipated in the epoxy layer between the test mass and the base. The shunt has insignificant energy dissipation and thus insignificant contribution to thermal noise degradation of the mirror.

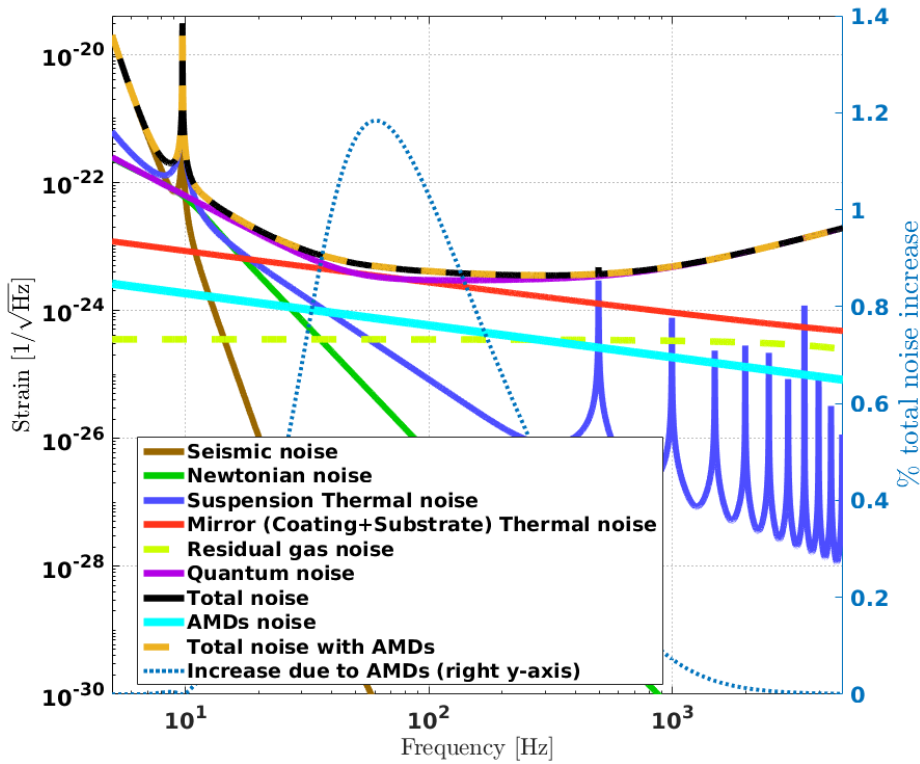


Figure 4.36: The thermal noise associated with 16 AMDs (4 per test mass) corresponds to the thick cyan line. The total noise with the AMDs is plotted in orange (dash line). The blue dot line, corresponding to the right y-axis, shows the excess on the total noise in percent as a result of adding 16 AMDs.

4.10 Installation

Overall, the AMDs present very promising performance while having an acceptable noise impact on the LIGO detection frequency band. The decision was therefore made to move on with installation. However, AMDs require to be installed directly on the test mass *in situ*, which is a risky operation, as human activity happens in an ultra-clean environment close to the glass suspended fibers.

The second observing run (O2) of LIGO took place from November 30, 2016 to August 25, 2017. After this period of observation and before the next run, a series of upgrades were planned [155]. One major update included the replacement of all ETM mirrors at both sites with new mirrors. The new test masses have optimized coating layers for light transmission, which should help the IFOs sensitivity in the future.

The first installation of AMDs has been done at Livingston in March 2018 on the X-arm ETM mirror. The motivation was to test the installation procedure, performance and noise degradation of the AMDs before the mirror swap. In this section, we will present the AMD assembly procedure, as well as the jig designed to install the four AMDs in chamber. We will then analyze the measured performance and thermal noise of the AMDs in the next section.

4.10.1 AMD assembly

A total of 12 AMDs have been made for the installation (4 main AMDs plus spares). All the AMD parts and tools used for the assembly were cleaned following LIGO vacuum requirements [156, 157] before use. The procedure is identical for each AMD.

1. Base and PZT bond

The AMD base and the PZT plate are bonded together with a drop of 302-3M epoxy mixed with graphite. The precision jig presented in figure 4.37 is used to properly centered the PZT plate on the base, with a maximum misalignment of $50\mu\text{m}$. A 24h-curing period is allowed to obtain a strong bond. During that curing period, a pressure of 55MPa is applied using the jig presented previously in section 4.7, figure 4.16. To ensure a bond thickness of $1.2\mu\text{m}$, we measure the parts before and after gluing with a sub-micrometer.

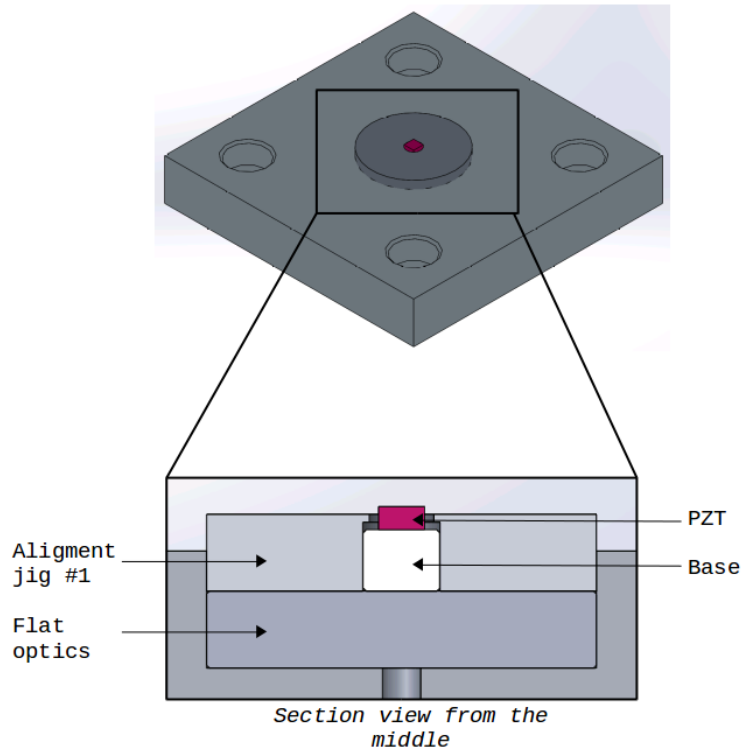


Figure 4.37: Overview of the alignment jig used to glue the PZT to the base. The base is sitting on a flat optics, which is embedded in the alignment jig. The jig has two different diameter holes, one to fit the base, one to fit the PZT plate.

2. Wire soldering

Each AMD requires 5-6 mm long wire in order to connect PZT electrodes with the resistor. The wire is made of hard tempered copper plated with $2.5 \mu\text{m}$ of gold. The diameter of this wire is $25 \mu\text{m}$. It is soldered to the base using an indium/silver based solder, which is the most adequate for soldering to gold (indium-based solders are known to cause appreciably less scavenging damage to gold compared to tin-based solders).

The amount of solder is kept to necessary minimum. The soldering is done manually by depositing a tiny amount of solder to the surface of the base, as well as to the wire's tip with a soldering gun. The tip of the wire is then put in the solder of the base with some pressure until melted to create the joint. During this process, one person holds the base with tweezers while the other applied pressure with a soldering gun on the indium-coated wire to the surface. Pictures of the final result is shown in figure 4.38.

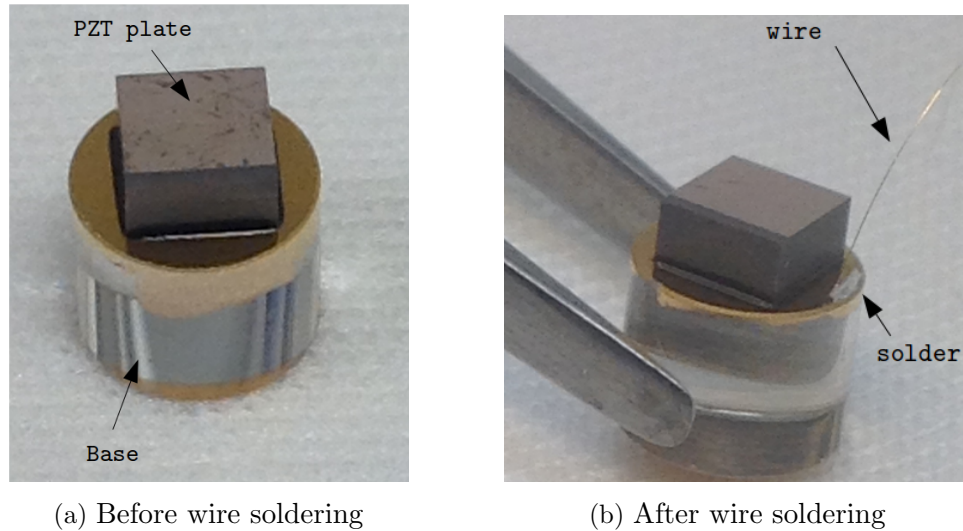


Figure 4.38: Pictures of the Base+PZT assembly without the wire soldered to the base (*left*) and with the wire soldered (*right*). The black rim around the PZT plate corresponds to a slight excess in epoxy.

3. Resistor soldering

A similar process is done to solder the resistor to the RM. Solder is pre-applied on the RM until melted. The resistor is then pushed into its designed slot.

4. Reaction mass and PZT bond

The RM is glued to the PZT plate with a drop of epoxy mixed with graphite. The same procedure than the base-to-pzt bond is applied. The precision jig used is shown in figure 4.39. It assures that the RM is centered on the PZT, but also that the RM is oriented properly with respect to the PZT polarization.

5. Wire to resistor soldering

Finally, the hanging tip of the wire is soldered to resistor. The fully assembled AMDs are shown in figure 4.44. After assembly, all AMDs have been vacuum-baked at 120°C for 48 hrs, and then pass a residual gas scan.

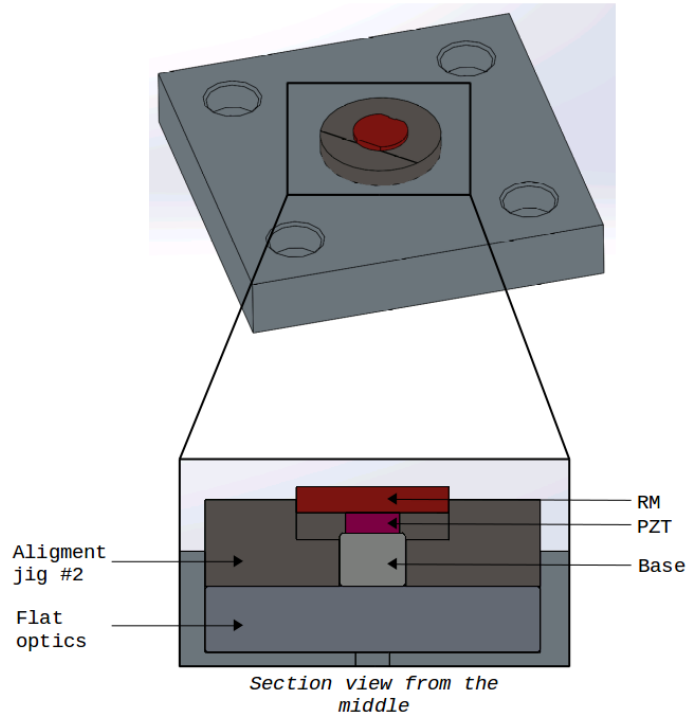
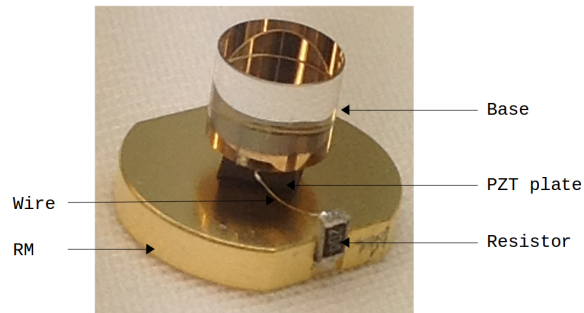


Figure 4.39: Overview of the alignment jig used to glue the RM to the PZT. On a flat optics is sitting the base, embedded in the alignment jig. The jig has two different diameter holes, one to fit the base, one to fit the RM (a different jig is require for each AMD.). On top of the jig is a groove to align the RM with regards to the PZT plate.



(a) AMD1



(b) Overview of the four AMDs

Figure 4.40: Pictures of the fully assembled AMD1, AMD2, AMD3 and AMD4 (in that order).

6. Testing

The resistivity and capacitance of the resistor and PZT plate have been checked for every AMD. This confirms the good conductivity of the assembly, as well as the health of the PZT plate and resistor after the vacuum bake.

7. Extra tests

The purpose of these tests is to confirm the good agreement between the model and the actual device. Extra AMDs have been assembled without the wire and resistor, and their resonance frequencies have been measured. The measurements have been done using the self-sensing actuation technique [158, 159]. It consists of a capacitance Wheatstone bridge circuit which allows to use the PZT plate simultaneously as a sensor and an actuator, as shown in figure 4.41. This simple circuit was enough to obtain decent transfer functions of the AMDs. The connection to the PZT electrodes was made by soldering a wire to the top of the base and to the top of the RM.

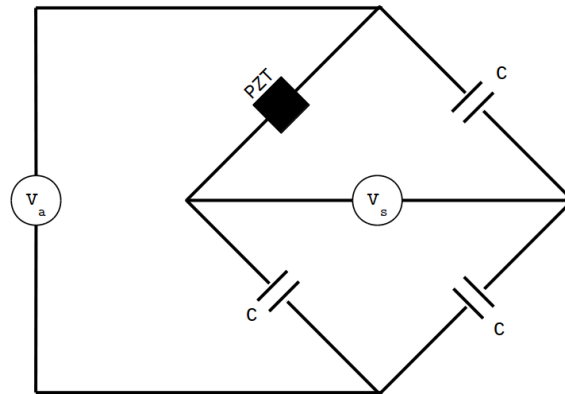


Figure 4.41: Simple self-sensing bridge applied to PZT. If C matches the capacity of the PZT, the resulting signal voltage V_s is independent from the control voltage V_a , and only proportional to the voltage generated by the PZT plate under stress.

A first series of test is done with the AMD in a free configuration (i.e. not clamped nor glued). This is a sanity test to verify the quality of the assembly. For the second series of test, the AMD is glued with epoxy 302-3M to a 100mm diameter x 40 mm height optics. Even if this optics is smaller than a LIGO test mass, the mass ratio between the AMD and the optics is big. The goal of this configuration is thus to simulate the clamped configuration of the AMD on the test mass, and check the viability of the AMD modes calculated and presented in figure 4.25. In both cases, we observe a good agreement between the model and measurements, as shown in table 4.10.

Table 4.10: Comparison between the FEA and the measured values of the AMDs modes in free and clamped configurations. The values marked as 'NA' refer to frequencies above 100kHz, which were not measured.

	Mode	Free		Clamped	
		FEA [kHz]	Measured [kHz]	FEA [kHz]	Measured [kHz]
AMD 1	Flag 1	58.3	56.9	16.8	17.0
	Flag 2	61.0	59.6	17.3	17.6
	Rotation	80.5	78.3	18.1	18.1
	Anti-flag 1	166	NA	40.3	39.9
	Anti-flag 2	170	NA	43.3	42.6
AMD 2	Flag 1	69.6	68.5	24.7	24.6
	Flag 2	76.6	75.3	25.5	25.3
	Rotation	85.4	82.6	30.0	29.9
	Anti-flag 1	171	NA	55.3	53.8
	Anti-flag 2	184	NA	62.3	60.8
AMD 3	Flag 1	82.6	83.6	35.0	36.1
	Flag 2	98.6	94.4	36.4	36.7
	Rotation	99.1	NA	51.1	50.3
	Anti-flag 1	182	NA	72.0	69.3
	Anti-flag 2	209	NA	76.5	71.7
AMD 4	Flag 1	NA	NA	46.9	47.0
	Flag 2	NA	NA	47.2	47.7

4.10.2 Installation jig

An installation jig has been designed and made to properly install the four AMDs at the desired locations on the test mass. The goal of this jig is also to apply the proper amount of force during the 24h-curing time of the bond. Note that the epoxy 302-3M doesn't have to be mixed with graphite in this case, as there is no need for conductivity. Therefore, the required force has been estimated using the method described in 4.4.3. In previous experiments, we applied a big force, knowing that the final thickness will be dictated by the graphite particles size. In this case however, it is important to precisely estimate the amount of force needed, as we don't want to apply too much force on the test mass and risk damage. The minimum estimated force to obtain a bond thickness of pure epoxy under $1.5\mu\text{m}$ is 2.5N.

The jig is made to install one AMD at a time. It is attached to the cage of the quadruple suspension with a cross-bar, as shown in figure 4.42. The cross-bar is marked with graduations to align it to the desired location. It supports an horizontal translation stage, which goal is to make the first contact between the AMD and the flat. To establish a proper contact, it compresses a soft spring by 5mm with very little force (low stiffness). Once this is done, a micrometer head comes into play to exert force via another stiffer spring. This second spring has a stiffness of 500N/m and is compressed by 5mm in order to apply the required force.

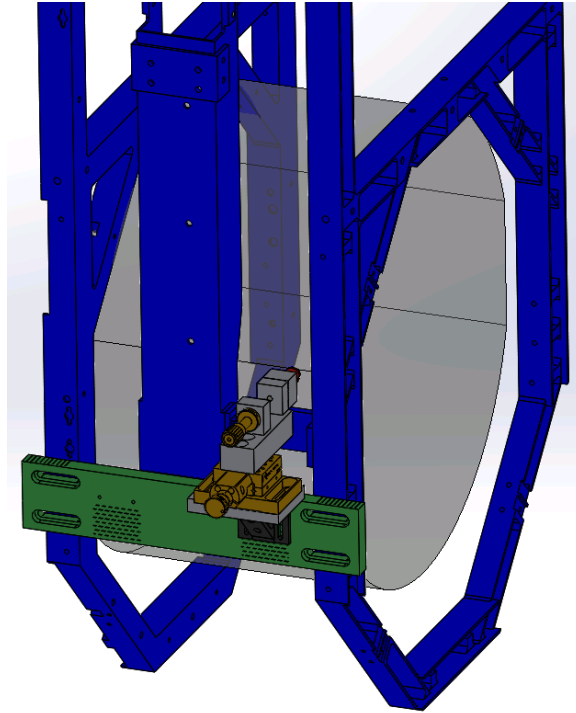


Figure 4.42: Overview of the AMD installation jig. The test mass is shown in transparent and the suspension's cage in blue. The hardware is not shown for clarity. The jig cross-bar (in green) can slide horizontally for adjustment. The angle bracket (in black) supporting the rest of the jig can slide vertically.

The AMD is attached to the tip of the jig by suction. A small pins holds a suction cup which, once pushed onto the RM top surface, will hold vacuum for at least 20 minutes (which is enough time for installation). The AMD is oriented properly before this step (using the jig shown in figure 4.43) to ensure that the PZT polarization is in the good direction (i.e. perpendicular to the laser beam direction). Once the AMD hangs, a drop of epoxy is deposit on the base's surface. Due to surface tension, the drop stays in place without trouble, and contact between the AMD and the flat can be made easily using the horizontal translation stage. This gluing process is summarized in figure 4.44.

The four AMDs were installed at L1 on the ETMX mirror without trouble. The mounting of the jigs went well and the correct amount of pressure has been applied to each AMD. However, we observed a tiny rim of epoxy around the AMD base (which indicates a homogeneous bond) only for AMD1, AMD3 and AMD4. It turns out that a small particle of dust got trapped in the AMD2 bond with the test mass. This underline that extreme vigilance is necessary during this installation. Pictures of the AMDs on the test mass are shown in figure 4.45.

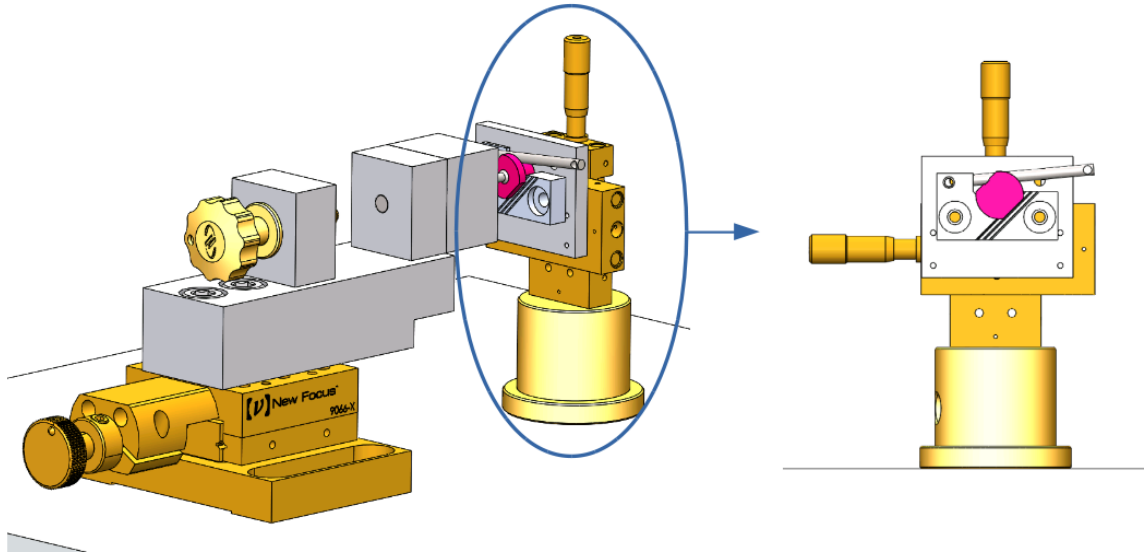
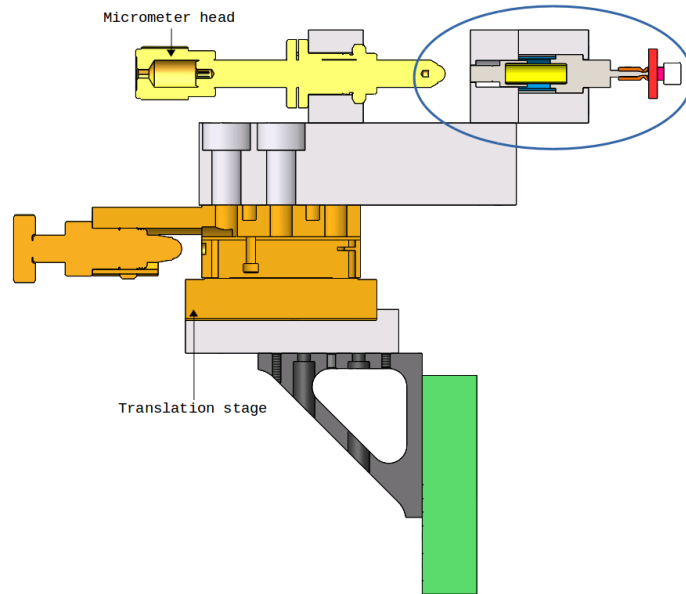
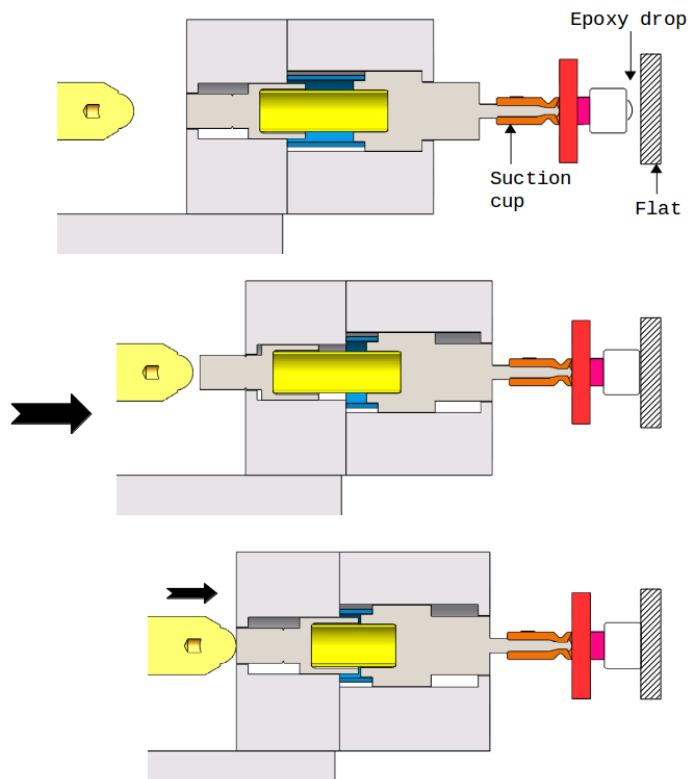


Figure 4.43: Overview of the AMD alignment jig. Before being installed, the AMD is oriented properly using the jig circled in blue and shown to the right. The RM (in pink) is oriented properly using the slanted marks of the jig. The AMD is then grabbed via a suction cup and the jig is transferred to the cross-bar installed on the quadruple suspension.



(a) Side cut view of the installation jig



(b) Three steps gluing process on the optics flat

Figure 4.44: The side cut view of the overall installation jig is shown at the top. The zone circled in blue is shown in more details at the bottom, with the different gluing steps. The soft spring is shown in blue and the stiff spring in yellow.

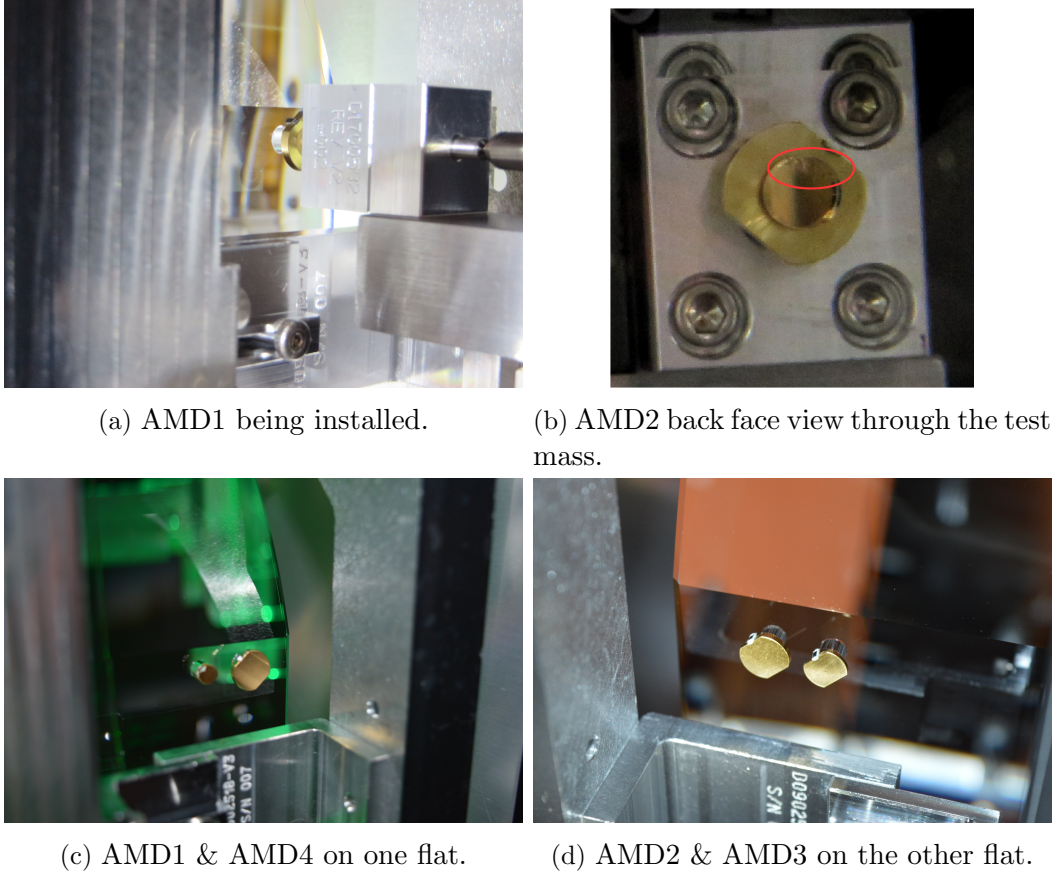


Figure 4.45: Pictures of the AMDs on the test mass during and after installation. Top right picture, we see some irregularities in the AMD2 bond due to a dust particle (circled in red).

4.11 Results

After the installation, a series of tests has been done to estimate the performance of the AMDs in terms of Q reduction of the test mass modes and noise degradation of the detector sensitivity.

4.11.1 AMDs performance

The quality factors Q_m of the different test mass modes have been measured prior to the AMDs installation. To do this measurement, the mirror is excited with the ESD while the IFO is locked. The quality factors can then be extracted by looking at the IFO output signal from the output photodiode. However, due to the increase of mode density with frequency, it is hard to identify the different mechanical modes above 30kHz. Therefore, it was possible to characterize only a limited numbers of modes.

The same measurement has been repeated after the AMDs installation. All the results are summarized in table 4.11 and figure 4.46. As expected, we observe a reduction of the quality factors for all the measured modes, with a reduction in agreement with our model within a factor of 2 on average. The biggest discrepancy between the measurement and the model is observed for the modes above 18kHz (mode #13 and above). According to our design, the Q reduction for modes in the [20kHz-30kHz] frequency bandwidth is mostly due to AMD2 damping. Because of the dust spotted between the test mass and base of AMD2 during installation, we suspect that the boundary conditions have changed and the resonance frequencies of AMD2 shifted, which would explain this important mismatch between model and experiment.

Table 4.11: List of the quality factors measured before and after AMDs installation. The last column corresponds at the corresponding quality factors calculated with the model presented in the previous section. The quality factors marked as 'NA' were too small to measure.

Mode #	Freq. [Hz]	Without AMDs		With AMDs	
		Measured Q [$\times 10^6$]	Measured Q [$\times 10^6$]	Model [$\times 10^6$]	Model [$\times 10^6$]
1	5948	29.3	19.1	15.56	
2	8158	20.2	16.7	8.19	
3	9101	21.8	11.8	6.75	
4	9338	27.6	3.55	2.13	
5	9827	26.9	18.9	12.03	
6	9878	15.7	7.73	9.97	
7	10216	21.2	8.03	5.8	
8	10424	33.3	22.8	7.54	
9	15006	59.3	2.39	2.91	
10	15071	11.4	0.45	0.63	
11	15538	27.1	1.05	0.49	
12	15630	20.6	0.11	0.18	
13	18001	4.65	0.134	0.025	
14	22662	29.1	NA	0.39	
15	22969	0.73	NA	0.42	
16	23049	10.9	NA	0.087	
17	23222	0.62	NA	0.056	
18	38106	9.5	0.019	0.012	
19	47468	2.3	0.03	0.006	
20	47485	5.3	0.041	0.029	

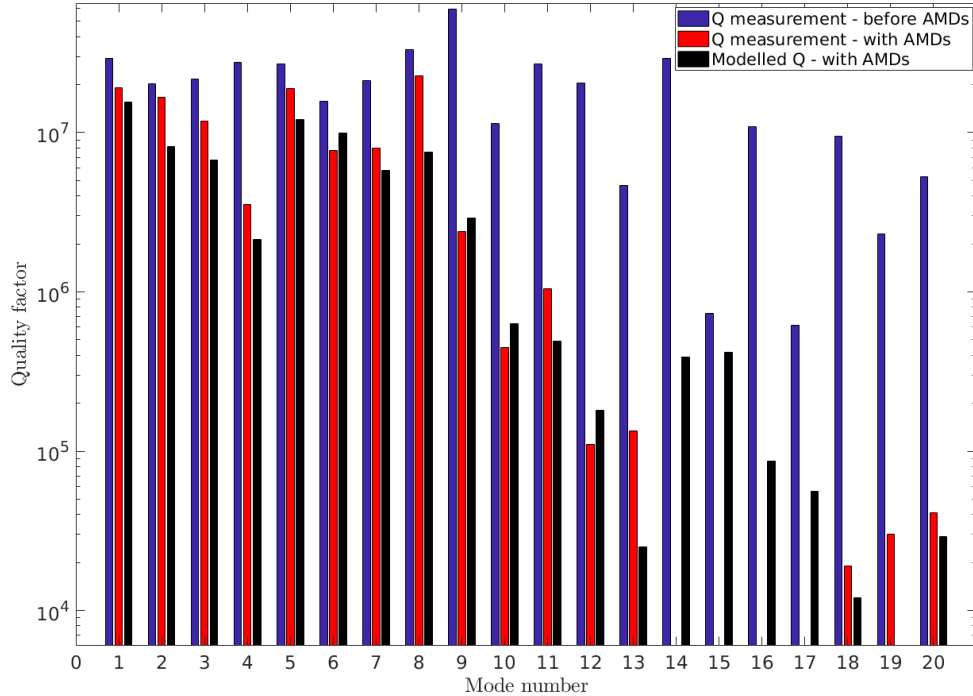


Figure 4.46: Representation of the measured quality factors without (*blue bars*) and with (*red bars*) AMDs, and comparison with the model (*black bars*). The mode numbers correspond to the mode numbers listed in table 4.11.

4.11.2 AMDs thermal noise

From the simulation presented in section 4.9.4, we expect a maximum increase of the total LIGO noise by 1.18% at 61Hz with 16 AMDs (4 AMDs per test mass). If we interpolate this result to our test case (i.e. 4 AMDs instead of 16), we expect a maximum increase in thermal noise by $\sim 0.3\%$.

The output of the locked IFO has been recorded for an extended period of time before and after the AMDs installation. The objective of these measurements is to compare the overall noise of the IFO and see if any increase is observable with the installed AMDs. However, the total noise of the IFO is mostly limited by quantum noise (see section 2.4.5), and thus the spectrum of classical noises is not directly observable. Therefore, the cross-correlation technique described in [160] is used to obtain the classical-noise spectrum hidden underneath the quantum noise. The resulting noise obtained after the cross-correlation is shown as dotted lines in figure 4.47. Overall, we observe close to identical outputs, we slightly higher noise at $\sim 80\text{Hz}$ and $\sim 110\text{Hz}$. We believe these changes are negligible and non-AMD related, as they appear at specific single frequencies. In conclusion, we see no significant addition to thermal noise after the AMDs installation.

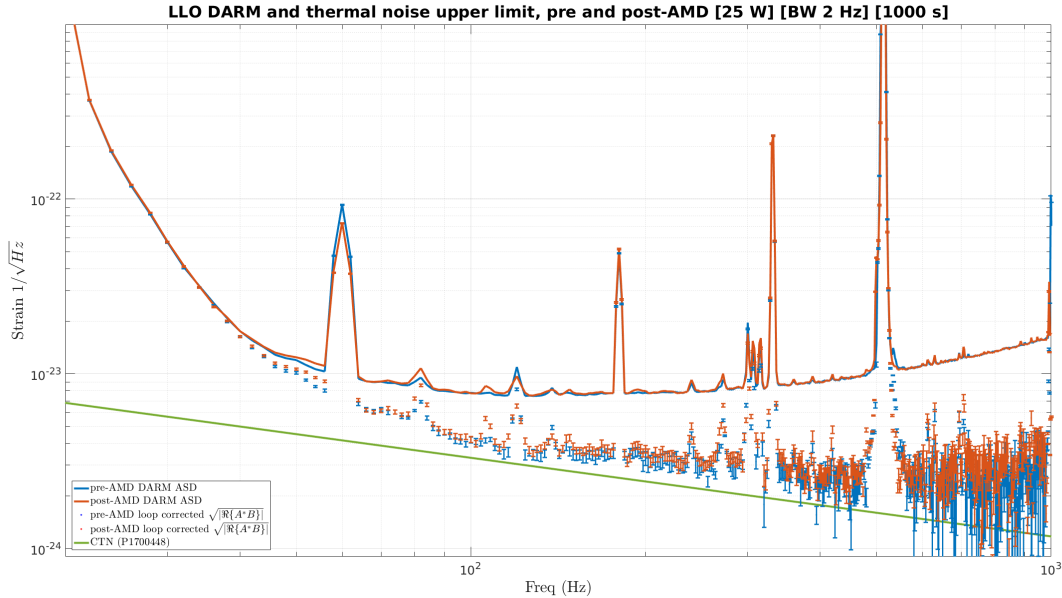


Figure 4.47: Noise spectra of the Livingston IFO pre and post-AMD. The blue and red solid lines show the total noise level of the IFO measured (classical + quantum noise). The dotted curves show the level of classical noise only, after the quantum has been subtracted via a cross-correlation technique. The solid green curve is the estimated coating thermal noise of Advanced LIGO.

4.12 Conclusion

In this chapter, we presented the problematic of parametric instabilities for large-scale interferometers and how it limits the current Advanced LIGO duty cycle and sensitivity. To mitigate this issue, the Acoustic Mode Damper device has been developed, designed and tested. The objective of the AMD is to provide broadband Q reduction to suppress parametric instabilities while limiting thermal noise increase in the LIGO detection frequency band. A suite of experimental measurements and simulations have shown that AMDs should be able to eliminate all the parametric instabilities endured by Advanced LIGO (even at full power) while limiting the amount of thermal noise to a $\sim 1\%$ increase. To verify this prediction, a first set of AMDs have been assembled and installed on one test mass of the Livingston detector. Experimental results were found to be in close agreement with our expectations.

Given the very promising results, it has been decided to install AMDs on all the LIGO test masses. At the time of writing, five out of eight test masses (four at Hanford, four at Livingston) have been populated with AMDs.

Conclusion

The first observations of gravitational waves by LIGO ushered a new era of astronomy and have uncovered information about astrophysical events that light could not give us. But gravitational-wave astronomy is still at its beginning, and a global network of advanced detectors is rapidly growing around the world. Furthermore, scientists are working hard to upgrade the LIGO detectors and mitigate the limitations encountered after the initial observation run. Indeed, we have shown that the two detectors were far from their optimal sensitivity and duty cycle due to a certain number of technical issues. In this thesis, we addressed two urgent matters regarding the improvement of LIGO duty cycle, namely the matter of earthquakes and the issue of parametric instabilities.

The biggest duty cycle limitation during O1 was due to earthquakes. We developed Seismon, an early-warning system to predict the arrival time of earthquake seismic waves at the sites and the impact they will have on the detectors. Based on this tool, different control strategies have been investigated to improve the interferometers' robustness. At the time of writing, only one out of the three strategies developed have been implemented and tested at one of the sites. This strategy improved the detector's robustness by reducing the tilt motion sensed by the LIGO seismic isolation platforms. It reduced the downtime due to earthquakes by 40% during the second LIGO observation run, which corresponds to a direct increase of the overall detector duty cycle by 1.6%. There is room for improvement in the future, as the remaining strategies still have to be tried. Also note that ground rotation sensors are currently being installed at the sites, which will open new control possibilities for future observation runs.

The second duty cycle limitation came from unstable opto-mechanical couplings in the LIGO cavities, referred to as parametric instabilities. To mitigate these instabilities, a variety of methods have been implemented during O1. Unfortunately, these methods require significant commissioning effort to function properly, reducing LIGO's effective observing time. We estimate that the tuning of the detectors to mitigate the parametric instabilities took an overall time of ~ 83 hours during O1, which represents a duty cycle reduction of 3%. Moreover, these techniques might become ineffective as LIGO interferometers go up in power. We therefore developed a device

called an Acoustic Mode Damper. This passive device requires no commissioning effort and should suppress all the parametric instabilities according to our model, even at high power. At the time of writing, Acoustic Mode Dampers have been designed, tested and are currently being installed at the sites.

Overall, the work presented in this thesis will help to improve the overall duty cycle of LIGO by 4.6% in the next run. This improvement seems rather small, but takes its full significance as a number of additional detections. During the four months period of O1, the LIGO detectors operated coincidentally 42.8% of the time and made two detections. This corresponds to a detection rate of 14.71 detections per year. By improving the duty cycle by 4.6%, the overall coincident time will go from 42.8% to 49%.⁴ Therefore, instead of making 6.3 detections per year, LIGO would make 7.2 detections per year, which corresponds to a $\sim 14\%$ increase in the number of detections.

⁴For simplicity, we assume that the duty cycle improvement of each detector by 4.6% will directly affect the coincident time, which might not necessarily be true.

Appendix A

Logistic cost function simplification

Equation 3.7 defines the logistic cost function as:

$$\theta_n := \theta_n - \alpha \frac{\partial}{\partial \theta_n} J(\theta) \quad (\text{A.1})$$

with

$$J(\Theta) = -\frac{1}{m} \sum_{i=1}^m [y^{(i)} \log(h_{\Theta}(x^{(i)})) + (1 - y^{(i)}) \log(1 - h_{\Theta}(x^{(i)}))]. \quad (\text{A.2})$$

Therefore:

$$\frac{\partial}{\partial \theta_n} J(\Theta) = -\frac{1}{m} \sum_{i=1}^m [y^{(i)} \frac{\partial}{\partial \theta_n} \log(h_{\Theta}(x^{(i)})) + (1 - y^{(i)}) \frac{\partial}{\partial \theta_n} \log(1 - h_{\Theta}(x^{(i)}))]. \quad (\text{A.3})$$

By decomposing equation A.3, we calculate:

$$\frac{\partial}{\partial \theta_n} \log(h_{\Theta}(x)) = \frac{\partial}{\partial \theta_n} \log\left(\frac{1}{1 + e^{-\Theta x}}\right) = \frac{1}{\ln(10)} \cdot \frac{x e^{-\Theta x}}{1 + e^{-\Theta x}} \quad (\text{A.4})$$

and

$$\frac{\partial}{\partial \theta_n} \log(1 - h_{\Theta}(x)) = \frac{\partial}{\partial \theta_n} \log\left(1 - \frac{1}{1 + e^{-\Theta x}}\right) = \frac{1}{\ln(10)} \cdot \frac{-x}{1 + e^{-\Theta x}}. \quad (\text{A.5})$$

Re-injecting these two expressions into equation A.3, we obtain:

$$\begin{aligned} \frac{\partial}{\partial \theta_n} J(\Theta) &= -\frac{1}{m} \sum_{i=1}^m \left[\frac{y^{(i)}}{\ln(10)} \cdot \frac{x^{(i)} e^{-\Theta x^{(i)}}}{1 + e^{-\Theta x^{(i)}}} + \frac{1 - y^{(i)}}{\ln(10)} \cdot \frac{-x^{(i)}}{1 + e^{-\Theta x^{(i)}}} \right] \\ &= -\frac{1}{m} \sum_{i=1}^m \left[\frac{x^{(i)}}{\ln(10)} \frac{1}{1 + e^{-\Theta x^{(i)}}} \cdot (y^{(i)}(1 + e^{-\Theta x^{(i)}}) - 1) \right]. \quad (\text{A.6}) \\ &= -\frac{1}{m} \sum_{i=1}^m \left[\frac{x^{(i)} h_{\Theta}(x^{(i)})}{\ln(10)} \cdot \left(\frac{y^{(i)}}{h_{\Theta}(x^{(i)})} - 1 \right) \right] = -\frac{1}{m} \sum_{i=1}^m \left[\frac{x^{(i)}}{\ln(10)} \cdot (y^{(i)} - h_{\Theta}(x^{(i)})) \right] \end{aligned}$$

Conclusion:

$$\frac{\partial}{\partial \theta_n} J(\Theta) = \frac{1}{m \cdot \ln(10)} \sum_{i=1}^m [(h_{\Theta}(x^{(i)}) - y^{(i)}) x^{(i)}]. \quad (\text{A.7})$$

Constant $\frac{1}{m \cdot \ln(10)}$ is absorbed into the α parameter of equation 3.8.

Appendix B

Radiation pressure calculation

The detailed calculation of equation 4.15. We define $G_{ret,n}^+ = E_{scat,n}G_n^+$ and $G_{ret,n}^- = E_{scat,n}G_n^-$

$$P_{rad} = \frac{2}{c} \cdot |\Psi_0 + \Psi_{ret}|^2 = \frac{2}{c} \left((\Psi_0 + \Psi_{ret}) \cdot (\Psi_0^* + \Psi_{ret}^*) \right) \quad (B.1)$$

$$= \frac{2}{c} \left(|\Psi_0|^2 + |\Psi_{ret}|^2 + \Psi_0 \Psi_{ret}^* + \Psi_0^* \Psi_{ret} \right) \quad (B.2)$$

$$\begin{aligned} &= \frac{2}{c} \left(f_0^2 |E_0|^2 + \sum_{n=0}^{\infty} f_n^2 |G_{ret,n}^+|^2 + \sum_{n=0}^{\infty} f_n^2 |G_{ret,n}^-|^2 + \sum_{n=0}^{\infty} f_n^2 G_{ret,n}^- G_{ret,n}^{+*} e^{-2j\omega_m t} \right. \\ &+ \sum_{n=0}^{\infty} f_n^2 G_{ret,n}^+ G_{ret,n}^{-*} e^{2j\omega_m t} + E_0 f_0 \sum_{n=0}^{\infty} f_n G_{ret,n}^{+*} e^{-j\omega_m t} + E_0 f_0 \sum_{n=0}^{\infty} f_n G_{ret,n}^{-*} e^{j\omega_m t} \\ &\left. + E_0^* f_0 \sum_{n=0}^{\infty} f_n G_{ret,n}^+ e^{j\omega_m t} + E_0^* f_0 \sum_{n=0}^{\infty} f_n G_{ret,n}^- e^{-j\omega_m t} \right). \quad (B.3) \end{aligned}$$

We are interested in the action of the radiation pressure at the mechanical mode frequency ω_m . Hence,

$$\begin{aligned} P_{rad,m} &= \frac{2}{c} \left(E_0 f_0 \sum_{n=0}^{\infty} f_n G_{ret,n}^{+*} e^{-j\omega_m t} + E_0 f_0 \sum_{n=0}^{\infty} f_n G_{ret,n}^{-*} e^{j\omega_m t} \right. \\ &\left. + E_0^* f_0 \sum_{n=0}^{\infty} f_n G_{ret,n}^+ e^{j\omega_m t} + E_0^* f_0 \sum_{n=0}^{\infty} f_n G_{ret,n}^- e^{-j\omega_m t} \right). \quad (B.4) \end{aligned}$$

We define:

$$z_1 = E_0 f_0 \sum_{n=0}^{\infty} f_n G_{ret,n}^{-*} e^{j\omega_m t} \quad \text{and} \quad z_2 = E_0^* f_0 \sum_{n=0}^{\infty} f_n G_{ret,n}^+ e^{j\omega_m t}. \quad (\text{B.5})$$

Equation B.4 becomes

$$\begin{aligned} P_{rad,m} &= \frac{2}{c} (z_2^* + z_1 + z_2 + z_1^*) = \frac{4}{c} (\Re(z_1) + \Re(z_2)) \\ &= \frac{4}{c} \left(E_0 f_0 \sum_{n=0}^{\infty} f_n G_{ret,n}^{-*} + E_0^* f_0 \sum_{n=0}^{\infty} f_n G_{ret,n}^+ \right) \cdot \cos(\omega_m t). \end{aligned} \quad (\text{B.6})$$

Therefore, the magnitude of the radiation pressure at the frequency ω_m is

$$|P_{rad,m}| = \frac{4}{c} \left(E_0 f_0 \sum_{n=0}^{\infty} f_n G_{ret,n}^{-*} + E_0^* f_0 \sum_{n=0}^{\infty} f_n G_{ret,n}^+ \right). \quad (\text{B.7})$$

By commodity, we write $|P_{rad,m}| = P_{rad,m}$ in the manuscript.

Appendix C

Relationship between HOM field and sideband field

The detailed calculation to go from equation 4.34 to 4.35:

$$\vec{E} = \mathbb{S} \cdot \vec{E} + \mathbb{I} \cdot \vec{E}^{SB} \quad (\text{C.1})$$

$$\mathbb{S}^{-1} \cdot \vec{E} = \mathbb{S}^{-1} \mathbb{S} \cdot \vec{E} + \mathbb{S}^{-1} \cdot \vec{E}^{SB} = \mathbb{I} \cdot \vec{E} + \mathbb{S}^{-1} \cdot \vec{E}^{SB} \quad (\text{C.2})$$

$$(\mathbb{S}^{-1} - \mathbb{I}) \cdot \vec{E} = \mathbb{S}^{-1} \cdot \vec{E}^{SB} \quad (\text{C.3})$$

$$\vec{E} = (\mathbb{S}^{-1} - \mathbb{I})^{-1} \mathbb{S}^{-1} \cdot \vec{E}^{SB} \quad (\text{C.4})$$

$$\vec{E} = (\mathbb{S}^{-1} - \mathbb{S} \mathbb{S}^{-1})^{-1} \mathbb{S}^{-1} \cdot \vec{E}^{SB} \quad (\text{C.5})$$

$$\vec{E} = (\mathbb{S}^{-1} (\mathbb{I} - \mathbb{S}))^{-1} \mathbb{S}^{-1} \cdot \vec{E}^{SB} \quad (\text{C.6})$$

$$\vec{E} = \mathbb{S} (\mathbb{I} - \mathbb{S})^{-1} \mathbb{S}^{-1} \cdot \vec{E}^{SB} \quad (\text{C.7})$$

$$\vec{E} = (\mathbb{I} - \mathbb{S})^{-1} \cdot \vec{E}^{SB} \quad (\text{C.8})$$

Appendix D

Calculation of the resistive shunt mechanical impedance

From equations 4.64 and 4.68:

$$\bar{Z}_M = \frac{1 - k_{33}^2}{1 - k_{33}^2 \left(\frac{R_{SH} C^T s}{R_{SH} C^T s + 1} \right)} \quad (\text{D.1})$$

$$= \frac{(1 - k_{33}^2)(R_{SH} C^T s + 1)}{R_{SH} C^T s + 1 - k^2 R_{SH} C^T s} \quad (\text{D.2})$$

$$= \frac{R_{SH} C^T s(1 - k_{33}^2) + 1 - k_{33}^2}{R_{SH} C^T s(1 - k_{33}^2) + 1}. \quad (\text{D.3})$$

We know that $C^S = C^T(1 - k_{33}^2)$ (equation 4.65), therefore:

$$\bar{Z}_M = \frac{R_{SH} C^S s + 1 - k_{33}^2}{R_{SH} C^S s + 1} = 1 - \frac{k_{33}^2}{R_{SH} C^S s + 1}. \quad (\text{D.4})$$

Appendix E

PZT materials tested

Material	Q	d_{33} $10^{-12}C/N$	d_{15} $10^{-12}C/N$	d_{31} $10^{-12}C/N$	k_{33}	k_{15}	d_{15}
Morgan							
PZT807	1200	260	294	93	0.69	-	0.29
PZT802	1000	250	300	97	0.64	0.55	0.30
PZT407	1200	325	480	150	0.74	0.70	0.38
PZT801	982	275	330	107	0.64	0.55	0.32
Channel							
PZT5800	1100	245	390	-107	0.67	0.60	-0.55
PZT5804	1050	240	382	-105	0.66	0.59	-0.32
PI Ceramics							
PIC181	2000	253	389	-108	0.66	0.63	0.32

Table E.1: List of all the piezoelectric materials considered for the AMD. Based on the listed characteristics in this table (from constructors), PIC181 has been selected.

Appendix F

Thermoelastic effect

A structural-thermal analysis has been conducted to confirm the effect of thermoelastic damping on the monolithic experiments. A 3D-model of the experiment is shown in figure F.1. All measurements were conducted in vacuum ($\sim 1.3\text{Pa}$) while the experiment was suspended by a wire (one-point contact).

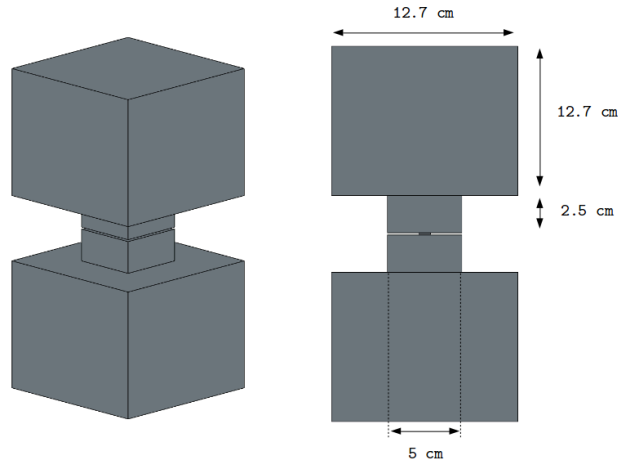


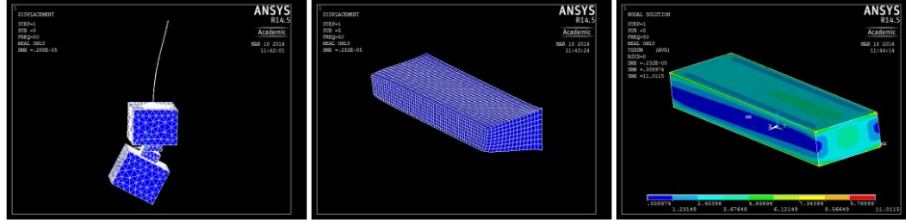
Figure F.1: Overview of one monolithic experiment used. The flexure size is $11 \times 3 \times 1.5$ mm height. The experiment is symmetric around the flexure. The experiment profile is smaller around the flexure to facilitate machining. It was suspended by a wire (single point contact).

For each mode, a FEA was resolved in harmonic regime, with an harmonic force load at the resonance frequency. The complex displacement of each element d_j is extracted, and the quality factor Q_{FEA} calculated:

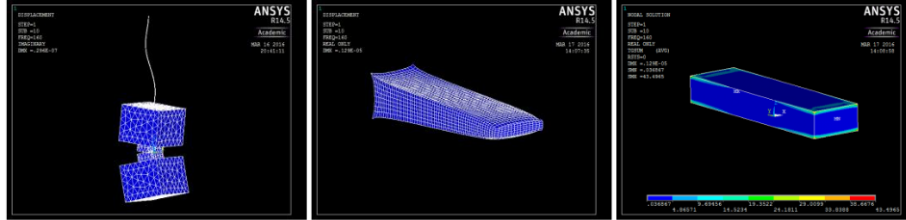
$$Q_{FEA} = \frac{\sum_{j=0}^{N_e} \Re[d_j]}{\sum_{j=0}^{N_e} \Im[d_j]} \quad (\text{F.1})$$

with N_e the total number of elements. The results are shown in figure F.2 and table F.1.

Flag-soft: (mode shape, flexure deformation, flexure thermal gradient)



Flag-stiff:



Rotation:

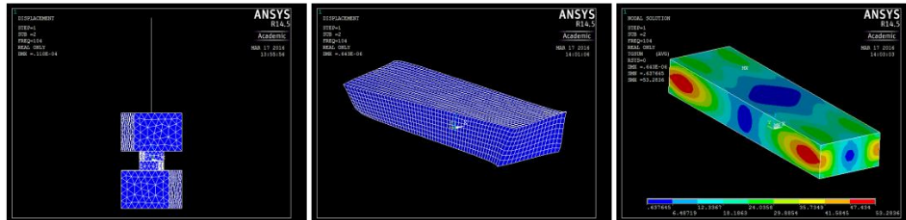


Figure F.2: Three modes have been studied, marked at 'flag soft', 'flag stiff' and 'rotation'. The mode shape is shown on the left part of the figure. The deformation of the flexure and its thermal gradient are shown next. The complex displacement is extracted and the quality factor computed.

Mode	Frequency [Hz]		Q-factor	
	Measured	FEA	Measured	FEA
Flag soft	53	55	389 ± 36	408
Rotation	100	103	1458 ± 44	1493
Flag stiff	148	157	1852 ± 46	2137

Table F.1: Comparison between the measurements and the FEA results.

Appendix G

Tuning of the mechanical oscillator

G.1 Tuning of the oscillator

The nomenclature and convention used in this section are shown in red in figure G.1.

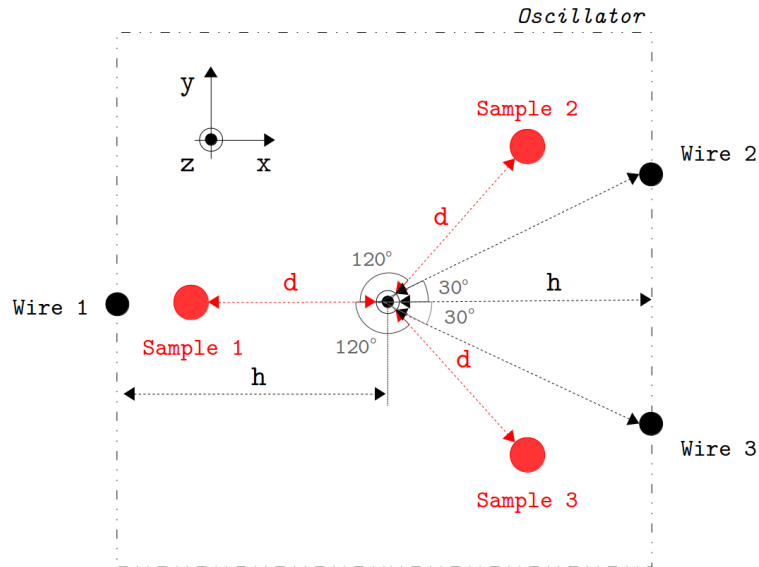


Figure G.1: Representation of the geometry and nomenclature used. The z -direction is the vertical direction. The samples are represented in red and the wires in black. Only the outline of the oscillator is shown for visibility.

The three samples are at a distance d from the oscillator's center. For the rotation mode (mode 1), the two aluminum blocks are rotating about their center of mass along the vertical axis. The resonant frequency of this mode is

$$f_{rot} = \frac{1}{2\pi} \cdot \sqrt{\frac{3k_s d^2}{I_1^z} + \frac{3k_s d^2}{I_2^z}} \quad (\text{G.1})$$

where I_1 and I_2 are the moment of inertia associated with the bottom and top mass respectively, and k_s is the stiffness of one sample in shear.

For the bending mode (mode 2), the masses are rotating around the horizontal y-axis. We assume a pure rotation about the oscillator's center of mass (no translation). The frequency of this mode is given by the following equation:

$$f_{bend} = \frac{1}{2\pi} \cdot \sqrt{\frac{3k_c d^2}{2I_1^x} + \frac{3k_c d^2}{2I_2^x}} \quad (\text{G.2})$$

where k_c is the stiffness of one sample in compression.

G.2 Tuning of the suspension

It is important to keep the resonant frequencies of the suspension and the resonant frequencies of the oscillator well separated (i.e. $f_{sus} \ll f_{osc}$) to limit the energy transferred between the two systems. Furthermore, a high-quality factor suspension (i.e. $Q_{sus} \gg 500$) is required to minimize energy dissipation in the joints.

The coupling mechanics between two modes can be understood using a 1-D model, as shown in figure G.2. The center of mass x_{cm} of the experiment serves as a reference, with $x_{cm} = 0$. We represent the geometrical overlap of modes with the coupling coefficient α , with $0 \leq \alpha \leq 1$, which determines how easily energy is transferred from a suspension mode to an oscillator mode. For example, the geometrical overlap of the yaw mode of the suspension with the rotation mode of the oscillator is $\alpha \approx 1$. On the other hand, the coupling between the pitch mode of the suspension and the rotation mode of the oscillator has $\alpha \approx 0$.

The energy dissipated per cycle by the suspension can be written as

$$W_{sus} = \oint F dx = \oint \alpha c_{sus} \dot{x}_1^2 dt = \oint \alpha c_{sus} \left(\frac{m_2}{m_1} \dot{x}_2 \right)^2 dt \quad (\text{G.3})$$

assuming a harmonic oscillator with a displacement motion of $x_2(t) = X_2 \sin(\omega t)$. Given a damping force F ,

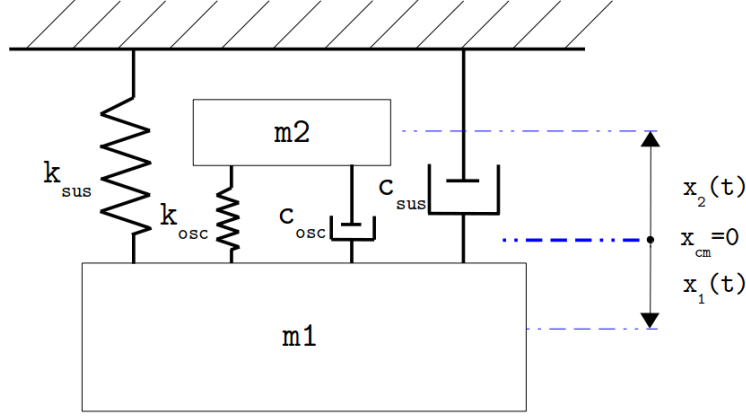


Figure G.2: Model of the coupling between one suspension mode, characterized by a stiffness k_{sus} and a damping factor c_{sus} , and an oscillator mode, characterized by a stiffness k_{osc} and a damping factor c_{osc} . The amount of energy transferred by the suspension mode to the oscillator mode is defined by the ratio α .

$$\begin{aligned} W_{sus} &= \alpha c_{sus} \left(\frac{m_2}{m_1} \right)^2 X_2^2 \omega^2 \int_0^{\frac{2\pi}{\omega}} \cos^2(\omega t) dt \\ &= \pi \omega \alpha c_{sus} \left(\frac{m_2}{m_1} \right)^2 X_2^2. \end{aligned} \quad (G.4)$$

Since

$$c_{sus} = \frac{m_1 \omega_{sus}}{Q_{sus}} \quad (G.5)$$

where ω_{sus} is the angular resonance frequency the suspension mode, we have

$$W_{sus} = \frac{\pi \omega \alpha m_1 \omega_{sus}}{Q_{sus}} \left(\frac{m_2}{m_1} \right)^2 X_2^2 \quad (G.6)$$

as the energy lost in the suspension per cycle.

Similarly, the energy lost per cycle by the oscillator itself is given by

$$W_{osc} = \oint c_{osc} \dot{x}_2^2 dt = \frac{\pi \omega m_2 \omega_{osc}}{Q_2} X_2^2. \quad (G.7)$$

Hence, the ratio of energy dissipated in the suspension to that dissipated in the oscillator is

$$\frac{W_{sus}}{W_{osc}} = \alpha \frac{Q_{osc} \omega_{sus} m_2}{Q_{sus} \omega_{osc} m_1}. \quad (\text{G.8})$$

Equation G.8 demonstrates the importance of having low-frequency suspension modes with high quality factors to limit the impact of dissipation in the suspension. It is also clear that condition $m_1 > m_2$ must hold to minimize coupling of the suspension to the oscillator.

In order to design a suspension with resonance frequencies which do not incur significant dissipation, it is useful to first compute the expected frequency of each mode of the suspension. The nomenclature and convention used to calculate the resonance frequencies are shown in black in figure G.1. The pendulum mode is defined by equation G.9, with g the gravitational acceleration and L the suspension length:

$$f_{pendulum} = \frac{1}{2\pi} \cdot \sqrt{\frac{g}{L}}. \quad (\text{G.9})$$

The yaw mode (oscillator rotating around its center of mass in the vertical axis) is defined by

$$f_{yaw} = \frac{1}{2\pi} \cdot \sqrt{\frac{11m_{osc}gh^2}{9I_{osc}^z L}} \quad (\text{G.10})$$

with m_{osc} the total mass of the oscillator, I_{osc}^z the oscillator's moment of inertia about the vertical axis and h the distance of the wires from the oscillator's center.

The bounce mode is the vertical translation of the oscillator where $k_{wire} = \frac{AE}{L}$ represents the axial stiffness of one wire (A being the cross-sectional area of the wire and E the Young's modulus):

$$f_{bounce} = \frac{1}{2\pi} \cdot \sqrt{\frac{3k_{wire}}{m}}. \quad (\text{G.11})$$

The two pitch mode frequencies are given by

$$f_{pitch_1} = \frac{1}{2\pi} \cdot \sqrt{\frac{2k_{wire}h^2}{3I_{osc}^y}} \quad (\text{G.12})$$

and

$$f_{pitch_2} = \frac{1}{2\pi} \cdot \sqrt{\frac{11k_{wire}h^2}{3I_{osc}^x}} \quad (\text{G.13})$$

with I_{osc}^x and I_{osc}^y the oscillator's moments of inertia with respect to the horizontal x and y directions.

G.2.1 Application

By taking the parameters from 4.6, and assuming $d=1.5$ cm, we obtain:

		Equation	Results [Hz]
<i>suspension</i>	Pendulum	$\frac{1}{2\pi} \cdot \sqrt{\frac{g}{L}}$	0.74
	Yaw	$\frac{1}{2\pi} \cdot \sqrt{\frac{11m_{osc}gw^2}{9I_{osc}^z L}}$	0.98
	Bounce	$\frac{1}{2\pi} \cdot \sqrt{\frac{3k_{wire}}{m}} \cdot \frac{1}{2\pi}$	33.9
	Pitch 1	$\frac{1}{2\pi} \cdot \sqrt{\frac{2k_{wire}w^2}{3I_{osc}^y}}$	13.7
	Pitch 2	$\frac{1}{2\pi} \cdot \sqrt{\frac{11k_{wire}w^2}{3I_{osc}^x}}$	40.3
<i>oscillator</i>	Rotation	$\frac{1}{2\pi} \cdot \sqrt{\frac{3k_s d^2}{I_1^z} + \frac{3k_s d^2}{I_2^z}}$	83.9
	Bend 1	$\frac{1}{2\pi} \cdot \sqrt{\frac{3k_c d^2}{2I_1^x} + \frac{3k_c d^2}{2I_2^x}}$	112.3
	Bend 2	$\frac{1}{2\pi} \cdot \sqrt{\frac{3k_c d^2}{2I_1^y} + \frac{3k_c d^2}{2I_2^y}}$	253.7
	Shear	$\frac{1}{2\pi} \cdot \sqrt{\frac{3k_s}{m_1} + \frac{3k_s}{m_2}}$	565.7

Table G.1: Analytical estimation of the suspension and oscillator modes for $d=1.5$ cm.

Modes	Pendulum	Yaw	Bounce	Pitch 1	Pitch 2
Rotation	0.021%	0.028%	0.97%	0.39%	1.15%
Bending 1	0.016%	0.021%	0.73%	0.29%	0.86%
Bending 2	0.007%	0.009%	0.32%	0.13%	0.38
Shear	0.003%	0.004%	0.15%	0.059%	0.17%

Table G.2: Estimation of the percentage of energy transferred from the suspension to the measured oscillator's modes. Estimation done for the worst case with $\alpha = 1$.

Appendix H

FEA analysis

An harmonic analysis has been done to estimate the PZT plate behavior for each AMD at low frequencies (i.e. 100Hz). This analysis is identical to the one presented in section 4.9.4 (see this section for more details). The strain $S = [S_1 S_2 S_3 S_4 S_5 S_6]^{-1}$ of all the PZT plates is extracted, and summarized in table H.1. We observe a predominant deformation in "4" direction for all the plates, which corresponds to a shear deformation in the laser beam direction).

Table H.1: Strain distribution of the PZT plates for each AMD at 100Hz.

	Strain [$\times 10^{-11}$]			
	AMD1	AMD2	AMD3	AMD4
S ₁	7.014	-5.647	1.863	0.619
S ₂	-35.33	-37.84	-46.72	-25.36
S ₃	49.28	49.28	45.30	25.33
S ₄	4956	-2792	-1513	474.2
S ₅	-9.315	13.07	12.35	-8.236
S ₆	3.063	1.724	0.785	0.246

Appendix I

Natural resonances of the AMDs

In this appendix, we list the resonance frequencies of each AMD from modal analysis. We have sorted the different mode shapes in five categories, marked as followed:

- **Flag 1:** Bending mode. Most of the energy is in the PZT plate.
- **Flag 2:** Bending mode. Most of the energy is in the PZT plate.
- **Anti-flag 1:** Bending mode. Most of the energy is in the PZT plate.
- **Anti-flag 2:** Bending mode. Most of the energy is in the PZT plate.
- **Rotation:** Rotation mode. Most of the energy is in the PZT plate. On the figure below, we notice that the mode is a little asymmetric due to the anisotropic properties of the PZT plate.

Note that we are not reporting on the modes where most of the energy is in the reaction mass (RM deformation), as these modes are less relevant for AMD performance.

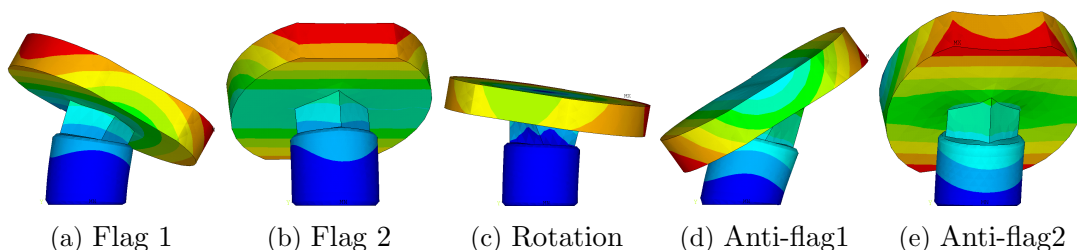


Table I.1: Frequencies of the different AMD resonance frequencies (in kHz).

	AMD1	AMD2	AMD3	AMD4
Flag 1	16.82	24.73	35.01	46.94
Flag 2	17.33	25.45	36.35	47.21
Rotation	18.14	29.99	51.11	> 80
Anti-flag 1	40.30	55.29	71.95	> 80
Anti-flag 2	43.28	62.34	76.45	> 80

Bibliography

- [1] B. Schutz, *A first course in general relativity*. Cambridge university press, 2009.
- [2] C. W. Misner, K. S. Thorne, and J. A. Wheeler, *Gravitation*. Princeton University Press, 2017.
- [3] A. Einstein, “Über Gravitationswellen,” *Sitzungsberichte der Königlich Preussischen Akademie der Wissenschaften (Berlin)*, Seite 154-167., 1918.
- [4] H. Minkowski *et al.*, “Space and time,” *The principle of relativity*, pp. 73–91, 1908.
- [5] P. R. Saulson, L. S. Collaboration, and the Virgo Collaboration, “Interferometric gravitational wave detectors,” *International Journal of Modern Physics D*, p. 1840001, 1994.
- [6] M. J. Pierce, D. L. Welch, R. D. McClure, S. van den Bergh, R. Racine, and P. B. Stetson, “The hubble constant and virgo cluster distance from observations of cepheid variables,” *Nature*, vol. 371, no. 6496, pp. 385–389, 1994.
- [7] P. Linsay, P. Saulson, R. Weiss, and S. Whitcomb, “A study of a long baseline gravitational wave antenna system,” 1983.
- [8] B. Caron, A. Dominjon, C. Drezen, R. Flaminio, X. Grave, F. Marion, L. Massonnet, C. Mehmél, R. Morand, B. Mours, *et al.*, “The virgo interferometer,” *Classical and Quantum Gravity*, vol. 14, no. 6, p. 1461, 1997.
- [9] E. Müller, M. Rampp, R. Buras, H.-T. Janka, and D. H. Shoemaker, “Toward gravitational wave signals from realistic core-collapse supernova models,” *The Astrophysical Journal*, vol. 603, no. 1, p. 221, 2004.
- [10] P. Jaranowski, A. Krolak, and B. F. Schutz, “Data analysis of gravitational-wave signals from spinning neutron stars: The signal and its detection,” *Physical Review D*, vol. 58, no. 6, p. 063001, 1998.
- [11] M. Zimmermann and E. Szedenits Jr, “Gravitational waves from rotating and precessing rigid bodies: Simple models and applications to pulsars,” *Physical Review D*, vol. 20, no. 2, p. 351, 1979.

- [12] J. Taylor, R. Manchester, and A. Lyne, “Catalog of 558 pulsars,” *The Astrophysical Journal Supplement Series*, vol. 88, pp. 529–568, 1993.
- [13] B. Abbott *et al.*, “Searches for gravitational waves from known pulsars with science run 5 ligo data,” *The Astrophysical Journal*, vol. 713, no. 1, p. 671, 2010.
- [14] B. Allen and J. D. Romano, “Detecting a stochastic background of gravitational radiation: Signal processing strategies and sensitivities,” *Physical Review D*, vol. 59, no. 10, p. 102001, 1999.
- [15] B. Abbott *et al.*, “An upper limit on the stochastic gravitational-wave background of cosmological origin,” *Nature*, vol. 460, pp. 990–4, 2009.
- [16] J. Weber, “Detection and generation of gravitational waves,” *Physical Review*, vol. 117, no. 1, p. 306, 1960.
- [17] R. Drever, “Laser interferometer gravitational radiation detectors,” in *AIP Conference Proceedings*, vol. 96, pp. 336–346, AIP, 1983.
- [18] R. Weiss, “Electromagnetically coupled broadband gravitational antenna,” tech. rep., Massachusetts Institute of Technology, Cambridge, U.S.A., 1972.
- [19] J. Miller, *On non-Gaussian beams and optomechanical parametric instabilities in interferometric gravitational wave detectors*. PhD thesis, University of Glasgow, 2010.
- [20] B. J. Meers, “Recycling in laser-interferometric gravitational-wave detectors,” *Physical Review D*, vol. 38, no. 8, p. 2317, 1988.
- [21] M. A. Arain and G. Mueller, “Design of the advanced ligo recycling cavities,” *Optics express*, vol. 16, no. 14, pp. 10018–10032, 2008.
- [22] B. Willke, P. Aufmuth, C. Aulbert, S. Babak, R. Balasubramanian, B. Barr, S. Berukoff, S. Bose, G. Cagnoli, M. M. Casey, *et al.*, “The geo 600 gravitational wave detector,” *Classical and Quantum Gravity*, vol. 19, no. 7, p. 1377, 2002.
- [23] J. Aasi, B. Abbott, R. Abbott, T. Abbott, M. Abernathy, K. Ackley, C. Adams, T. Adams, P. Addesso, R. Adhikari, *et al.*, “Advanced ligo,” *Classical and quantum gravity*, vol. 32, no. 7, p. 074001, 2015.
- [24] T. Accadia, F. Acernese, F. Antonucci, P. Astone, G. Ballardin, F. Barone, M. Barsuglia, A. Basti, T. S. Bauer, M. Bebronne, *et al.*, “Status of the virgo project,” *Classical and Quantum Gravity*, vol. 28, no. 11, p. 114002, 2011.
- [25] Y. Aso, Y. Michimura, K. Somiya, M. Ando, O. Miyakawa, T. Sekiguchi, D. Tatum, H. Yamamoto, K. Collaboration, *et al.*, “Interferometer design of the kagra gravitational wave detector,” *Physical Review D*, vol. 88, no. 4, p. 043007, 2013.

- [26] C. Unnikrishnan, “Indigo and ligo-india: scope and plans for gravitational wave research and precision metrology in india,” *International Journal of Modern Physics D*, vol. 22, no. 01, p. 1341010, 2013.
- [27] K. Danzmann, L. S. Team, *et al.*, “Lisa: Laser interferometer space antenna for gravitational wave measurements,” *Classical and Quantum Gravity*, vol. 13, no. 11A, p. A247, 1996.
- [28] B. Abbott *et al.*, “Detector description and performance for the first coincidence observations between ligo and geo,” *Nuclear Instruments and Methods in Physics Research Section A: Accelerators, Spectrometers, Detectors and Associated Equipment*, vol. 517, no. 1-3, pp. 154–179, 2004.
- [29] B. Abbott *et al.*, “Ligo: The laser interferometer gravitational-wave observatory,” *arXiv:0711.3041*, 2007.
- [30] B. Abbott *et al.*, “Ligo: the laser interferometer gravitational-wave observatory,” *Reports on Progress in Physics*, vol. 72, no. 7, p. 076901, 2009.
- [31] B. Abbott *et al.*, “Search for gravitational waves from low mass binary coalescences in the first year of ligo’s s5 data,” *Physical Review D*, vol. 79, no. 12, p. 122001, 2009.
- [32] B. Abbott *et al.*, “All-sky ligo search for periodic gravitational waves in the early fifth-science-run data,” *Physical Review Letters*, vol. 102, no. 11, p. 111102, 2009.
- [33] B. Abbott *et al.*, “Stacked search for gravitational waves from the 2006 sgr 1900+ 14 storm,” *The Astrophysical Journal Letters*, vol. 701, no. 2, p. L68, 2009.
- [34] G. M. Harry, L. S. Collaboration, *et al.*, “Advanced ligo: the next generation of gravitational wave detectors,” *Classical and Quantum Gravity*, vol. 27, no. 8, p. 084006, 2010.
- [35] J. R. Smith, L. S. Collaboration, *et al.*, “The path to the enhanced and advanced ligo gravitational-wave detectors,” *Classical and Quantum Gravity*, vol. 26, no. 11, p. 114013, 2009.
- [36] D. V. Martynov *et al.*, “The sensitivity of the advanced ligo detectors at the beginning of gravitational wave astronomy,” *arXiv:1604.00439*, 2016.
- [37] B. Abbott *et al.*, “Observation of gravitational waves from a binary black hole merger,” *Physical review letters*, vol. 116, no. 6, p. 061102, 2016.
- [38] B. Abbott *et al.*, “Gw151226: Observation of gravitational waves from a 22-solar-mass binary black hole coalescence,” *Physical Review Letters*, vol. 116, no. 24, p. 241103, 2016.

- [39] B. Abbott *et al.*, “Gw170104: Observation of a 50-solar-mass binary black hole coalescence at redshift 0.2,” *Phys. Rev. Lett.*, vol. 118, p. 221101, Jun 2017.
- [40] B. Abbott, R. Abbott, T. Abbott, F. Acernese, K. Ackley, C. Adams, T. Adams, P. Addesso, R. Adhikari, V. Adya, *et al.*, “Gw170608: Observation of a 19 solar-mass binary black hole coalescence,” *The Astrophysical Journal Letters*, vol. 851, no. 2, p. L35, 2017.
- [41] B. Abbott *et al.*, “Gw170814: A three-detector observation of gravitational waves from a binary black hole coalescence,” *Physical Review Letters*, vol. 119, no. 14, p. 141101, 2017.
- [42] B. Abbott *et al.*, “Gw170817: Observation of gravitational waves from a binary neutron star inspiral,” *Phys. Rev. Lett.*, vol. 119, p. 161101, Oct 2017.
- [43] A. Goldstein *et al.*, “An ordinary short gamma-ray burst with extraordinary implications: Fermi -gbm detection of grb 170817a,” *The Astrophysical Journal Letters*, vol. 848, no. 2, p. L14, 2017.
- [44] V. Savchenko *et al.*, “Integral detection of the first prompt gamma-ray signal coincident with the gravitational-wave event gw170817,” *The Astrophysical Journal Letters*, vol. 848, no. 2, p. L15, 2017.
- [45] P. Kwee, C. Bogan, K. Danzmann, M. Frede, H. Kim, P. King, J. Pödl, O. Puncken, R. L. Savage, F. Seifert, *et al.*, “Stabilized high-power laser system for the gravitational wave detector advanced ligo,” *Optics express*, vol. 20, no. 10, pp. 10617–10634, 2012.
- [46] R. Abbott and P. King, “Diode-pumped nd: Yag laser intensity noise suppression using a current shunt,” *Review of scientific instruments*, vol. 72, no. 2, pp. 1346–1349, 2001.
- [47] C. L. Mueller, M. A. Arain, G. Ciani, R. T. DeRosa, A. Effler, D. Feldbaum, V. V. Frolov, P. Fulda, J. Gleason, M. Heintze, *et al.*, “The advanced ligo input optics,” *Review of Scientific Instruments*, vol. 87, no. 1, p. 014502, 2016.
- [48] M. E. Zucker and S. E. Whitcomb, “Measurement of optical path fluctuations due to residual gas in the ligo 40 meter interferometer,” in *Proceedings of the Seventh Marcel Grossman Meeting on recent developments in theoretical and experimental general relativity, gravitation, and relativistic field theories*, pp. 1434–1436, 1996.
- [49] R. K. Cessaro, “Sources of primary and secondary microseisms,” *Bulletin of the Seismological Society of America*, vol. 84, no. 1, pp. 142–148, 1994.
- [50] K. Venkateswara, C. A. Hagedorn, J. H. Gundlach, J. Kissel, J. Warner, H. Radkins, T. Shaffer, B. Lantz, R. Mittleman, F. Matichard, *et al.*, “Subtracting tilt from a horizontal seismometer using a ground-rotation sensor,” *Bulletin of the Seismological Society of America*, vol. 107, no. 2, pp. 709–717, 2017.

- [51] S. Aston, M. Barton, A. Bell, N. Beveridge, B. Bland, A. Brummitt, G. Cagnoli, C. Cantley, L. Carbone, A. Cumming, *et al.*, “Update on quadruple suspension design for advanced ligo,” *Classical and Quantum Gravity*, vol. 29, no. 23, p. 235004, 2012.
- [52] F. Matichard, B. Lantz, R. Mittleman, K. Mason, J. Kissel, B. Abbott, S. Biscans, J. McIver, R. Abbott, S. Abbott, *et al.*, “Seismic isolation of advanced ligo: Review of strategy, instrumentation and performance,” *Classical and Quantum Gravity*, vol. 32, no. 18, p. 185003, 2015.
- [53] *GWINC: Gravitational-Wave Interferometer Noise Calculator*. <http://lhocds.ligo-wa.caltech.edu:8000/advligo/GWINC>.
- [54] P. R. Saulson, “Terrestrial gravitational noise on a gravitational wave antenna,” *Physical Review D*, vol. 30, no. 4, p. 732, 1984.
- [55] S. A. Hughes and K. S. Thorne, “Seismic gravity-gradient noise in interferometric gravitational-wave detectors,” *Physical Review D*, vol. 58, no. 12, p. 122002, 1998.
- [56] J. C. Driggers, J. Harms, and R. X. Adhikari, “Subtraction of newtonian noise using optimized sensor arrays,” *Physical Review D*, vol. 86, no. 10, p. 102001, 2012.
- [57] H. B. Callen and T. A. Welton, “Irreversibility and generalized noise,” *Physical Review*, vol. 83, no. 1, p. 34, 1951.
- [58] Y. Levin, “Internal thermal noise in the ligo test masses: A direct approach,” *Physical Review D*, vol. 57, no. 2, p. 659, 1998.
- [59] P. R. Saulson, “Thermal noise in mechanical experiments,” *Physical Review D*, vol. 42, no. 8, p. 2437, 1990.
- [60] G. González, “Suspensions thermal noise in the ligo gravitational wave detector,” *Classical and Quantum Gravity*, vol. 17, no. 21, p. 4409, 2000.
- [61] A. M. Gretarsson, G. M. Harry, S. D. Penn, P. R. Saulson, W. J. Startin, S. Rowan, G. Cagnoli, and J. Hough, “Pendulum mode thermal noise in advanced interferometers: a comparison of fused silica fibers and ribbons in the presence of surface loss,” *Physics Letters A*, vol. 270, no. 3, pp. 108–114, 2000.
- [62] G. M. Harry, M. R. Abernathy, A. E. Becerra-Toledo, H. Armandula, E. Black, K. Dooley, M. Eichenfield, C. Nwabugwu, A. Villar, D. Crooks, *et al.*, “Titania-doped tantala/silica coatings for gravitational-wave detection,” *Classical and Quantum Gravity*, vol. 24, no. 2, p. 405, 2006.
- [63] V. Braginsky, M. Gorodetsky, and S. Vyatchanin, “Thermodynamical fluctuations and photo-thermal shot noise in gravitational wave antennae,” *Physics Letters A*, vol. 264, no. 1, pp. 1–10, 1999.

- [64] C. M. Caves, “Quantum-mechanical noise in an interferometer,” *Physical Review D*, vol. 23, no. 8, p. 1693, 1981.
- [65] W. Edelstein, J. Hough, J. Pugh, and W. Martin, “Limits to the measurement of displacement in an interferometric gravitational radiation detector,” *Journal of Physics E: Scientific Instruments*, vol. 11, no. 7, p. 710, 1978.
- [66] M. Punturo, M. Abernathy, F. Acernese, B. Allen, N. Andersson, K. Arun, F. Barone, B. Barr, M. Barsuglia, M. Beker, *et al.*, “The third generation of gravitational wave observatories and their science reach,” *Classical and Quantum Gravity*, vol. 27, no. 8, p. 084007, 2010.
- [67] D. Martynov, E. Hall, B. Abbott, R. Abbott, T. Abbott, C. Adams, R. Adhikari, R. Anderson, S. Anderson, K. Arai, *et al.*, “Sensitivity of the advanced ligo detectors at the beginning of gravitational wave astronomy,” *Physical Review D*, vol. 93, no. 11, p. 112004, 2016.
- [68] B. Abbott, R. Abbott, T. Abbott, M. Abernathy, F. Acernese, K. Ackley, C. Adams, T. Adams, P. Addesso, R. Adhikari, *et al.*, “Observing gravitational-wave transient gw150914 with minimal assumptions,” *Physical Review D*, vol. 93, no. 12, p. 122004, 2016.
- [69] S. A. Usman, A. H. Nitz, I. W. Harry, C. M. Biwer, D. A. Brown, M. Cabero, C. D. Capano, T. Dal Canton, T. Dent, S. Fairhurst, *et al.*, “The pycbc search for gravitational waves from compact binary coalescence,” *Classical and Quantum Gravity*, vol. 33, no. 21, p. 215004, 2016.
- [70] *Instrument Science White Paper 2015*. <https://dcc.ligo.org/LIGO-T1500290>.
- [71] S. Biscans, J. Warner, R. Mittleman, C. Buchanan, M. W. Coughlin, M. Evans, H. Gabbard, J. Harms, B. Lantz, N. Mukund, *et al.*, “Control strategy to limit duty cycle impact of earthquakes on the ligo gravitational-wave detectors.,” *Classical and Quantum Gravity*, 2018.
- [72] J. Rollins, “Distributed state machine supervision for long-baseline gravitational-wave detectors,” *Review of Scientific Instruments*, vol. 87, no. 9, p. 094502, 2016.
- [73] M. Coughlin, P. Earle, J. Harms, S. Biscans, C. Buchanan, E. Coughlin, F. Donovan, J. Fee, H. Gabbard, M. Guy, *et al.*, “Limiting the effects of earthquakes on gravitational-wave interferometers,” *Classical and Quantum Gravity*, vol. 34, no. 4, p. 044004, 2017.
- [74] B. Kennett and E. Engdahl, “Traveltimes for global earthquake location and phase identification,” *Geophysical Journal International*, vol. 105, no. 2, pp. 429–465, 1991.

- [75] H. Jeffreys and K. E. Bullen, *Seismological tables*. Office of the British Association, 1958.
- [76] A. M. Dziewonski and D. L. Anderson, “Preliminary reference earth model,” *Physics of the earth and planetary interiors*, vol. 25, no. 4, pp. 297–356, 1981.
- [77] *Improving earthquake monitoring for gravitational-wave detectors with historical seismic data*. <https://dcc.ligo.org/LIGO-P1800130>.
- [78] R. Biswas, L. Blackburn, J. Cao, R. Essick, K. A. Hodge, E. Katsavounidis, K. Kim, Y.-M. Kim, E.-O. Le Bigot, C.-H. Lee, *et al.*, “Application of machine learning algorithms to the study of noise artifacts in gravitational-wave data,” *Physical Review D*, vol. 88, no. 6, p. 062003, 2013.
- [79] K. Kim, I. W. Harry, K. A. Hodge, Y.-M. Kim, C.-H. Lee, H. K. Lee, J. J. Oh, S. H. Oh, and E. J. Son, “Application of artificial neural network to search for gravitational-wave signals associated with short gamma-ray bursts,” *Classical and Quantum Gravity*, vol. 32, no. 24, p. 245002, 2015.
- [80] P. McCullagh and J. A. Nelder, “Generalized linear models, no. 37 in monograph on statistics and applied probability,” 1989.
- [81] G. H. John and P. Langley, “Estimating continuous distributions in bayesian classifiers,” in *Proceedings of the Eleventh conference on Uncertainty in artificial intelligence*, pp. 338–345, Morgan Kaufmann Publishers Inc., 1995.
- [82] C. J. Burges, “A tutorial on support vector machines for pattern recognition,” *Data mining and knowledge discovery*, vol. 2, no. 2, pp. 121–167, 1998.
- [83] C. Buchanan, *LLO Long-Term Seismic Noise Floor Study*. <https://dcc.ligo.org/LIGO-G1500516-v4>.
- [84] E. Daw, J. Giaime, D. Lormand, M. Lubinski, and J. Zweizig, “Long-term study of the seismic environment at ligo,” *Classical and Quantum Gravity*, vol. 21, no. 9, p. 2255, 2004.
- [85] F. Matichard, B. Lantz, K. Mason, R. Mittleman, B. Abbott, S. Abbott, E. Allwine, S. Barnum, J. Birch, S. Biscans, *et al.*, “Advanced ligo two-stage twelve-axis vibration isolation and positioning platform. part 2: Experimental investigation and tests results,” *Precision engineering*, vol. 40, pp. 287–297, 2015.
- [86] R. Abbott, R. Adhikari, G. Allen, S. Cowley, E. Daw, D. DeBra, J. Giaime, G. Hammond, M. Hammond, C. Hardham, *et al.*, “Seismic isolation for advanced ligo,” *Classical and Quantum Gravity*, vol. 19, no. 7, p. 1591, 2002.
- [87] R. Abbott, R. Adhikari, G. Allen, D. Baglino, C. Campbell, D. Coyne, E. Daw, D. DeBra, J. Faludi, P. Fritschel, *et al.*, “Seismic isolation enhancements for initial and advanced ligo,” *Classical and Quantum Gravity*, vol. 21, no. 5, p. S915, 2004.

- [88] B. Lantz, *Description of the Sensor Correction FIR and IIR Filter Components*, 2012. <https://dcc.ligo.org/LIGO-T1200285/public>.
- [89] W. Hua, R. Adhikari, D. B. DeBra, J. A. Giaime, G. D. Hammond, C. Hardham, M. Hennessy, J. P. How, B. T. Lantz, M. Macinnis, *et al.*, “Low-frequency active vibration isolation for advanced ligo,” in *Gravitational Wave and Particle Astrophysics Detectors*, vol. 5500, pp. 194–206, International Society for Optics and Photonics, 2004.
- [90] B. Lantz, R. Schofield, B. O’Reilly, D. Clark, and D. DeBra, “Requirements for a ground rotation sensor to improve advanced ligo,” *Bulletin of the Seismological Society of America*, vol. 99, no. 2B, pp. 980–989, 2009.
- [91] R. T. DeRosa, “Performance of active vibration isolation in the advanced ligo detectors,” 2014.
- [92] H. Bradner and M. Reichle, “Some methods for determining acceleration and tilt by use of pendulums and accelerometers,” *Bulletin of the Seismological Society of America*, vol. 63, no. 1, pp. 1–7, 1973.
- [93] V. Graizer, “Tutorial on measuring rotations using multipendulum systems,” *Bulletin of the Seismological Society of America*, vol. 99, no. 2B, pp. 1064–1072, 2009.
- [94] R. D. Peters, “Tutorial on gravitational pendulum theory applied to seismic sensing of translation and rotation,” *Bulletin of the Seismological Society of America*, vol. 99, no. 2B, pp. 1050–1063, 2009.
- [95] F. Matichard and M. Evans, “Tilt-free low-noise seismometry,” *Bulletin of the Seismological Society of America*, vol. 105, no. 2A, pp. 497–510, 2015.
- [96] M. Barton, J. Greenhalgh, and N. Robertson, *Cross-coupling in quadruple pendulum suspension*, 2004. <https://dcc.ligo.org/LIGO-T040143>.
- [97] K. Strain, *x-coupling, some thoughts*, 2011. <https://dcc.ligo.org/LIGO-T1100175>.
- [98] G. Gonzalez, *Angular Noise in GW Detectors: Thermal Noise and Cross Couplings*, 2000. <https://dcc.ligo.org/LIGO-G000182>.
- [99] A. Pele, *Length-to-angle update CSWG meeting (Sep 21st 2017)*, 2017. <https://dcc.ligo.org/LIGO-G1701848>.
- [100] M. Bouchon and K. Aki, “Strain, tilt, and rotation associated with strong ground motion in the vicinity of earthquake faults,” *Bulletin of the Seismological Society of America*, vol. 72, no. 5, pp. 1717–1738, 1982.
- [101] R. Kurdyumov, C. Kucharczyk, and B. Lantz, *Blend Switching User Guide*, 2012. <https://dcc.ligo.org/LIGO-T1200126/public>.

- [102] V. Braginsky, S. Strigin, and S. P. Vyatchanin, “Parametric oscillatory instability in fabry–perot interferometer,” *Physics Letters A*, vol. 287, no. 5, pp. 331–338, 2001.
- [103] M. Evans, L. Barsotti, and P. Fritschel, “A general approach to optomechanical parametric instabilities,” *Physics Letters A*, vol. 374, no. 4, pp. 665–671, 2010.
- [104] L. Brillouin, “Diffusion de la lumière et des rayons x par un corps transparent homogène-influence de l’agitation thermique,” in *Annales de physique*, vol. 9, pp. 88–122, EDP Sciences, 1922.
- [105] M. Evans, S. Gras, P. Fritschel, J. Miller, L. Barsotti, D. Martynov, A. Brooks, D. Coyne, R. Abbott, R. X. Adhikari, *et al.*, “Observation of parametric instability in advanced ligo,” *Physical review letters*, vol. 114, no. 16, p. 161102, 2015.
- [106] A. Siegman, *Lasers*. University Science Books, 1986.
- [107] H. Kogelnik and T. Li, “Laser beams and resonators,” *Applied optics*, vol. 5, no. 10, pp. 1550–1567, 1966.
- [108] K. Arai, *On the accumulated round-trip Gouy phase shift for a general optical cavity*. <https://dcc.ligo.org/LIGO-T1300290>.
- [109] P. Barriga, B. Bhawal, L. Ju, and D. G. Blair, “Numerical calculations of diffraction losses in advanced interferometric gravitational wave detectors,” *JOSA A*, vol. 24, no. 6, pp. 1731–1741, 2007.
- [110] S. Gras, C. Zhao, D. Blair, and L. Ju, “Parametric instabilities in advanced gravitational wave detectors,” *Classical and Quantum Gravity*, vol. 27, no. 20, p. 205019, 2010.
- [111] K. Numata, S. Otsuka, M. Ando, and K. Tsubono, “Intrinsic losses in various kinds of fused silica,” *Classical and Quantum Gravity*, vol. 19, no. 7, p. 1697, 2002.
- [112] S. D. Penn, P. H. Sneddon, H. Armandula, J. C. Betzwieser, G. Cagnoli, J. Camp, D. Crooks, M. M. Fejer, A. M. Gretarsson, G. M. Harry, *et al.*, “Mechanical loss in tantala/silica dielectric mirror coatings,” *Classical and Quantum Gravity*, vol. 20, no. 13, p. 2917, 2003.
- [113] R. Flaminio, J. Franc, C. Michel, N. Morgado, L. Pinard, and B. Sassolas, “A study of coating mechanical and optical losses in view of reducing mirror thermal noise in gravitational wave detectors,” *Classical and Quantum Gravity*, vol. 27, no. 8, p. 084030, 2010.
- [114] P. Sneddon, S. Bull, G. Cagnoli, D. Crooks, E. Elliffe, J. Faller, M. Fejer, J. Hough, and S. Rowan, “The intrinsic mechanical loss factor of hydroxycatalysis bonds for use in the mirror suspensions of gravitational wave detectors,” *Classical and Quantum Gravity*, vol. 20, no. 23, p. 5025, 2003.

- [115] J. R. Smith, G. M. Harry, J. C. Betzwieser, A. M. Gretarsson, D. A. Guild, S. E. Kittelberger, M. J. Mortonson, S. D. Penn, and P. R. Saulson, “Mechanical loss associated with silicate bonding of fused silica,” *Classical and Quantum Gravity*, vol. 20, no. 23, p. 5039, 2003.
- [116] E. E. Ungar and E. M. Kerwin Jr, “Loss factors of viscoelastic systems in terms of energy concepts,” *The Journal of the acoustical Society of America*, vol. 34, no. 7, pp. 954–957, 1962.
- [117] S. D. Penn, A. Ageev, D. Busby, G. M. Harry, A. M. Gretarsson, K. Numata, and P. Willems, “Frequency and surface dependence of the mechanical loss in fused silica,” *Physics Letters A*, vol. 352, no. 1, pp. 3–6, 2006.
- [118] *aLIGO Parametric Instabilities* *wikipedia*. <https://awiki.ligo-wa.caltech.edu/aLIGO/Parametric%20Instability>.
- [119] C. Blair, S. Gras, R. Abbott, S. Aston, J. Betzwieser, D. Blair, R. DeRosa, M. Evans, V. Frolov, P. Fritschel, *et al.*, “First demonstration of electrostatic damping of parametric instability at advanced ligo,” *Physical Review Letters*, vol. 118, no. 15, p. 151102, 2017.
- [120] S. Gras, D. Blair, and C. Zhao, “Suppression of parametric instabilities in future gravitational wave detectors using damping rings,” *Classical and Quantum Gravity*, vol. 26, no. 13, p. 135012, 2009.
- [121] S. Schediwy, C. Zhao, L. Ju, D. Blair, and P. Willems, “Observation of enhanced optical spring damping in a macroscopic mechanical resonator and application for parametric instability control in advanced gravitational-wave detectors,” *Physical Review A*, vol. 77, no. 1, p. 013813, 2008.
- [122] A. Green, D. Brown, and A. Freise, *Numerical Modelling of Parametric Instabilities*. <https://dcc.ligo.org/LIGO-G1600513>.
- [123] S. Gras, P. Fritschel, L. Barsotti, and M. Evans, “Resonant dampers for parametric instabilities in gravitational wave detectors,” *Physical Review D*, vol. 92, no. 8, p. 082001, 2015.
- [124] A. Meitzler, H. Tiersten, A. Warner, D. Berlincourt, G. Couquin, and F. Welsh III, “Ieee standard on piezoelectricity,” 1988.
- [125] T. Ikeda, *Fundamentals of Piezoelectricity*. Oxford science publications, Oxford University Press, 1996.
- [126] N. W. Hagood and A. von Flotow, “Damping of structural vibrations with piezoelectric materials and passive electrical networks,” *Journal of Sound and Vibration*, vol. 146, no. 2, pp. 243–268, 1991.
- [127] J. D. Ferry, *Viscoelastic properties of polymers*. John Wiley & Sons, 1980.

- [128] M. Lalanne, P. Berthier, and J. Der Hagopian, “Mechanical vibrations for engineers,” 1984.
- [129] N. P. Bansal and R. H. Doremus, *Handbook of glass properties*. Elsevier, 2013.
- [130] C. Zener, “Internal friction in solids,” *Proceedings of the Physical Society*, vol. 52, no. 1, p. 152, 1940.
- [131] G. Harry and J. Newport, *Mechanical Loss of TRA-DUCT 2902 Epoxy*. <https://dcc.ligo.org/LIGO-G1300207>.
- [132] *TRA-CON[®] TRA-DUCT2902 Technical Data Sheet*. https://bondlab-qa.web.cern.ch/bondlab-qa/glues/data-sheets/tra-con_tra-duct-2902.pdf.
- [133] *EPO-TEK[®] 302-3M Technical Data Sheet*. http://www.epotek.com/site/administrator/components/com_products/assets/files/Style_Uploads/302-3M.pdf.
- [134] *EPO-TEK[®] 353ND Technical Data Sheet*. http://www.epotek.com/site/administrator/components/com_products/assets/files/Style_Uploads/353ND.pdf.
- [135] *Graphite (C) Nanopowder / Nanoparticles (C, 400nm - 1.2 um, 99.9Graphite, Hydrophobic)*. <http://www.us-nano.com/inc/sdetail/145>.
- [136] *LIGO Vacuum Compatible Materials List*. <https://www.picceramic.com/en/>.
- [137] *Piezo Ceramic Technology*. <https://www.picceramic.com/en/>.
- [138] G. E. Martin, “Determination of equivalent-circuit constants of piezoelectric resonators of moderately low q by absolute-admittance measurements,” *The Journal of the Acoustical Society of America*, vol. 26, no. 3, pp. 413–420, 1954.
- [139] S. Sherrit, S. P. Leary, B. P. Dolgin, and Y. Bar-Cohen, “Comparison of the mason and klm equivalent circuits for piezoelectric resonators in the thickness mode,” in *Ultrasonics Symposium, 1999. Proceedings. 1999 IEEE*, vol. 2, pp. 921–926, IEEE, 1999.
- [140] H. N. Shekhani and K. Uchino, “Characterization of mechanical loss in piezoelectric materials using temperature and vibration measurements,” *Journal of the American Ceramic Society*, vol. 97, no. 9, pp. 2810–2814, 2014.
- [141] F. Seifert, “Resistor current noise measurements,” *Open access LIGO document LIGO-T0900200-v1*, 2009.
- [142] A. E756-98, *Standard Test Method for Measuring Vibration-Damping Properties of Materials*, 2010. <https://doi.org/10.1520/E0756-05R10>.

- [143] C. Liang, F. Sun, and C. Rogers, “An impedance method for dynamic analysis of active material systems,” *Journal of Vibration and Acoustics*, vol. 116, no. 1, pp. 120–128, 1994.
- [144] S. Oyadiji and G. Tomlinson, “Determination of the complex moduli of viscoelastic structural elements by resonance and non-resonance methods,” *Journal of Sound and Vibration*, vol. 101, no. 3, pp. 277–298, 1985.
- [145] Y. Jimbo and K. Itao, “Energy loss of a cantilever vibrator,” *Journal of the Horological Institute of Japan*, vol. 47, pp. 1–15, 1968.
- [146] A. Akanda and T. Onsay, “Material property characterization of foilback damping treatments using modified astm equations,” tech. rep., SAE Technical Paper, 2003.
- [147] H. Nouria, E. Foltête, L. Hirsinger, and S. Ballandras, “Investigation of the effects of air on the dynamic behavior of a small cantilever beam,” *Journal of Sound and Vibration*, vol. 305, no. 1, pp. 243–260, 2007.
- [148] C. L. Berli and A. Cardona, “On the calculation of viscous damping of microbeam resonators in air,” *Journal of Sound and Vibration*, vol. 327, no. 1, pp. 249–253, 2009.
- [149] S. Biscans, S. Gras, M. Evans, P. Fritschel, C. Pezerat, and P. Picart, “Method for determining damping properties of materials using a suspended mechanical oscillator,” *Journal of Sound and Vibration*, vol. 423, pp. 118 – 125, 2018.
- [150] C. Zener, “Internal friction in solids ii. general theory of thermoelastic internal friction,” *Physical Review*, vol. 53, no. 1, p. 90, 1938.
- [151] G. Cagnoli, L. Gammaitoni, J. Kovalik, F. Marchesoni, and M. Punturo, “Suspension losses in low-frequency mechanical pendulums,” *Physics Letters A*, vol. 213, no. 5-6, pp. 245–252, 1996.
- [152] R. C. Buchanan, *Ceramic materials for electronics*, vol. 68. CRC press, 2004.
- [153] T. Jordan and Z. Ounaies, “Piezoelectric ceramics characterization,” tech. rep., INSTITUTE FOR COMPUTER APPLICATIONS IN SCIENCE AND ENGINEERING HAMPTON VA, 2001.
- [154] S. Sherrit, T. J. Masys, H. D. Wiederick, and B. K. Mukherjee, “Determination of the reduced matrix of the piezoelectric, dielectric, and elastic material constants for a piezoelectric material with c_{∞} symmetry,” *IEEE transactions on ultrasonics, ferroelectrics, and frequency control*, vol. 58, no. 9, 2011.
- [155] *Plans for Detector Commissioning after O2*. <https://dcc.ligo.org/LIGO-G1701037>.

- [156] *LIGO Clean and Bake Methods and Procedures*. <https://dcc.ligo.org/LIGO-E960022>.
- [157] *In-vacuum components of the Acoustic Mode Damper for Advanced LIGO*. <https://dcc.ligo.org/LIGO-E1700421>.
- [158] J. J. Dosch, D. J. Inman, and E. Garcia, “A self-sensing piezoelectric actuator for collocated control,” *Journal of Intelligent material systems and Structures*, vol. 3, no. 1, pp. 166–185, 1992.
- [159] G. E. Simmers Jr, J. R. Hodgkins, D. D. Mascarenas, G. Park, and H. Sohn, “Improved piezoelectric self-sensing actuation,” *Journal of Intelligent Material Systems and Structures*, vol. 15, no. 12, pp. 941–953, 2004.
- [160] D. V. Martynov, V. Frolov, S. Kandhasamy, K. Izumi, H. Miao, N. Mavalvala, E. Hall, R. Lanza, B. Abbott, R. Abbott, *et al.*, “Quantum correlation measurements in interferometric gravitational-wave detectors,” *Physical Review A*, vol. 95, no. 4, p. 043831, 2017.

Titre : Optimisation du cycle de service de l'observatoire d'ondes gravitationnelles LIGO par réduction des instabilités paramétriques et des impacts environnementaux.

Mots clés : onde gravitationnelle, isolation sismique, instabilité paramétrique, matériau, contrôle.

Résumé : Le projet LIGO a pour but la détection et l'étude d'ondes gravitationnelles via un réseau de détecteurs. LIGO possède deux détecteurs d'architecture et de fonctionnement identiques, situés aux États-Unis. Chaque détecteur est une version améliorée d'un interféromètre de Michelson avec des bras optiques de 4 km de long. Ces interféromètres ont observé une onde gravitationnelle pour la première fois en septembre 2015, suivi par cinq autres détections à ce jour. Ces détections marquent le début d'une nouvelle ère pour l'astrophysique, en liaison étroite avec la physique des trous noirs et des étoiles à neutrons. Depuis, un grand nombre d'activités sont en développement pour perfectionner les interféromètres. Cette thèse a pour objectif d'améliorer le temps de service des détecteurs, en répondant en particulier à deux problématiques majeures :

le problème des impacts environnementaux, et notamment celui des tremblements de terre, ainsi que le problème lié à des couplages opto-mécaniques instables dans les cavités optiques, appelés instabilités paramétriques. Les stratégies de contrôle et les outils développés pour résoudre ces problématiques sont présentés. Les résultats préliminaires montrent une réduction du temps d'arrêt généré par les tremblements de terre d'environ 40%. De plus, le dispositif 'Acoustic Mode Damper' développé pendant la thèse devrait complètement résoudre le problème des instabilités paramétriques pour LIGO. En conclusion, il sera démontré en quoi les problématiques résolues ont permis d'améliorer le cycle de service des détecteurs de LIGO de 4,6%, ce qui correspond à une augmentation du nombre d'ondes gravitationnelles détectées par an de 14%.

Title : Optimization of the Advanced LIGO gravitational-wave detectors duty cycle by reduction of parametric instabilities and environmental impacts

Keywords : gravitational-wave, seismic isolation, parametric instability, materials, controls.

Abstract : The LIGO project is a large-scale physics experiment the goal of which is to detect and study gravitational waves of astrophysical origin. It is composed of two instruments identical in design, located in the United States. The two instruments are specialized versions of a Michelson interferometer with 4km-long arms. They observed a gravitational-wave signal for the first time in September 2015 from the merger of two stellar-mass black holes. This is the first direct detection of a gravitational wave and the first direct observation of a binary black hole merger. Five more detections from binary black hole mergers and neutron stars merger have been reported to date, marking the beginning of a new era in astrophysics. As a result of these detections, many activities are in progress to improve the duty cycle and sensitivity of the detectors.

This thesis addresses two major issues limiting the duty cycle of the LIGO detectors: environmental impacts, especially earthquakes, and the issue of unstable opto-mechanical couplings in the cavities, referred to as parametric instabilities. The control strategies and tools developed to tackle these issues are presented. Early results have shown a downtime reduction during earthquakes of ~40% at one of the LIGO sites. Moreover, the electro-mechanical device called 'Acoustic Mode Damper' designed and tested during the thesis should completely solve the issue of parametric instabilities for LIGO. In conclusion, we will show that the problems tackled in this thesis improved the overall duty cycle of LIGO by 4.6%, which corresponds to an increase of the gravitational-wave detection rate by 14%.